Probing the photointermediates of light-driven Na^+ pump KR2 by DNP-enhanced solid-state NMR

Dissertation

zur Erlangung des Doktorgrades

der Naturwissenschaften

vorgelegt beim Fachbereich 14

Biochemie, Chemie, Pharmazie der Johann Wolfgang Goethe - Universität

Frankfurt am Main

Von

Orawan Jakdetchai

aus Bangkok, Thailand

Frankfurt am Main, 2021

Dieser Arbeit wurde in der Arbeitsgruppe von Prof. Dr. Clemens Glaubitz im Institut für Biophysikalische Chemie an der Johann Wolfgang Goethe - Universität in Frankfurt am Main durchgeführt und vom Fachbereich 14 (Biochemie, Chemie und Pharmazie) als Dissertation angenommen.

Dekan: Prof. Dr. Clemens Glaubitz

1. Gutachter: Prof. Dr. Clemens Glaubitz
2. Gutachter: Prof. Dr. Josef Wachtveitl

Datum der Disputation: _____

“Learn from yesterday,

live for today,

hope for tomorrow.

The important thing is not to stop questioning.”

Albert Einstein

Table of Contents

Summary

KR2 is a light-driven sodium ion pump found in marine flavobacterium *Krokinobacter Eikastus*.[1] The protein belongs to the microbial rhodopsin family, which is characterized by seven transmembrane helices and a retinal cofactor covalently bound to a conserved lysine residue through a Schiff base linkage. Specific features of KR2 and other sodium pumping rhodopsins are the NDQ motif, the N-terminal helix capping the protein at the extracellular side, and the sodium ion bound at the protomer interface in the pentameric structure. Under physiological conditions, it functions solely as a sodium ion pump, but it can also pump small cations like lithium ions and protons. The ability to pump sodium ions was a surprising discovery since the positive charge at the Schiff base was long thought to hinder the transport of non-proton cations and the Grotthuss mechanism could not be applied to explain the Na^+ transport. Numerous efforts, including time-resolved absorption[2], Fourier transform infrared (FTIR)[3], Raman[4], solid-state nuclear magnetic resonance (ssNMR) spectroscopies[5,6], static and time-resolved crystallography[7,8], quantum mechanics/molecular mechanics (QM/MM) simulation[9], and site-directed mutagenesis[1,10], have been made to elucidate the molecular mechanism of the ion transport since the discovery of KR2 in 2013. However, fine structural details especially for the chromophore at an atomic level in the dark and intermediate states are still missing. The objective of this thesis is therefore to probe light-induced KR2 photointermediates by dynamic nuclear polarization (DNP) enhanced ssNMR. The advantage of DNP is the significant signal enhancement by which also low populated, cryo-trapped photointermediates can be probed.

The photocycle of KR2 revealed by flashed photolysis and ultrafast femtosecond absorption spectroscopy consists of consecutive intermediates, named J, K, L, M, and O.[2] After light activation, the retinal is isomerized from *all-tran*s to *13-cis* conformation. The J-state, which is known as a vibrational hot state (excited state), is formed after the relaxation from the excited state through the canonical intersection. After relaxation, the K-state which is red-shifted with respect to the dark state forms Next, a blue-shifted L-intermediate is populated, followed by the deprotonation of the Schiff base and the formation of M intermediate, which exits in equilibrium with the L-state. Thereafter, the O-intermediate occurs, which involves uptake and the transient internal binding of Na^+. The protein then releases the Na^+ and relaxes back to the dark state.

In this thesis, DNP-enhanced ssNMR was used to analyze various aspects of these intermediate states. **In chapter 5,** procedures for light-induced cryo-trapping of photointermediates are

described. The K/L-state can be generated and trapped by *in-situ* illumination inside the magnet at 110 K. The trapping of L-state together with the K-state at this temperature is unexpected as this usually leads to the trapping of only K-state in bacteriorhodopsin (BR)[11], proteorhodopsin (PR)[12], and channelrhodopsin 2 (ChR2)[13]. This observation suggests a lower energy barrier between K- and L-state in KR2. For the O-state, which has the longest lifetime, the intermediate was generated by illuminating outside the magnet, followed by rapid freezing in liquid nitrogen and transfer to the magnet. The J-state is an excited state and could not be trapped and the blue-shifted M-state, characterized by the deprotonated Schiff base, was also not detected here as its population is under the detection limit. All the intermediates were cryogenically trapped at around 100 K for the DNP detection.

Based on these procedures, the retinal conformation and the electrostatic environment at the Schiff base in KR2 dark, K-, L- and O-intermediates were probed using ^{13}C-labeled retinals bound to ^{15}N-labeled KR2 by both 1D and 2D magic angle spinning (MAS) NMR experiments. The obtained data show an *all-trans* retinal conformation with the distortion of 150° at H-C14-C15-H in the dark state whereas the retinal has a *13-cis, 15-anti* conformation in the K- and L-state after light activation. Differences between K- and L-intermediates were observed. The retinal chemical shifts of the K-state show a large deviation from the model compound behavior[14] between the middle and end part of the polyene chain. In the L-state, these differences are much less pronounced. These observations indicate that the light energy stored in the K-state dissipates into the protein in the subsequent photointermediate states. Furthermore, an additional shielding observed for C14 in L-state indicates the slight rotation toward a more compact *13-cis, 15-syn* conformation. The distortion of the H-C14-C15-H angle in the L-state (136°) is larger than in the dark state. This twist of the retinal in the L-state would play an important role in lowering the pKa of the Schiff base, which is a prerequisite for the proton transfer from the Schiff base to the proton acceptor (D116). The electrostatic environments at the Schiff base in K- and L-states causes a de-shielding of the ^{15}N nitrogen compared to the dark state. This indicates a stepwise stronger interaction with the counterion as the Schiff base proton moves away from the Schiff base and comes closer to the D116 in the transition from K- to L-state and approaches the proton transfer step during the M-state formation.

In the O-state, the retinal was found to be in the *all-trans* conformation but differed to the dark state in the C13, C20, and Schiff base nitrogen chemical shifts. The largest effects (9 ppm) was observed for the Schiff base nitrogen. The large de-shielding at the Schiff base in the O-state could be explained by the effect of the positive charge of bound Na^+ near the Schiff base in the

O-state, coordinated by N112 and D116 as observed in the O-state crystal structure in the pentameric form.[8] The binding of Na^+ at D116 carbonyl side chain may also lower the pKa of D116 and accelerate the reprotonation of the Schiff base upon O-state formation as proposed previously by the MD simulations. The additional shielding observed at C13 in the O-state is likely to arise from the interrupted charge localization from the protonated Schiff base due to a kink at C14 observed in the O-state crystal structure as well as the possible effect of the surrounding residues.[8]

In **chapter 6**, the structural change at the opsin followed the retinal isomerization and the energy transfer from the chromophore to the surrounding were investigated using various amino acids labeling schemes. First, the chemical shift changes at K255, which is covalently bound to the retinal were probed. The chemical shift perturbation at Cε-K255 indicated a *15-anti* conformation in the dark, K- and L-state but with a slight twist toward a *15-syn* conformation in the L-state. The data obtained for Cε-K255 in the K- and L-state supports the results obtained for the retinal and the Schiff base in chapter 5. Next, an effort was made to search for communication between retinal and the tryptophan residues in the KR2 retinal binding pocket that might induce further structural change. However, due to the weak dipolar coupling between the ^{13}C (C10-C15) labeled retinal atoms and $^{15}N\varepsilon$-Trp, only the dipolar coupling of $^{13}C12$ and $^{13}C14$ with $^{15}N\varepsilon$-Trp in the dark state could be unambiguously observed. Furthermore, the arginine gate (R109) separating the retinal binding pocket with the ion release cavity was probed using the dipolar coupling between $^{15}N\eta$-R109 and ^{13}C-Y247. No considerable chemical shift perturbation was observed in the intermediates. The distance between R109 and Y247 in the dark state was measured but not in the intermediates because of the peak overlapping. The data show the closing of R109 gate in the dark, K- and L-state. In the O-state, the dipolar coupling between $^{15}N\eta$-R109 and $^{13}C\beta$-Y247 was perturbed but the contact between $^{15}N\eta$-R109 and ^{13}CO-Y247 was observed, suggesting the closing of the gate also in the O-state.

Chapter 7 is dedicated to the investigation of methyl groups in the retinylidene chromophore using ^{1}H-^{13}C heteronuclear Overhauser effect (hNOE) cross relaxation in combination with cross effect (CE)-DNP.[15] First, the chemical shifts of C16, C17, and C18 methyl groups at the retinal cyclohexene ring were determined in the dark and upon light-induced cryo-trapping of the K/L states to probe for structural perturbation at the β-ionone ring. However, no chemical shift changes could be detected, but the intensity buildup for C16/C17 in the K/L-intermediates is faster than in the dark state, suggesting that the methyl rotation rate at C16/C17 might be perturbed after the isomerization. Furthermore, the dynamics of C20 was probed. The

temperature dependent hNOE buildup time of C20 methyl group in the dark state indicates a fast rotation (faster than the Larmor frequencies of ^{1}H and ^{13}C). Interestingly, the C20 exhibits a slow methyl rotation in the K-state since it was not possible to observe the signal based on hNOE whereas the C20 dynamic in the L-state is in a fast region similar to that of in the dark state. The data obtained here further support the relaxation in the L-state as also observed from the retinal chemical shift perturbation in chapter 5.

In **chapter 8,** ^{23}Na MAS NMR was applied to probe the bound Na^+ in KR2. The Na^+ bound at the extracellular protomer interface in the pentameric KR2 could be detected using one-pulse excitation. The ion was found to be in slow exchange with bulk Na^+. The [Na^+] titration curve shows the saturation of the bound Na^+ at around 100 mM NaCl and a K_d of 32 mM. The competitive titration experiments against Li^+ and K^+ show a high binding affinity to Na^+. A high [K^+] is necessary to replace the bound Na^+ whereas Li^+ is not able to replace Na^+ binding at all. The dynamics of bound Na^+ is slower than that of bulk Na^+ resulting in different T1 relaxation times, which was used for spectral filtering of the bound Na^+ population.

In summary, DNP-enhanced ssNMR was successfully applied to gain an insight into the retinal isomerization, and alterations in retinal conformation and Schiff base electrostatic environment between dark state and K-, L- and O-intermediates of KR2. Furthermore, ssNMR was also applied to probe light-induced changes directly within the opsin. However, compared to the chromophore, it was more difficult to draw a clear conclusion due to the low resolution of the acquired spectra at cryogenic temperature and the difficulties in signal assignment. The applications of ^{1}H-^{13}C hNOE in combination with CE-DNP for the study of retinylidene methyl groups and ^{23}Na MAS NMR for the study of bound Na^+ in KR2 were demonstrated as a proof-of-concept, providing a perspective for future studies.

Zusammenfassung

KR2 ist eine lichtaktivierte Natriumionenpumpe, die im Meeresflavobakterium *Krokinobacter Eikastus* entdeckt wurde.[1] Das Protein gehört der Familie der mikrobiellen Rhodopsine an, deren gemeinsame Eigenschaften durch die sieben Transmembranhelices (7TM) und den Retinal-Chromophor, der an einem konservierten Lysin über eine Schiff'sche Base gebunden ist, gekennzeichnet werden.[16,17] Für die spezielle Ionenselektivität von KR2 ist in erster Linie das einzigartige NDQ- Motiv verantwortlich. Weitere strukturelle Besonderheiten im Vergleich zu anderen Vertretern der Proteinfamilie sind die N-terminale Helix, die das Protein gegen den extrazellulären Raum abdeckt, sowie die interprotomer gebundenen Natriumionen im nativ pentameren Protein. Unter physiologischen Bedingungen funktioniert KR2 als Natriumionenpumpe, aber es kann bei niedriger vorliegender Natriumionenkonzentration auch Protonen und Lithiumionen pumpen.[1] Die Entdeckung der Funktion als Natriumionenpumpe war überraschend, da die positive Ladung der Schiff´schen Base das Durchkommen von Natriumionen verhindert und der Grotthuss-Mechanismus nicht für Natriumionen gilt. Zahlreiche Studien mittels zeitaufgelöster Absorptions-[2], FTIR-[3], Raman-[4], sowie FK-NMR Spektroskopie[5,6], Kristallstrukturanalyse[16,17], QM/MM-Simulation[9] und die ortsgerichtete Mutagenese[1,10] wurden seit dessen Entdeckung im Jahr 2013 durchgeführt, um den molekularen Mechanismus der Natriumionenpumpe aufzuklären. Trotz dieser umfangreichen Arbeiten fehlt eine detaillierte atomistische Strukturinformation insbesondere des Chromophors in den Photointermediaten. Das Ziel dieser Doktorarbeit ist es daher zur Aufklärung der Funktionsweise von KR2 durch hochaufgelöste Details beizutragen, die mittels DNP-signalverstärkter Festkörper-NMR gewonnen werden können. Ein Vorteil von Festkörper-NMR Spektroskopie ist die Möglichkeit die elektronische Umgebung eines Atoms auch in sehr großen Proteinen direkt in der Membran charakterisieren zu können. Die Signalverstärkung von DNP ermöglicht es hierbei auch wenig populierte Intermediate zu analysieren, die unter kryogenen Bedingungen eingefangen wurden.

Blitzlichtphotolyse sowie zeitaufgelöste Femtosekundenabsorptionsspektroskopie zeigen mehrere Zwischenprodukte im KR2 Fotozyklus auf, nämlich J, K, L, M und O.[1,2] Nach der Lichtaktivierung isomerisiert das Retinal-Chromophor und das J-Zwischenprodukt, das als angeregter Schwingungszustand bezeichnet wird, entsteht. Danach führt es zur Entstehung des K-Zwischenzustands. Als Nächstes entsteht der L-Zwischenzustand im Gleichgewicht mit dem M-Zwischenzustand, bei dem die Schiff´-sche Base das Proton an den Protonenakzeptor D116 abgibt. Der O-Zwischenzustand entsteht als Letztes, involviert die Aufnahme des Natriumions

und besitzt hierfür eine transiente Bindungsstelle. Danach setzt das Protein das Natriumion frei und geht zurück in den Ruhezustand.

In dieser Doktorarbeit wurde die DNP signalverstärkte Festkörper-NMR Spektroskopie eingesetzt, um KR2 Photointermediate zu analysieren. In **Kapital 5** geht es um die Untersuchung der Retinal-Konformation und die elektrostatische Umgebung der Schiff´-schen Base der KR2-Zwischenzustände mittels mehrdimensionaler NMR-Experimente. Diese Zustände wurden erzeugt durch Beleuchtung des Proteins im Magneten (K/L-Zustände) oder außerhalb des Magneten kurz vor dem Einfrieren in Flüssigstickstoff (O-Zustand). Alle Photointermediate konnten bei einer Temperatur von 110 K langfristig stabilisiert werden. Der J-Zustand konnte nicht eingefangen werden, da es sich um einen angeregten Zustand handelt und der M-Zustand konnte nicht detektiert werden, weil er nur sehr gering besetzt ist. Für die hier beschriebenen Experimente wurde verschiedene ^{13}C-Isotopen-markierte Retinale in ^{15}N-markiertes KR2 eingebaut. Die chemischen Verschiebungen der Kohlenstoffe des Retinals als auch des Stickstoffs an der Schiff´-schen Base stellen eine empfindliche spektroskopische Signatur dar mit der sich der Photozyklus verfolgen lässt. Die Daten zeigen eine *all-trans* Konformation mit einem Torsionswinkel von 150° um die H-C14-C15-H Kohlenstoffbindung im Ruhezustand und eine *13-cis, 15-anti* Konformation im K- und L-Zustand nach der Beleuchtung. Die Spektren der K- und L-intermediate unterschieden sich deutlich. Die chemischen Verschiebungen des Retinals im K-Zustand zeigen eine große Abweichung von Modell-Substanzen[14]. Im L-Zustand sind diese Abweichungen weniger stark ausgeprägt. Dies deutet auf die Übertragung der gespeicherten Energie vom Retinal im K-Zustand zum Protein im L-Zustand hin. Die chemische Verschiebung von C14 im L-Zustand weist sowohl auf eine molekulare Drehung vom K-Zustand in Richtung *13-cis, 15-syn* aber auch noch auf eine *13-cis, 15-anti* Konformation hin. Der Torsionswinkel an der Stelle H-C14-C15-H von 136° bedeutet eine weitere Drehung dieses Kettensegmentes im Vergleich zum Ruhezustand. Die damit entstehende Retinalorientierung kann auch eine Rolle bei der Übertragung des Protons durch die Verringerung des pKa-Werts der Schiff´-sche Base spielen. Die Änderung der chemischen Verschiebung des Stickstoffs der Schiff´-schen Base im K- und L-Zustand weist auf eine schrittweise Verstärkung der Interaktion zwischen Stickstoff Protonenakzeptor D116 hin, die den Übergang des Wasserstoffatoms von der Schiff´-schen Base zu D116 im M-Zustand vorbereitet.

Im O-Zustand stimmen die chemischen Verschiebungen des Retinals mit einer *all-trans* Konformation überein, die sich jedoch vom Ruhezustand an den Stellen C13, C20 und am Stickstoff der Schiff´-schen Base unterscheiden. Letzteres, die Entschirmung am Stickstoff, weist

auf den Einfluss des positiven Natriumions hin, das sich in der Nähe der Schiff´-schen Base zwischen D116 und N112 befindet, wie in der kürzlich publizierten O-Zustands-Kristallstruktur zu sehen ist.[8] Die Bindung des Natriumions könnte auch die Re-Protonierung der Schiff´-schen Base unterstützen, wie es von de MD-Simulationsdaten vorgeschlagen wurde.[9] Die beobachtete elektrostatische Abschirmung von C13 kann sowohl aus der unterbrochenen Lokalisation der positiven Ladung entstehen, denn laut der O-Zustand Kristallstruktur[8] gibt es einen Knick an der C14-Position, als auch die Folge des Einflusses umliegender Aminosäuren sein.

Das Kapitel 6 behandelt strukturellen Änderungen im Opsin als Folge der Retinal-Isomerisierung sowie der Energieübertragung vom Chromophor an die Umgebung. Hierfür wurden verschiedene Isotopenmarkierungen eingesetzt. Die chemische Verschiebung der Aminosäure K255, die direkt mit dem Retinal kovalent verbunden ist, zeigt eine 15-*anti* Konformation in K- und L-Zustand und eine leichte Drehung in die *15-syn* Richtung im L-Zustand. Diese Beobachtungen stimmen mit den am Retinal beobachteten Daten überein. Des Weiteren wurde der Kontakt zwischen Retinal und den zwei Tryptophanen in der Retinal-Bindetasche untersucht, um eine mögliche Interaktion zwischen Retinal und dem Protein zu identifizieren. Hierfür wurden TEDOR Experimente durchgeführt, um die dipolaren Kopplungen zwischen ^{13}C12 / ^{13}C14 und ^{15}Nε-Trp im Ruhezustand zu detektieren. Neue Interaktionen konnten in Photointermediaten jedoch nicht beobachtet werden, da diese zu gering besetzt waren. Weiterhin wurde R109, welches eine Schranke zwischen Retinal-Bindetasche und Freisetzungstasche der Ionen bildet, untersucht. Allerdings wurde hier keine Störung der chemischen Verschiebung in den Zwischenzuständen detektiert. Messungen der dipolaren Kopplung zwischen R109 und Y247 weisen auf eine räumliche Nähe beider Reste in K, L und O-Zuständen hin, was im Einklang mit einer geschlossenen R109-Schranke wäre.

Das Kapitel 7 beschreibt Untersuchungen an den Retinal-Methylgruppen mittels ^{1}H-^{13}C hNOE in Kombination mit CE-DNP. Als Methylsonden wurden C16/C17 und C18 am Ring des Retinals benutzt, um mögliche Änderungen am oder in der Nähe des Rings während des Photozylus zu detektieren. Es konnte allerdings keine Änderungen beobachtet werden. Jedoch erfolgt der hNOE Signalaufbau von C16/C17 in K/L schneller als im Ruhezustand, wohingegen C18 unverändert bleibt. Dies weist auf eine dynamische Änderung der Methylgruppe hin. Die Dynamik der C20-Methylgrupe im Ruhezustand wurde mittels Temperatur-abhängiger hNOE Experimente charakterisiert. Die Signalaufbau-Zeiten bei unterschiedlichen Temperaturen weisen auf eine schnelle Rotation der Methylgruppe (schneller als die Larmor-Frequenz von ^{1}H und ^{13}C) hin. Im Gegensatz zum Ruhezustand ist die C20-Rotation im K-Zustand sehr langsam, sodass keine

Signalaufbau mittels hNOE detektiert wurde. Für den L-Zustand ist das Retinal relaxiert und die C20-Rotation ist schnell genug, um die Übertragung der Polarisation durch hNOE zu ermöglichen.

Im **Kapitel 8** wird die Untersuchung von Natriumionen durch ^{23}Na MAS Festkörper-NMR beschrieben. Das gebundene Na^+ zwischen den Protomeren in der pentameren KR2 Struktur wurde mittels Ein-Puls-Anregung detektiert. Temperatur-abhängige Experimente weisen auf den langsamen Austausch zwischen den an KR2 gebundenen Natriumionen und den ungebundenen sowie oberflächlichen Na^+ hin. Natriumionen-Titrationsexperimente zeigten eine Sättigung gebundener Na^+ bei einer Konzentration von 100 mM und einen K_d-Wert von 32 mM. Bei der Zufuhr von hohen KCl Konzentration konnten die gebundenen Na^+ ersetzt werden, jedoch nicht im Fall von LiCl. Die ^{23}Na-T1 Relaxation deutet die langsamere Dynamik der gebundenen Na^+ als die der ungebundenen Na^+ an. Da der T1-Wert der gebundenen Na^+ sehr kurz ist, kann das Signal der gebundenen Na^+ durch T1-Filter-Experimente selektiv detektiert werden.

Zusammenfassend ist zu sagen, dass DNP-signalverstärkte-Festkörper-NMR Experimente erfolgreich durchgeführt wurden, um die detaillierten Retinal-Konformationänderungen und die elektrostatische Umgebung der Schiff´-schen Base im Ruhezustand, sowie in den K-, L- und O-Zuständen zu bestimmen. Die Anwendung von ^{1}H-^{13}C hNOE im Rahmen der Retinal-Methylgruppen-Studie in KR2 wurde demonstriert und die Charakterisierung von gebundenen Na^+ in KR2 konnte durch ^{23}Na MAS NMR durchgeführt werden. Die erhaltene Strukturinformation des Ruhezustands sowie der Zwischenzustände trägt zur molekularen Aufklärung des Ionen-Pumpmechanismus bei.

Chapter 1: Light-driven sodium ion pump KR2

1.1. Retinal proteins

Light is one of the most essential elements that drive biological processes in all domains of life. It is the primary energy source and is used to deliver information from the surrounding world.[18] Retinal proteins are light-sensitive photoreceptor proteins that use the bound retinal chromophore capped inside an apoprotein called opsin to receive photons from light to induce protein conformational changes that further drive biological processes. Retinal proteins can be divided into animal rhodopsins and microbial rhodopsins (Figure 1).[19,20]. All of them have a common scaffold, a seven transmembrane (7TM) helical structure with retinal bound to the lysine residue through a Schiff base linkage but share nearly no sequence similarity. Animal rhodopsins are employed in eyes and other organs of animals to perform functions involving vision and non-visual sensation of light such as circadian rhythms, body color change, and seasonal reproduction. Most animal rhodopsins contain an *11-cis* retinal, which is isomerized to an *all-trans* retinal upon light activation. The isomerization induced conformational changes activate heterotrimeric the G-protein and arrestin, triggering a downstream signal transduction cascade. They are defined as the rhodopsin-like GPCR subfamily.

On the other hand, microbial rhodopsins have an *all-trans* retinal, bound to the opsin, which is isomerized to *13-cis* conformation upon illumination.[21,22] Microbial rhodopsins have diverse functions ranging from active ion pumps, signal transduction to passive ion transport like channels (Figure 2 and Table 1). The first discovered microbial rhodopsin is bacteriorhodopsin (BR), found in Archaea, *Halobacterium salinarum,* in 1971.[23] BR acts as an outward proton pump. It is the most and intensively studied microbial rhodopsin and often serves as a model protein in many research fields. BR possesses the specific sequence motif (DTD) which is crucial for the proton transport and conserved among all other outward proton pumps in its class. Following the discovery of BR, another Archaea rhodopsin, halorhodopsin (HR) with a TSA motif was found in 1977.[24] HR was first characterized as an outward Na^+ but later proved to be an inward Cl^- pump in 1982 by Schobert and Lanyi.[25] The active ion pumping in BR and HR contributes to the formation of membrane potential and involves in the light-energy conversion process. Besides BR and HR, *H. Salinarum* also possesses two signal transduction rhodopsins, called sensory rhodopsin I and II (SRI and SRII), which are responsible for positive and negative phototaxis, respectively.[26,27] Another microbial rhodopsin from Archaea working oppositely to

BR is xenorhodopsin, which functions as an inward proton pump. It has a unique motif (WDSAPK), differently from the other proton pump (RDTDDK).[28,29]

The discovery of BR leads later to the finding of other microbial rhodopsins in *Eubacteria* and lower *Eukaryota*. Anabaena sensory rhodopsin (ASR) is the first microbial rhodopsin found in Eubacteria.[27] It acts as a sensor that activates a soluble transducer. In the group of green algae, channelrhodopsins found in the algal eye function as light-gated cation channels that depolarize plasma membrane under light absorption. The depolarization signal is transferred to the flagellar membrane to control the orientation of alga to the light source. The discovery of channelrhodopsin[30,31] has opened applications in the field of optogenetics, providing important tools for the studies of neurons.[32,33]

Metagenomic researches have further identified thousands of new microbial rhodopsins from marine bacteria, leading to the discovery of proteorhodopsin (PR)[34], an outward proton pump similar to BR found in Archaea and is one of the most abundant microbial rhodopsin found in oceans. Most PR possess DTE motif[35]. The inward Cl^- pumps (ClR) found in marine bacteria recently[36,37] are different from HR and possess an NTQ motif. However, similarly to HR, the Cl^- is located near Schiff base in the resting state, stabilizing its positive charge. Another class of microbial rhodopsin found in marine bacteria is Na^+ pump (NaR), which has a unique NDQ motif.[1] Compare to the DTD motif in BR, The proton acceptor D85 and the proton donor D96 are replaced with Asn and Gln, respectively, whereas T89 position in BR is changed to Thr in ClR and Asp in NaR.[10]

Understanding the key residues involving in the ions transports in microbial rhodopsins permits the possibility to manipulate the pumping activities.[38,39] Site directed mutagenesis was applied to convert pumping activity. By converting the proton accepter in BR, D85T pumps Cl^- inwardly similar to HR. Inoue et al. demonstrated the asymmetric functional conversion among light-driven ion pumps and proposed the functional evolution in Eubacteria.[40] Introduction of the H^+ and Cl^- pumping motifs to the NaR pumping motif leads to the successful $Na^+ \rightarrow H^+$ (Q123E-KR2) and $Na^+ \rightarrow Cl^-$ (D116T-KR2) functional conversion. In a similar way, Cl^- pumping rhodopsin can be also converted to an H^+ pump (T114D-FR). However, the attempt to reversely converse $H^+ \rightarrow Na^+$, $H^+ \rightarrow Cl^-$ and $Cl^- \rightarrow Na^+$ were unsuccessful. These data suggested that a new function is gained during natural evolution while retaining the key structural mechanism of ion transport.

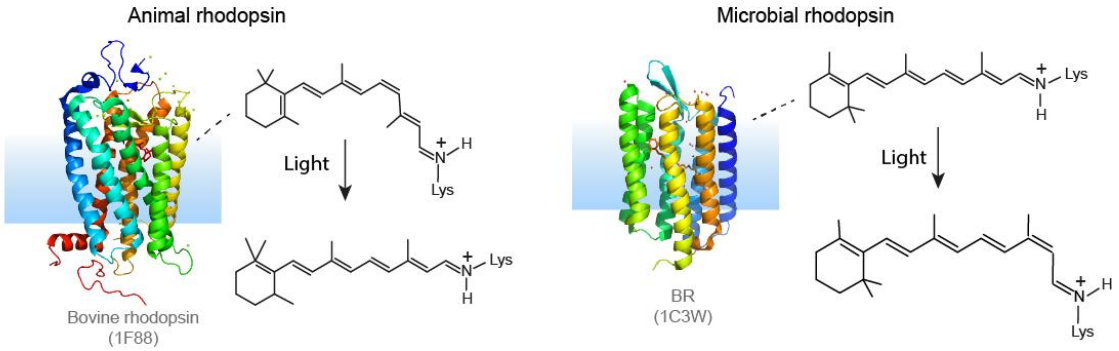

Figure 1: Animal and microbial rhodopsins. The characteristic photoisomerization upon light activation in animal and microbial rhodopsin is shown. Bovine rhodopsin, representing the proteins in the animal rhodopsins family. It possesses a *11-cis* retinal in the resting state, which isomerizes to an *all-trans* retinal upon illumination. For the microbial rhodopsins, the retinal has mostly an *all-trans* conformation in the resting state (light adapted state in bacteriorhodopsin), which converts to a *13-cis* conformation upon light activation.

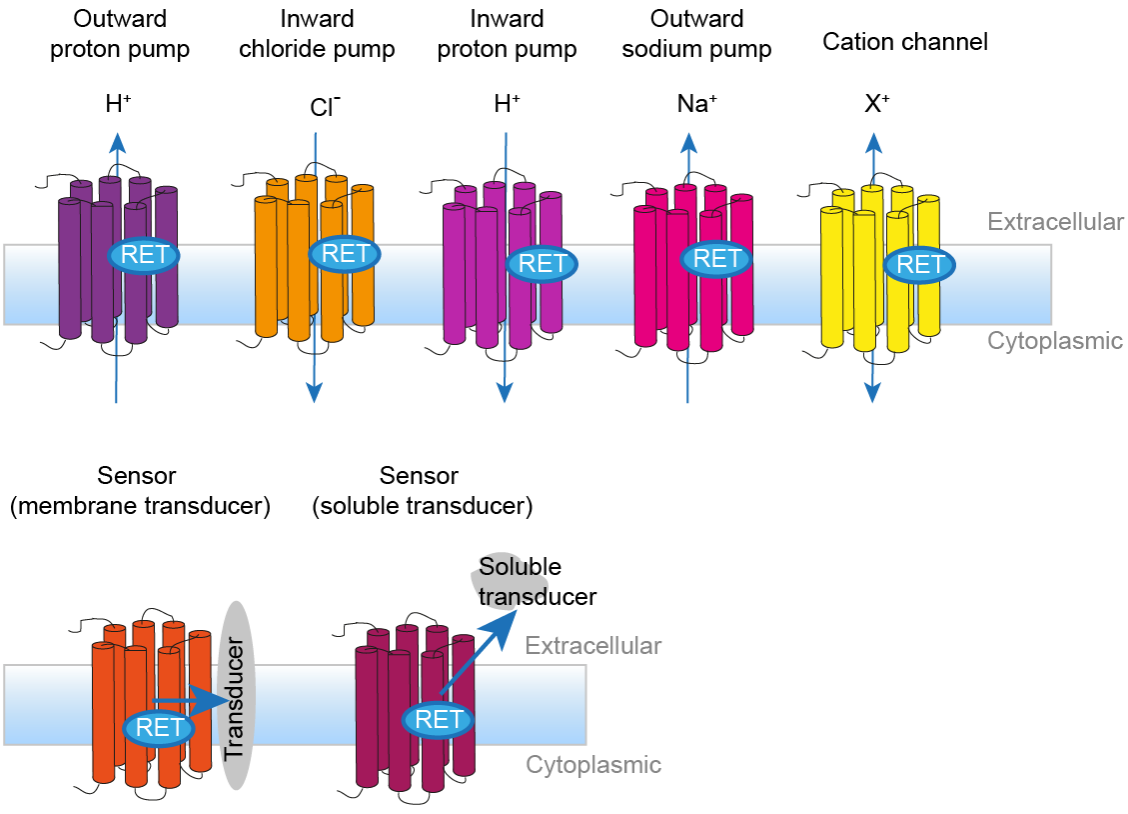

Figure 2: Functions of rhodopsins. Microbial rhodopsins have diverse functions, acting as pumps (H^+, Cl^- and Na^+), cation channels (X^+) and light-sensors. Animal rhodopsins can be classified as sensors, activating on soluble transducers.

Table 1: Microbial rhodopsin classified according to their origins.

Archaea				Algae	Eubacteria		
Outward proton pumps	Inward proton pumps	Inward Chloride pumps	Sensors	Channels	Outward proton pump	Inward Chloride pump	Sodium pump
DTD motif (helix C)	WDSAPK motif	TSA Motif (helix C)			DTD /DTX motif (helix C)	NTQ Motif (helix C)	NDQ Motif (helix C)
HsBR	NsXeR	HsHR	HvSRI	ChR1	GPR	FR	KR2
AR1		NpHR	HsSRI	ChR2	BPR	CbClR	GlNaR
AR2		SrHR	SrSRI		KR1	CsClR	NdNaR
AR3			HsSRII		NdR1	SpClR	laNaR
HwBR			HvSRII		XR		TrNaR1
			NpSRII		GR		TrNaR2

HsBR, bacteriorhodopsin from *H. salinarum*; HwBR, bacteriorhodopsin from *Haloquadratum walsbyi*. [41] NsXeR, the inward proton pump from the nanohalosarchaeon *Nanosalina*. [28] HsHR, NpHR and SrHR are halorhodopsin from *H. salinarum*, *N. pharaonic* and *S. ruber*, respectively. HvSRI, HsSRI and SrSRI are sensory rhodopsin I from *Haloarcula vallismortis*, *H. salinarum*, and *Salinibacter ruber*, respectively. HsSRII, HvSRII and NpSRII are sensory rhodopsin II from *H. salinarum*, *Haloarcula vallismortis*, *Natronomonas pharaonic*, respectively. GPR, green-absorbing proteorhodopsin; BPR, blue-absorbing proteorhodopsin. KR1, proton pump from *K. Eikastus*, NdR1, proteorhodopsin from *N. dokdonensis DSW-6*, XR, Xanthorhodopsin; GR, rhodopsin from *Gloeobacter violaceus* PCC 7421. FR, chloride-pumping rhodopsin from *Fulvimarina pelagi*; CbClR, CsClR, SpClR are ClR from *Citromicrobium bathyomarinum*, *Citromicrobium sp.* JLT1363, *Sphingopyxis baekryungensis* DSM 16222, respectively. KR2, GlNaR, NdNaR, IaNaR, TrNaR1, and TrNaR2 are NaR from *Krokinobacter Eikastus*, *Gillisia limnaea*, *Nonlabens dokdonensis*, *Indibacter alkaliphilus*, and two NaR from *Truepera radiovictrix*, respectively.[19,42] ChR1 and ChR2, light gated proton channel and cation channel from green alga *Chlamydomonas reinhardtii*, respectively.[43]

1.2. Discovery of KR2

Microbial rhodopsin family comprises a variety of functional proteins, ranging from inward and outward pumps, channels, to sensors. Before the discovery of sodium ion pumping KR2, there was no microbial rhodopsin that functions as a non-proton cation pump. The absence of the possible non-proton cation-pumping rhodopsin was based on the thought that the positive charge

of the Schiff base at the conserved lysine residue, the typical feature of all microbial rhodopsins, would hinder the transport of a non-proton cation, since the Grotthuss mechanism, employed in the case of proton pump, could not be applied. However, Inoue, et al. discovered in 2013 the first natural outward sodium ion pump in marine flavobacterium, *Krokinobacter Eikastus*.[1] A new class of microbial rhodopsins was thereafter classified, followed by the discovery of other sodium ion pumping rhodopsins (NaR).[44–47] The authors observed firstly two types of gene products functioning at the different stages of growth. The genes were subsequently cloned in *E. coli* C41(DE3) and the expressed proteins were named KR1 and KR2. KR1 is shown to be an outward proton pump, similar to BR and PR since the pH drop under illumination was observed but disappeared when the protonophore CCCP was added. KR2 was demonstrated to be a sodium ion pump as the pH increase was observed and even accelerated by CCCP under illumination. The observed pH increase is cation dependent. It increases in NaCl and LiCl buffer but decreases in KCl, RbCl, and CsCl buffer, whereas it is independent of the types of anions (NaCl, NaBr, and Na_2SO_4). These activity assays demonstrated that KR2 pumps small cations likes Na^+ and Li^+ but proton in the presence of large cations like K^+, Rb^+, and Cs^+.

Kinetic studies showed that the rate constant of proton uptake is much larger (> ~1000) than that of Na^+ uptake.[48] However, under physiological conditions, the Na^+ concentration is much greater than proton, therefore KR2 works solely as a sodium ion pump in nature. The gene expression of KR2 was shown to rise with illumination and scarcity of nutrients.[49]

1.3. Crystal structures and important residues

Since the discovery of KR2 in 2013, a number of KR2 crystal structures were reported in the protein database (PDB) mainly by two groups, Kato, et al.[16] and Gushchin and Kovalev, et al.[17,50] From the total 18 structures, 12 of them are wild type and 6 are mutants which include two potassium ion pump versions of KR2 and two monomeric mutants. The general features of KR2 are similar to those of other microbial rhodopsins and include an N-terminal helix, 7 transmembrane (TM) helices, 3 intracellular loops (ICLs), and 3 extracellular loops (ECLs) with retinal bound to the conserved lysine residue (K255) of the helix G. The 7 TM helices are bundled together and form three hydrophilic cavities, named ion uptake cavity, Schiff base cavity, and ion released cavity according to their functions. The unique structure features of KR2, which are not found in other microbial rhodopsin, are the N-terminal helix that covers the ion released cavity from the bulk solvent and the ion uptake cavity that is open to the bulk solvent.

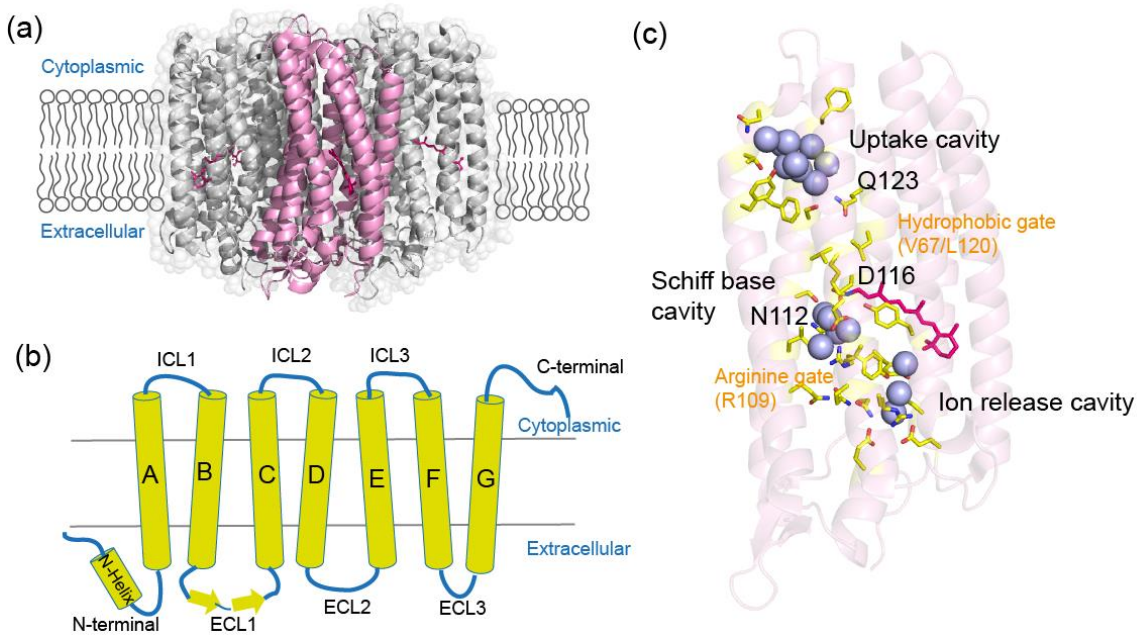

Figure 3: General structural features of KR2 in the pentameric form. (a) crystal structure crystallized at pH 8.0 (6REW), (b) Illustration of seven TM helix topology (A-G), N-terminal helix and two β-sheets at B-C loop. (c) KR2 crystal structure of the protomer, showing the NDQ motif and water-containing hydrophilic cavities, uptake cavity, Schiff base cavity and ion release cavity. The spheres illustrate the water molecules inside the cavities.

The main difference among the reported crystal structures is the crystallized pH conditions, which lead to different colors and oligomeric states, monomeric or pentameric. The protein crystallized at acidic pH (4.0) condition has a purple color with a red-shifted absorption maximum at 536 nm and forms a monomeric structure. The side chain of proton acceptor, D116, is protonated and does not form an H-bond with the Schiff base but instead with S70 and N112. The structure at acidic pH serves as the model for the M-state in which the Schiff base is deprotonated and the D116 carboxylic group is protonated. Kato, et al. showed that by soaking the crystal crystallized at pH 4.0 with a pH 8.0-9.0 buffer, the crystal changed its absorption maximum to 526 nm and two rotamers of D116 side chain were found.[51] One rotamer is the same as in the acidic crystal structure and the other one is flipped toward Schiff base and forms an H-bond. This structure was proposed to be the functional structure of the resting state at neutral pH conditions.

Kovalev, et al. demonstrated that the monomeric structure acquired at acidic conditions is distinct in several aspects from the pentameric structure, crystallized at pH 8.0, where the protein functions.[50] First, the pentameric structure crystallized at neutral or higher pH has the 7 TM

helices oriented perpendicular to the lipid membrane so that the uptake cavity protruded into the bulk solvent whereas the monomeric structure is around 70° tilted and embedded into the lipid bilayers. As a result, the ion uptake cavity of the monomeric structure is nearly closed or narrow opened as compared to the pentameric structure, which is widely opened. Second, the retinal binding cavity is expanded and larger in the pentameric structure because of the flipping away of the N112 and the arrangement of L74 that enable the accommodation of 4 water molecules inside the cavity as compared to only one water molecule found in the compact structure crystallized at the acidic condition. Three of the water molecules are well-ordered and form H-bond with the key residues D116, N112, S70, and D251. The carboxylic side chain of D116 forms an H-bond with the Schiff base like in the second rotamer observed in the neutrally soaked crystal. Third, there is a bound sodium ion found at the protomer interface in the pentameric structure. This Na^+ is demonstrated not to be essential for the ion transport by site directed mutagenesis, but it may involve in the release of ion through the replacement model by which the transport ion passes through the Schiff base to the internal Na^+ binding site and then replaces the extracellular bound Na^+, which is further released to the bulk solution. Interestingly, there is no sodium ion, which is the substrate, bound inside protein found in all crystal structures like in the case of proton and chloride ion pumps.

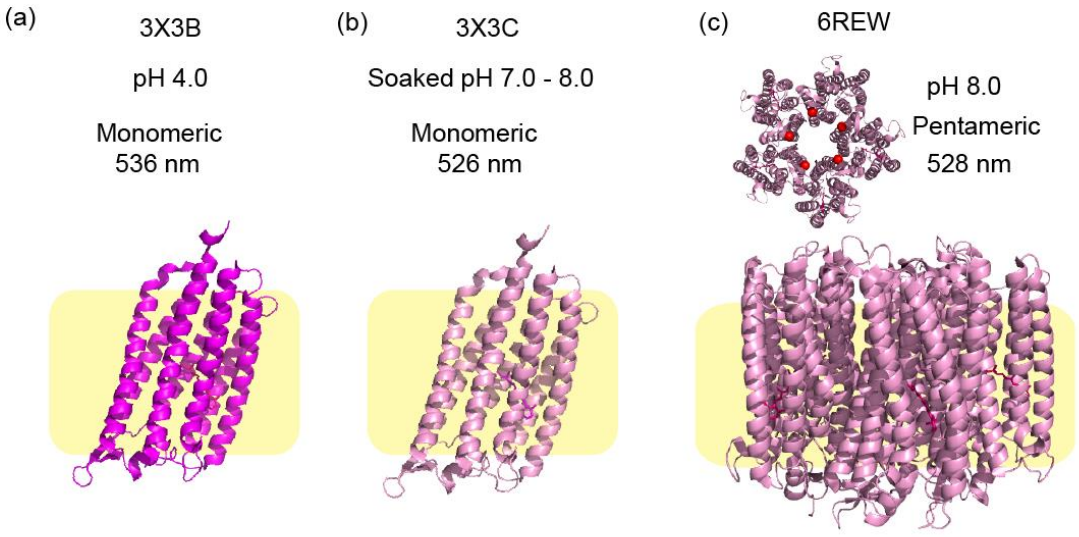

Figure 4: Comparison of reported crystal structures of KR2, crystallized at different conditions. (a) Monomeric crystal structure at acidic pH, where D116 is protonated. (b) structure of the crystal soaked with pH 8.0-9.0 buffer (The final pH is 7.0-8.0). (c) Pentameric crystal structure crystallized at pH 8.0. The bound sodium ions at the protomer interface at the extracellular side are shown as red spheres.

Recently, the crystal structure of O-state with Na^+ bound near the Schiff base was reported.[8] The O-state was generated by cryogenic trapping and continuous illumination at room temperature. Both crystals showed a similar photocycle to the reconstituted protein in lipid and gave good diffracted patterns with a resolution of 2.1 and 2.6 Å, respectively. The residual dark state was negligible as observed from the difference electron density map. The main differences between the dark state and the O-state happen in the extracellular part of helices B and C (1~1.8 Å, respectively). The minor displacement was also found in the extracellular side of helices A, D, and G (~0.7 Å). Nearly at the same time as the published O-state crystal structure, Standfuss and coworkers published crystal structures of KR2 in a time-serial manner from 800 fs to 20 ms based on time-resolved serial femtosecond X-ray crystallography (TR-SFX), giving an informative insight into how the retinal isomerized and how the sodium ion is transported through the membrane.[7] The details regarding these intermediate structures are described in section 1.4.

Table 2: KR2 Crystal structures reported on the protein data bank (PDB) by Kato et al.[16], Gushchin et al.[17], Kovalev et al.[8,50] and Skopintsev, et al.[7]

PDB Number	Crystal condition	Oligomeric state	Resolution (Å)	References
Wild type (WT)				
3X3B	pH 4.0	Monomeric	2.3	Kato, et al.
3X3C	pH 7-8	Monomeric	2.3	Kato, et al.
4XTL	pH 4.3	Monomeric	1.45	Gushchin et al.
4XTN	pH 4.9	Pentameric	2.2	Gushchin et al.
4XTO	pH 5.6	Pentameric	2.8	Gushchin et al.
6REW	pH 8.0	Pentameric	2.2	Kovalev, et al.
6REX	pH 6.0	Pentameric	2.7	Kovalev, et al.
6REZ	pH 5.0	Pentameric	2.6	Kovalev, et al.
6RF5	pH 6.0	Monomeric	2.3	Kovalev, et al.
6RF7	pH 8.9	Monomeric	2.6	Kovalev, et al.
5JRF	Iodide bound	Monomeric	2.5	Melnikov, et al.
6XYT	pH 8.0, O-state	Pentameric	2.1	Kovalev, et al.
6TK1-6	Time-resolved structures (800fs – 20 ms)	Monomeric	1.6 – 2.5	Skopintsev, et al.

G263F (K^+ pumping activity)				
6RF3	pH 8.0	Pentameric	2.4	Kovalev, et al.
6RFC	pH 4.3	Monomeric	2.0	Kovalev, et al.
S254A (K^+ pumping activity)				
6RF4	pH 8.0	Pentameric	2.4	Kovalev, et al.
6RFB	pH 4.3	Monomeric	2.1	Kovalev, et al.
Y154F (Monomeric KR2)				
6RF9	pH 8.0	Monomeric	1.8	Kovalev, et al.
H30K (monomeric KR2)				
6RFA	pH 8.0	Monomeric	2.2	Kovalev, et al.

1.3.1. Retinal binding cavity

The retinal binding cavity is located at the middle part of the protein, expanding from the hydrophobic gate L120/V67 to the R109, which separated the cavity from the ion uptake cavity and the extracellular ion release cavity, respectively. The retinal covalently bound to K255 has an *all-trans* conformation and is sandwiched between 2 tryptophan residues (W113 and W215). There are two water molecules hydrogen bonded to the tryptophan. w1 links to W113 and D251 through H-bonds and w2 coordinated W215 with the backbone oxygen of S254. Disturbing the protein at this position resulted in the gaining of K^+ pump activity in S254A and a red shifting of the protein absorption to 40 nm in P219T/254A. The cavity accommodates key residues such as D116, N112, and S70, which build the important H-bonding network with the Schiff base and the proton acceptor, D116. Mutation at these residues reduces or demolishes the pumping activity.[1]

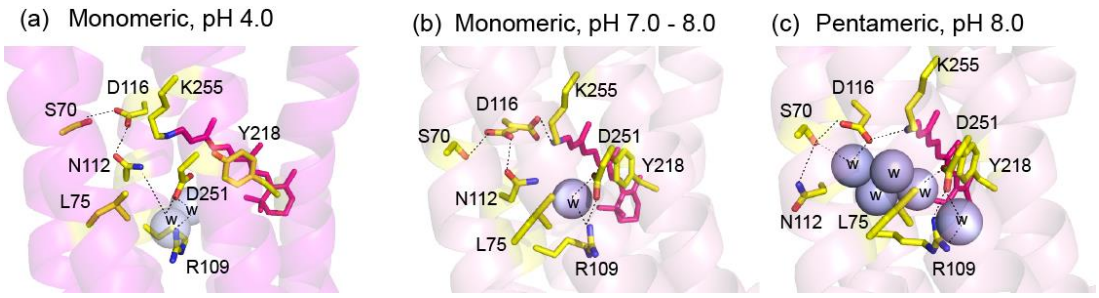

Figure 5: Details of the Schiff base cavities of KR2 crystallized at different conditions. (a) The compact structure found in the crystal at acidic condition (3X3B). (b) The two rotamers of D116 obtained after soaking the crystal to neutral condition, pH 7.0 – 8.0 (3X3C). (c) The expanded form observed in the pentameric structure (6REW). Blue spheres represent water molecules involved in H-bonds. The dashed lines indicate the H-bonding network.

Table 3: Comparison of pumping activities between KR2 wild type (WT) and mutants of the NDQ motive.[1]

KR2 Mutants	Na+	H+
N112A	×	✓
N112D	less	less
D116N	×	×
D116A	×	×
D116E	less	less
Q123A	less	less
Q123D	✓	✓
Q123E	less	✓
D251A	×	×
D251E	×	×

1.3.2. Ion uptake cavity

The uptake cavity is hydrophilic and opened in KR2, composing of hydrophilic residues like T49, N52, Y45, N61, S60, S64, and G263, and protruded from the protein surface to Q123. Q123 is part of the NDQ motive, located at the position of proton donor in BR and PR, and is believed to be involved in the uptake of transported ions. The mutation of Q123 to alanine slows down the photocycle. The cavity is separated from the retinal binding cavity through hydrophobic residues, L120 and V67. Several ordered water molecules are found in the cavity. The residue N61 and G263 are shown to play an important role in the ion selectivity. The mutation at these positions resulted in the gaining of pumping activities besides Na^+, such as K^+ and Cs^+.

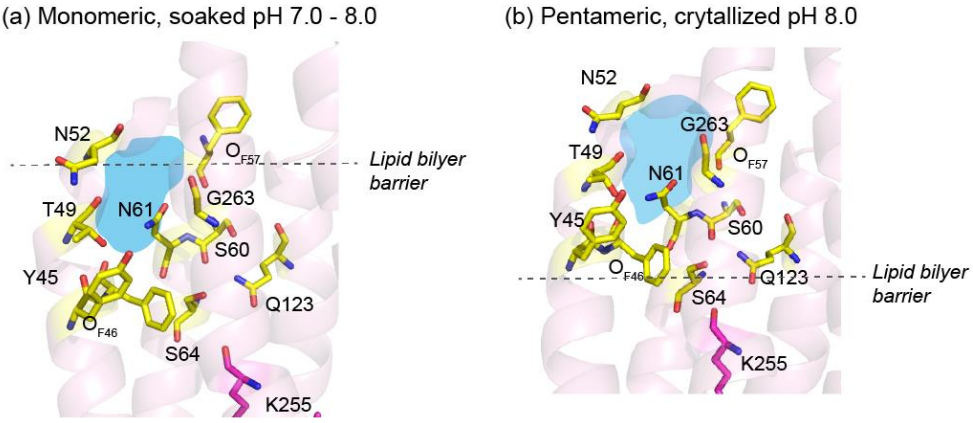

Figure 6: Ion uptake cavities in monomeric (3X3C) and pentameric crystal structures of KR2 (6REW). (a) The ion uptake cavity in monomeric KR2 embedded in the lipid bilayer boundary is smaller than

in the pentameric form. (b) Ion uptake cavity in the pentameric form crystallized at pH 8.0 protrudes in the cytoplasmic bulk and is opened. The dash line shows the lipid bilayer boundary and the blue area illustrated the water accessible area.

Table 4: Comparison of pumping activity between KR2 wild type (WT) and mutants of the ion uptake cavity.[16,17,39]

KR2 mutants	Na+	K+	Cs+
WT	✓	×	×
G263W	✓	✓	×
G263F	✓	✓	×
N61P	✓	×	×
N61P/G263F	✓	✓	×
N61P/G263W	✓	✓	×
N61L	✓	×	×
N61L/G263F	✓	✓	✓
N61L/G263W	×	×	×
N61Y	✓	✓	×
N61Y/G263F	✓	✓	×
N61Y/G263W	×	×	×
N61W	×	×	×
N61M	✓	×	×

1.3.3. Ion release cavity

The ion release cavity contains many polar residues such as Q78, Y110, Q157, N106, R243, Q244, and Y247, and several water molecules. Residue R109 separates this cavity from the retinal binding pocket to the extracellular side and the N-terminal helix shields it from bulk solvent. E11 of the N-helix forms an H-bonding cluster with D160 of helix D and R243 of helix G. The residues are shown to be important for the stability but not the function. The ECL1 (BC-loop) of KR2 differs from BR, forming an antiparallel-β-sheet, composing of 4 carboxylic acids, E90, E91, D98, D102, which oriented toward bulk solvent. These residues are not essential for the ion pumping since the substitution of these residues does not abolish the pumping activity.[1] However, it was proposed that these residues may involve in the Na^+ release pathway.[9] Recently, Kovalev, et al. proposed another alternative ion release cavity that is different from BR.[8] The second putative ion release cavity (pIRC2) is located at the between helix B and B' protomer interface at the extracellular side of the inside core of pentamer assembly, separating just only from Q78

residue. The MD simulation shows that 8 of 10 sodium ions were released from the second release cavity whereas only 2 of 10 passed through the first ion release cavity.

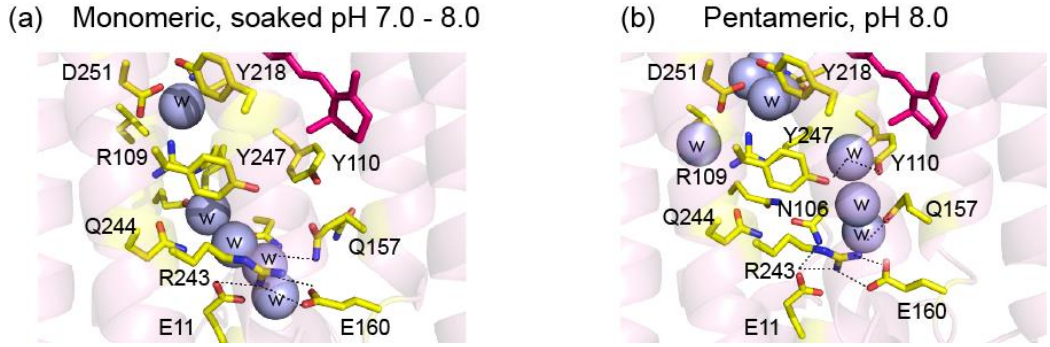

Figure 7: Ion release cavities in (a) the monomeric (crystallized at pH 4.0 and soaked with pH 8.0 - 9.0 buffer to pH 7.0 - 8.0, 3X3C) and (b) the pentameric (crystallized at pH 8.0, 6REW) crystal structures. The blue sphere and dash lines show water molecules and H-bonding networks, respectively.

Table 5: Effect of mutations at residues in loops and N-helix of KR2.

KR2 Mutants	Na+	H+	Reference
AB-loop (D54N)	✓	✓	Inoue, et al.[1]
BC-loop (E90Q/E91Q/D98N/D102N)	✓	✓	Inoue, et al.
DE-loop (E160Q)	✓	✓	Inoue, et al.
EF-loop (E191Q/E194Q)	✓	✓	Inoue, et al.
FG-loop (D231N/E237Q/D238N)	✓	✓	Inoue, et al.
E11A	✓ (unstable)	✓ (unstable)	Kato, et al.[16]
E160A	✓ (unstable)	✓ (unstable)	Kato, et al.
R243A	✓ (unstable)	✓ (unstable)	Kato, et al.

1.3.4. Oligomeric state

The oligomeric state of KR2 crystal structure depends strongly on the pH. KR2 forms a monomer at low pH and a pentamer at neutral pH. Kovalev, et al. demonstrated the importance of the oligomeric state for the pumping activity.[50] By disturbing the residues at the oligomer interface (H30K, H30L, Y154F, Y154A), a monomeric crystal structure is formed instead of a pentamer. The crystal structures of these mutants have a compact form similar to the structure crystallized at low pH except at the mutated positions. The crystal structure of the pentameric wide type, crystallized at pH 8.0 shows an extended H-bond network between protomers at the oligomer interface, both intracellular and extracellular sides. At the intracellular side, K55 and Q58 of helix B form water-mediated H.-bond with N52´ and L48´ carbonyl group of helix A´. At the extracellular side, the interactions between helices B-B´ and D-A´ were found. Moreover, a sodium ion binding side between D102 of one protomer and Y25´, $O_{F86´}$, $O_{T83´}$ of another protomer was found. The sodium ion is octahedrally coordinated with the residues and one water molecule.

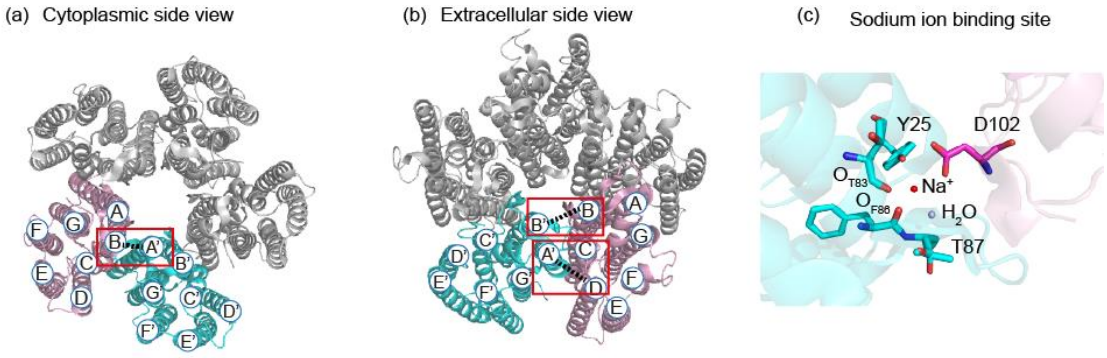

Figure 8: Oligomeric interface between protomers in the pentameric crystal structure (6REW): (a) cytoplasmic side, showing the interactions between helix B and helix A' of next protomer; (b) extracellular side view, showing the interactions between helix A' and D of the adjacent protomer; (c) extracellular sodium ion binding site.

Table 6: Mutation effect of residues at the oligomeric interface.

KR2 Mutants	Oligomeric state	Na+	Reference
H30K	Monomer	Reduced	Kovelev, et al.[50]
H30L	Monomer	Reduced and unstable	Kovelev, et al.
Y154F	Monomer	Reduced	Kovelev, et al.
Y154A	Monomer	-	Kaur, et al.[6]
H30A	✓	×	Inoue, et al.[1]
D102N	✓	✓	Kato, et al.[16]

1.4. Photocycle and the pumping mechanism.

Light activation triggers the photocycle in all retinal proteins. The proteins go stepwise through structural and conformational changes leading to diverse functions. The functions are designed by the specific architecture of each protein, evolved during the evolution. The details of photocycle and structural intermediates of BR have been intensively studied. The later discovered microbial rhodopsins are usually compared to BR in order to try to understand the unique characteristics and common features among them. BR possesses two conformations in the resting state, called dark-adapted (BR_{555}) and light-adapted (BR_{568}). The numbers indicate the absorption wavelength of the proteins. The light-adapted BR has an *all-trans* retinal conformation whereas the dark-adapted BR has a *13-cis*, *15-syn* retinal conformation which changes to an *all-trans* conformation upon light absorption. By absorbing a photon, BR goes through intermediates, named J, K, L, M_o, M_n, N, and O.

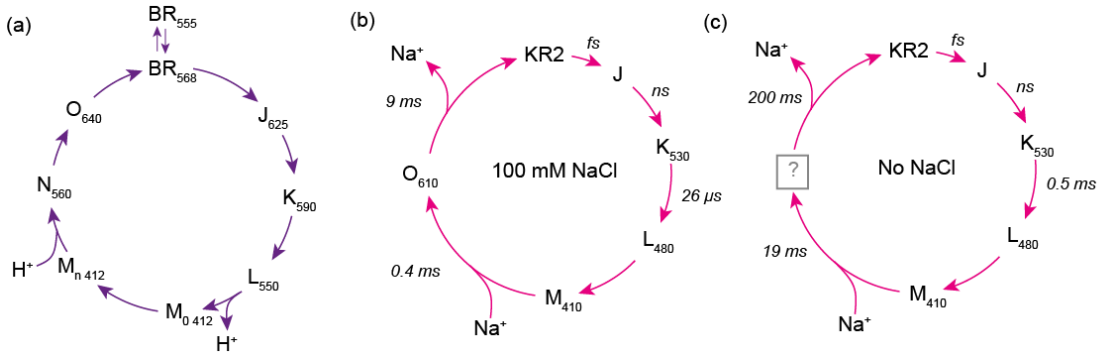

Figure 9: Photocycle of (a) bacteriorhodopsin (BR)[11] and (b) KR2 in the presence of NaCl and (c) the absence of NaCl.[52]

The non-proton cation pumping activity of KR2 has attracted a lot of interest from researchers. Numerous efforts have been made to elucidate the pumping mechanism of KR2. The photocycle was studied by various methods, including the time-resolved ultra-fast absorption[1,2,10,48,53], FTIR[3,52,54] and Raman[4] spectroscopies, QM/MM simulation[9], and time-resolved serial femtosecond crystallography (TR-SFX) using X-ray free electron laser (XFEL)[7]. The photointermediates of KR2 are named according to the intermediates of BR. Upon photon absorption J intermediate detected by time-resolved visible spectroscopy at 77 K is formed in ~200 fs[2], which is shorter than the J-state in BR (~500 fs)[55–57]. The J-state is usually known as the vibrational hot state, forming after the relaxation along the excited state through the conical intersection (CI) before it relaxes further to the ground state red-shifted K-intermediate. The blue-

shift L-intermediate is formed thereafter, following by the proton transfer from the Schiff base to the proton acceptor (D116), and the formation of M intermediate, which exits in equilibrium with the L-state. The O-intermediate with the characteristic absorption at ~600 nm is formed after the uptake of Na^+ to the transient Na^+ binding site.[52] The kinetics of O-state formation is dependent on the Na^+ concentration.[44] At last, the protein relaxes back to the dark state, involving the release of Na^+ to the bulk solution.

Skopintsev et al. reported recently the high-resolution time-resolved crystal structures of the monomeric KR2, crystallized under acidic condition and soaked with Na^+ containing buffer to increase the pH to the functional region, in 10 pump-probe delays (800 fs, 2 ps, 100 ps, 1 ns, 16 ns, 1 µs, 30 µs, 150 µs, 1 ms and 20 ms).[7] At 800 fs (+ 2ps), the retinal is fully isomerized. The rearrangements of W406 (H-bonded with N112, W113, and D251) and D116 side chain were observed, which is similar to BR but less pronounced, and the C20 methyl moved toward the helix C (instead of helix G in BR). In the ns timescale, the early conformation change in the protein backbone was observed. The C20 methyl is pushed sideways against V117. The distance between D116 and the Schiff base becomes shorter (Δ0.6 Å), favoring the proton transfer in the next step. For the µs timescale, which would correspond to the L↔M state formation, the extended structural change in helix C, following the flip of V117 was seen from the different electron density map. This step involves the uptake and Na^+ translocation. In the 1 µs structure, Y218 (helix F) and S254 (helix G) approach the position of retinal in the dark state. The D116-SB distance is widened, indicating the deprotonation of SB in the M-state. The ms timescale corresponds to the rising of O-state and involves the transient binding of Na^+. From the electron density map, it is difficult to differentiate between Na^+ and H_2O molecule, however, the environment of the interacted atoms can help to decide whether which atom or molecule is bounded. At this stage, a new density peak is observed at 2.5 Å away from N112 and D251, which is the ideally coordinated distance for Na^+ and agrees with the previously proposed binding. The authors also performed QM/MM calculation and showed that the red-shifted absorption of 55 nm is obtained if the Na^+ is bound which is in line with the experimental value of 66 nm whereas a blue-shifted absorption is predicted in the case of water binding at this position. The 20 ms structure envisions the release of Na^+, involving the rearrangement of R109 and Q78 residues. At this stage, the second binding site close to E11, N106, and E160 is found and the R243 side chain is flipped away. A new density peak at 2.4 Å and 2.5 Å from N106 and E11 is observed. The alteration at the asparagine side chain contributing to the Na^+ binding was also observed by time-resolved IR spectroscopy, with the marker band at 1688 cm^{-1}.

The pentameric crystal structure of the O-state, which crystallized at pH 8, provides valuable information to elucidate the pumping mechanism of KR2.[8] The retinal in the trapped O-state crystal shows an *all-trans* conformation with distortion at C14. The Schiff base cavity has a compact conformation with two water molecules pushed to the small cavity formed near S70 at the pentameric interface, one is moved to the Schiff base cavity 2 (SBC2) located near L75 and R109 and one remained at the same place. A bound Na^+ near the Schiff base, coordinated by the side chain of N112, D116, and S70 and the carbonyl group of V67 was found, confirming the reported results from the mutational analysis. The side chain of L74 was simultaneously flipped away upon Na^+ binding to avoid the steric effect with N112. The sodium binding is similar to the chloride ion binding site in light-driven chloride pumps, which is coordinated by N98 and T102 of the NTQ motif.

The transient Na^+ binding site in the pentameric O-state crystal structure is different from the structure from the TR-SFX, by which the Na^+ is bound between N112 and D251. This variation may arise from the oligomeric state of the crystals. Interestingly, the organizations for both uptake and release region in the O-state crystal structure are very similar to the dark state. For the uptake, a logical argument would be that after uptake of Na^+ to the transient binding site, the protein needs to rearrange the uptake region back to prevent the backflow. However, the similarity of the ion release pathway suggests an alternative pathway beside the ion release pathway via the cavity closed to E11, N106 E160 (putative iron release cavity 1, pIRC1). Indeed, the SBC2 is separated from the concave aqueous basis connect to the extracellular bulk solution in the center of the pentameric assembly, called pIRC2, just only via Q78. The pIRC2 is comprised of Q78, N81, Y108, S85, H30'and Q26' and is located near the extracellular Na^+ binding site between the protomer interface. The metadynamics simulations were performed to verify the probability of these two ion release pathways. The ion passed through the pIRC2 in 8 of 10 snapshots, by which, some replaced the bound Na^+ at the extracellular side, whereas 2 of the simulations goes through the pIRC1 and further to the bulk solution. The alternative release pathway through pIRC2 was supported also by the mutation analysis, by which the substitution of E11, E160, and R242 with alanine or non-charged residue does not abolish the pumping activity.

1.5. Aim and scope of this thesis

Since the discovery of the light-driven Na^+ pump KR2, great progress based on biochemical and biophysical methods has been achieved in understanding its molecular mechanism. Nevertheless, many open questions remain to be answered for which ssNMR methods, which permit studies directly within the lipid bilayer, offer a powerful approach. The advantage of ssNMR technique is the ability to precisely detect the fine electrostatic adjustment at an atomic level at the nuclei of interest. Together with the dynamic nuclear polarization technique, the sensitivity problem, and the difficulty to detect low populated intermediate states can be overcome. The aim of this thesis is therefore to contribute to the understanding of the molecular ion-pumping mechanism of KR2 by ssNMR spectroscopy for which four different approaches are used:

(i) The retinal conformation as well as the Schiff base-counterion interaction during the photocycle has been analyzed by applying DNP-enhanced ssNMR (chapter 5). For that, cryo-trapping protocols had to be established, which were verified using difference absorption spectroscopy. Subsequently, chemical shifts of the retinal chromophore and the Schiff base in KR2 dark state and photointermediates were determined. These data reflect the stepwise structural alterations that follow the light activation and retinal isomerization. Next, the torsion angle near the Schiff base (H-C14-C15-H) was measured to assess the possible twist of the retinal embedded in the protein pocket in the dark state and intermediates and define its role in the ion transport mechanism. The obtained data are discussed in the context of recently determined X-ray structures.

(ii) The second approach is to probe the change at the opsin after the isomerization and how light energy is transferred to the surrounding, using several specific labeling schemes (chapter 6). These include the K255 side chain, and the R109 gate separating the Schiff cavity and the ion release cavity, which was investigated based on long-range dipolar coupling with Y247 to probe the possible gate opening and closing. Furthermore, a unique pair labeling strategy using L111/N112 was also tested to search for the specific role of N112, which is a part of the NDQ motif.

(iii) The third approach is to investigate the role of β-ionone ring and the effect of light activation on the retinal methyl group dynamic in KR2 photointermediates based on ^{1}H-^{13}C heteronuclear Overhauser effect (hNOE) cross relaxation (chapter 7).

(iv) At last, the fourth approach is to probe the sodium ion binding in KR2 using ^{23}Na MAS NMR (chapter 8). The temperature dependent experiments, competitive titrations against K^+ and Li^+ and T1 measurements were performed to probe the dynamics and the binding

affinity of the sodium ion at the protomer interface of KR2. Moreover, the T1-filtered experiment was tested to suppress the unwanted bulk Na^+ signal and demonstrate the application of ^{23}Na as a potential method for the studying of Na^+ in biological samples.

Chapter 2: Solid-state NMR and Dynamic Nuclear Polarization (DNP)

2.1. Interactions in solid-state NMR

Solid-state NMR has been established to be an indispensable versatile method for structure determinations and studies of dynamics in organic, inorganic and biological systems, especially fibrils and membrane proteins.[58–71] In this thesis, ssNMR was applied as the main technique to study the functional related structure of KR2 in dark state and its photointermediates in the synthetic lipid bilayer to elucidate the ion transport mechanism and to understand how the nature converts light energy into the chemical gradient and membrane potential. The advantages of the technique include the possibility to study target membrane proteins in their native-like lipid bilayer environments and the possibility to avoid crystallizing the proteins. The technique is based on the subtle nuclear spin interactions with the surroundings, resolving to the local structural and chemical properties of the nuclei.

The nuclear spin interactions[72–74] can be divided into external and internal interactions. The external interaction is the Zeeman interaction, which is an interaction between a nuclear spin and an applied magnetic field, leading to the splitting of energy states according to the nuclear quantum number. The internal nuclear interactions consisted of different contributions and can be described as follows:

$$\hat{H}_{int} = \hat{H}_{CS} + \hat{H}_D + \hat{H}_J + \hat{H}_Q \qquad (1)$$

CS, D, J and Q are abbreviations for chemical shift, dipolar coupling, *J*-coupling, and quadrupole interactions, respectively. For the observation of ^{13}C and ^{15}N nuclei in this thesis, only the first three terms contribute to the spectra whereas for the ^{23}Na NMR spectra, the quadrupole interaction will also contribute to the Hamiltonian. The J-coupling term is usually very small compared to the other terms and is therefore often ignored in ssNMR.

Chemical shift interaction is the effect from small magnetic fields induced by circulated currents of electrons, leading to either an increase (shielding) or decrease (de-shielding) of the external magnetic field felt by the nucleus. The chemical shift interaction is orientation dependent. The anisotropy of this interaction, called chemical shift anisotropy (CSA), is important for the studies of solid samples by NMR spectroscopy. The anisotropy results from the fact that electron distributions around nuclei are rarely spherical and symmetric. Instead it can be described by a tensor typically elongated along bonds or nonbonding *p*-orbitals. The CS

Hamiltonian is shown in equation 2. The perpendicular components of the magnetic field can be ignored because the shielding field is orders of magnitude less than B_0.

$$\hat{H}_{CS} = -\gamma_I \cdot \boldsymbol{I} \cdot \overleftrightarrow{\boldsymbol{\delta}}_{\boldsymbol{LAB}} \cdot \vec{\boldsymbol{B}}_{\mathbf{0}} = -\gamma_I \cdot I_z \cdot \delta_{ZZ}^{LAB} \cdot B_0 \qquad (2)$$

$$\boldsymbol{I} = [I_x \quad I_y \quad I_z]; \qquad \vec{\boldsymbol{B}} = \begin{bmatrix} 0 \\ 0 \\ B_z \end{bmatrix}; \qquad \overleftrightarrow{\boldsymbol{\delta}}_{\boldsymbol{LAB}} = \begin{bmatrix} \delta_{xx} & \delta_{xy} & \delta_{xz} \\ \delta_{yx} & \delta_{yy} & \delta_{yz} \\ \delta_{zx} & \delta_{zy} & \delta_{zz} \end{bmatrix}$$

The Hamiltonian in the laboratory frame can be transformed into the principal axis system using Euler angles. The NMR resonance accounting for Zeeman and CS interactions can then be expressed as:

$$\omega = -\gamma B_0\left(1 + \delta_{zz}^{LAB}(\alpha, \beta)\right)$$

$$= -\gamma B_0(1 + \delta_{XX}^{PAS} sin^2\beta cos^2\alpha + \delta_{YY}^{PAS} sin^2\beta sin^2\alpha + \delta_{ZZ}^{PAS} cos^2\beta) \qquad (3)$$

The Hamiltonian can be expressed in terms of anisotropy (δ_{aniso}), and as asymmetry (η) as:

$$\hat{H}_{CS} = -\gamma_I \cdot I_z \cdot (\,\delta_{iso} + {}^1\!/_2\,\delta_{aniso}(3cos^2\beta - 1 - \eta sin^2\beta cos2\alpha)) \cdot B_0 \qquad (4)$$

where $\delta_{iso} = {}^1\!/_3\,(\delta_{XX} + \delta_{YY} + \delta_{ZZ})$ (5)

with $|\delta_{ZZ} - \delta_{iso}| > |\delta_{iso} - \delta_{XX}| > |\delta_{iso} - \delta_{YY}|$

$$\eta_{CS} = \frac{\delta_{YY} - \delta_{XX}}{\delta_{aniso}}, \qquad \delta_{aniso} = \delta_{ZZ} - \delta_{iso} \qquad (6)$$

where θ and φ are the Euler angles defining the orientation of the chemical shift tensor in the magnetic field B_0.

In liquid-state NMR, molecular tumbling is very rapid and therefore the CSA is averaged for all possible orientations, leaving only the isotropic component of the chemical shift. The situation is different in the solid-state, where the molecular tumbling is slow and restricted. CSA of different orientation will cause line broadenings of spectra. In the powder samples, a vast number of random orientations are possible and the powder pattern, depending on anisotropy, will be observed. The line broadening due to CSA can be eliminated by spinning samples at the magic angle (54.74°). The rapid spinning will average the CSA, projecting all anisotropy on the rotation axis and the magic angle will eliminate the anisotropic term, making spectra look isotropic.

Dipolar coupling interaction originates from the classical interaction between two magnetic dipole moments and therefore operates through space. The full form of the dipolar coupling interaction between spins I_j and I_k is represented in the spin Hamiltonian by the following term:

$$\hat{H}_{jk}^{D} = b_{jk}(3(\hat{I}_j \cdot e_{jk})(\hat{I}_k \cdot e_{jk}) - \hat{I}_j \cdot \hat{I}_k \quad (7)$$

$$b_{jk} = -\frac{\mu_0}{4\pi}\frac{\gamma_j \gamma_k \bar{h}}{r_{jk}^3} \quad (8)$$

e_{jk} is a unit vector parallel to the line joining the center of two nuclei. In the real system, there are more than two spins. The dipolar coupling is the ensemble of each pair of dipolar coupling and can be described as:

$$\hat{H}_{jk}^{D} = \sum_k \sum_j^{k-1} \hat{H}_{jk}^{D} \quad (9)$$

The non-secular part of dipolar coupling in high magnetic field can be ignored. The secular part of dipolar coupling interaction is different between heteronuclear and homonuclear dipolar coupling. The Hamiltonians can be formulated as:

$$\hat{H}_{jk}^{D(hetero)}(\theta) = d_{jk}(2\hat{I}_{jz}\hat{I}_{kz}) \quad (10)$$

$$\hat{H}_{jk}^{D(homo)}(\theta) = d_{jk}(3\hat{I}_{jz}\hat{I}_{kz} - \hat{I}_j \cdot \hat{I}_k) \quad (11)$$

$$d_{jk} = b_{jk}\frac{1}{2}(3cos^2\theta_{jk} - 1) \quad (12)$$

, where θ_{jk} is the angle between the vector joining the spins and the external magnetic field. The dipolar coupling interaction is axial symmetric and thus the tensor ***d*** has no antisymmetric component. The isotropic component is zero and the dipolar coupling interaction will not affect the chemical shift for liquid state NMR, even though, it is a primary cause of relaxation. In solid state, the dipolar coupling will cause a spectral splitting. The magnitude depends on the strength of the interaction and the orientation. At the magic angle ($\theta = 54.74°$), the interaction will be zero because $3cos^2\theta_{jk} - 1 = 0$. The dipolar interaction contains structural important information. Various recoupling schemes have been developed to regain specific dipolar coupling that can be used for the distance determinations as well as angle measurements.

Indirect coupling (*J* coupling) derives from a spin-spin coupling via electrons and is thus through bonds. It gives information regarding molecular level connectivity. For solution-state NMR, it is highly important, but for the solid-state NMR, it is not prominent because of its small magnitude (<< 1 kHz for small nuclei) compared to other interactions. It has actually a tensor property, ***J***, however, the anisotropy (ΔJ) is generally small and usually neglected or treated as isotropic. The contribution of the *J* coupling to the spin energy state for the nuclei *j* and *k* is given as:

$$\hat{H}_J = \boldsymbol{I} \cdot \overleftrightarrow{\boldsymbol{J}}_{IS} \cdot \boldsymbol{S} = J_{IS} I_z I_z = (J_{iso}^{IS} + \frac{1}{3}(3cos^2\beta - 1)\Delta J^{IS}) I_z S_z \quad (13)$$

For the system consisting more than one coupled spin pair, the contribution from all pairs have to be summed together. The term is orientation dependent and under MAS the anisotropy term is diminished. As the J coupling is via electron circulation, it is generally confined to intramolecular interactions, but also included the hydrogen bonds between molecules which is valuable information and can be recognized based on J-coupling interactions.

Quadrupolar coupling exists for nuclides with spin quantum number greater than ½. Quadrupolar coupling is an electric interaction (not magnetic), involving the nuclear electric *quadrupole moment*, *eQ*. The *Q* value can be positive or negative, depending on the nature of charge distribution within the nucleus. The quadrupole moment coupling with the *electric field gradient* (EFG), ***eq***, originating from the surrounding electrons. EFG is a traceless tensor. Its isotropic average value, $1/3(q_{XX} + q_{YY} + q_{ZZ})$, equals zero and thus in solution, it does not affect the resonance frequencies but still contribute to the relaxation which leads to the line broadening. In solids, it becomes important, since the quadrupole coupling constant can be as large as hundreds of megahertz. For the quadrupole nuclei in cubic symmetry, the EFG is in principle zero. The quadrupole interaction can be described using *nuclear quadrupole coupling constant*, χ, and the *quadrupolar asymmetry*, η, which are defined as:

$$\chi = \frac{e^2 Q q_{ZZ}}{h} \qquad (14)$$

$$\eta = \frac{q_{YY} - q_{XX}}{q_{ZZ}} \qquad (15)$$

The Hamiltonian for the quadrupole interaction can be written as follows:

$$\widehat{H}_Q = \frac{e^2 Q}{2I(2I-1)} I \cdot \overleftrightarrow{q} \cdot I \qquad (16)$$

Based on the perturbation theory, the Hamiltonian can be solved and treated as:

$$\widehat{H}_Q = \widehat{H}_Q^{(1)} + \widehat{H}_Q^{(2)} \qquad (17)$$

If the quadrupole interaction is much smaller than the Zeeman interaction, the energy can be treated as a first order perturbation and can be given as:

$$h^{-1} E_Q^{(1)} = \left\{\frac{3m_I^2 - I(I+1)}{8I(2I-1)}\right\} [(3cos^2\theta - 1) + \eta cos2\phi sin^2\theta]\chi \qquad (18)$$

, where m_I is the spin-component quantum number and θ and ϕ are the polar angle of q_{ZZ} in $\mathbf{B_0}$.

For the half-integer nuclei, the situation is unique because the first-order quadrupole affects both ½ and -½ energy levels equally, resulting in the unperturbed central transition (CT), see Figure 10. For the satellite transitions (ST), e.g. 3/2 → 1/2 and -1/2 → -3/2, the NMR transition are strongly dependent on θ and therefore the NMR signal will spread over a wide frequency range in the polycrystalline sample. The first-order quadrupole interaction can be removed under MAS, however, if χ is large, the second-order effect becomes prominent and this will cause the line broadening for quadrupole nuclei.

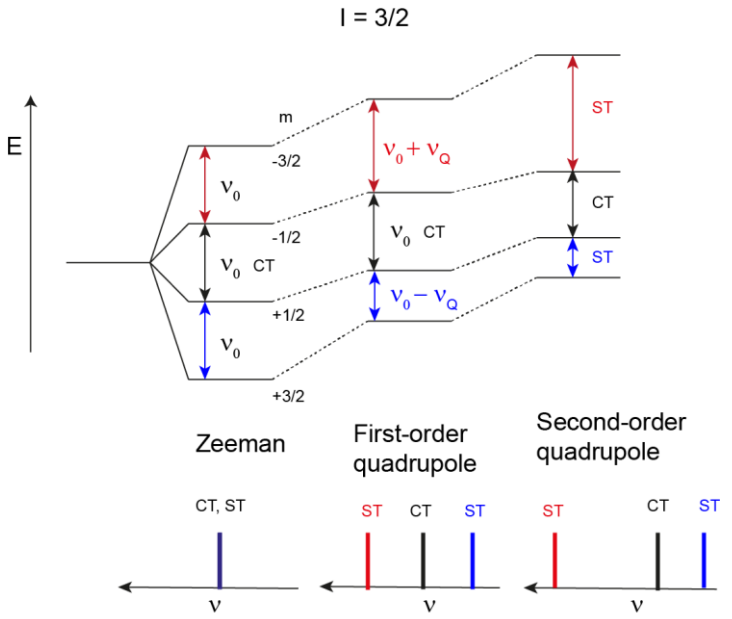

Figure 10: Energy scheme showing the Zeeman splitting, first-order and second-order quadrupole perturbation for spin 3/2. The central transition and the satellite transitions are shown in black and Red/blue, respectively.

2.2. Basic solid-state NMR experiments

2.2.1. Cross polarization (CP) experiment

Cross polarization refers to the polarization transfer from the nuclei of one element to those of another by matching the nutation rate (Hartmann-Hahn condition: $\nu_1^H = \nu_1^X$).[75] It is commonly employed to transfer polarization from abundant ^{1}H to diluted X nuclei such as ^{13}C and ^{15}N. The prerequisite of the transfer is the interaction (usually dipolar coupling) between the two types of nuclei. CP experiment offers several advantages: (1) the signal is enhanced by a factor of $\frac{\gamma^H}{\gamma^X}$, which is ~4 for ^{13}C and ~10 for ^{15}N, (2) the recycle delay is limited to the recovery of T_1^H, which is much shorter than T_1^X, allowing the faster repetition of experiments, leading to tremendously

decrease of experiment time. If the MAS is applied, the spinning rate (ν_r) has to be considered and the matching condition becomes:[76–78]

$$\nu_1^H = \nu_1^X \pm n\nu_r \qquad (19)$$

For a small MAS rate, it does not much affect the CP condition but at the high MAS rate the condition is shifted to the side binds and becomes narrower and less robust. The CP sequence is shown in Figure 11. The 90°-phase shifted ^{1}H pulse is initially applied to spin lock the magnetization and during this period (contact time) another pulse is applied simultaneously at X frequency. The signal of X spin then measured during acquisition time under ^{1}H-decoupling. The ramped CP[79] usually applied to cover the delicate range of matching condition, in which the RF nutation rate of one nucleus is swept through the matching condition, the matching conditions at different parts of the sample will be then achieved at some points in the ramp, leading to a higher CP efficiency.

CP can also be applied to transfer the magnetization form ^{15}N to the adjacent coupled ^{13}C in the so-called NCO[80] and NCA[80] experiments or vice versa in CANCO[81] experiment, which are used for the backbone assignment in NMR.

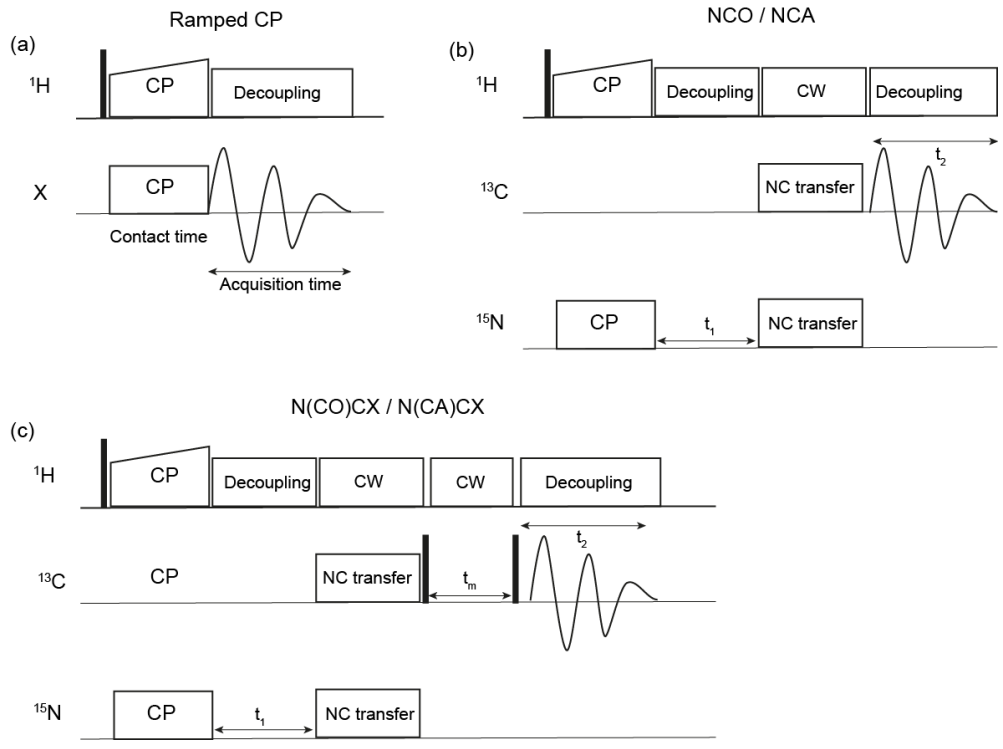

Figure 11: (a) Ramped cross polarization pulse sequence from ^{1}H to X nuclei, (b) 2D NCO / NCA pulse sequence, employing one CP from ^{1}H to ^{15}N and another CP from ^{15}N to ^{13}C and (c) 2D

N(CO)CX / N(CA)CX pulse sequence in which a mixing time is introduced after the NC transfer step to permit the magnetization exchange between the coupled ^{13}C via spin diffusion.

2.2.2. Spectral correlation experiments

Correlation experiments involve two or more dimensional experiments that correlate one-dimension spectra to that of the same or other nuclei in the second or other dimensions. The principle of 2D NMR is that the evolution time, t_1, is inserted after the initial excitation. The spin magnetization evolves during t1 period, which followed by the mixing period, in which the polarization is allowed to transfer or exchange to other nuclei. The NMR signals are detected thereafter in the t_2 period (direct detection). The evolution during t_1 period is detected indirectly, by which the amplitude of the signals in t_2 is modulated by the evolution in t_1 period and is thus sampled by repeating the experiments with regularly increment in t_1 to obtain the data set in second dimension. The correlation experiments are important for the peak assignment and structural determination, especially when the NMR signals are crowded, overlapped, and too complicated to be interpreted in 1D spectra. The mixing period is the key step which can be performed via different magnetization transfer pathway.

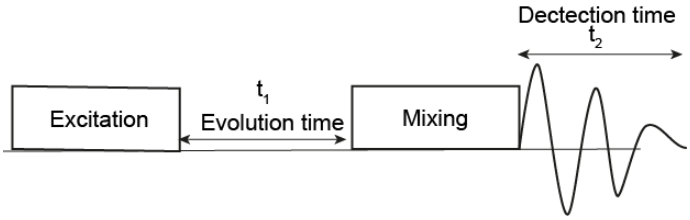

Figure 12: Schematic illustration of 2D NMR pulse sequence. In 2D NMR experiment, t_1 is added after excitation, during which the magnetization evolves. Thereafter, the mixing step is introduced to let the magnetization exchange between coupled spins, followed by the detection in t_2 period.

2.2.2.1. Homonuclear correlation experiments

In solid-state NMR, dipolar coupling is usually exploited to transfer the magnetization between coupled spins as it is in general much larger than the J coupling. The homonuclear proton dipole coupling network is so strong that it is only significantly affected by high MAS rates. Therefore, for ^1H, the spin diffusion is so effective so that the magnetization is transferred within millisecond timescale between protons. For ^{13}C-^{13}C, the spin diffusion is less effective than ^1H and a stronger dipolar coupling and longer mixing time are necessary for the magnetization transfer. The quantitive interpretation of cross peaks is difficult as the peak intensities do not solely depend on the spatial proximity but also on frequency differences between the correlated spins, which affects the spin diffusion rate.

Proton Diffusion Spin Diffusion (PDSD) experiment[82] is a homonuclear correlation experiment and commonly recorded first to study a protein sample to assess the general spectral quality, one can achieve for the sample (Figure 13). The ^{1}H spin is first excited, and the polarization is transferred to the diluted nuclei of interest, X (^{13}C or ^{15}N), via cross polarization. The spin magnetization of spin X evolves during t_1. A 90° pulse is applied on X nuclei to bring the magnetization to the z-axis, where the magnetization is allowed to exchange via spin diffusion during the mixing period. At last, another 90° is applied to flip the magnetization to the transversal plan for detection. The coupled nuclei within a certain distance, depending on the mixing time, are observed as crosspeaks. For the longer contact (long mixing time), the dipolar assisted rotational resonance (DARR)[83,84] is usually employed. The difference between PDSD and DARR experiment is that the continuous wave decouple pulse is applied during the mixing time in DARR, which enables the more efficient magnetization exchange.

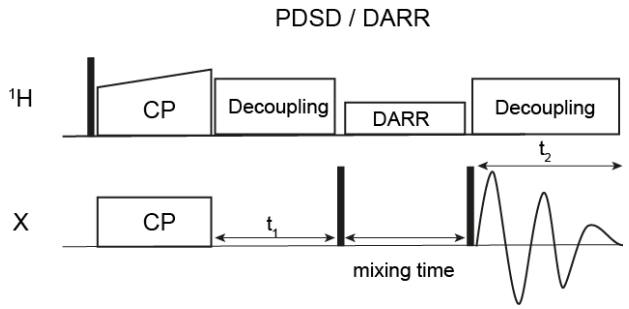

Figure 13: Schematic illustration of homonuclear correlation experiment, PDSD and DARR. There is no decoupling applied during the mixing time in PDSD experiment whereas for DARR experiment, continuous wave (cw) dipolar coupling is applied to achieve the efficient polarization transfer during the mixing time.

2.2.2.2. Heteronuclear correlation experiments

The heteronuclear correlation between directly bound ^{13}C and ^{15}N can be achieved by CP as described in the 2.2.1. as in NCO and NCA experiments. However, for the long-range contact between ^{13}C and ^{15}N, a dipolar recoupling scheme has to be applied to reintroduce the dipolar coupling that is suppressed by MAS. The reintroducing of dipolar coupling is very important in structural determination because it contains distance information between the coupled nuclei. Rotational-echo double-resonance (REDOR)[85,86] is the most commonly used method to recouple the low-γ heteronuclear spin pairs. REDOR is based on a rotor synchronized π pulse scheme to dephase the transversal S-spin magnetization. The S-spin echo intensities with and without I-spin dephasing pulses as a function of dephasing time depends on the strength of I-S dipolar coupling and hence can provide the I-S distance up to ~6 Å. The π pulse is usually phase-alternated to compensate for the pulse imperfections and resonance offsets.

The natural abundance S-spin background often complicates the interpretation and affect the heteronuclear distance measurement. However, the dipolar coupled spins can be selected from the background by using the coherence transfer from one spin of the heteronuclear pair to the other which is achieved by applying a pair of $\pi/2$ pulse to I and S spin pair. This procedure is called transferred echo double resonance (TEDOR).[87–89] Fig shows the 2D-TEDOR pulse sequence used in this thesis. CP is first applied to transfer the polarization from ^{1}H to ^{13}C (S-spin), followed by the REDOR π pulse train to ^{15}N (I-spin) which recouple the ^{13}C-^{15}N dipolar coupling. After that a pair of $\pi/2$ pulse is applied to transfer the magnetization to ^{15}N, which evolves during t_1 period. Another pair of $\pi/2$ pulse is applied to transfer the magnetization back to ^{13}C and another REDOR pulse train is applied to recouple the dipolar coupling.

Two z-filter periods are inserted before evolution time (t_1) and acquisition time (t_2) periods to suppress the anti-phase and MQ coherences arising from the ^{13}C-^{13}C J-coupling (J ~ 30-60 Hz in peptide[90]) during the mixing period, which leads to the spurious cross-peak and phase twisted lines in 2D spectra and further interferes with the extraction of distance measurement.

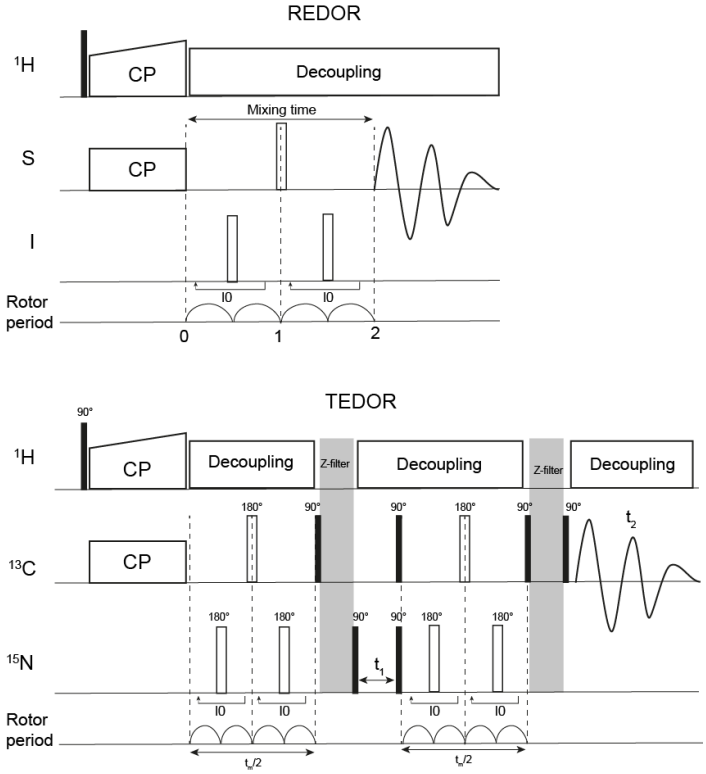

Figure 14: REDOR pulse sequence shows the rotor synchronized dephasing π pulses applied to the I-spin at half rotor period to reintroduce the S-I spin dipolar coupling under MAS. 2D TEDOR pulse sequence shows the coherence transfer from ^{13}C to ^{15}N spin after the first REDOR period, followed by a z-filter and the t_1 evolution. Another pair of $\pi/2$ to ^{13}C and ^{15}N spin returns the magnetization

back to ^{13}C and the second REDOR is applied. At last another z-filter period is inserted and the ^{13}C signal is detected.

2.2.3. Double quantum filter (DQF) experiment

Double quantum (DQ) can be utilized to suppress the signals from isolated spins and select the signals from coupled spin pairs. This technique is very useful for the simplification of spectra, helping the assignment and the suppression of natural abundance background.[91] The coupled spin pairs can be easily distinguished from the isolated spins via the radio frequency (RF) phase shift of the DQ coherence. The DQ coherence of the coupled spins can be achieved via dipolar coupling and scalar coupling. The dipolar coupling is the choice for ssNMR because it is the dominating interaction in solid-state and the dipolar coupling of the directly bonded spins is 5 times larger than the two-bonded spins.[92] The strong dipolar coupling allows the fast excitation, reducing the signal loss caused by the T_2 relaxation. In ssNMR, MAS, employed to suppress the anisotropic chemical shift interaction in powder samples, also averages out the dipolar coupling. Therefore, a RF pulse sequence must be applied to reintroduce the dipolar coupling. Several techniques have been developed to reintroduce the homonuclear dipolar coupling such as rotational resonance and RF homonuclear recoupling pulse sequences. Among them, C7 is one of the most efficient homonuclear recoupling pulse scheme for powder or unordered samples.[93] Moreover, it is robust to all forms of chemical shift, radio frequency amplitude imperfection, and its average Hamiltonian is low orientation dependent. The C7 pulse sequence exploits the rotor synchronized RF pulse cycle with sevenfold-symmetric phase shift scheme that fulfills the condition $\omega_1 = 7\omega_r$. The sequence is timed so that the full seven steps end up at two rotor periods. The ^{13}C-^{13}C DQF experiment with C7 components is shown in Figure 15. After the CP step, a 90° flips the magnetization to the z-axis. The C7 sequence with duration τ_{exc} converts the z-magnetization into DQ coherence. After that, another C7 pulse sequence with duration τ_{rec} (same as τ_{exc}) reconverts the DQ coherence back to longitudinal magnetization. At last, another 90° pulse is applied to convert the magnetization to transverse magnetization for detection. Initially, the C_ϕ element exploited a sequence of two 2π pulses with opposite phase (0° + ϕ and π + ϕ). Later, the variant of C7, named permutationally offset stabilized C7 (POST-C7) was developed to improve the tolerance of C7 toward isotropic and anisotropic chemical shift offsets, and radio frequency inhomogeneity.[94] In the POST-C7 sequence, the two 2π pulses are replaced with $(\pi/2)_\phi\ (2\pi)_{\pi+\phi}(3\pi/2)_\phi$. The permutation transforms the error term into a form that can be eliminated by the z rotations of the sevenfold-symmetric phase shift cycle.

DQ coherence can also be exploited in a 2D manner called DQSQ experiment which is similar to the INADEQUATE in solution-state NMR. For that, the evolution period is introduced after the

DQ excitation (POST-C7), followed by pulse sequence (POST-C7) that converts the DQ to SQ. Finally, the 90° pulse is applied to transform the magnetization to the transversal magnetization for detection.[92] In DQSQ experiment, the sum of chemical shifts of the coupled spins that survived the DQ filter will appear in the indirect dimension and the chemical shifts of the SQ are shown in the direct dimension. The advantage of DQSQ is that only the coupled spins that are directly bonded will appear on the spectrum and therefore, the coupled spins with small chemical shift difference can be clearly observed without interference from the diagonal peaks. The assignment can be done in a sequential walking way. Since the evolution time has to be rotor synchronized, to achieve a large spectral width which is usually required for the studies of biological molecules, the increment of t_1 can be set to match the element of C7, $t_1 = \tau_C = 2\tau_r/7$. The phase of the reconversion C7 pulse sequence has to be shifted by $\Delta\phi = 2\pi/7$ in order to gain the reconversion block that is the same as excitation block.

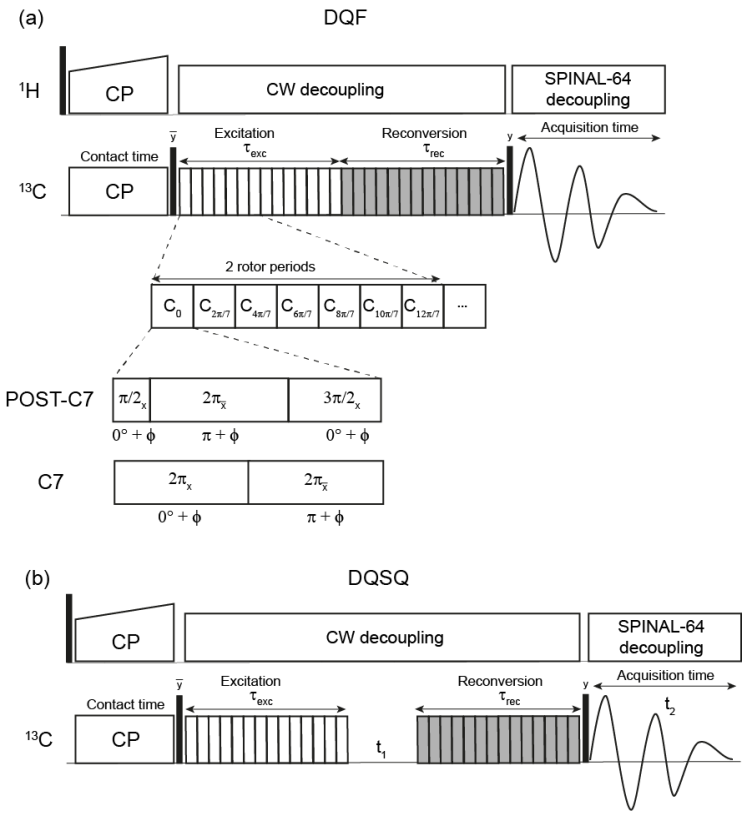

Figure 15: Pulse sequence of (a) double quantum filter experiment (DQF) and (b) double quantum single quantum experiment (DQSQ). The homonuclear dipolar coupling based on POST-C7 is applied to create the DQ coherence in the DQ excitation and DQ-SQ reconversion. The C7 and POST-C7 pulse components and the sevenfold phase switched RF pulse cycle are shown in (a). The sevenfold pulse cycle is timed to end in two rotor periods.

2.2.4. Double quantum heteronuclear local field experiment (2Q-HLF)

The torsion angle is a detailed structural parameter that is important for the structural determination in addition to the interatomic distances. The 2Q-HLF can be applied to determine torsion angle (H-C-C-H) of unordered sample under MAS.[95] The pulse sequence relies on the relative orientation of two magnetic spin-spin coupling tensors (^{13}C-^{1}H) in a $^{13}C_2$-labeled sample. It exploits the DQ coherence and the influence of the heteronuclear dipolar fields from the neighboring protons, which depends on the spin states of ^{1}H and the geometry of the ^{13}C-^{1}H coupling tensor. Under MAS, the dipolar fields are modulated in time, yielding the 13C-13C DQ side band pattern, depending on the H-C-C-H torsion angle. The pulse was applied to measure the torsion angle of 11,12-$^{13}C_2$-retinylidene rhodopsin in dark and bathorhodopsin state.[96] The pulse sequence is shown in Figure 16. After the CP step, POST-C7 dipolar recoupling pulse scheme is applied to generate the DQ coherence. During the variable t_1 period, the DQ ^{13}C-^{13}C coherence evolves and the phase-modulated Lee-Goldburg (PMLG)[97,98] is applied to decouple the ^{1}H-^{1}H homonuclear dipolar interactions. A 180° pulse is applied in the middle of t_1 to refocus the ^{13}C chemical shift evolution. The DQ coherence is convert back to SQ by another recoupling pulse sequence and a 90° pulse is applied for detection. The t_1 period is incremented stepwise to the maximum two rotor periods and the signal intensities are plotted against the dephasing time (t_1). The torsion angle can be extracted by fitting the experimental dephasing curve with the simulated one.

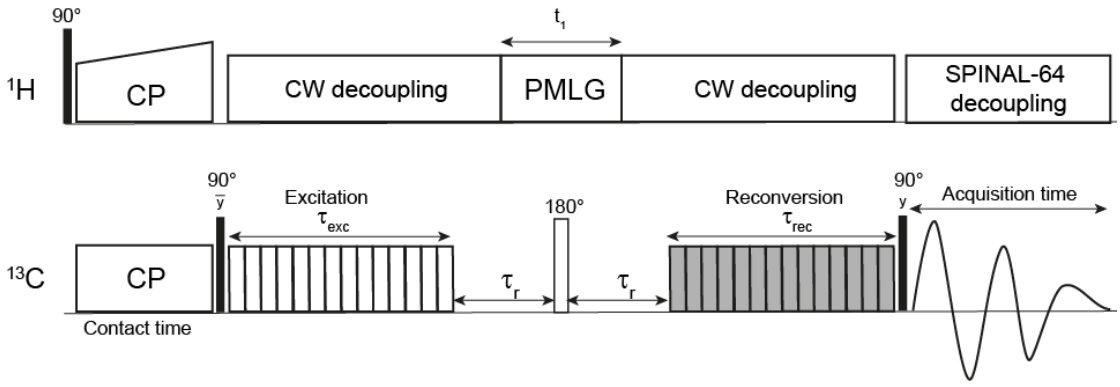

Figure 16: 2Q-HLF pulse sequence for the determination of H-C-C-H torsion angle in a $^{13}C_2$-labeled sample under MAS. The homonuclear recoupling pulse sequence POST-C7 is applied for DQ excitation and reconversion, and the PMLG homonuclear decoupling is exploited during the variable evolution period (t_1). SPINAL-64 decoupling scheme is applied during the detection period.

2.3. Dynamic nuclear polarization (DNP)

2.3.1. Development of DNP

DNP refers to the polarization transfer from electron spin to nuclear spins by microwave irradiation.[99–102] It can help overcome the sensitivity issue in NMR, resulted from the small Zeeman splitting and the modest Boltzmann spin populations difference between lower (α) and higher (β) energy states. The nuclear polarization (P) for spin I = ½ can be given as:

$$P = \frac{N^+ - N^-}{N^+ + N^-} = \tanh\left(\frac{\gamma \bar{h} B_0}{2kT}\right) \qquad (20)$$

N^+ and N^- are the population of spins in α and β states at thermal equilibrium, respectively. The spin population distribution depends on the magnetic field (B_0), gyromagnetic ratio (γ) and temperature (T). The strategies to boost the sensitivity by transferring the magnetization from nuclei with high magnetic ratio like proton have been long developed and routinely used to boost the sensitivity of low γ nuclei like ^{13}C and ^{15}N by INEPT[74] and CP experiments in conventional NMR spectroscopy, leading to the increase in signal intensity of a factor of 4 for ^{13}C ($\gamma_H/\gamma_C \sim 4$) and 10 for ^{15}N ($\gamma_H/\gamma_C \sim 4$). In a similar way, the sensitivity enhancement will be dramatically much higher, if the polarization is transferred from an electron spin since the gyromagnetic ratio of electron is far beyond the nuclei; γ_e/γ_H is ~ 660 and γ_e/γ_C ~ 2600.

The idea to transfer the polarization from electron to nuclei was originally proposed by Overhauser in 1953[103] and was later experimentally verified by Carver and Slichter on ^7Li metal[104] and further on ^{23}Na and ^{23}Na dissolved in anhydrous liquid ammonia.[105] Later in 1958, Abragam and Procter later extended this idea to solid dielectrics and firstly characterized the solid effect.[106] Thereafter, Kessenikh et al demonstrated experimentally the first cross effect in polyethylene in 1963[107], following by Hwang and Hill who also observed the effect of e-e dipolar coupling in dynamic polarization with different enhancement profile from SE.[108,109]

The combination of DNP with MAS ssNMR was pioneered by Wind et al, who performed DNP-enhance MAS NMR on coal and polystyrene doped with BDPA radical in 1983.[110] The experiment was further employed to study materials such as polymers, fibers and diamond films.[111–116] The NMR enhancement has permitted the studies of surface which would require an impossible measurement time by a conventional NMR experiment. Schaefer et al also demonstrated the use of MAS DNP in selectively study of undoped PC in the homogeneous mixture with PS doped with BDPA.[114] Zhao et al applied to MAS DNP to the study of ^{13}C in natural and synthetic diamond.[112] Generally, in the initial phase, the MAS DNP were mainly applied to the studies of polymers and materials and the experiments were limited to the low

fields (~1.4 – 1.8 T). The progress to the high field was limited by the lack of strong enough μw power source necessary to saturate electron transition at the field higher than 94 GHz on that time and the theoretical prediction of the diminishing polarization transfer at high fields.[102]

The movement toward the high-field (> 5 T) MAS DNP was pioneered mainly by Griffin's group at MIT, in which (1) the development of hardware such as high-power μw power source (gyrotron) and the cryogenic MAS, (2) the introduction of the biradicals with different EPR lines that matches the nuclear Larmor frequency (see cross effect), and (3) the employment of frozen glass forming solvent (d^8-glycerol, D_2O and H_2O) are the key factors of the success.[102] These developments have opened the pathway to study biological molecules via DNP-enhanced MAS ssNMR.[117] The DNP MAS spectrometers have transferred from the home-built stage to the commercialized state and the development of the technique to higher fields is continuing.[118]

2.3.2. DNP mechanism

2.3.2.1. Solid effect (SE)

SE describes the DNP mechanism arising from a two-spin coupling system, composing of one electron (e) and one nuclear spin (n). The coupling of electron and nuclear spins can be illustrated as in Figure 17. The Hamiltonian of the system can be expressed as follows:

$$\hat{H}_{SE} = \frac{\mu_B}{\hbar}\vec{B}\boldsymbol{g}\vec{\boldsymbol{S}} - \frac{\mu_n g_n}{\hbar}\vec{B}\vec{\boldsymbol{I}} + \vec{\boldsymbol{S}}\boldsymbol{A}\vec{\boldsymbol{I}} \qquad (21)$$

The first and second terms described the electron and nuclear Zeeman interactions, respectively and the third term is the hyperfine coupling interaction. SE relies on the excitation of the forbidden electron-nuclear (e-n) ZQ (|2> → |3>) or DQ (12> → |4>) transition driven by the coherence with microwave (μw) irradiation. These forbidden transitions are partially allowed due to the mixing of electron and nuclear spin states driven by hyperfine coupling interaction (HFI). The DQ and ZQ transitions will lead to the positive and negative DNP enhancement observed in field dependent DNP profile. The mixed eigenstates deviate slightly from the Zeeman based energy states as the hyperfine coupling usually two or more order of magnitude smaller than the nuclear Zeeman interaction. In the μw rotating frame, the connected eigenstates are degenerated, and the ZQ and DQ transitions can occur when the SE matching conditions are fulfilled:

$$\omega_{\mu w} = \omega_{0S} \pm \omega_{0I} \qquad (22)$$

The effective Hamiltonian can be written as:

$$H''_{\mu w} = \frac{\omega_{1S}}{2}\left\{(\boldsymbol{S'}_+ + \boldsymbol{S'}_-) - \frac{B}{4\omega_{0I}}[(\boldsymbol{S'}_+ I'_+ + \boldsymbol{S'}_- \boldsymbol{I'}_-) - (\boldsymbol{S'}_+ \boldsymbol{I'}_- + \boldsymbol{S'}_- \boldsymbol{I'}_+]\right\} \qquad (23)$$

The details regarding theoretical aspect of SE can be found in the review written by Thankamony and Corzilius et al.[100] The DQ and ZQ terms in the effective µw Hamiltonian are scaled by the factor of $\frac{B}{4\omega_{0I}}$, where B is the secular hyperfine coupling parameter. This leads to a relatively low transition probability ($10^{-4} \sim 10^{-8}$) relative to SQ transition, making the SE an inefficient DNP mechanism at high field and a large µw field is necessary. SE requires a polarizing agent (PA) with narrow linewidth like trityl or BDPA. If the anisotropy and the variation in eigenstate energy levels are large, SQ, ZQ and DQ will occur alternatively, resulting in the inflicting transferable polarization to nuclear spins.

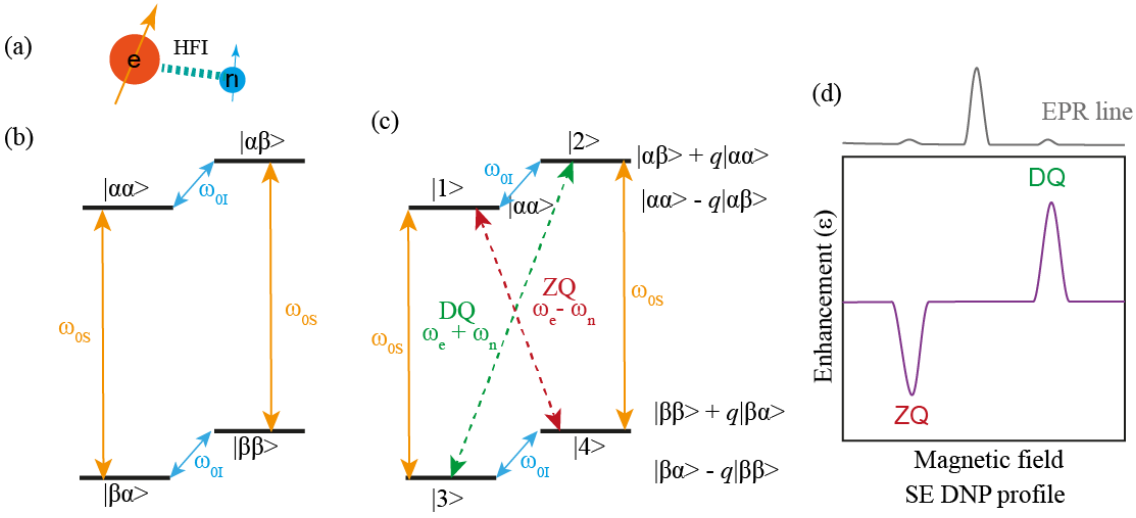

Figure 17: (a) Illustration of electron spin (S=1/2) and nuclear spin (I=1/2) coupled system. (b)-(c) Energy scheme of two-spin system the Zeeman basis (b)and in the Eigenbasis of the static spin Hamiltonian including HFI (c); *q* is the Eigenstate mixing coefficient. (d) Illustration of EPR line with a narrow linewidth and SE-DNP enhancement profile, showing the negative and positive enhancement, arising from ZQ and DQ transition, respectively.

2.3.2.2. Cross effect

CE is a three-spin process, requiring two coupled electron spins coupled to the nuclear spin via hyperfine coupling (at least one of the electron spin). The Hamiltonian becomes more complicated as it included second electron Zeeman interaction and e-e dipolar coupling and HFI with both electron spins terms.

$$\hat{H}_{CE} = \frac{\mu_B}{\hbar}\vec{B}(\boldsymbol{g_1}\vec{\boldsymbol{S}}_1 + \boldsymbol{g_2}\vec{\boldsymbol{S}}_2 - \frac{\mu_n g_n}{\hbar}\vec{B}\vec{\boldsymbol{I}} + \vec{\boldsymbol{S}}_1\boldsymbol{D}\vec{\boldsymbol{S}}_2 + (\vec{\boldsymbol{S}}_1\boldsymbol{A_1} + \vec{\boldsymbol{S}}_2\boldsymbol{A_2})\vec{\boldsymbol{I}} \qquad (24)$$

The difference in effective Larmor frequencies between two coupled electron spins have to match the nuclear Zeeman frequency and at the same time one of the two electron spins is on resonance:

$$\Delta\omega_{0S} = \omega_{0S,1} - \omega_{0S,2} = \pm\omega_{0I} \ \ and \ \omega_{\mu w} = \omega_{0S,1} \ or \ \omega_{0S,2} \qquad (25)$$

Satisfying this matching condition is not arduous. The CE concept was first proved by using the mixing of trityl and BDPA, which roughly satisfy the condition.[119] Thereafter, biradicals with two TEMPO moieties linked like BTnE[120], TOTAPOL[121], bTurea[122] were developed. A lot of efforts have been made to design the polarizing agents that perfectly match the required CE-DNP condition and the needed sample solubilization properties.[123] The bis-nitroxide radical with broad EPR linewidth, bTurea was further modified by the introduction of molecular rigidity like in bTbK family[124], increasing aqueous solubility and molecular weight in PyPOL and AMUPol[125], and slow down the electron spin relaxation in TEKPol family[126,127]. Recently, AsymPolPOK, designed based on the computational assisted simulation, was demonstrated to efficiently yield the DNP enhancement and reduce the quenching effect at 9.4 T as well as at 18.8 T.[128] Theses developments of the efficient polarizing agent have largely contributed to the development and establishment of DNP applications at high fields.

Differently from SE, CE does not require microwave driven irradiation, the polarization transfer is driven by the e-e coupling and hyperfine interaction in the e-e-n three spins (flip-flop-flip) manner. The mixed eigenstates are shown in Figure 18. The flip-flop-flip transition moment is equal to D_0B_Δ/ω_{0I}, where D_0 is the e-e interaction parameter and B_Δ is the hyperfine coupling parameter (see reference for more details). Compared to the SE, CE is more efficient due to the allowed transition (~2500 higher transition possibility).[100] CE can induce both negative and positive enhancement, depending on that which electron spins is irradiated.

MAS affects the CE considerably. The theoretical description of CE in static condition was published by Hu et al and Hovav et al.[129,130] whereas the CE under MAS was described by Thurber and Tycko et al.[131] and Mentink-vegier et al.[132], nearly at the same time. MAS causes the rotation of Zeeman, e-e couplings, and HIF tensors within the permanent magnetic field, leading to the periodically modulation of energy separation, which induce severally the level anti-crossing events (LACs) during the rotor period. The LAC event results in the separation of μw irradiation and the CE matching condition. If there is a sufficiently strong mixing interaction, the spin population can exchange adiabatically. The rate of level crossing/degeneracy and the mixing potential therefore have to be considered under MAS. For the CE relevant LAC events, the adiabatic factor is small (0.1%), however, the longitudinal nuclear spin relaxation is relatively long (~10^3-10^4 rotor cycles), leading to the accumulation of the effect to more than two order of magnitude.[100] The field dependent enhancement profile is shown in Figure 18. The enhancement can be both negative and positive, depending on that which electron spin (S_1 or S_2) is excited. The enhancement reflected the Larmor frequencies of electron spins. CE has emerged to become

the common applied mechanism for the studies of biological molecules by DNP-enhanced ssNMR.

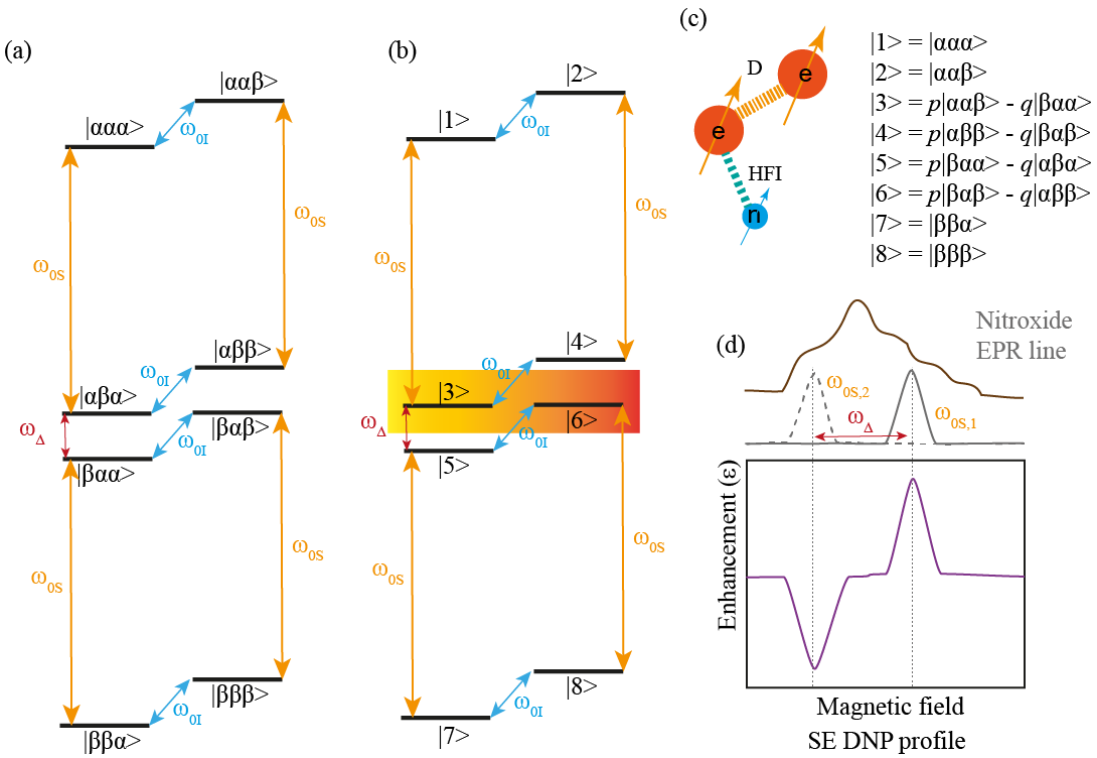

Figure 18: Energy scheme of three-spin system consisting of two electron spins (S_1 and S_2 (S=1/2)) and one nuclear spin (I=1/2) in (a) the Zeeman basis and (b) in the Eigenbasis of the static spin Hamiltonian including e-e interaction and HFI of electrons with nuclear spins. The degenerated states are highlighted. (c) Illustration of the three-spins system and the mixed eigenstate, where *p* and *q* are cosine and sine coefficients, respectively, arising from e-e coupling. (d) Illustration of the relations between EPR line shape of two coupled electrons, in which the difference in Larmor frequencies equals nuclear Larmor frequency and CE-DNP enhancement profile.

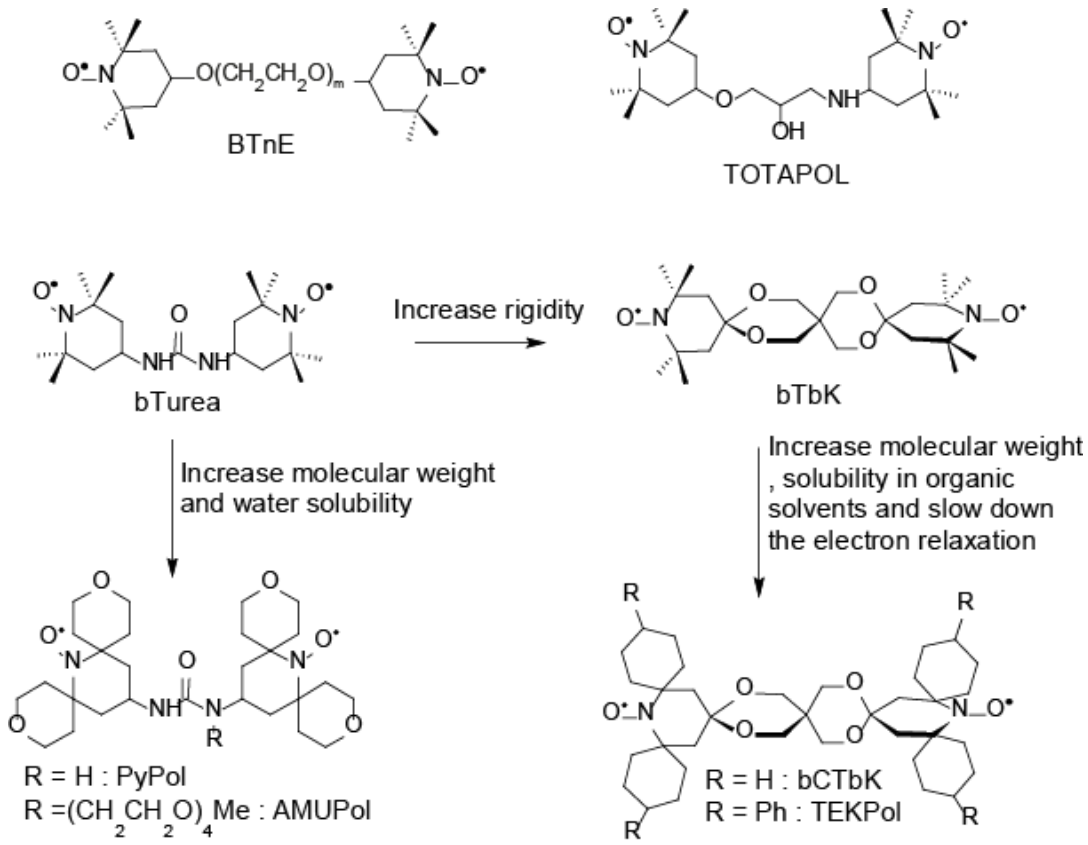

Figure 19: Development of polarizing agents for CE-DNP.[121,126,127,133]

2.3.2.3. Overhauser effect (OE)

OE describes the time-dependent polarization transfer from electron to nuclear spin through the dipolar and scalar coupling relaxation. Considering exclusively the OE, the Hamiltonian[100] can be described as follows:

$$\widehat{H}_{OE} = \gamma_S \bar{h}(\boldsymbol{S}\cdot\boldsymbol{B_0}) + \gamma_I \bar{h}(\boldsymbol{I}\cdot\boldsymbol{B_0}) + \bar{h}J_{IS}(\boldsymbol{I}\cdot\boldsymbol{B_0}) + \gamma_S\gamma_I\bar{h}^2\left(\frac{3(\boldsymbol{I}\cdot r)(\boldsymbol{S}\cdot r)}{r^5} - \frac{\boldsymbol{I}\cdot\boldsymbol{S}}{r^3}\right) \qquad (26)$$

The first and second terms are electron and nuclear Zeeman interactions, respectively, where the third and fourth terms are scalar and dipolar coupling terms, respectively. J_{IS} is the scalar coupling constant. OE relies on the molecular dynamics which cause the fluctuation of dipolar and scalar HFI that leads to the e-n cross relaxation. If the correlation time that describes the internal dynamics is in the range of $\omega_{0s} \pm \omega_{0I}$, SQ, DQ and ZQ transitions can occur. OE can be quantitatively described based on Solomon equation[134] using the system with one electron (S=1/2) and one nuclear spin (I=1/2), coupled with HFI:

$$\frac{dI_z}{dt} = -(\rho_I + W_0)(I_z - I_0) - \sigma_{IS}(S_z - S_0) \qquad (27)$$

, where ρ_I and σ_{IS} are electron and nuclear auto-relaxation rate constants which are defined from SQ (W_1), ZQ (W_0) and DQ (W_2) transition rates; $\rho_I = W_0 + 2W_1 + W_2$ and $\sigma_{IS} = W_2 - W_0$. Under dipolar coupling relaxation, W_2 and W_0 can occur, however, under the scalar coupling relaxation only W_0 is possible. At the steady state, where $\frac{dI_z}{dt} = 0$, the OE-DNP enhancement (ε_{OE}) can be written as:

$$\varepsilon_{OE} = 1 - \zeta f s \frac{\gamma_S}{\gamma_I} \qquad (28)$$

ζ is the coupling factor, $\zeta = \frac{\sigma_{IS}}{\rho_I} = \frac{W_2 - W_0}{W_0 + 2W_1 + W_2}$. The OE-DNP enhancement is strongly dependent on the coupling factor and therefore the imbalance between the ZQ and DQ transitions. f is the leakage factor, accounting from the e-n spin relaxation compared to other mechanisms and is given by $f = 1 - \frac{T_{1R}}{T_{10}}$, where T_{1R} and T_{10} are the longtitudinal relaxation with radical and without radical, respectively. The saturation factor, *s*, describes the degree of electron saturation by microwave power. It ranges from 0 to 1 and can be derived from Bloch equation under continuous irradiation, $s = \frac{\gamma_e^2 B_1^2 T_{1s} T_{2S}}{1 + \gamma_e^2 B_1^2 T_{1s} T_{2S}}$. OE-DNP If the sufficiently high μw is given, the off-resonance electron transition can also occur, resulting in the board DNP enhancement profile, relatively to the EPR line. OE was thought to be vanishing at high field due to the requirement of extremely fast motion.[135] However, Prisner et al.[136] and Bennati et al[137,138] have demonstrated the high DNP enhancements at high fields in liquids. For solid-state, a high enhancement factor was observed in an amorphous matrix with BDPA[139], flavodoxin with flavin mononucleotide semiquinone radical sytem[140], and in lipid bilayer with nitroxide radicals[141]. In order to explain the phenomenon observed, the short correlation time arising from the transient contact between the solvent and the PA as well as the local internal molecular rotation and vibration modes should be extendedly considered in addition to the rotational and translational motion described by Hausser and Stehlik[142].

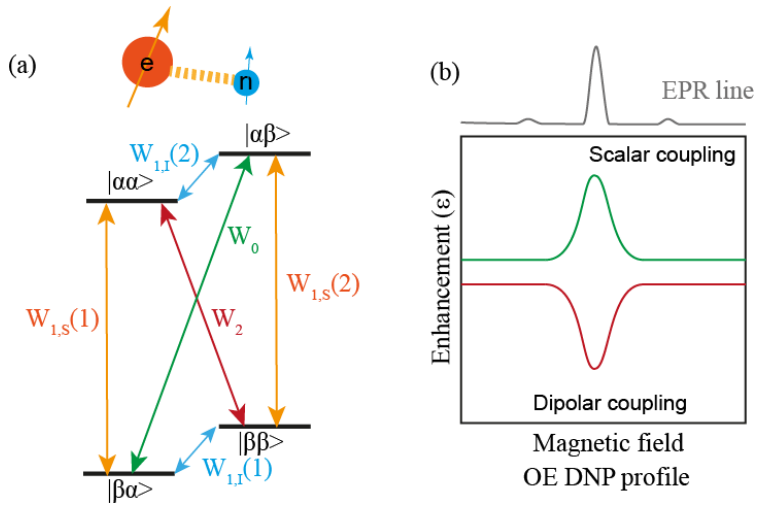

Figure 20: (a) Energy diagram of two-spin system, consisting of one electron spin (S=1/2) and one nuclear spin (I=1/2). W_1, W_0 and W_2 are transition rates for SQ, ZQ and DQ, respectively. (b) Illustration of the OE-DNP enhancement profile and the corresponded EPR line. The scalar and dipolar coupling leads to the positive and negative enhancement, respectively.

2.3.2.4. Thermal mixing (TM)

TM mechanism described the DNP process in the system with a high electron spin concentration, in which the e-e coupling is large. Similar to CE, it relies on the three-spins flip and the extent of e-e coupling factor is the determining factor, however, for CE the coupling between electron spins is weak compared to nuclear Larmor frequency, whereas for TM the e-e coupling is stronger.[143] TM usually involves the ensemble of coupled electron spins and the difference in Larmor frequency among these spins depend on the difference in dipolar coupling fields experienced by the participating spins. TM explained the polarization transfer in the thermodynamic fashion in that each spin has a spin temperature. The µw irradiated electron spins acting as the hot-spot reservoir, giving the heat to the coupled non-Zeemann electron and nuclear spins, which are treated as cooled reservoirs, through to the three-spin flip transitions and the temperature equalization and hence named thermal mixing. Guarin et al characterized the TM-DNP using the nitroxide radicals at 3.5 T[144] and Jähning et al. investigated the TM in different nitroxide radical concentration at 3.5 T and 7 T[145]. Karabanov and coworkers described the quantum mechanics of TM-DNP and predicted that the strong asymmetry in the e-e coupling is essential for the efficient TM based polarization transfer.[146] Kundu and coworkers further suggested that electron-electron double resonance (ELDOR) can be employed to identify the TM-DNP mechanism and differentiate between the CE and the TM.[147] Recently, Equbal et al. observed the crossover from a SE to TM in ^{1}H DNP experiments using Triryl-OXO063 at high concentration and at 7 T.[148] The finding was surprising as the *g* anisotropy of Triryl-OXO063 is much smaller than ^{1}H Larmor

frequency. TM-DNP offers a perspective towards an effective DNP enhancement due to its low microwave power requirements, high polarization transfer rates and high efficiency at high fields.

2.3.3. Applications of DNP on membrane proteins and biological systems

DNP has been developed so far from the proof-of-concept into an established analytical tool for the studies of materials, biological molecules, and complex systems. In the biomolecular DNP field, the development, mostly pioneered by Griffin and coworkers, who have started from a co-dissolved labeled amino acid like glycine and arginine with radical in frozen solution and extended further to ^{15}N-Alanine labeled T4 lysozyme in frozen glycerol-water solution doped with TEMPO.[149,150] MAS DNP NMR is nowadays commercialized and applied to study biological membranes, amyloid fibrils as well as biological molecules in large complex systems.[99,117,151] The signal enhancement offered by DNP dramatically reduce the measurement time and enables the detection of low populated target molecules such as intermediates, surface anchored molecules and biomolecules in large complex environments as well as natural abundance molecules, in which it is not possible by conventional ssNMR.[100]

For the studies of membrane proteins, Griffin group applied DNP-enhanced MAS NMR to study the photointermediates of purple membrane bacteriorhodopsin (BR), in which the enhancement envisions the small population of important intermediates as well as the shunt states.[11,152–154] Moreover, the cryogenic temperature required for CE-DNP provides the tremendous condition for the trapping of photointermediates, generated by *in-situ* illumination. The unique Schiff base chemical shifts of K, L, M and N intermediates were determined by ^{15}N CP experiment, revealing the key electrostatic change at the Schiff base.[153] By using the 2D ^{15}N-^{13}C correlation experiment, the ^{13}C chemical shifts of retinal carbon atoms, containing characteristic structural conformation for each intermediate, could be obtained and analyzed.[11] The DNP also permitted the measurement of ^{15}N-^{1}H bond lengths of the Schiff base in intermediates using 2xDIPSHIFT experiment and the ^{1}H-^{15}N 2D correlation spectra revealed the proton transfer mechanism to the proton acceptor D85 via T89, which was also supported by the close contact detected in ^{13}C-^{13}C correlation spectra between D85-C_γ and T89-C_β in L and M_0 state but not in light adapted BR and N state.[154]

Following the works done on BR, the studies of retinal conformations and its functional related structures by DNP MAS NMR in microbial rhodopsin were performed by Glaubitz group. Mao et al applied DNP to investigate the color tuning mechanism in GPR, in which the one mutation at L105 position to Glutamine resulted in the blue switch.[155] The data showed that the locally perturbed conjugation between the imine linkage and the isomerization region is responsible for

the absorption wavelength change. Becker-Baldus et al.[13] investigate the retinal conformation changes during the photocycle of ChR2, the light-gated ion channel widely used to stimulate neural activities by light.[31] The retinal conformation in the dark state and three intermediates, generating from in-situ illumination and thermal relaxation or continuous illumination, were determined and analyzed. In the similar way to ChR2, the photocycle of PR, which is the most abundant retinal protein on earth, is studied by Mehler et al.[12] The photoisomerized product K and the two M states arising after the proton transfer step were trapped and the chemical shift perturbations along thee retinal chain form C10 to C15 and the Schiff base were analyzed. The large alternating chemical shift alteration pattern along the polyene chain away from the Schiff base in K-intermediate and the structural rearrangement after the proton transfer from the Schiff base to the proton acceptor D97 in M-state were observed. Moreover, the protein-protein interactions at the protomer interfaces, determining the forming of specific oligomerization (pentamer or hexamer), was investigated in GPR, using the mixed ^{13}C or ^{15}N labeled protomers.[156] The salt bridge interaction between R51 and D52' (adjacent protomer) favors the formation of pentamer. The mutation at D52 and R51 (D52N and R51A) disturbed the interaction, leading to the formation of hexamer instead of a pentamer. In addition, the role of E50 in stabilization of the oligomeric state through the hydrogen bonds with R51 is also proposed. The study was extended to address the question whether the oligomerization has a functional important role in the ion pumping mechanism. The conserved H75 residue located at the protomer interface was investigated.[157] The data showed that the tautomerization from τ to π-tautomer of histidine and the change of its ring orientation is coupled to W34 of the cross-protomer and stabilized the proton acceptor D97 in a Asp-His-Trp triad.

For the studies of membrane transporters, DNP was applied to study the ligand binding in the small multidrug resistance (SMR) transporter, EmrE, the transporter found in the inner membrane of bacterial, responsible for the exports of positively charged polyaromatic toxic compounds in exchange for protons.[158] The 19-fold enhancement provided by CE-DNP enables the unambiguous detection of the long assumed direct interaction between E14 residue in helix I of EmrE and the TPP^+. Furthermore, the DNP MAS-NMR also contributes to the studies of ABC transports both in prokaryotes and eukaryotes. The backbone conformation of the optimized bound peptide and its specific interaction to the human transporter associated with antigen processing (TAP), which plays a critical role in the adaptive immune system, were identified, elucidating the structural peptide recognition and the chemical basis of the substrate selection rules.[159] For the bacterial ABC transporter, the DNP MAS-NMR is employed to the study of MsbA, an ATP-driven lipid-A flippase, to observe the though-space contact between the ^{15}N-

label nucleotides and the uniformly ^{13}C-labeled MsbA in the various trapped catalytic states and identify the nucleotide binding sites.[160] Moreover, the effects of drug binding, Hoechst 33342 and darunobicin, on the specific sites in transmembrane helices 4 and 6 of MsbA was also envisioned by DNP MAS NMR using unique pair labeling strategy.[161]

The enhancement provided by DNP is very beneficial for the studies of proteins, that are difficult to obtain in a large amount like G-protein coupled receptors (GPCRs), which are one of the most important signal transducers in higher eukaryotes, regulating key physiological processes and thus are attractive drug targets. Joedicke and Mao et al. applied DNP MAS NMR together with advanced molecular modeling and docking techniques to elucidate the molecular basis of the subtype-specific ligand selectivity in human brandykinin receptors. The study showed that the conserved middle segments of the bound peptides determine the distinct molecular structure of the N and C termini that approach the receptor. The N-termini selection is mainly through the electrostatic interaction with charged residues whereas the C-terminal is recognized through conformation and interactions.[162]

Koers et al exploited the signal enhancement by DNP to study liposomal peptide vaccines, by which the study by conventional ssNMR is hindered by the low lipid concentration relative to the amount of lipid.[163] Furthermore, Baldus lab demonstrated the prospected improvement of DNP spectral resolution at 800 MHz as compared to the commonly used 400 MHz in the different functional states of KcsA potassium channel, using AMUPol or TOTAPOL as polarizing agent, even though the enhancement is reduced at higher field.[151]

Chapter 3: Materials and methods

3.1. Sample preparation

3.1.1. Plasmid construction

The KR2 construct used in this thesis was kindly provided by Dr. Christian Bamann from the Max Planck Institute for Biophysics, Frankfurt am Main. The KR2 gene with 6x His tag attached to the C-terminal (see KR2 nucleotide sequence in appendix) was cloned in pET26b vector between *Xho*I and *Eco*RI restriction sites and with kanamycin resistance. KR2 amino acid sequence is shown as follows:

```
        10         20         30         40         50         60
MTQELGNANF ENFIGATEGF SEIAYQFTSH ILTLGYAVML AGLLYFILTI KNVDKKFQMS

        70         80         90        100        110        120
NILSAVVMVS AFLLLYAQAQ NWTSSFTFNE EVGRYFLDPS GDLFNNGYRY LNWLIDVPML

       130        140        150        160        170        180
LFQILFVVSL TTSKFSSVRN QFWFSGAMMI ITGYIGQFYE VSNLTAFLVW GAISSAFFFH

       190        200        210        220        230        240
ILWVMKKVIN EGKEGISPAG QKILSNIWIL FLISWTLYPG AYLMPYLTGV DGFLYSEDGV

       250        260        270        280
MARQLVYTIA DVSSKVIYGV LLGNLAITLS KNKELVEANS LEHHHHHH
```

There are in total 288 amino acid residues (including 6x His) in the KR2 gene. The amino acid composition analysis is shown in Table 7.

Table 7: Sequence analysis of KR2 containing 6X His tag. The number of amino acids and its percentage compositions in the sequence are shown in the table.

Amino acids	Number of amino acids	Composition
Ala (A)	19	6.6%
Arg (R)	4	1.4%
Asn (N)	17	5.9%
Asp (D)	7	2.4%
Cys (C)	0	0.0%
Gln (Q)	10	3.5%
Glu (E)	13	4.5%
Gly (G)	21	7.3%
His (H)	8	2.8%

Ile (I)	22	7.6%
Leu (L)	36	12.5%
Lys (K)	11	3.8%
Met (M)	10	3.5%
Phe (F)	23	8.0%
Pro (P)	5	1.7%
Ser (S)	24	8.3%
Thr (T)	15	5.2%
Trp (W)	7	2.4%
Tyr (Y)	15	5.2%
Val (V)	21	7.3%

3.1.2. Transformation

KR2 plasmid with kanamycin resistance was transferred into *E. coli* C43 (DE3) cells via heat shock method. The competent cells were thawed on ice and two 50 µl aliquots were transferred into two pre-chilled tubes. One is for the transformed cells and another one is for the control. 1.5 µl of plasmid solution (~70 ng/ µl) was added to one of the competent cells tube and incubated on ice for 15 minutes to let the DNA attached to cells. Heat shock was performed for 90 seconds at 42°C. The tubes were immediately placed on ice for 2 minutes. 400 µl LB media was then added to the cells (both transformed and control tubes) and the mixture was incubated at 37°C for 20-60 minutes. 50 µl of transformed cells and control cells were each thereafter plated on kanamycin containing agar plates (0.1 mg/ml) and the plates were incubated at 37° overnight to let the colonies grow.

3.1.3. Protein expression

The cell culture for KR2 was done in two steps: pre-culture and main culture. First, a colony from the transformation plate was picked and transferred to 100 ml pre-culture media (LB) containing kanamycin antibiotics (0.1 mg/ml). The transformed cells were grown in the pre-culture media overnight at 37°C, 220 rpm in a bacteria shaker to reach a high cell density. Second, a small fraction of the cells pre-culture (5 ml for each 0.5 L cells culture) was centrifuged down (6400 x g for 10 minutes) and the cells pallet was transferred to the main media M9 (Table 8). The compositions of the media were adjusted according to the labeling scheme. For the uniformly labeled ^{13}C and ^{15}N, the glucose and the NH_4Cl were replaced with ^{13}C-Glucose and $^{15}NH_4Cl$, respectively. For the labeling of specific amino acids, the unlabeled amino acids were additionally

added to the M9 media, and the labeled amino acids were added at OD_{600} of 0.2-0.3. Not all amino acids can be specific labeled because there are metabolic pathways of the *E. coli.* that lead to the scrambling. The cells were further grown in main media at 37°C, 220 rpm until the OD_{600} of 0.6-0.8 was reached. 250 µl of 1 M IPTG solution for 0.5 L culture (final concentration 0.5 mM) was added to induce the protein expression and *all-trans* retinal (10 mg/ml) was added to the media (final concentration 7-10 µM). The cells were grown overnight further at 27°C, 220 rpm for the M9 media, and at 20°C, 220 rpm for the M9 rich media (with amino acids) for 17-18 hours.

Table 8: Components of M9 media

M9 media components	0.5 L	1L
(Autoclaved)		
K2HPO4	3.39 g	6.78 g
KH2PO4	1.5 g	3.0 g
NaCl	0.25 g	0.5 g
NH4Cl	0.5 g	1 g
(Added before the main culture)		
40% Glucose (autoclaved)	5 ml	10 ml
0.01 M FeCl3 (autoclaved)	0.5 ml	1 ml
1 M MgSO4 (sterile filtered)	1 ml	2 ml
Sterile filtered trace elements (See table below)	5 ml	10 ml
Antibiotic (100 mg/ ml):	0.5 ml	1 ml

Table 9: Components of sterile filtered trace elements

Sterile filtered trace elements	For 50 ml
$CaCl_2$ x $2H_2O$	10 mg
$ZnSO_4$ x $7H_2O$	10 mg
$MnSO_4$ x H_2O	10 mg
Thiamine (B1)	250 mg
Niacin	250 mg

Table 10: Components for rich M9 media

Amino acids	For 0.5 L (g)	For 1 L (g)
(Autoclaved)		
Alanine	0.25	0.5
(Cysteine)	0.025	0.05
Glycine	0.25	0.5
Histidine	0.05	0.1
Isoleucine	0.115	0.23
Leucine	0.115	0.23
Lysine hydrochloride	0.125	0.25
Methionine	0.125	0.25
Proline	0.05	0.1
Serine	0.2	0.4
Threonine	0.115	0.23
Valine	0.115	0.23
Phenylalanine	0.065	0.13
(not autoclaved)		
Arginine	0.2	0.4
Aspartic acid	0.2	0.4
Glutamine	0.2	0.4
Glutamic acid	0.325	0.65
Tyrosine	0.085	0.17
Tryptophane	0.025	0.05
Asparagine	0.2	0.4

3.1.4. Cell disruption and purification

After growing the cells in the main culture overnight, the cells were thereafter harvested by centrifugation at 4° C, 6675 × g for 12 minutes. The pellets were suspended in lysis buffer (50 mM HEPES, pH 7.5, DNAseI, and protease inhibitor). The cells in the lysis buffer were pass through the cell disruptor (IUL instrument) at 1.85 kBar 3-4 times. The membrane was then separated by ultracentrifugation at 4° C, 214,382 g for 1 hour 15 minutes. The supernatant was removed and the membrane containing KR2 was homogenized in suspension buffer (50 mM HEPES, 100 mM NaCl, pH 7.5).

The membrane suspension was solubilized in the solubilize buffer (1.5% DDM, 50 mM HEPES, 300 mM NaCl, 5 mM imidazole, pH 7.5, with protease inhibitor) for 21 hours at 4° C under stirring. The insolubilized part was separated from the membrane solution by ultracentrifugation at 4° C, 310523 g for 1 hour. The supernatant containing KR2 was then incubated with Ni-NTA resin (previously washed with ddH_2O to eliminated ethanol and equilibrated with wash-1 buffer (50 mM HEPES, 300 mM NaCl, 0.05% DDM, 5 mM imidazole, pH 7.5) for 1.5 hours). After incubation, the protein bound Ni-NTA resin was loaded in a column and washed with wash-1 (50 mM HEPES, 300 mM NaCl, 5 mM Imidazole, 0.05% DDM, pH 7.5), wash-2 (50 mM HEPES, 300 mM NaCl, 20 mM Imidazole, 0.05% DDM, pH 7.5) and wash-3 (50 mM HEPES, 300 mM NaCl, 50 mM Imidazole, 0.05% DDM, pH 7.5) buffers to eliminate the impurities. The protein was then eluted with elution buffer-1 (50 mM HEPES, 300 mM NaCl, 0.05% DDM, 400 mM Imidazole, pH 7.5) until no protein was observed on the resin. The resin was further eluted with Elution buffer-2 (50 mM HEPES, 300 mM NaCl, 0.05% DDM, 500 mM Imidazole, pH 7.5) The protein concentration as well as expression yield were determined by UV-Vis absorption spectroscopy. The protein was further characterized by SDS and BN-PAGE electrophoresis and size exclusion chromatography.

3.1.5. Reconstitution

KR2 is a membrane protein and the structural study of KR2 in its native-like environment (lipid bilayer) is of interest. After purification, the protein was therefore reconstituted in a synthetic lipid bilayer, constituted of DMPC and DMPA (9:1 weight/weight). The unilamellar DMPC: DMPA liposome was prepared by the extrusion method. First, 27 mg DMPC and 3 mg DMPA were dissolved in Chloroform/Methanol mixture (2:1 vol/vol). The lipid solution was dried first under nitrogen gas flow until no liquid was observed and subsequently dried further overnight by rotary evaporator overnight. 10 ml of lipid buffer (50 mM HEPES, 50 mM NaCl, pH 7.5) was added to the dried lipid. The lipid was detached from the surface by short sonication. The emulsion was extruded through a 0.2 μm membrane 13 times. This final liposome concentration is 3 mg/ml. KR2 in elution buffer-1 was added to the liposome solution and stirred at room temperature for 30 min. Biobeads (autoclaved in ddH_2O) were slowly three times stepwise added to remove the detergent and let the protein form proteoliposomes. First, 80 mg/ml of biobeads were added to the protein/liposome mixture and gently mixed (falcon rotator) for 2 hours. Then the same amount of biobeads was added (second time) and the falcon was rotated overnight at 4°C. Next, biobeads (same amount) were added for the third time and mixed for further 2 hours at room temperature. The biobeads were removed with a sieve and the proteoliposome was pelleted by ultracentrifugation at 4°C, 310523 g.

3.1.6. NMR/DNP sample preparation

The prepared KR2 proteoliposome was washed 2 times with NMR buffer to bring the protein into the desired buffer condition. For this thesis, Tris buffer with pH 8.5 was used as NMR buffer (50mM Tris, 5 mM $MgCl_2$). For the study of KR2 in sodium ion pump mode, 30 mM, or 100 mM NaCl was used and the Tris concentration was reduced to 25 mM. For the DNP-enhanced ssNMR studies, the DNP juice (20mM AMUPol, D_2O:H_2O:d^8-glycerol (3:1:6), containing 25 mM Tris, 30 mM or 100 mM NaCl and 5 mM $MgCl_2$) was added on the proteoliposome pellet and incubated overnight at 4°C for 20 hours. The supernatant was then removed, and the sample is packed in an NMR rotor. For the illumination study, the proteoliposome pellet was distributed on the wall of sapphire rotor to maximize the illumination yield.

3.1.7. Preparation of KR2 with labeled retinal

The 10-18-$^{13}C_9$-retinal and 14,15-$^{13}C_2$-retinal used in this thesis were synthesized by the research group of Prof. Richard Brown from the University of Southampton. The 12,13,20-$^{13}C_3$-retinal was obtained from Dr. Jiafei Mao from the research group of Prof. Clemens Glaubitz, Goethe University Frankfurt. The preparation of KR2 with a labeled retinal was performed by the expression of opsin without retinal added to the media. The expression was induced at OD_{600} of 0.5-0.6 and the bacteria were grown overnight (17-18 hours). The cells were then harvested and disrupted in a similar way to the normal expression with an unlabeled retinal. The membrane from a 0.5 L expression was resuspended in 30 ml suspension buffer. The labeled retinal was then added to the suspension buffer (final concentration 7-10 µM). The falcon was rotated in the cold room (4°C) for 2 hours under dark condition. The pink-colored membrane showed the success of retinal incorporation. The protein was purified and reconstituted in the same manner as that of for the unlabeled retinal sample.

3.1.8. Plasmid extraction

KR2 constructed plasmid can be extracted from the transformed *E. coli* cells grown in LB media overnight at 37°C using QIAprep® Spin Miniprep kit. 20 ml of pre-culture was used for extracting 0.2 ml of plasmid DNA solution. The overgrowth which may lead to plasmid yields should be avoided. 20 ml overnight bacterial culture was pelleted by centrifugation at 8000 rpm (6800 x g) for 3 minutes at room temperature. The pelleted bacterial cells were resuspended in 1 ml P1 buffer. 250 µl each was transferred to four 1.5 ml tubes. 250 µl P2 buffer was added to each tube and mixed by inverting for 4-6 times. (The lysis procedure should not proceed more than 5 minutes.). 350 µl of N3 buffer was added to the tubes and mixed immediately by inverting the tubes until the solution turns colorless. The tubes were centrifuged at 13000 rpm (Biofuge

pico desktop centrifuge) for 10 minutes. Only the clear solution was loaded on the QIAprep® spin column and the column were centrifuged at 13000 rpm for 1 minute. The DNA attached to the column was washed with 750 µl PE buffer. After centrifugation for 1 minute, the supernatant was removed. The column was centrifuged again for 1 minute to remove the rest liquid. The column was then transferred to new clean tubes for the DNA collection. 50 µl was added to each column and left for 15 minutes, followed by centrifugation at 13000 rpm for 1 minute. The quantity of DNA was determined by measuring with Nanodrop. The A260/A280 ratio should be more than 1.8 for the high purity DNA solution.

3.2. Biochemical characterization

3.2.1. UV-Vis absorption spectroscopy

UV-Vis absorption spectroscopy was used to determine protein concentration in detergent after purification. The amount of protein eluted was calculated using Beer-Lambert law:

$$A_{524} = \varepsilon \cdot c \cdot l \qquad (29)$$

A_{524} = Absorption at 524 nm

c = Concentration (mg/ml)

l = Cuvette path length (cm)

ε = Extinction coefficient (for KR2 1.46 ml·mg^{-1}·cm^{-1} at 524 nm)

The absorption at 524 nm was used for the calculation of protein concentration because it exhibits the bound retinal to the opsin. The ratio of A_{280}/A_{524} should be around 2 for high purity protein and the full retinal incorporation.

3.2.2. SDS PAGE

Sodium dodecyl sulfate polyacrylamide gel electrophoresis (SDS-PAGE) was used to prove the expression and quality of purified proteins. The method allows the protein to be separated by its mass. SDS is an anion detergent carrying negative charges and binds to the polyamide chain. The negative charge of SDS will denature the protein and carry the protein through the pores of polyacrylamide gel to the anode in an electric field. In the polyacrylamide gel, large molecules will migrate slower than small molecules, resulting in the separation of protein according to their molecular weights. In this thesis, the precast high-resolution gels from *expedeon* were used. The gel was first equilibrated with MES buffer (50 mM MES, 50 mM Tris base, 0.1% SDS, 1mM EDTA). The buffer was used as both anode and cathode electrolytes. The flow through (FT), wash-1 (W1), wash-2 (W2), wash-3 (W3), elution-1 (E1), elution-2 (E2), and proteoliposome

sample were mixed with loading buffer NuPAGE™ LDS Sample Buffer (4X) and loaded in the pocket of the equilibrated gel. SDS-PAGE molecular weight standard mixture used as a marker was loaded together to quantify the molecular weight of purified protein. The gel was run at 135 V for approximately 1 hour. The gel was then stained with staining buffer containing 0.2% (wt/v) Coomasie Brilliant Blue G250, 50% ethanol (v/v), and 10% acetic acid (v/v) for 1 hour. The stained gel was destained with the destained buffer containing 7% acetic acid (v/v) and 10% ethanol (v/v) or with water until the background color was gone.

Table 11: Components for the SDS-PAGE sample preparation

Components	Sample amount (µl)	Loading buffer (µl)
FT	22	8
W1	22	8
W2	22	8
W3	22	8
E1	3.5	1,5
E2	3.5	1.5
Proteoliposome	3.5	1.5

3.2.3. Blue native PAGE

Blue native polyacrylamide gel electrophoresis (BN-PAGE) can be applied to determine protein masses and oligomerization in their native states. In contrast to SDS, which denatures the protein, Coomasie Brilliant Blue G250 used in BN-PAGE will attach to the hydrophobic part of the protein, providing the required negative charges to the protein and enable the protein to migrate along the polyacrylamide gel. In this thesis, NuPAGE™ 4-12% Bis-Tris protein gel was used. The components for cathode, anode, and sample buffers are listed in Table 12 and Table 13:

Table 12: Components of the cathode, anode, and sample buffers for BN-PAGE

Cathode buffer (1X)	Amount
Native PAGE Running buffer (20X)	10 ml
Native PAGE Cathode Additive (20X)	10 ml
Deionized water	180 ml
Total volume	200 ml
Anode buffer (1X)	Amount
Native PAGE Running buffer (20X)	30 ml

Deionized water	570 ml
Total volume	600 ml
Native PAGE Sample Buffer (1X)	4X for 20 ml
50 mM Bis-Tris (MW 209.4)	0.836 g
50 mM NaCl (MW 58.44)	1 ml of 4M stock
6 N HCl	0.2 ml
10% wt/v glycerol	8 g
0.001% Ponceau S (MW672.63)	0.8 mg
pH 7.2	*No need to adjust

Stock solution	Amount
Native PAGE Running buffer (20X)	For 1 L
1 M Bis-Tris	209.2 g
1 M Tricine	179.2 g
pH 6.8	*No need to adjust
Native PAGE Cathode Additive (20X)	For 250 ml
0.4 % Coomasie G250	1g of Coomasie G-250 in ddH2O

Table 13: Components of the sample preparation for BN-PAGE

Components	Sample amount (µl)
Sample buffer	5
Sample (FT, W1, W2, W3, E1, E2)	10
0.4 % Coomasie G250	1
Deionized water	4

3.2.4. pH titration

pH titration was used to determine pKa of D116, which forms a direct hydrogen bond with Schiff base nitrogen in KR2. The protonation of D116 residue, therefore, affect the absorption maximum of KR2. Changes in the absorption maximum of KR2 were monitored at various pH. The purified protein solution was first 4x concentrated with a molecular weight cut concentrator (50 kDa). KR2 forms a pentamer, having a total molecular weight of 166 kDa, will not pass through the filter. The elution buffer was exchanged to the pH-titration combi-buffer containing 50 mM Tris,

50 mM Sodium phosphate, 50 mM Boric acid, 50 mM Sodium citrate, 100 mM NaCl, 0.05% DDM, pH 7.17) using PD10 (GE Healthcare) column (See the manufacturer protocol). 3.5 ml of KR2 in the combi-buffer was divided into two tubes. The first tube was stepwise acidified by slowly adding 4M HCl. The pH change was monitored by a pH meter. 100 µl of the sample were taken at every 0.5 pH change. This was continued until pH 3 was reached. Another tube was used in a similar manner but for the titration to the basic direction (from pH 7 to 12) using 4M NaOH and 100 µl of samples were taken every 0.5 pH change. The samples were then loaded on the sample plate and the absorption maxima were measured by TECAN microplate reader (Infinite® 200 PRO). The absorption maximum of KR2 at each pH was plotted against the sample pH and the obtained curve was fitted to a sigmoidal curve (equation 29) using the OriginPro program. The pKa of the sample is then determined according to the Henderson-Hasselbach equation.

$$y = \frac{A_1 - A_2}{1 + e^{(x - x_0)/dx}} + A_2 \qquad (30)$$

Henderson-Hasselbach equation: $$pH = pK_a = \frac{\log_{10}[A^-]}{[HA]} \qquad (31)$$

3.2.5. Size exclusion chromatography

Size exclusion chromatography (SEC) was used in this thesis to examine the quality and homogeneity of the purified protein. SEC, also known as gel filtration, is a chromatography technique, in which molecules are separated by sizes as they pass through an SEC resin packed in a column. The SEC resin is composed of a porous matrix of spherical particles that do not react or absorb. After the sample was applied, molecules that larger than the pores cannot diffuse into the beads and will elute first. Molecules that are smaller can penetrate into the pores varying based on their sizes. The smallest molecule will enter the smallest pore and then will elute last. Based on molecular size, molecules under investigation will therefore pass through the column at a different time and can be separately detected and collected.

In this thesis, a GE Superdex 200 increase 10/300 column was used. The column is connected to a Biorad chromatography system, placed in a cold room (4°C). The column, usually stored in 20% ethanol solution, was first washed with 2 column volume (CV) of ddH_2O and then equilibrated with SEC buffer (50 mM HEPES, 150 mM NaCl, 0.05% DDM) using a flow rate of 0.1 ml/min. 500 µl of 4X concentrated protein (~0.7 mg/ml) in 0.05% DDM was first filtrated to ensure there is no aggregation before loaded to the column. The absorptions at 524 nm, 280 nm, and 340 nm were monitored. The sample was collected with 0.5 ml per fraction. After use, the column was then washed with 2 column volume ddH_2O and 2 column volume 20% ethanol in H_2O.

3.2.6. Transport activity assay

KR2 is an outward sodium ion pumping microbial rhodopsin. The pumping activity can be measured by monitoring the pH change upon light activation[1]. When the KR2 overexpressed cells pump Na^+ out, the cells will uptake H^+ into the cells to balance the membrane potential, resulting in a pH increase. After spinning down the KR2 overexpressed cells, the cells were resuspended in 100 mM NaCl solution (without buffer) to reach an OD of 12. 1 ml of cell suspension was placed in 2 ml tubes with a small magnetic stirrer. The pH was monitored every 4 seconds. The cells were left in dark for 1 minute and then the green light was turned on for 4-5 minutes. After that, the light was turned off for another 2 minutes. The pH change was calculated and plotted against time

3.3. Trapping of the photointermediates

3.3.1. K/L-intermediates

K-intermediate of KR2 can be cryogenically trapped inside NMR magnet by illumination with LED lamp (470 nm, 3.3 W, Mightex) at 110 K for 40 minutes. At this cryogenic temperature, the protein cannot progress to the next step of the photocycle and was thermodynamically trapped. L-intermediate can also be trapped by illuminating at 110 K inside the magnet. It exists in an equilibrium with K-intermediate. Upon increasing the temperature in the probehead to 190 K. The equilibrium shifted from K- to L-intermediate as proven by cryo-UV/Vis absorption spectroscopy (incorporation with Peter Eberhard from Wachtveitl group, see 0). At 210 K, no more K-intermediate was observed (Figure 39).

3.3.2. O-intermediate

To trap the O-intermediate of KR2, the sample was illuminated with green LED lamp (525 nm, 1.3 W) for several seconds shortly and directly before rapidly freezing in liquid nitrogen. The method is called in this thesis flash freezing. The frozen rotor was then quickly inserted into the magnet cooled to 110 K. The difference absorption spectra at 605 nm of the O-intermediate trapped by this method was proven by cryo-UV-Vis difference absorption spectroscopy (Figure 40).

3.3.3. Cryo-UV-Vis absorption spectroscopy (carried out by Peter Eberhard)

To assign the trapped intermediate under DNP condition to optically identified intermediates, UV-Vis difference absorption spectra at cryogenic temperature were recorded by Peter Eberhard from Wachtveitl group, Institute for Physical and Theoretical Chemistry, Frankfurt university. The UV/vis Spectroscopy under cryogenic conditions were recorded with a fiber-optic

spectrometer (USB2000+, Ocean Optics). Probe light was provided by a balanced deuterium halogen-source (DH-2000-BAL, Ocean Optics). The sample temperature was controlled with the help of a liquid nitrogen cooled cryostat (Oxford Instruments, OptistatDN). For illumination, a ThorLabs light emitting diode (LED) controlled by a ThorLabs DC4100-driver was coupled into the cryostat and the sample was irradiated for ~1 minute at the target temperature. For the spectra recorded at 110 K and 160 K, a 490 nm LED was used, for the spectra at 230 K and the flash freezing a 530 nm LED was used as a pump source. The sample was prepared in a shortened 1x10 mm quartz cuvette (100-QS, Hellma). For cryo-protection similar to the DNP sample and the reduction of light scattering, 60% v/v of glycerol (Sigma-Aldrich, spectrophotometric grade) was added to the purified DDM (0.05%) in 25 mM Tris buffer containing 5 mM $MgCl_2$ and 30 mM NaCl. All difference spectra were obtained by subtracting the dark spectrum of the protein obtained at the same temperature before irradiation.

3.4. Solid-state NMR (ssNMR)

3.4.1. Dynamic nuclear polarization (DNP)-enhanced ssNMR

All experiments were performed on a Bruker 400 DNP system consisting of a 400 MHz WB Advance II NMR spectrometer connected with a 263 GHz Gyrotron as a microwave source via waveguide. A 3.2 mm HCN Cryo-MAS probe and a MAS frequency of 8 kHz or 10 kHz was used in all experiments. The ^{13}C and ^{15}N chemical shifts were referenced indirectly to DSS and liquid ammonia, respectively, using ^{13}C CO-alanine at 179.85. The setup and process parameters for cross polarization (CP) step, double quantum filter (DQF), proton diffusion spin diffusion (PDSD), double quantum single quantum (DQSQ), double quantum-heteronuclear local field (2Q-HLF), TEDOR and N(CO)CX are summarized in the Table 14.

Table 14: NMR experiment setup parameters.

Experiment	CP	DQF	PDSD	DQSQ	2Q-HLF	TEDOR	N(C)CX
Dimensionality	1D	1D	2D	2D	1D	2D	2D
Temperature (K)	110	110	110	110	110	110	110
Recycle delay (s)	3	3	3	3	3	3	3
1H decoupling during acquisition (kHz)	SPINAL 100 kHz	SPINAL 100 kHz	SPINAL 100 kHz	SPINAL 100 kHz	SPINAL 100 kHz	SPINAL 100 kHz	SPINAL 100 kHz
Number of scans	128	1024	128	256	3200	1312	1024
Sweep width	29.8	29.8	29.8	29.8	29.8	29.8	40.8
Acquisition time (ms)	10	10	10	10	10	10	9
Indirect increments	-	-	320	320	-	60	64
Sweep width (kHz)	-	-	30.2	56	-	8	8
Acquisition time (ms)	-	-	5.3	2.9	-	3.75	4
CP	^{1}H ramp (80-100%) 100 kHz Contact time: 1.2 ms	^{1}H ramp (80-100%) 100 kHz Contact time: 1.2 ms	^{1}H ramp (80-100%) 100 kHz Contact time: 1.2 ms	^{1}H ramp (80-100%) 100 kHz Contact time: 1.2 ms	^{1}H ramp (80-100%) 100 kHz Contact time: 1.2 ms	^{1}H ramp (80-100%) 100 kHz Contact time: 1.2 ms	^{1}H ramp (80-100%) 100 kHz Contact time: 1.2 ms
Others		POST-C7 Excitation (0.5 ms) Reconversion (0.5 ms)	Mixing time: 20 ms	POST-C7 Excitation (0.5 ms) Reconversion (0.5 ms)	POST-C7 PMLG-9 for homonuclear decoupling (105 kHz) ^{1}H CW during constant period (105 kHz)	TEDOR Mixing time: 6 ms	DCP (4.5 ms) 13C: 3.5 x ν_r, 15N: 2.5 x ν_r Spin diffusion: 50 ms
Process parameters Direct: Zero filled Window function Line broadening Indirect: Zero filled Window function	 8192 points Exponential 50 Hz 	 8192 points Exponential 50 Hz 	 4096 points, Gaussian window 20 Hz 2048 points Square cosine	 8192 points, Gaussian window 20 Hz 4096 points Square cosine	 8192 points Exponential 50 Hz 	 4096 points, Gaussian window 20 Hz 1024 points Square cosine	 2048 points, Square cosine 20 Hz 1024 points Square cosine

The ^{1}H-^{13}C cross-polarization (CP) was achieved using a ramped spin-lock pulse (100 kHz) for protons and a constant amplitude spin lock pulse for carbons. The contact time was optimized in the 0.8 to 1.5 ms range. The 2D Proton Diffusion Spin Diffusion (PDSD) ^{13}C-^{13}C correlation experiment was constructed with a mixing time of 20 ms. In the indirect dimension, an acquisition time of 5.3 ms, 320 increments (128 scans per increments) were used. ^{13}C-double quantum filter (DQF) experiments were obtained using the POST-C7 sequence double quantum excitation and reconversion at 0.5 ms each. The 2D Double Quantum Single Quantum (DQSQ) spectra were recorded with 300 increments and 17.86 us dwell time in the indirect dimension. 256 scans were recorded in each increment. For the ^{15}N-^{13}C correlation spectra, a Transfer Echo Double Resonance (TEDOR) sequence with z-filter (1 rotor period) and a mixing time of 6 ms was applied for the long length detection. 60 increments with 125 us dwell time or 28 increments with 250 us dwell time were used in the indirect dimension. The N(C)CX spectra were acquired by double cross polarization (DCP) with PDSD pulse sequence. A constant lock field of 2.5 x ν_r field strength and 3.5 x ν_r with a linear ramp was applied on ^{15}N and ^{13}C, respectively. The spin diffusion was accomplished with 50 ms. The acquisition time was 9 ms and 4 ms in the direct and indirect dimensions, respectively.

For the HCCH torsional angle measurements, a double quantum heteronuclear local field experiment was applied. Two POST-C7 sequences during two rotor periods were used for double quantum excitation and reconversion. The phase-modulated Lee Goldburg sequence (PMLG-9) at 105 kHz was used for the homonuclear decoupling and a ^{1}H CW irradiation at 105 kHz was used during the POST-C7 sequence. Each data point was recorded with 3200 scans. The peaks corresponding to different photointermediates were fitted with Topspin 3.5 solid line shape analysis. The peaks are subsequently integrated, and the signal intensities were plotted against the dephasing time. The dephasing curves were compared with the simulated data with various torsion angles to find the best-fit torsion angle. The simulated data were obtained using SIMPSON[164] for the two ^{13}C and two ^{1}H spin system. The PDB files with different torsion angles were created with the C-H and C-C bond length of 1.42 and 1.1 Å[155], respectively, and the H-C-C angle of 115°. The PDB files with the positions of atoms for each dihedral angle were transformed to spin system files (spinsys) containing dipolar coupling between all nuclear pairs. The C-C dipolar coupling strength was reduced by a scaling factor. The scaling factor was varied to find the best fit dephasing curve. The scaling factor of 0.4 was found to fit the best under the experimental condition performed in this thesis. The SIMPSON script used here was published previously by Dr. Jiafei Mao.[155]

3.4.2. High-field ssNMR

High field spectra were recorded using a Bruker Avance II 850 MHz spectrometer equipped with a triple resonance DVT 3.2 mm HCN probe or HX probe for the illumination experiments. The spectra were recorded at 275 K with MAS spinning rate of 14 kHz or at 247 K and MAS of 12 kHz. Chemical shift referencing is carried out indirectly with respect to DSS through CO-Alanine at 179.85 ppm. For all experiments, 83.3 kHz decoupling using SPINAL64 was applied during acquisition. The recycle delay for the 2 mM Gadolinium-DOTA doped sample was set to 1 s.

3.4.3. ^{23}Na NMR

Solid-state ^{23}Na NMR experiments were performed on a Bruker Avance II 850 MHz or a Bruker Avance II 600 MHz spectrometer operating at 224.92 MHz and 158.75 MHz, respectively, using an HX probe. The ^{23}Na chemical shifts were referenced to NaCl(s) at 7.0 ppm. The ^{23}Na NMR spectra were recorded with a spinning rate of 10 kHz. A cooling gas was used to maintain the sample temperature of 275 K. Single-pulse excitation of 4 µs with 100 ms acquisition time, 1260 ppm spectral width, and 1s delay time was used to record the spectra. An Inversion recovery experiment was used to measure spin-lattice relaxation time (T_1) for the free and bound sodium ion.

3.4.4. ^{13}C-^{15}N distance determination using TEDOR experiments

Distances information between two labeled nuclei can be gained from a TEDOR buildup curve. 1D TEDOR spectra with varied mixing time between 0 to 80 rotor period (8 kHz MAS) were recorded. After the Fourier transforms, the peaks from each spectrum were fitted with TOPSPIN solid line analysis and integrated. The peak intensities were plotted against the number of rotor periods. The TEDOR buildup curves were then fitted with the TEDOR equation reported by Müller, et al.[165] using MATHLAB program:

$$\frac{S_T}{S_0} = \frac{1}{2}\left\{\left[J_0\left(\sqrt{2}\lambda_{m-n}\right)\right]^2 - \left[J_0\left(\sqrt{2}\lambda_{m+n}\right)\right]^2\right\} - \sum_{k=1}^{\infty}\frac{1}{16k^2-1}\left\{\left[J_k\left(\sqrt{2}\lambda_{m-n}\right)\right]^2 - \left[J_k\left(\sqrt{2}\lambda_{m+n}\right)\right]^2\right\} \quad (32)$$

$$\lambda_{m\pm n} = (m \pm n)D\tau_R \quad (33)$$

S_T = TEDOR signal intensity

S_0 = TEDOR signal intensity at 0 mixing time

D = Dipolar coupling (Hz)

τ_R = one rotor period time (µs)

m = dephasing period (number of rotor)

n = refocusing period (number of rotor)

Because the spin magnetization dephasing during the mixing time due to T2 relaxation. The TEDOR intensities obtained from equation was further treated, accounted for the T2 relaxation.

$$S_{TEDOR}^{Damp} = \frac{S_T}{S_0} Exp\left(-n \times \frac{\tau_R}{T_2}\right) = \frac{S_T}{S_0} Exp(-n \times \tau_R \times \pi \times LB) \quad (34)$$

T_2 = transversal relaxation (s)

LB = line broadening (Hz)

Chapter 4: KR2 expression and biochemical characterization

All KR2 containing 6x His tag used in this thesis was overexpressed in *E. coli* 43 (DE3) using M9 medium or M9 rich medium (containing amino acids) as described in chapter 3.1. After the expression, the protein was purified and characterized using biochemical and biophysical methods to quantify the yield and prove the purity and quality of the samples.

4.1. UV-Vis Absorption

UV-Vis absorption spectroscopy was applied to characterize and quantify the purified KR2 in 0.05% DDM solution. The chromophore bound to the conserved lysine residue (K255) has a characteristic absorption maximum at around 524 nm. The absorption at this wavelength was used to calculate the concentration of protein solution and the expression yield. The yields for the expressions in M9 and M9 rich medium were ~15 mg/L and ~23 mg/L, respectively. The absorption at 280 nm is mainly from tryptophan and tyrosine residues of opsin. A_{280}/A_{524} ratio of < 2 indicates a high purity of the sample and the full incorporation of retinal in KR2. Figure 21 shows UV-Vis absorption spectra of KR2 overexpressed in M9 (A_{280}/A_{524} = 1.6) and M9 rich medium (A_{280}/A_{524} = 1.9). Both samples exhibit high purity and full incorporation of retinal.

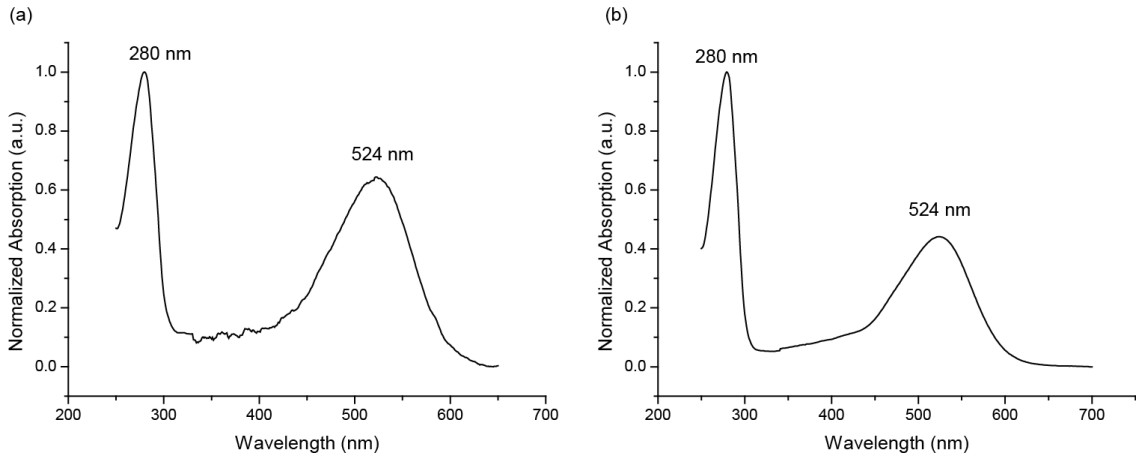

Figure 21: UV-Vis absorption spectra of KR2 in elution buffer (50 mM HEPES, 300mM NaCl, 400 mM Imidazole and 0.05% DDM, pH 7.5) expressed in (a) M9 medium and (b) M9 rich medium.

4.2. SDS-PAGE

To monitor and track the purification and reconstitution steps, the flow through (FT) after incubation with Ni-NTA beads, wash-1, wash-2, wash-3, elution-1, elution-2, and proteoliposome samples were analyzed by SDS-PAGE. The purified KR2 in DDM (elution-1) for both M9 and M9 rich media expression was obviously observed at around 20 kDa as a single band in the SDS-gels (Figure 22). The band appeared shifted from the actual molecular weight size (32.6 kDa) because of the incomplete unfolding of KR2 by SDS. This kind of observation was reported previously for membrane proteins.[166] The impurity bands of the elution-1 are very pale compared to the protein band, showing a high purity of the samples. After reconstitution of KR2 in DMPC:DMPA (9:1) liposome, the KR2 band appeared at the same position as that for the sample in DDM solution. This demonstrated the success of protein reconstitution in the liposome.

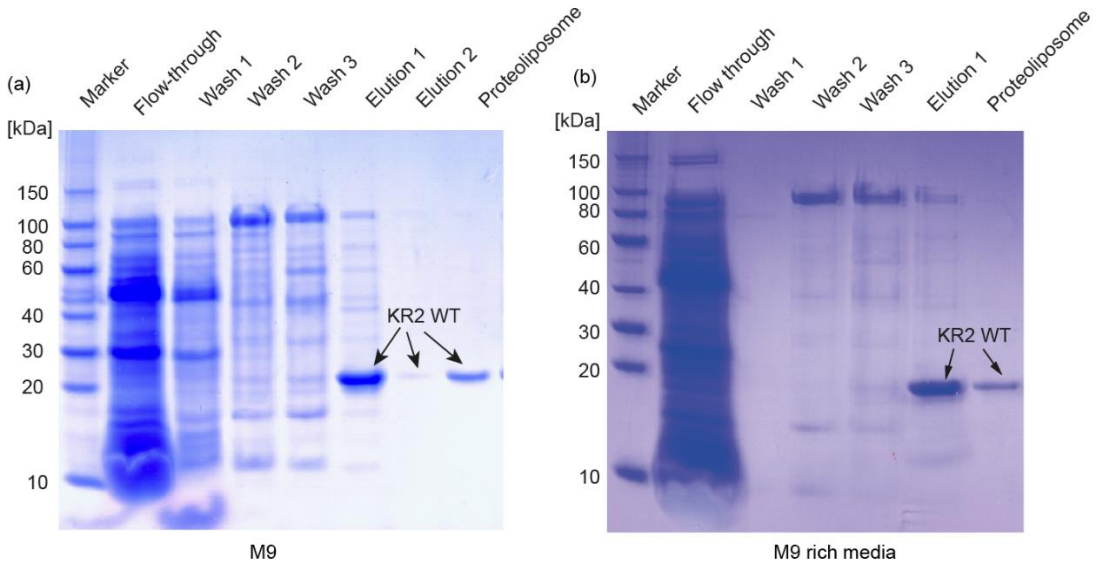

Figure 22: SDS gel of flow through, wash-1, wash-2, wash-3, elution-1, elution-2 and proteoliposome for the KR2 samples expressed in (a) M9 and (b) M9 rich media. The single band of KR2 (WT) at around 20 kDa shows the high purity of the samples in elution-1 buffer and proteoliposome.

4.3. Size exclusion chromatography

Size exclusion chromatography was applied to analyze the purity, homogeneity, and oligomerization of proteins. KR2 in 0.05% DDM was eluted as a single sharp peak at around 11-14 ml elution volume, indicating that the protein is pure, homogeneous, and has only one oligomeric state.

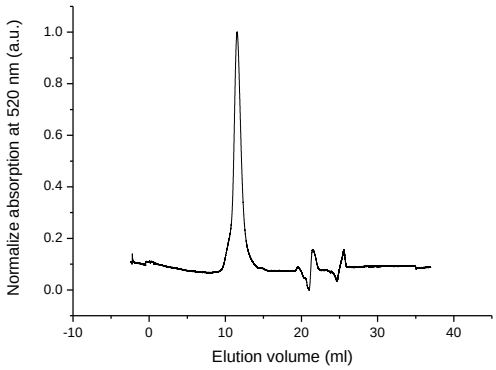

Figure 23: Size exclusion chromatogram of KR2 in detergent micelles (50 mM HEPES, 300mM NaCl, 400 mM Imidazole and 0.05% DDM, pH 7.5) shows a high purity and homogeneity of the protein sample.

4.4. BN-PAGE

BN-PAGE was used to analyze the oligomeric states of proteins. The purified KR2 samples in detergent micelles (elution-1 and elution-2, after SEC) and after reconstitution (proteoliposome) show a single band in BN-PAGE gel (Figure 24), indicating that KR2 forms one stable oligomer. The molecular mass of a membrane protein observed in BN-PAGE gel has to be corrected with a factor of 1.8 due to the binding of Coomasie brilliant blue G250 used as a charge carrier molecule.[167] From the crystal structures crystallized at neutral conditions, pH 5.6 (4XTO) and 8.0 (6REW), KR2 assembles to a pentamer. Since KR2 has a molecular weight of 32.6 kDa, a pentameric band should arise at around 293 kDa (32.6 x 5 x 1.8). This is in line with the band observed on the BN-PAGE gel at slightly above 242 kDa. This confirms the pentameric structure of KR2.

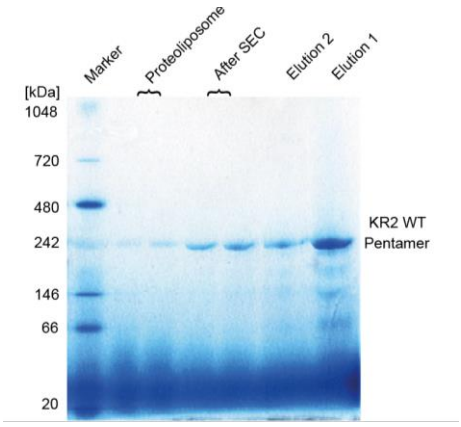

Figure 24: BN-PAGE gel of purified KR2 in detergent micelles (elution 1 and 2), after size exclusion chromatography (SEC) and reconstituted in DMPC/DMPA (9:1) liposomes (proteoliposome). The band slightly above 242 kDa shows the pentameric structure of KR2.

4.5. pH Titration

D116 is the proton acceptor in KR2, that receives proton from the Schiff base upon M-state formation. Because the residue forms a direct hydrogen bond with the Schiff base nitrogen, a change in the protonation state of D116 is going to affect the absorption of KR2. Based on this principle, pKa of D116 can be determined using UV-Vis absorption spectroscopy. The maximum absorption of KR2 bound retinal at different pH was measured and plotted against the sample pH. Based on the Henderson-Hasselbach equation, pKa of D116 is found to be 4.5 ± 0.8 (see Figure 25). This means that D116 is protonated at pH < 4.5 and deprotonated at pH > 4.5. Note that the plateau of the sigmoidal curve at pH < 3 was not reached due to the instability of protein and the loss of the retinal at an extreme acidic condition. The value is lower than the pKa reported by Inoue et al. (pKa = 6.26±0.11).[1] This may be explained by the different data analyzing method. Inoue et al. use the change in absorption at 586 nm and 501 nm to determine the pKa value while in this thesis, the absorption maximum wavelength relative to pH was exploited. Interestingly, the mutation at the position far away from the retinal binding pocket in G263F-KR2 has an effect on the absorption and pKa of the protein. G263 is the residue that plays an important role in the ion selectivity of KR2. The substitution of glycine with phenylalanine leads to the additional K^+ pumping activity.[17]

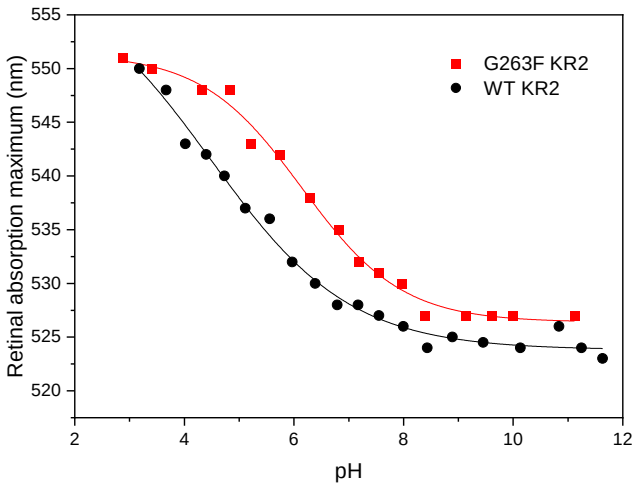

Figure 25: pH titration curves of KR2 WT and its G263F mutant in detergent micelles (50 mM Tris, 50 mM Sodium phosphate, 50 mM Boric acid, 50 mM Sodium citrate, 100 mM NaCl, 0.05% DDM, pH 7.2). Retinal absorption maxima (nm) were plotted against sample pH. The data were fitted with Boltzmann equation (equation 29) using OriginPro program.

4.6. Transport assay

The function of overexpressed KR2 was verified by the transport assay (see 3.2.6).[1] The KR2 overexpressed *E.coli* cells were centrifuged down and washed with unbuffered salt solution (100 mM NaCl). The pH changed upon light activation was observed. After light activation, sodium ions were pumped out, leading to the influx of proton into the cells to balance the membrane potential. This resulted in an increase in pH (Figure 26). When the light was turned off, the cells adjusted the pH back to the normal level. The data showed that the overexpressed KR2 functions properly as a light-driven sodium ion pump.

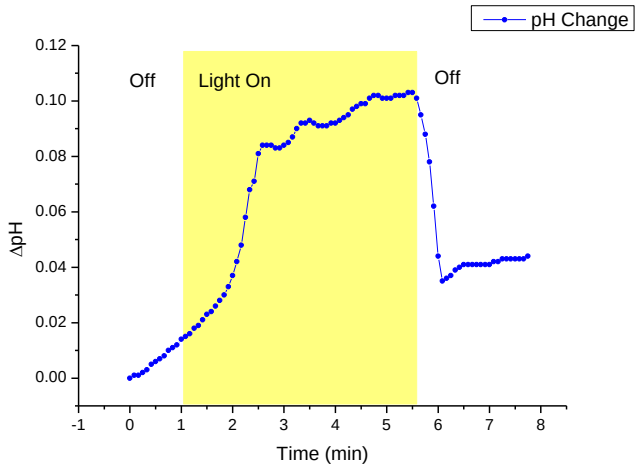

Figure 26: Pumping activity of KR2 WT expressed in *E.coli.* cells (OD 12 in 100mM NaCl solution). An increase in pH was observed after light (green) activation, and when the light was turned off, the pH decreased.

Chapter 5: Retinal conformation and Schiff base interaction during the photocycle of KR2

5.1. Introduction

Light-sensitive photoreceptor proteins are found in all domains of organisms. They possess bound chromophores, e.g. bilin in biliproteins[168], flavin in flavoproteins[169], and retinal in retinylidene proteins[18] to absorb photons for energy conversion or inter/intracellular signaling. Among them, KR2 is the first discovered light-driven outward sodium ion pump, a new class of microbial rhodopsin, found in marine flavobacteria.[1] The pumping of sodium ion, a non-proton cation, is relatively a new function for microbial rhodopsins. The ability to pump sodium ions out of cells initiates the potential of applying KR2 as an optogenetic tool to hyperpolarize cells. The advantage of cells hyperpolarization using sodium ion instead of proton is the capability to manipulate the cell membrane potential without affecting pH of the cells.[170,171]

After the discovery, numerous studies based on time-resolved visible[2,48], FTIR[3,52,54,172], Raman[4], NMR spectroscopies[5,173], X-ray crystallography[16,17,50], and site directed mutagenesis[1,16,17,38,40] have been performed to elucidate the molecular mechanism and ion transport pathway of the protein. Crystal structures of the wild type and important mutants in the dark state[16,17,50] have been reported on the PDB database. The differences among these crystal structures are mainly the crystallized pH conditions or the soaking buffer pH, that result in the different oligomeric states (monomeric or pentameric), major variations at the retinal binding pocket, and the presence and absence of bound sodium ion at the protomer interface (see Chapter 1 for detail). Four main types of intermediates after light activation, named K, L, M, and O, are identified and characterized by time-resolved visible absorption and vibrational spectroscopies.[1–3] Recently, the crystal structure of O-intermediate with Na^+ bound near retinal and the time-resolved crystal structures from 800 fs to 20 ms, based on time-resolved serial femtosecond crystallography (TR-SFX) using free electron laser, were reported by Kovalev, et al.[8] and Skopinsevt, et al.[7], respectively, providing an important insight into the molecular mechanism. Nevertheless, all these knowledges are still not able to complete the puzzle and fully elucidate the molecular mechanism of the light-activated ion transport across the membrane due to their resolution limit. Here, DNP-enhanced ssNMR can come to play a role by providing the fine electrostatic structural information that helps to elucidate the sodium ion pumping mechanism.

In KR2, the retinylidene chromophore is bound to the conserved lysine residue, K255, through Schiff base linkage, located in the retinal binding pocket of the opsin. The key residues in the

retinal binding pocket, like D116, N112, S70, D251, W113, and W215 revealed by site directed mutagenesis and crystal structure in the resting state, determine specific steric and electrostatic interactions, key water molecules, and H-bonding networks. The alteration of retinal conformation after light activation is the main gear that drives the protein in a multistep process to different photointermediate states of the photocycle, leading to the ion transport across the membrane. In order to understand the molecular mechanism of the light-activated sodium ion transport by KR2, it is therefore important to understand the conformation of retinal and the Schiff base interaction with the proton acceptor in KR2 dark and intermediate states in the presence of Na^+ in detail.

The retinal of KR2 in the dark state was demonstrated to have an *all-trans* conformation.[5,16,17] Time-resolved resonance Raman spectroscopy suggested the distortion near Schiff base already in the dark state. After light activation, a red-shift primary intermediate (λ_{max} ~ 560 nm), called K-intermediate, is formed in picosecond to nanosecond, in that the retinal is isomerized from *all-trans* to *13-cis* conformation. After that, the protein goes to the blue-shifted L-intermediate. Time-resolved vibrational spectroscopies demonstrated that the retinal conformation in K- and L-intermediate has a distorted 13-cis conformation.[172] However, the detail regarding the conformation and the difference between these two intermediates are still missing.

Following the L-intermediate, M intermediate is formed when the proton is transferred from the protonated Schiff base to the proton acceptor, D116, resulting in the neutralization of the Schiff base. The uptake of sodium ion is proposed to occur after this step, whereby the positive charge barrier is gone, allowing the positively charged sodium ion to pass through to the internal binding site, forming the O-intermediate. The proton transfer step is the critical event occurring during the photocycle. The isomerization must affect the H-bonding that stabilized the Schiff base in the dark state in the way that it is energetically preferable to transfer the proton to the carboxylic counterion. It is still not clear that how this process happens.

The O-intermediate is demonstrated to involve the sodium ion binding near the Schiff base since the population of O-intermediate is proportional to the sodium ion concentration. The retinal conformation of the O-intermediate is controversial. The FTIR study of trapped intermediate at 240 K and time-resolved Raman spectroscopy suggested a 13-cis conformation[172] whereas the crystal structure of O-intermediate demonstrated an *all-trans* conformation.[8] The Schiff base in the O-intermediate is generally understood to be protonated because of the red-shift absorption maximum.[174]

Solid-state NMR is proved to be a powerful and sensitive method to study the conformation of retinal and the electrostatic interaction of the Schiff base.[11–13] However, the low sensitivity of the conversional NMR technique limited the studies of photointermediates, which usually existed in a low population and often as mixed states. DNP-enhanced ssNMR comes to solve this problem. The technique was successfully applied to study the conformation of several microbial rhodopsins, e.g., BR[11,175], PR[12], and ChR2[13]. Moreover, the cryogenic temperature needed for the cross-effect DNP can be used for the cryogenic trapping of photointermediates. Different photointermediates can be generated by controlling the illumination and specific temperatures. In this thesis, three types of labeled retinal are incorporated in KR2 reconstituted in liposome to mimic the natural lipid bilayer environment. This permits us to study the conformation of retinal in intermediates in detail. The protein is either uniformly ^{15}N labeled or specifically ^{15}N labeled at the Lysine residues. The unique chemical shift of the Schiff base allows the unambiguous assignment and provides the electrostatic environmental information.

5.2. Results

To monitor the conformational changes of retinal during the photocycle, the retinal conformation bound to the K255 lysine residue in the dark state was characterized by DNP enhanced ssNMR. Figure 27a illustrates the [$^{13}C_9$-retinal, U-^{15}N]-KR2 reconstituted in the lipid bilayer which mimics the natural membrane environment. The details of sample preparation for DNP experiments can be found in chapter 3.1. A signal enhancement of ~40 was gained when the microwave was on (Figure 27c). This corresponds to a ~1600-fold time saving. The ^{13}C CP spectrum (Figure 27c) shows the resonances of lipid, glycerol, and the labeled retinal. C16-18 resonance signals are embedded under the lipid signals and are not further considered here. The natural abundance signals from lipid and glycerol can be filtered out using a double quantum filter (DQF) experiment. Only signals from the directly bound carbons ^{13}C (C10-C15) will appear in the spectrum.

5.2.1. KR2 dark state

The chemical shifts of C10-C15 in the dark state were assigned using [$^{13}C_9$-Retinal, U-^{15}N]-KR2 sample based on 1D DQF and 2D PDSD and DQSQ spectra (Figure 27b, d, e). The resonances of C10-C15 were unambiguously assigned (Table 15). The chemical shifts were compared to BR which is commonly used as the prototypical model for the studying of microbial rhodopsin. The 133.9 ppm C12 retinal resonances in KR2 is similar to that of in light-adapted bacteriorhodopsin (BR_{568}), which is known to have an *all-trans* conformation (the *13-cis* conformation in dark-

adapted BR_{555} has C12 resonance at around 124.9 ppm, which is around 9 ppm more shielded).[11] The C12 chemical shift value confirmed the *all-trans* conformation in the dark state of KR2 as was previously reported in the literature based on X-ray crystallography[16,17], ssNMR[6,173], and FTIR[3] spectroscopies. The C14 resonance of KR2 at 123.7 ppm indicated a *15-anti* conformation similar to BR_{568} (C14 resonance at 123.1 ppm).[11] The chemical shifts of C11, C13, and C15 in KR2 deviate from that of light-adapted BR around 5 – 10 ppm due to the different retinal binding pocket architecture.

C20 resonance was determined based on the DQF spectrum using another labeling scheme [$^{13}C_3$-Retinal, $^{15}N\zeta$-Lys]-KR2 (Figure 28). The C12 and C13 resonances assigned on this sample match well with the value assigned based on [$^{13}C_9$-Retinal-U-^{15}N]-KR2. Likes C12, C20 resonance is also indicative for *all-trans* and *13-cis* conformation. The obtained C20 resonance also clearly indicates *all-trans* conformation in the dark state.

The chemical shift of protonated Schiff base in KR2 dark state was determined by ^{15}N CP experiment. The Schiff base peak of [$^{15}N\zeta$-Lys]-KR2 at 173.3 ppm measured under DNP condition agrees with the value measured at a non-cryogenic temperature, 275 K, at an 850 MHz spectrometer (Figure 29), indicating that the sample preparation for DNP signal enhancement does not affect the Schiff base environment. However, the cryogenic probe temperature (110 K) under the DNP condition caused a heterogeneous line broadening (160 Hz and 370 Hz of linewidth at half height for 850 MHz and DNP 400 MHz, respectively).

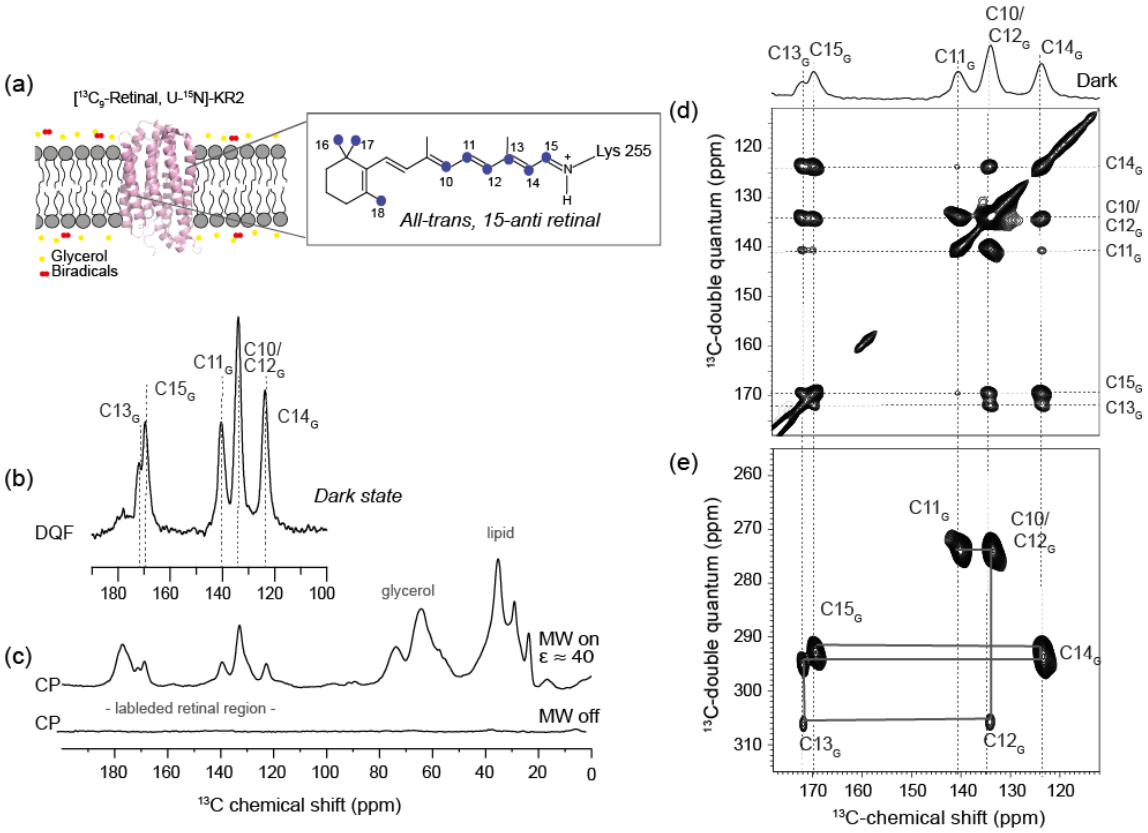

Figure 27: Assignment of $^{13}C_9$ retinal chemical shift of KR2 in dark state. (a) Illustration of [10-18-$^{13}C_9$-Retinal, U-^{15}N]-KR2 reconstituted in liposome in 30 mM NaCl Tris buffer (pH 8.5), doped with 20 mM AMUPol used as polarizing agent, and glycerol as cryoprotectant. For detail regarding sample preparation, see materials and methods. (b) DQF spectrum shows the resonance peaks of retinal ^{13}C10-15 after filtered the natural abundance signals. C16-18 were not observed in the spectra. (c) ^{13}C CP spectra recorded with microwave on and off shows the signal enhancement of ~40. (d) PDSD (mixing time 20 ms) and (e) DQSQ spectra of [10-18-$^{13}C_9$-retinal-U-^{15}N]-KR2 shows the assignment of cross peaks. The solid line shows the sequential walk along retinylidene chain (C10-C15) in DQSQ spectrum.

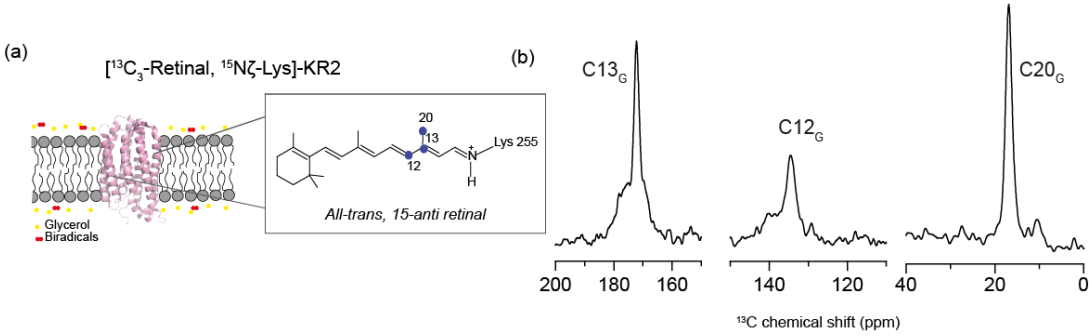

Figure 28 : (a) Illustration of [12, 13, 20-$^{13}C_3$-Retinal, ^{15}Nζ-Lys]-KR2 reconstituted in liposome in 100 mM NaCl Tris buffer (pH 8.5) and doped with 20 mM AMUPol and glycerol used as polarizing agent and cryoprotectant, respectively. (b) DQF spectrum shows the peak of C13, C12 and C20 in KR2 dark state.

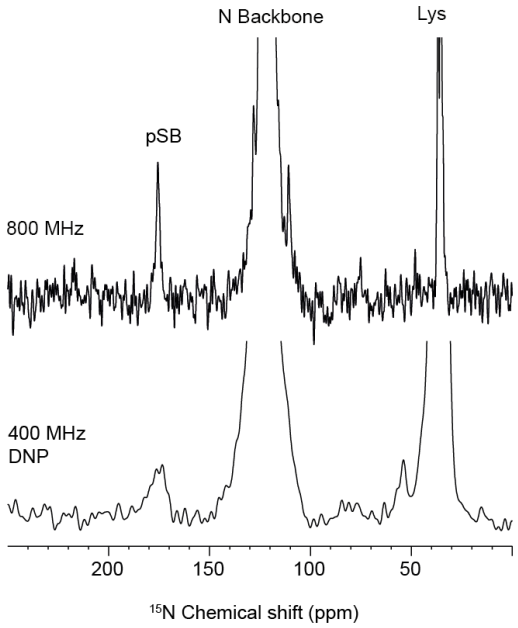

Figure 29: KR2 dark state Schiff base resonance. ^{15}N CP spectra of [^{15}Nζ-Lys]-KR2 reconstituted in DMPC:DMPA (9:1) liposome in Tris buffer (pH 8.5) containing 30 mM NaCl recorded at 270 K on 850 MHz spectrometer and at 110 K under DNP condition (400 MHz) show signals from protonated Schiff base (pSB), natural abundance nitrogen backbone and lysine residues. The Schiff base chemical shift obtained under DNP condition (bottom) is the same as the value acquired from the sample without doping with 20 mM AMUPol in d^8-glycerol:D_2O:H_2O matrix (top) at high field (850 MHz) but the peak is broader due to the heterogeneity at cryogenic temperature.

Table 15: Retinal (C10-C15 and C20) and Schiff base resonance (pSB) of KR2 in dark state compared to BR[11,153], PR[12,176] and ChR2[13]. Error estimation for ^{13}C and ^{15}N chemical shift for KR2 are estimated to be 0.5 and 1 ppm, respectively. All ^{13}C and ^{15}N chemical shifts were referenced indirectly to DSS and liquid NH_3, respectively, using the ^{13}C signal of CO-alanine at 179.85 ppm.

Retinal atoms	KR2	BR568	BR555	PR	ChR2
C10	133.9	-	-	132.7	-
C11	140.5	135.3	138.5	140.1	-
C12	133.9	133.4	124.9	132.8	-
C13	172.0	166.1	-	166.4	-
C14	123.7	123.1	111	122.4	126.3
C15	169.7	160.0	163.2	164.0	166.5
C20	17.0	13.1	23.5	16.2	
pSB	173.3	165.2	171.1	181.0	196.5

5.2.2. KR2 early states intermediates (K- and L-states)

5.2.2.1. Trapping of photointermediates K and L

The first step toward the study of retinal conformation of KR2 photointermediates was to establish the trapping protocol. Light can be induced to the sample inside the NMR magnet through a glass fiber as shown in Figure 30. KR2 has an absorption maximum at 524 nm, which is in the green light region. The green LED lamp was first applied to generate K-intermediate at 110 K. However, it was not possible to generate a considerable amount of the intermediate at 110 K by illuminating with the green LED (525 nm, 1.3 W) because the power of the light reaching the sample was not enough (Figure 31c). Therefore, the blue LED lamp (470 nm) with a higher power (3.3 W) was applied instead. After illuminating the sample inside the NMR magnet for several minutes, several new peaks can be observed. C11 peak intensity (peak height) was used to monitor the buildup of intermediates and the illumination yield because it is the most less overlapped peak. The intensity of $C11_G$ and $C11_{K/L}$ decreased and increased, respectively with illuminating time and reached its equilibrium after around 40 minutes (Figure 31a, b). Using the decreased peak intensity of the $C11_G$ and the conversion yield is estimated to be 45%.

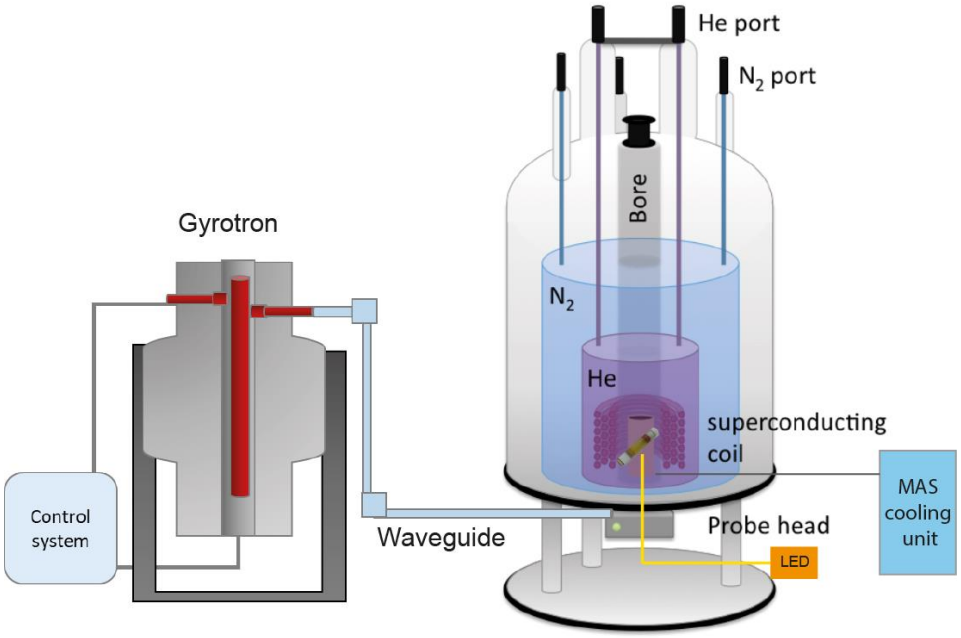

Figure 30: Hardware setting for DNP-enhanced solid-state NMR experiment. Gyrotron generates microwave irradiation (for electron transition) which is transferred to the NMR magnet through the waveguide. The LED light used for illumination is introduced to the probe via the lightguide.

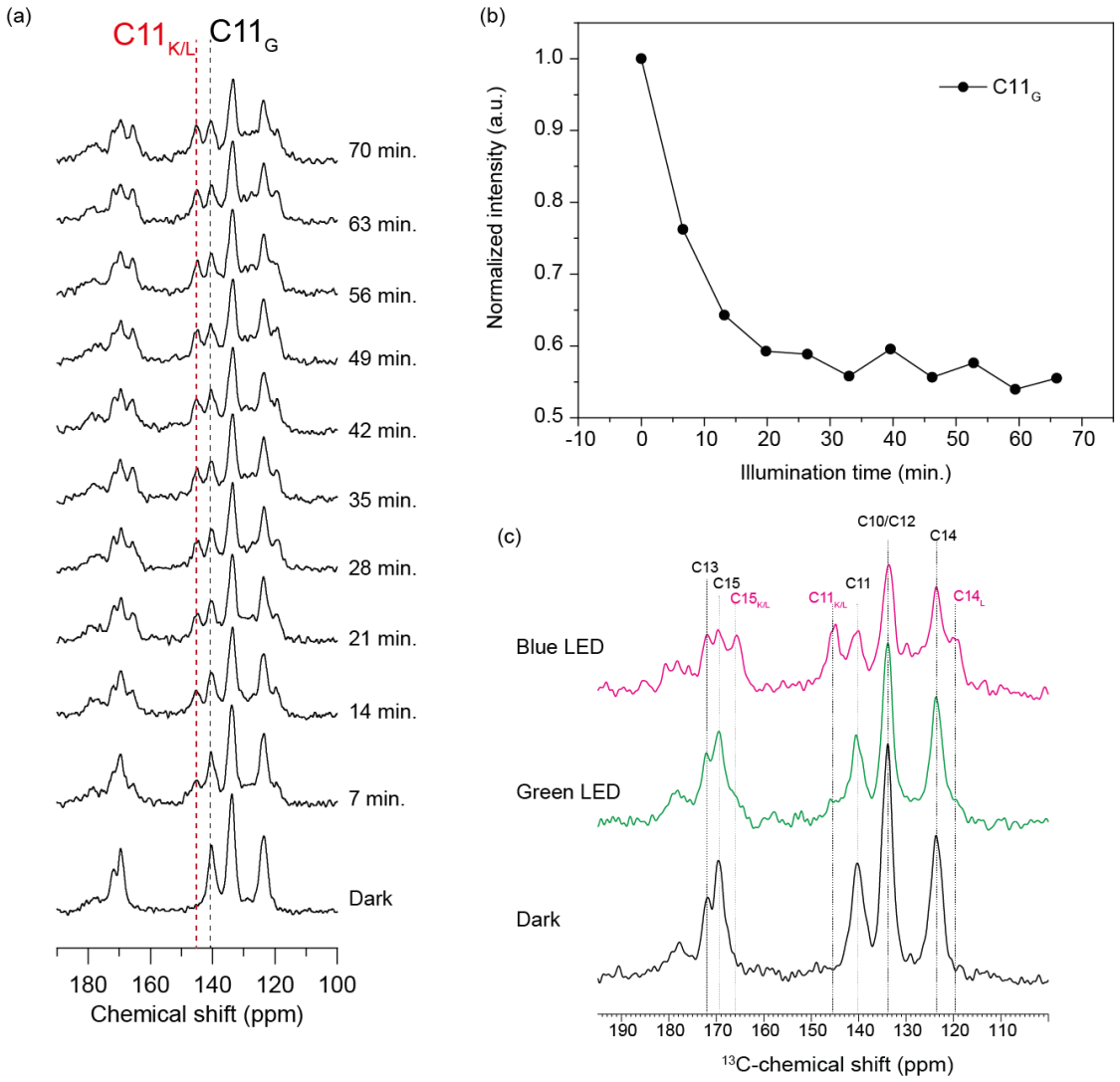

Figure 31: KR2 intermediates buildup: (a) DQF spectra of KR2 [10-18-$^{13}C_9$-Retinal, U-^{15}N]-KR2 in dark state (G) and after illumination with blue light (470 nm) for 7-70 minute. (b) The decrease of $C11_G$ (140.5 ppm) peak intensity upon illumination. (c) DQF spectra of KR2 dark state and after illumination with green (525 nm, 1.3 W) and blue LED (470 nm, 3.3 W) for 63 minutes. The assignment is based on 2D spectra in Figure 33.

5.2.2.2. Retinal resonance assignment and chemical shift perturbation in the early state intermediates (K and L)

The early state intermediates were generated and trapped by *in-situ* illuminating inside the magnet at cryogenic temperature (110 K). A manifold of new peaks was observed in the DQF spectrum after illumination, indicating the isomerization (Figure 32b). Unfortunately, it is not possible to convert all the sample to photointermediates. The difference spectra show the negative peaks of the dark state and the positive peaks of the photointermediates (Figure 32c). The pure photointermediate spectra can be gained by subtracting the remained dark state spectrum (55%),

(Figure 32d). To assign those new peaks, 2D PDSD and DQSQ spectra were recorded (Figure 33). By carefully analysis, it can be seen that the photointermediates that came up by illuminating at 110 K belong to two states populations, which were tentatively assigned to K and L. The assignment of K- and L-state was verified by thermal relaxation experiment and cryo-absorption spectroscopy (see section 0).

By thermally relaxing to 190 K, the crosspeaks of one population in the PDSD spectrum disappeared whereas another population remained and dominated (Figure 34a), suggesting the equilibrium shift between photointermediates. Because of the crowded spectra for the $^{13}C_9$-retinal labeled sample, the equilibrium shift between two intermediates was confirmed by comparing 1D spectra of [$^{13}C_2$-Retinal, U-^{15}N]-KR2 sample in the dark state, after illumination at 110 K and after relaxing to 190 K. Figure 34b shows that upon relaxing to 190 K, the $C14_L$ peak increased and $C14_K$ peak decreased, indicating the equilibrium shift from one state to another. A similar result upon relaxing to 190 K was also observed on the $^{13}C_3$-retinal labeled sample and at 210 K no peak of K-state was observed anymore, indicating the full relaxation to L-state. Therefore, the peaks that disappeared at 190 K and *vice versa* the peaks that remained at higher temperatures were assigned to K- and L-state, respectively. The assigned resonances of C10 to C15 and C20 of Dark, K- and L-state are shown in Table 16.

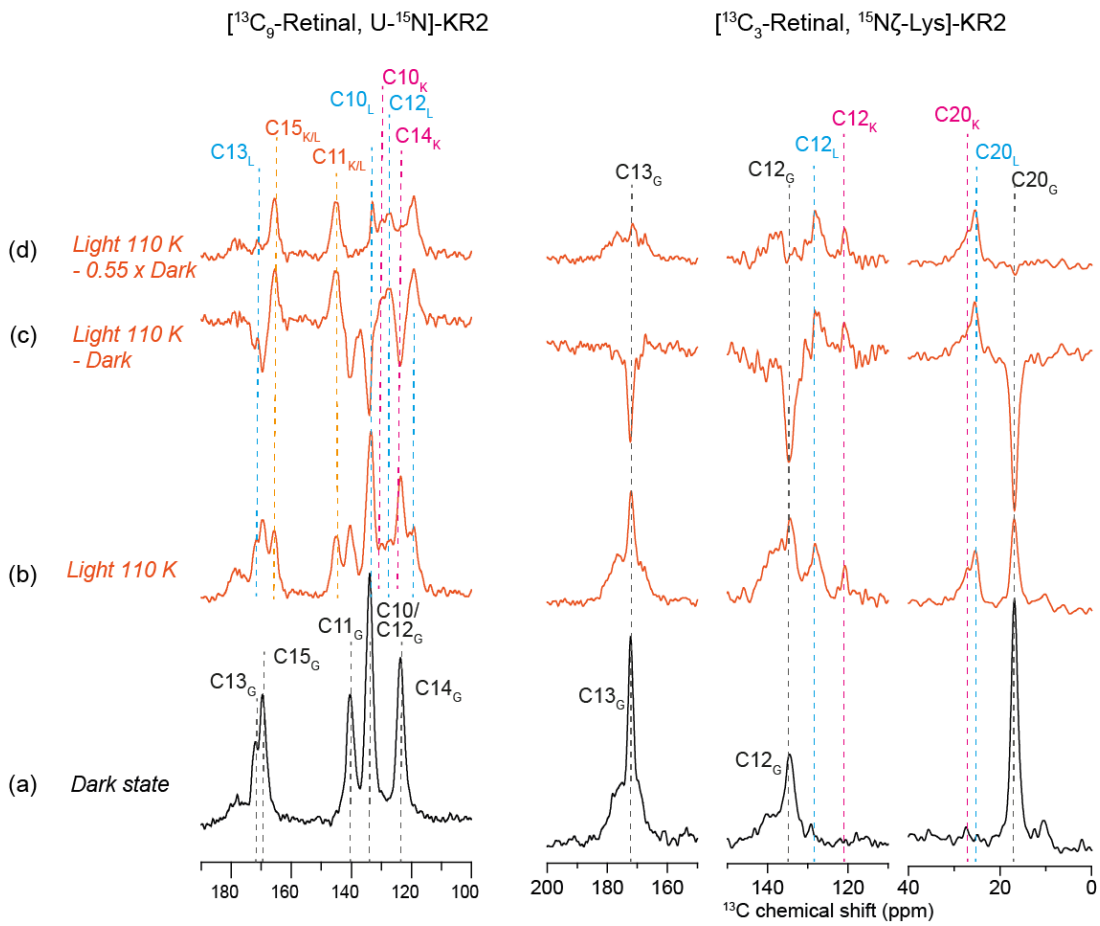

Figure 32: Illumination induced retinal chemical shift change in KR2 early state intermediates. DQF spectra of [10-18-$^{13}C_9$-Retinal-U-^{15}N]-KR2 (30 mM NaCl) and [12, 13, 20-$^{13}C_3$-Retinal, 15Nζ-Lys]-KR2 (100 mM NaCl) in (a) dark state and (b) after illumination at 110 K for 40 minutes, (c) The difference spectra (light 110 K – dark), and (d) Pure spectra of photolyzed states after subtraction of the remained dark state (55%) for [10-18-$^{13}C_9$-Retinal-U-^{15}N]-KR2 and [12, 13, 20-$^{13}C_3$-Retinal, ^{15}Nζ-Lys]-KR2. The assignment was based on 2D PDSD and DQSQ spectra (Figure 33).

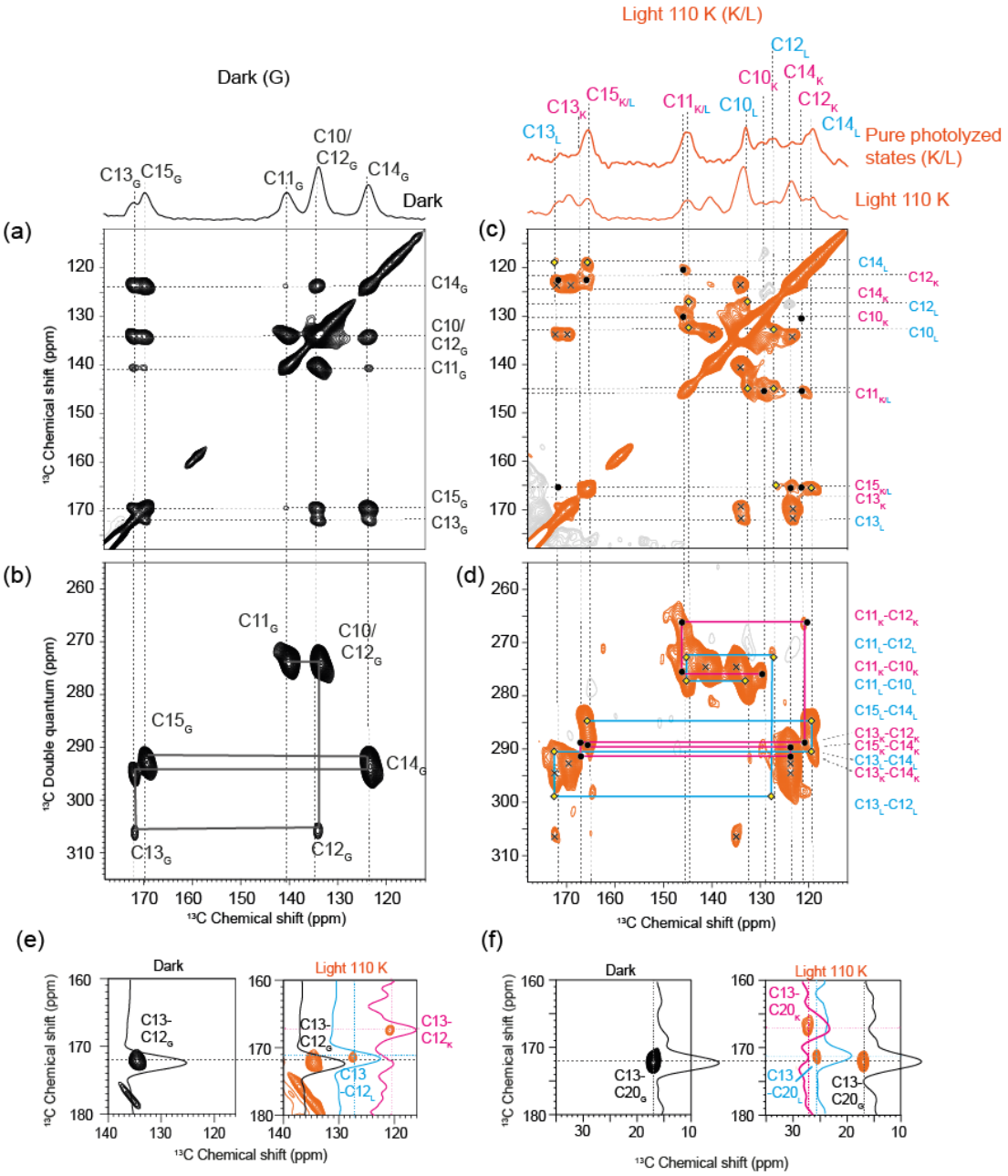

Figure 33: Proton-driven spin diffusion (PDSD) and double quantum single quantum (DQSQ) spectra of [10-18-$^{13}C_9$-Retinal, U-^{15}N]-KR2 (30 mM NaCl) in dark state (G), (a) and (b), and after illuminated at 110 K (c) and (d). After light activation, two separate spin systems corresponding to K- and L-states in addition to a residual ground state population were detected. The G, K and L cross peaks are illustrated with x, • and ◊ symbols, respectively. Crosspeaks belonging to the same spinsystem are connected (G: black, K: pink, L: blue) in the DQSQ spectra (b and d). 1D spectra of dark state and after illumination and subtracting the residual ground state are shown on top. (e)-(f) PDSD spectra of [12, 13, 20$^{13}C_3$-Retinal, U-^{15}N]-KR2 (100 mM NaCl) shows C13-C12 and C13-C20 crosspeaks in dark, K- and L-state.

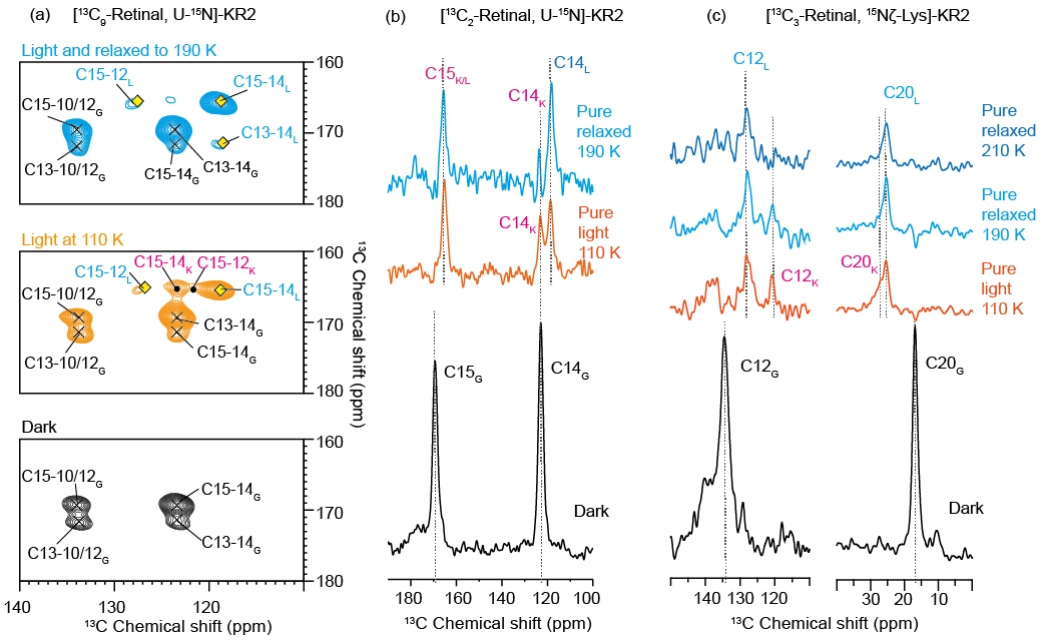

Figure 34: K and L equilibrium shift. (a) ^{13}C-^{13}C PDSD spectrum of [10-18-$^{13}C_9$-Retinal, U-^{15}N]-KR2 (30 mM NaCl) in dark state (black), illuminated at 110 K (orange) and relaxed to 190 K (blue) shows the disappearance of the K-state cross peaks (•) and the remaining of the L-state crosspeaks (◊) upon relaxing to 190 K. Cross peaks from the remaining dark state population are labelled by (x). For comparison, (b) DQF spectra of [14,15-$^{13}C_2$-Retinal, U-^{15}N]-KR2 and [12, 13, 20-$^{13}C3$-Retinal, $^{15}N\zeta$-Lys]-KR2 in the dark state and the pure photointermediates spectra upon illumination at 110 K (K/L) and followed by relaxation to 190 K and 210 K for 2 minutes. The pure photointermediates spectra were created by subtracting the residual dark state contribution (~55%). The spectra shows the shifting of photointermediates form K to L upon thermal relaxation.

Table 16: Retinal resonances C10-C15 and C20 of KR2 in dark state (G), K- and L-state in the Na^+ pump mode and the chemical shift pertubation due to light-activated isomerization. The chemical shift value error is estimated to be ± 0.5 ppm.

Atom	Dark (G) (ppm)	K (ppm)	L (ppm)	G – K (ppm)	G – L (ppm)	K-L (ppm)
C10	133.9	130.0	132.9	3.9	1.0	-2.9
C11	140.5	145.8	144.8	-5.3	-4.3	1.0
C12	133.9	121.1	127.5	12.8	6.4	-6.4
C13	172.0	167.3	171.4	4.7	0.6	-4.1
C14	123.7	123.8	119.2	-0.1	4.5	4.6
C15	169.7	165.8	165.8	3.9	3.9	0
C20	17.0	27.3	25.5	-10.3	-8.5	1.8

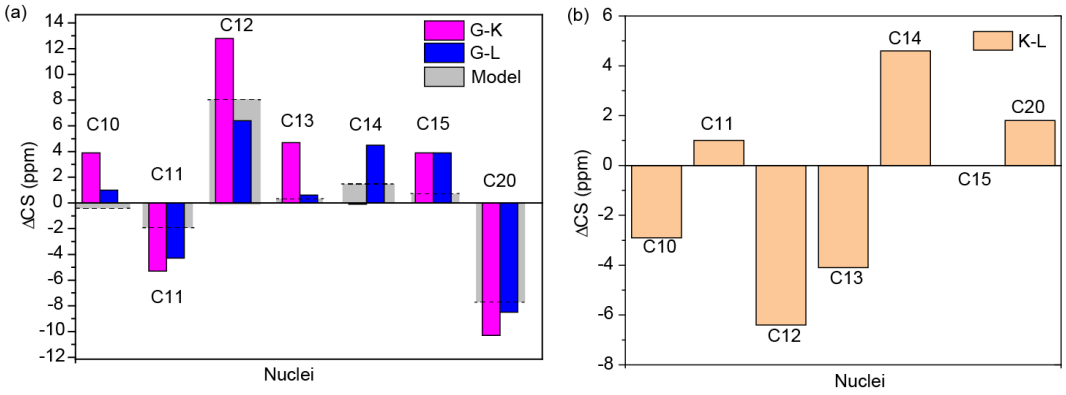

Figure 35: Chemical shift pertubation (CSP) at retinal C10-C15 and C20 in the K- and L-state. (a) Chemical shift differences between dark state and photointermediates. (b) Chemical shift differerences between K- and L-state. The CSP (ΔCS) was compared with the *all-trans* to *13-cis* isomerisation of *N-retinylidenebutylamine* (model)[14] for C10-C15 and to free retinal in ethanol[177] for C20. The positive and negative ΔCS indicate shieding and de-shielding at the nuclear, respectively.

To analyze the conformational change, the resonance shifts were calculated by subtracting the dark state chemical shift with that of K- and L-state (Table 16 and Figure 35). The positive and negative numbers indicate the shielding and de-shielding after isomerization, respectively. Data are compared to chemical shift changes observed for the all-trans to 13-cis isomerization of the model compound N-retinylidenebutylamine in the solution for C10-C15 and to free retinal in ethanol for C20.[14,177] The chemical shifts of C12 and C20 are very sensitive to the *13*-cis isomerization. Both chemical shift changes at C12 and C20 indicate a 13-cis conformation in K-state as well as in the L-state. However, it deviates up to 4 ppm from the model compound, suggesting the possible distorted conformation in the middle of the polyene chain and near the Schiff base.

In the K-state, the chemical shift perturbations deviate from the model compound, especially for C10, C11, C12, and C13, the deviation is more than 4 ppm (Figure 35). This suggests steric stress from the middle part of the polyene chain to the Schiff base region. The deviation overall is slightly relaxed in the L-state, except at C14. The CSP (ΔCS) from the dark state at C13 and C14 are strongly different between the K- and L-intermediates: C13 chemical shift shifted 4.7 ppm in K-state but relaxed back in L-state, vice versa the K-state C14 chemical shift was similar to the dark state but showed an additional 4 ppm shielding in the L-state. The shielding at C14 in L-state suggested the steric effect that might come from the retinal bound lysine residue, K255 (see Figure 53). In contrast, C15 displayed a shielding higher than the model compound in both K-

and L-states. Altogether, these observations suggest a fine adjustment of the chromophore upon illumination and a distortion near the Schiff base region in early state intermediates. The chromophore distortion was therefore further investigated by the dihedral angle measurement (see section 5.2.2.4).

5.2.2.3. Verification of K- and L-intermediates trapping by UV-Vis spectroscopy

The definition and assignment of photointermediates are usually based on optical absorption spectra, therefore it is necessary to correlate the cryogenically trapped intermediates for the NMR study here with the optically assigned photostates. This could be derived from the cryo-UV/VIS absorbance spectra of samples trapped in the same way as for the NMR study.

First, temperature dependent flash photolysis experiments were first performed to derive photocycle kinetics for KR2 in its Na^+-pumping mode. Lifetime density analysis (LDA) of the datasets recorded at 283 and 293 K (Figure 36) revealed the presence of four dominant components, which are assigned to K (S1), L (S2), M (S3), and O (S4). Both datasets were fitted to a sequential kinetic scheme with four states, which results in the so-called evolution associated difference spectra (EADS). Figure 36 shows the evolution associated spectra (EAS) obtained after correction of the EADS for the ground state bleach. The non-single Gaussian shape of the EAS indicates that each EAS describes various equilibrations of the photocycle intermediates K, L, M, and O. The spectra of S1 (K) and S4 (O) are least affected by the change in the measurement temperature. However, the spectra of S2 (L) show the most prominent temperature effect. At 293 K, the S2 spectrum shows the higher contribution from the blue-shifted intermediates (L, M) and lower from the red-shifted intermediate (K), while at 283 K the contributions are reversed. This indicates the K ↔ L equilibrium shifts towards the K-intermediate at lower temperatures. Therefore, the EAS obtained at 283 K is used to compare with the spectra recorded under cryogenic conditions to account for the lower amount of L-intermediate present.

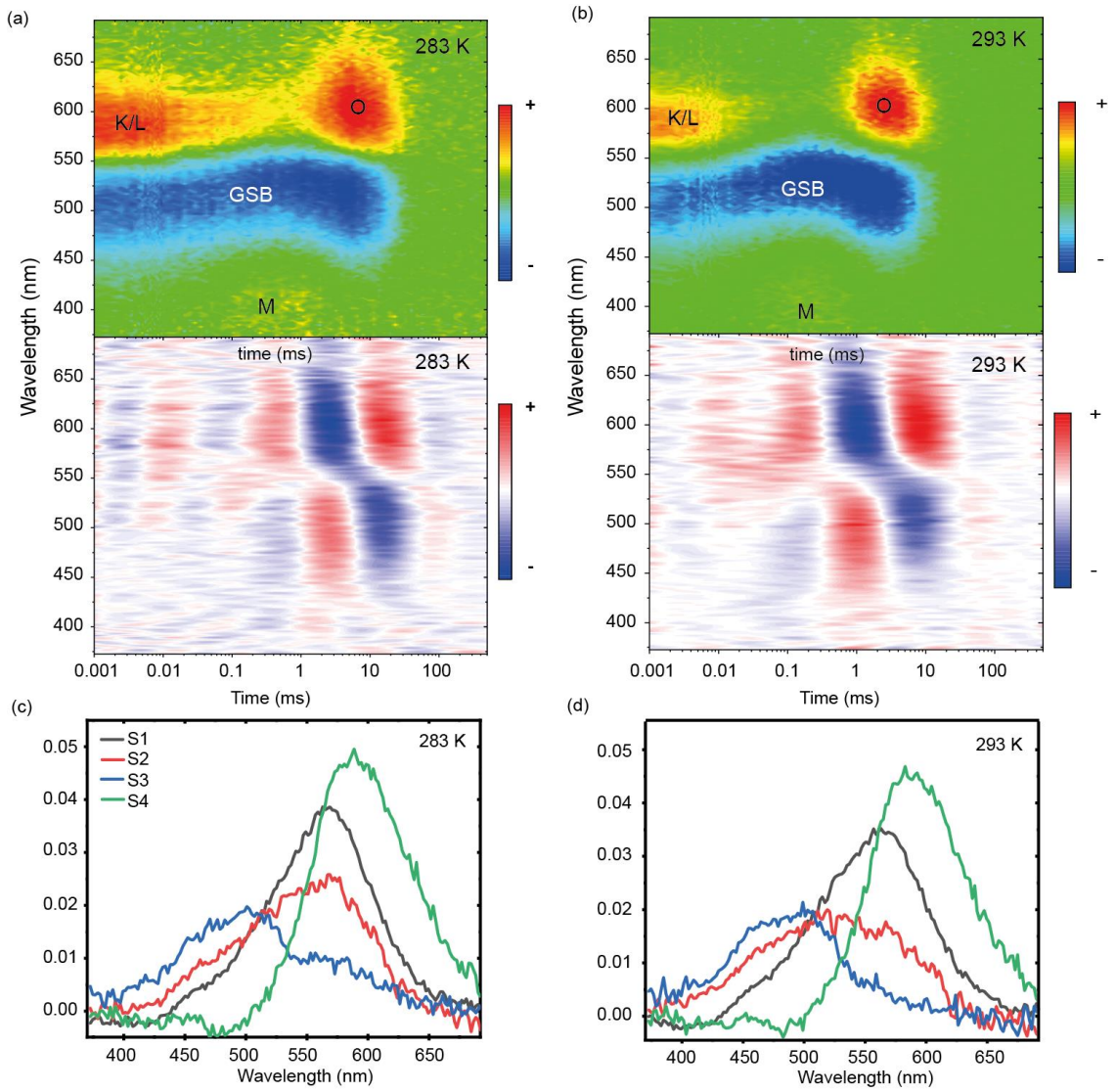

Figure 36: Broadband flash photolysis spectra of KR2 in 50mM NaCl buffer, pH 8.5 at (a) 283 K and (b) 293 K. The amplitudes are color coded. Red, green, and blue indicate positive, zero and negative absorbance changes, respectively. Corresponding Lifetime Density Map (LDM) obtained from lifetime distribution analysis of the time resolved flash photolysis data are shown at the bottom. Amplitudes are color coded: red (positive) indicates decay of absorption or rise of bleach and blue (negative) indicates rise of absorption or decay of bleach. (c) and (d) Ground state corrected evolution associated spectra (EAS) of the transient data at 283 K and 293 K, respectively. The figures are provided by Peter Eberhardt from Wachtveitl group, Goethe University Frankfurt.

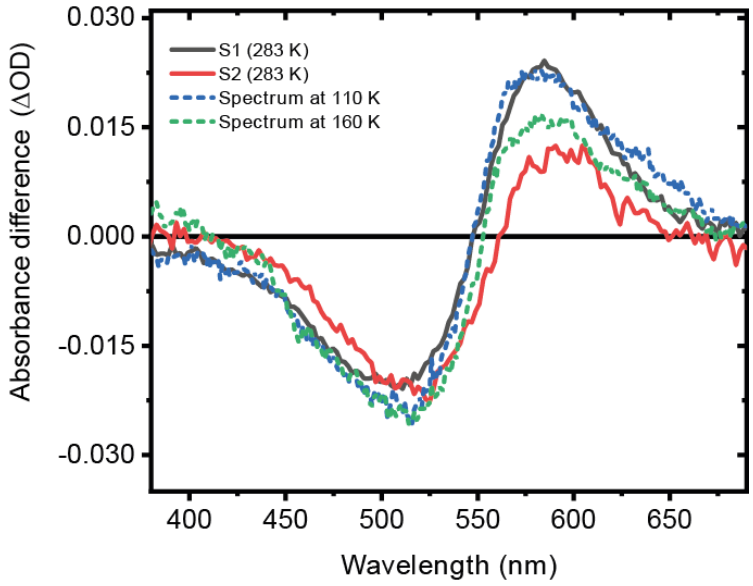

Figure 37: Verification of the trapping of K- and L-intermediates. S1 (K) and S2 (L) EADS of the transient flash photolysis data recorded at 283 K are compared with the cryo UV/vis difference absorption spectra recorded at 110 and 160 K respectively. The figure shows the trapping of K-state at 110 K and the shift from K- to L-intermediate at 160 K. The figure is provided by Peter Eberhardt from Wachtveitl group, Goethe University Frankfurt.

After assigning the intermediates, the EADS obtained by the flash photolysis at 283 K is compared with the difference spectra from the cryo UV/vis experiment (Figure 37). The difference spectrum taken at 110 K resembles the S1 difference spectrum at 283 K, while the 160 K difference spectrum is closer to the S2 (L) difference spectrum. Thus, the temperature increase from 110 K to 160 K leads also to an increase in the contribution of the blue-shifted L-intermediate and a concomitant decrease of the contribution of red-shifted K-intermediate. We expected this effect to be stronger at 190 K, but due to the phase transition in this temperature region, no spectra could be obtained. These observations are in line with the DNP-enhanced ssNMR data, which showed a shift in the equilibrium between two structural intermediates from 110 K to 190 K, which now can be unambiguously assigned to the shift in the K ↔ L equilibrium based on the optical spectroscopy data.

5.2.2.4. Chromophore distortion in dark and L-state

Since the retinal chemical shift perturbation from *all-trans* to *13-cis* isomerization deviated largely from the model compound, the retinal conformation must be distorted because of the limited space in the retinal binding pocket. To address this question, the H-C14-C15-H dihedral

angle near the Schiff base was measured. 14,15-$^{13}C_2$-retinal was incorporated in [U-^{15}N]-KR2 similarly to the other retinal labeled sample.

2Q-HLF experiments (see chapter 2.2.4) were performed to extract the H-C14-C15-H dihedral angle. The details regarding NMR experiment setup and torsion angle determination are described in materials and methods (chapter 3.4.1). Figure 38 shows the dephasing time dependent intensity of the C14 peak in the dark state. The dephasing curve is compared to the simulation curves and found to best fit with the 150° torsion angle. The number demonstrates that the retinal is substantially twisted already in the dark state.

The chromophore distortion at this position in the dark state of KR2 is around 7-15° more than light-adapted BR[11], PR[155], and ChR2[13] (Figure 38e). After obtained the dihedral angle information in the dark state, the sample was illuminated according to the previously established protocol, leading to the new peaks that belong to the K- and L-intermediates. Unfortunately, it is not possible to measure the dihedral angle in K-intermediate because of the peak overlapping with that dark state for C14 and the L-state for C15. However, the L-intermediate has a unique C14 chemical shift, therefore C14 peak intensities were used for the dihedral angle measurement. The experimental dephasing curve of L-intermediate corresponds to the simulation curve at 136° (Figure 38d). Interestingly, the H-C14-C15-H dihedral angle in the L-state is 14° twisted further more than in the dark state. The twist of retinal at this position supports the chemical shift perturbation observed at C14 in that L-state compared to the dark and K-state. The twist of retinal near the Schiff base in the early intermediates was also observed in the photocycle of PR[12] and ChR2[13], suggesting that it is a common mechanism among microbial rhodopsins. The turning and twisting of the retinal may work as an important gear that drives the protein to the next stage of the photocycle.

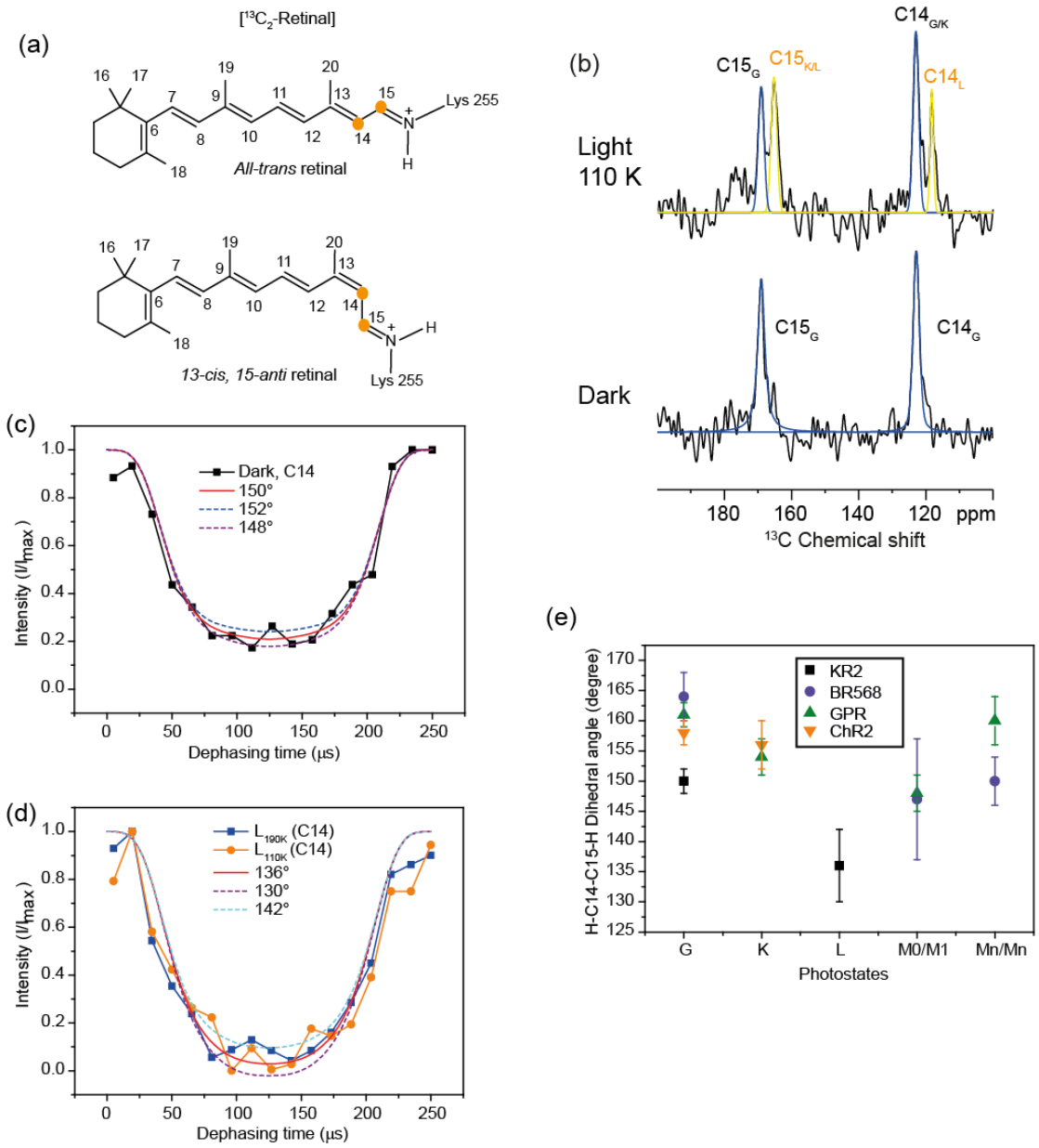

Figure 38: Dihedral angle measurement at H-C14-C15-H position of retinal in KR2 dark and L-state (a) 14, 15-$^{13}C_2$-retinal in *all-trans* and *13-cis* conformation; (b) Fitting of 2Q-HLF spectra of [14, 15-$^{13}C_2$-Retinal, U-^{15}N]-KR2 in dark state and after illumination at 110 K using solid line analysis in TOPSPIN program. (c)-(d) HCCH dephasing curves of C14-C15 spin system in (c) dark state and (d) after illumination at 110 K. The curves were obtained from analyzing the C14 signal intensity of dark state and L-state. (e) H-C14-C15-H dihedral angles of KR2 dark and L-state in comparison with light adapted bacteriorhodopsin (BR568)[11], green proteorhodopsin (GPR)[12] and channelrhodopsin 2 (ChR2)[13].

5.2.2.5. Schiff base resonance in K- and L-intermediates

The electrostatic environment alteration at Schiff base in K- and L-intermediates was investigated based on 1D ^{15}N CP and 2D ^{15}N-^{13}C correlation experiments. Upon illumination of [^{15}Nζ-Lys]-KR2 in Tris buffer (pH 8.5) containing 30 mM NaCl at 110 K, new low-field shifted resonances could be observed, indicating an electrostatically change at the Schiff base (Figure 39a). However, the peaks are broad and not resolved. 2D ^{15}N-^{13}C correlation experiment (TEDOR) was therefore performed to assign the Schiff base chemical shift in the early-state intermediates (Figure 39b). Because C15 resonance of K- and L-intermediates is different from the dark state and C14 resonances of K- and L-intermediates are distinct, it is possible to unambiguously assign the crosspeaks to dark state (G), K- and L-intermediates.

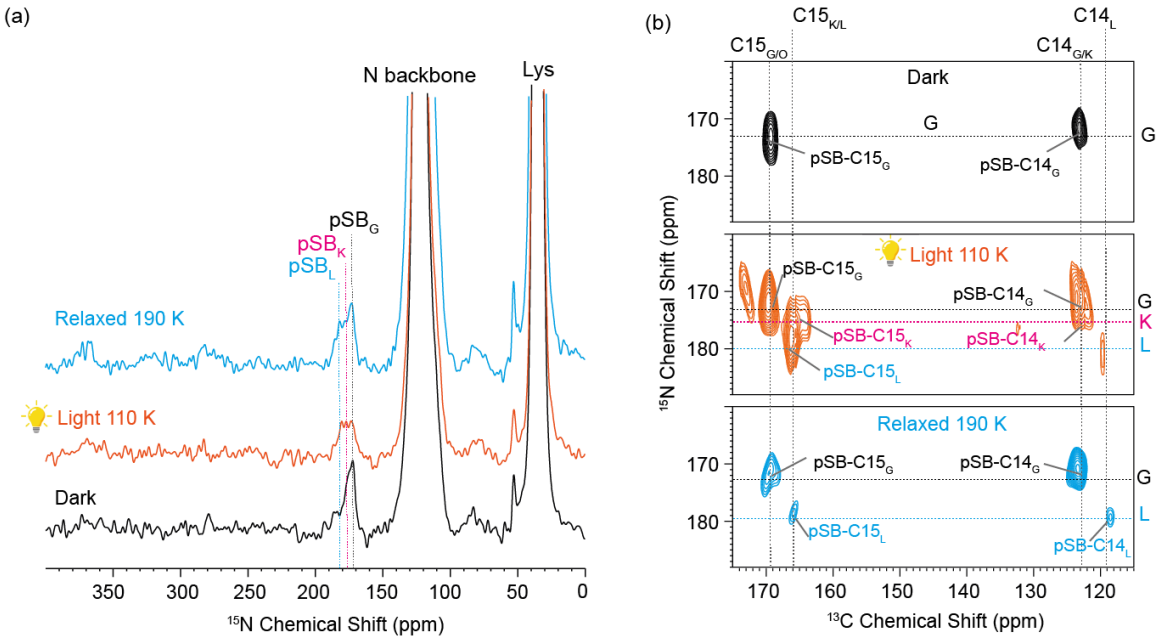

Figure 39: Assignment of protonated Schiff base resonances in dark state (G), K- and L- intermediates. (a) DNP-enhanced ^{15}N CP spectra of [^{15}Nζ-Lys]-KR2 dark state, after illumination at 110 K and relaxed to 190 K for 2 minutes. The spectra were recorded with 10 kHz MAS to avoid the spinning sideband around 300 ppm. (b) ^{15}N-^{13}C correlation spectra (TEDOR) of [$^{13}C_9$-Retinal, U-^{15}N]-KR2 (8 kHz MAS, 6 ms mixing time) in dark, after illumination (light 110 K) and relaxed to 190 K show the ^{15}N pSB and C15 and C14 cross peaks of dark, K- and L-state. The assignment is based on the chemical shifts of C15 andC14 in each state.

The TEDOR spectrum of light 110 K shows low-field shifted Schiff base resonances at 176.1 and 181.3 ppm for K- and L-state, respectively. By relaxing the illuminated sample to 190 K, the crosspeaks associated with the K-intermediate disappeared. This confirms again the equilibrium shift between K- and L-intermediates upon thermal relaxation as observed in the DQF and PDSD spectra (Figure 34). Note that because of the inefficiency magnetization transfer in the TEDOR

experiment, only the crosspeaks between pSB and C15 and C14 were observed. The low-field shift of chemical shift, which is -2.8 ppm for K-state and -8 ppm for L-state, indicate the electronic de-shielding provided by the drawing of Schiff base proton toward the proton acceptor D116 as compared to the dark state, by which the effect is stronger in L- than in the K-state.

Table 17: Schiff base (SB) resonances of KR2 in the dark state (G), K- and L-intermediates and the chemical shift change from dark state for K- and L-intermediates.

KR2	Protonated SB resonance (ppm)	Chemical shift change (ppm) G - K/L
Dark (G)	173.3 ± 1	-
K	176.1 ± 1	-2.8
L	181.3 ± 1	-8.0

5.2.3. O-state intermediate

5.2.3.1 Trapping of O-intermediate and thermal relaxation experiment

After the retinal conformations and the Schiff base-counterion interaction in the early-state intermediates (K and L) were determined, the thermal relaxation experiment was performed to thermally permit the light activated state to relax and go to the later state of photocycle. Figure 40 shows the DQF spectra of [$^{13}C_3$-Retinal, $^{15}N\zeta$-Lys]-KR2 after illuminated and relaxed to 250 K. The C12 and C20 are sensitive to *all-trans – 13-cis* isomerization and therefore used to monitor the isomerization and reisomerization. It can be seen that at the temperature above 230 K, most of the 13-cis population has reisomerized back to *all-trans* conformation. Cryo-difference absorption spectroscopy was therefore applied to identify the intermediate trapped by relaxing to 230 K. The absorption spectra of KR2 illuminated at 230 K is closed to the absorption of O-state, however, it does not resemble the real O-state absorption (S4).

In order to better trap O-intermediate, the flash freezing method, by which the sample is illuminated outside the magnet followed a rapid freezing in liquid nitrogen, was performed. The advantage of this trapping method is that the sample is not frozen during the illumination, allowing the better uptake of sodium ion. The flash-frozen sample was then quickly transferred for cryo UV-VIS absorption measurement for optical study or to the magnet for ssNMR study. The cryo UV-Vis absorption spectrum of sample trapped by flash freezing method resembles perfectly the characteristic absorption of O-state (S4) derived from flash photolysis (Figure 41), indicating the successful of the method for O-state trapping.

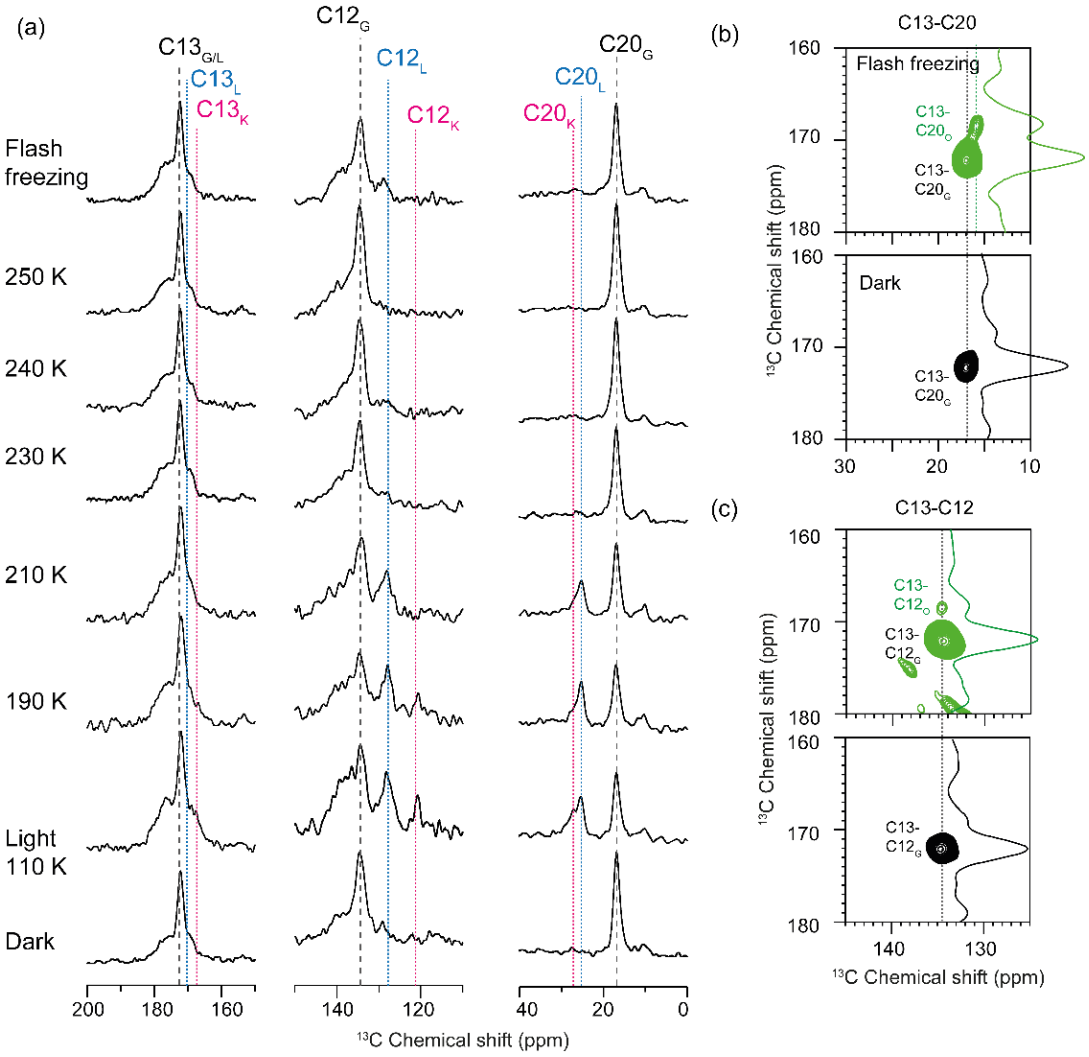

Figure 40: (a) DNP-enhanced DQF spectra of [$^{13}C_3$-Retinal, $^{15}N\zeta$-Lys]-KR2 (100 mM NaCl) in dark state, after illumination at 110 K and relaxed up to 250 K and the sample trapped by flash freezing. (b)-(c) DNP-enhanced PDSD (20 ms mixing time) spectra showing the crosspeaks C13-C20 (b) and C13-C12 (c) of dark and O-state trapped by flash freezing protocol.

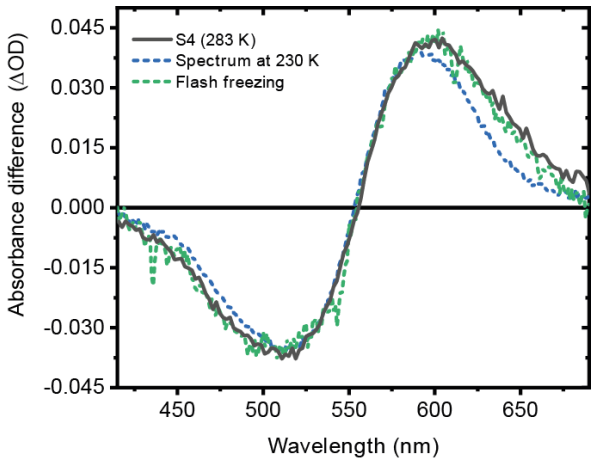

Figure 41: Verification of O-intermediate trapping. S4 (O) EADS of the transient flash photolysis data was compared with the cryo-UV/vis difference absorption spectra of KR2 illuminated and trapped by flash freezing (green) and illuminated at 230 K (blue). The KR2 sample was in 0.5% DDM solution containing 25 mM Tris (pH 8.5), 5 mM $MgCl_2$, 30 mM NaCl and 60% (v/v) glycerol for cryo-protection and light scattering reduction. The figure is provided by Peter Eberhardt from Wachtveitl group, Goethe University Frankfurt.

The 1D DQF spectra of the sample trapped by flash freezing method looks similar to the dark state (Figure 40), however, the 2D-PDSD spectra show new crosspeaks after illumination. These new peaks were assigned to O-intermediate. The resonance C12 of O-intermediate resemble the resonance in dark state but the C13 and C20 resonances are 3.5 ppm and 1 ppm different, respectively. The C12 and C20 chemical shifts indicated the *all-trans* conformation in the O-state similar to the dark state. However, the electrostatic perturbations at C13 and C20 suggest the uptake of Na^+ which passes through the protonated Schiff base gate and binds to the internal Na^+ binding site near Schiff base, upon the decaying of M-state. C13 resonance is sensitive to the positive charge localization through the retinal polyene chain. The shielding observed at C13 might cause by the kink at C14 observed in the recently published O-state crystal structure which interrupts the positive charge localization from Schiff base. The C20 chemical shift is a sensitive indicator for interactions/steric contacts between retinal chromophore and residues in the binding pocket. The 1 ppm chemical shift perturbation at C20 might arise from an altered electrostatic environment at the methyl group, which is in a contact with residues such as W215 within the binding pocket.

Similar to [$^{13}C_3$-Retinal, $^{15}N\zeta$-Lys]-KR2, the thermal relaxation experiment was performed also on [$^{13}C_9$-Retinal, U-^{15}N]-KR2 sample in Tris buffer containing 30 mM NaCl. A similar trend was observed, showing the reisomerization to start at around 230 K. However, in the $^{13}C_9$-retinal labeled sample, the peaks were overlapped, hindering the clear interpretation.

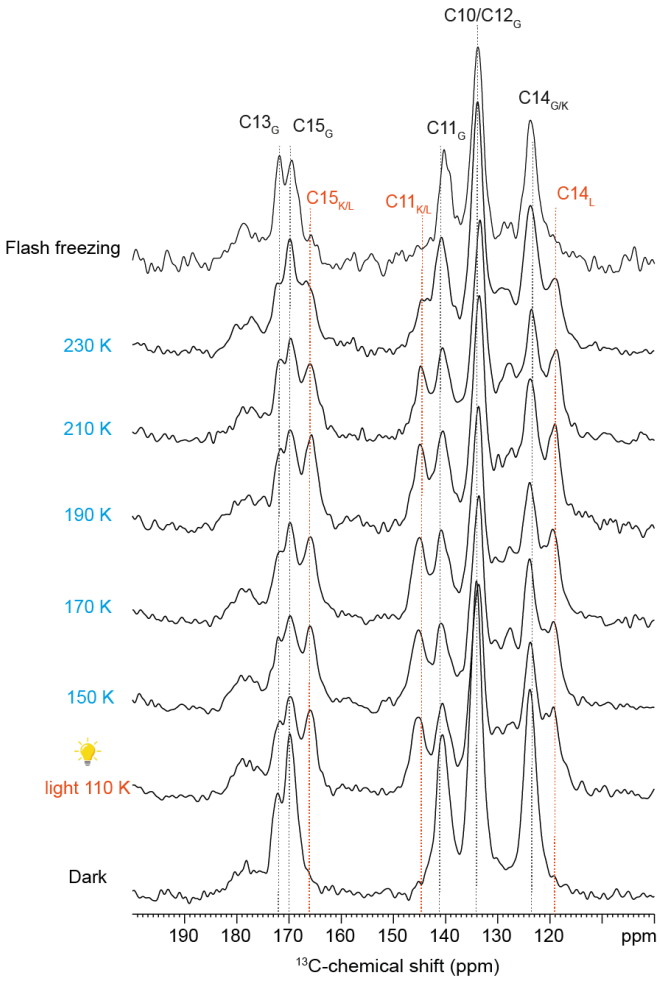

Figure 42: DNP-enhanced DQF spectra (1024 scans) of [$^{13}C_9$-Retinal, U-^{15}N] (30 mM NaCl) in dark state, after illumination at 110 K and relaxed up to 230 K and trapped by flash freezing.

5.2.3.2 Schiff base and retinal resonances in O-intermediate

The Schiff base peaks in KR2 dark state and intermediates at cryogenic temperature are relatively broad. ^{15}N CP spectra of [$^{13}C_3$-Retinal, $^{15}N\zeta$-Lys]-KR2 after illumination and thermally relaxed to 210 K show the non-fully resolved signal of protonated Schiff base in dark, K- and L-state, which were assigned from 2D spectra in the previous section (Figure 39b). The thermal relaxation experiment shows the disappearance of low-field shifted Schiff base resonance (K/L-intermediates) above 230 K. This resembles the reisomerization back to *all-trans* conformation observed in thermal relaxed ^{13}C DQF spectra (Figure 40 and Figure 42). However, for the sample trapped by flash freezing, which was demonstrated to be the method for O-state trapping (Figure 41), an additional low-field shifted peak was observed in the ^{15}N CP spectrum (Figure 43). This suggested the unique Schiff base chemical shift of O-intermediate.

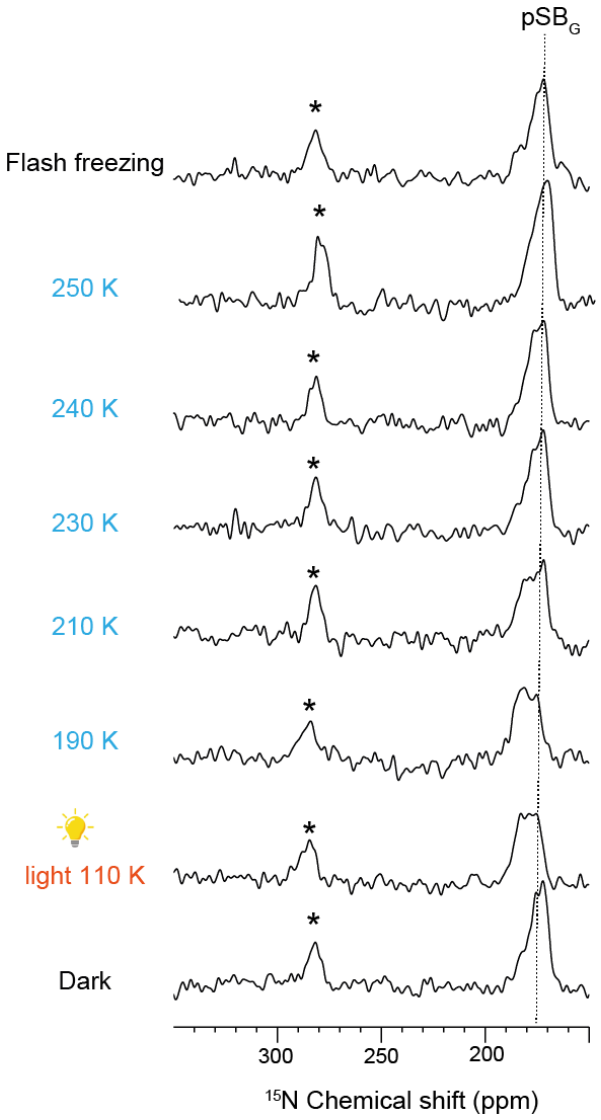

Figure 43: DNP-enhanced ^{15}N CP spectra of [$^{13}C_3$-Retinal, $^{15}N\zeta$-Lys]-KR2 (100 mM NaCl) in dark state, after illumination at 110 K and relaxed up to 250 K and the sample trapped by flash freezing. * indicates the spinning side bands. There was no deprotonated Schiff base signal (usually around 320 ppm) observed.

To further investigate the Schiff base resonance of O-intermediate, 2D ^{15}N-^{13}C correlation experiment (TEDOR) was performed. The TEDOR spectrum of [$^{13}C_9$-Retinal, U-^{15}N]-KR2 illuminated and trapped by flash freezing exhibits the new crosspeak with similar C15 resonance to dark state but with ^{15}N resonance that is 9 ppm deshielded than the dark state (Figure 44), similarly to the observation in ^{15}N CP spectrum. The new peak is assigned to pSB-C15$_O$ cross peak. Because of the inefficiency magnetization transfer in TEDOR experiment, only the pSB-C15 crosspeak was observed for O- intermediate. To better gain the magnetization transfer from Schiff base to other labeled retinal carbon nuclei, a double cross polarization experiment with

spin diffusion similar to N(CO)CX experiment was performed. The N(C)CX spectrum of dark state shows a good signal to noise ratio and the magnetization transfer from Schiff base to C15 and so on to C14-C10 was observed.

The N(C)CX spectra of sample trapped by flash freezing exhibit an O-state population that has around 9 ppm deshielded Schiff base signal than the dark state, confirming the result from TEDOR experiment. The crosspeak between pSB and C15 is clearly seen with weak crosspeak but above the noise level of pSB-C14 and -C12. The pSB-C13 crosspeak was not observable because it was hidden behind the pSB-C15 peak. However, the $C13_O$ was determined using [$^{13}C_3$-Retinal, $^{15}N\zeta$-Lys]-KR2 sample. The ^{13}C slice at 182.5 ppm in dark state exhibits no signal whereas the similar slice in the flash freezing spectrum shows the signal from O-intermediate. Moreover, the ^{15}N slice at $C15_O$ (169.5) ppm also exhibit the Schiff base signal at 182.5 ppm. The data confirmed the trapping of O-state as observed in [$^{13}C_3$-Retinal, $^{15}N\zeta$-Lys]-KR2 sample. Chemical shift perturbation in O-state show nearly no difference between dark and O-state, except for C13 (3.5 ppm), C20 (1 ppm) and pSB (-8.7 ppm).

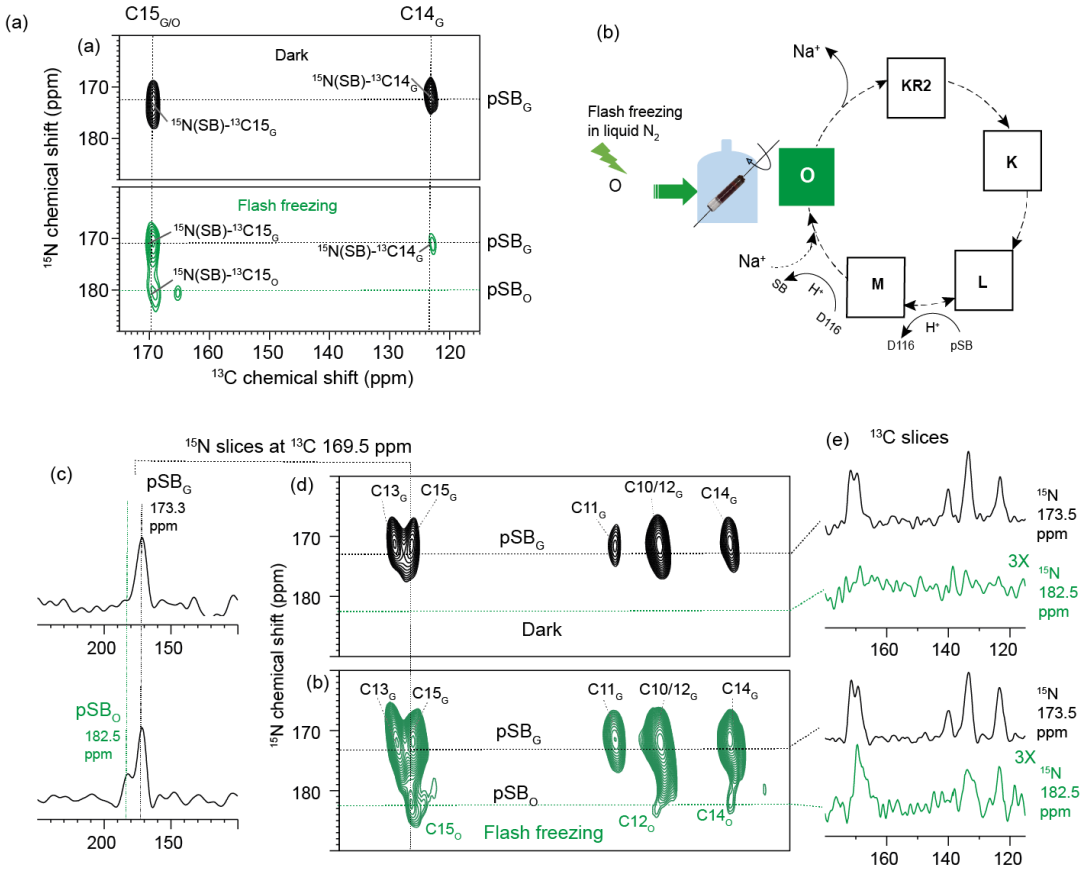

Figure 44: Resonances assignment of O-intermediate. (a) TEDOR spectra of [$^{13}C_9$-Retinal, U-^{15}N]-KR2 in dark and illuminated and trapped by flash freezing (30 mM NaCl). (b) photocycle of KR2 in the sodium ion pump mode and the trapping illustration of O-intermediate. (d) N(C)CX spectra in dark state and after flash freezing. (c) ^{15}N slices at ^{13}C 169.5 ppm shows ^{15}N resonances of O-state at 182.5 ppm and dark state at 173.3 ppm. (e) ^{13}C slices at 173.5 and 182.5 ppm of dark and O-state crosspeaks.

Table 18: Retinal resonance (C10-C15, C20) and Schiff base (SB) of O-intermediate compared with the dark state (G).

Atom	Dark (G), (ppm)	O, (ppm)	G – O (ppm)
C10	133.9 ± 0.5	-	-
C11	140.5 ± 0.5	-	-
C12	133.9 ± 0.5	133.7 ± 0.5	0.2 ± 1
C13	172.0 ± 0.5	168.5 ± 0.5	3.5 ± 1
C14	123.7 ± 0.5	123.8 ± 0.5	-0.1 ± 1
C15	169.7 ± 0.5	169.3 ± 0.5	0.4 ± 1
C20	17.0 ± 0.5	15.9 ± 0.5	1.1 ± 1
pSB	173.3 ± 1	182.0 ± 2	-8.7 ± 3

5.2.4. Retinal conformation and Schiff base interaction in the proton pump mode

KR2 was determined as a light driven sodium ion pump under physiological condition (high NaCl concentration). However, it can also pump proton in the absence of sodium ion.[1] The kinetic studies of KR2 photocycle by flash photolysis show a diverse photocycle equilibrium and kinetics between these two pump modes.[48,52] The photocycle in the proton pump mode was shown to be longer than in the sodium ion pump mode.[1] The maximum absorptions in the early state intermediate are the same but the O-state characteristic absorption at 605 nm in the sodium ion pump mode is not observed in the absence of sodium ion.[52] Structurally, there is the difference between the presence and absence of NaCl in protein environment at extracellular side of protomer interface where the sodium ion binding site is.[17] The effect of extracellular sodium ion binding site on the structure is still not clear. However, the mutagenesis studies together with the transport assay show that this bound sodium ion at protomer interface are not functionally relevant but only for the stability of protein.[1]

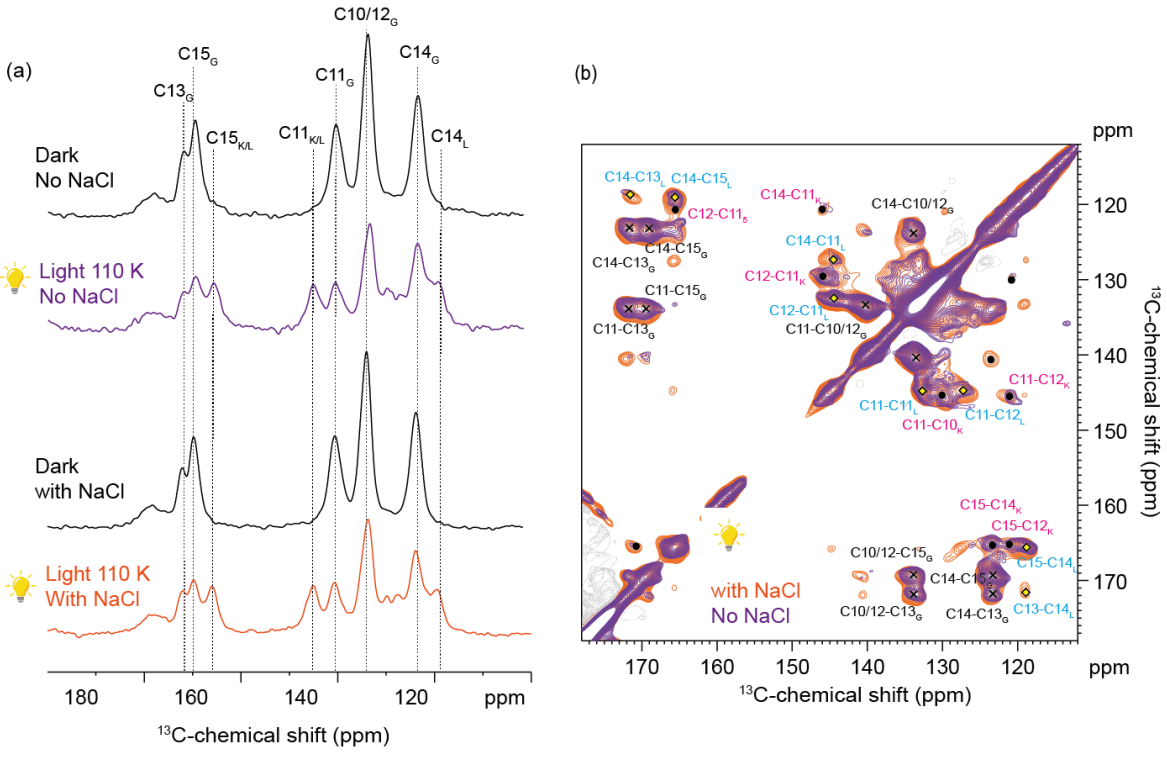

Figure 45: DNP-enhanced (a) DQF and (b) PDSD spectra (20 ms mixing time) of [$^{13}C_9$-Retinal, U-^{15}N]-KR2 in the absence and presence (30 mM NaCl) of sodium ions show similar retinal conformations in dark state and upon light activation at 110 K (K- and L-state).

The DQF spectra of [$^{13}C_9$-Retinal, U-^{15}N]-KR2 dark state do not show any difference between the sample with and without NaCl in the buffer (Figure 45a). The illuminated DQF spectra which contain mixed Dark (G), K and L populations also exhibit a similar pattern (Figure 45a). Moreover, the 2D PDSD spectrum in the absence of NaCl shown in Figure 45b also resembles the spectrum of the sample in the presence of NaCl (Figure 45b). To prove further whether the chromophore distortion near Schiff base in the absence of NaCl is the same as in the presence of NaCl, the dihedral angle H-C14-C15-H in dark and L-state were measured (Figure 46). The chromophore distortion in the dark state (150° ± 2) and L-state (138° ± 4) are nearly the same as for the sample in 30 mM NaCl environment. These data demonstrate the similar retinal conformation in dark, K- and L-state among these two environments. This agrees with the data reported in the literature based on optical spectroscopy, showing similar absorption maxima in the early-state intermediates in both ion pump modes.[1,52]

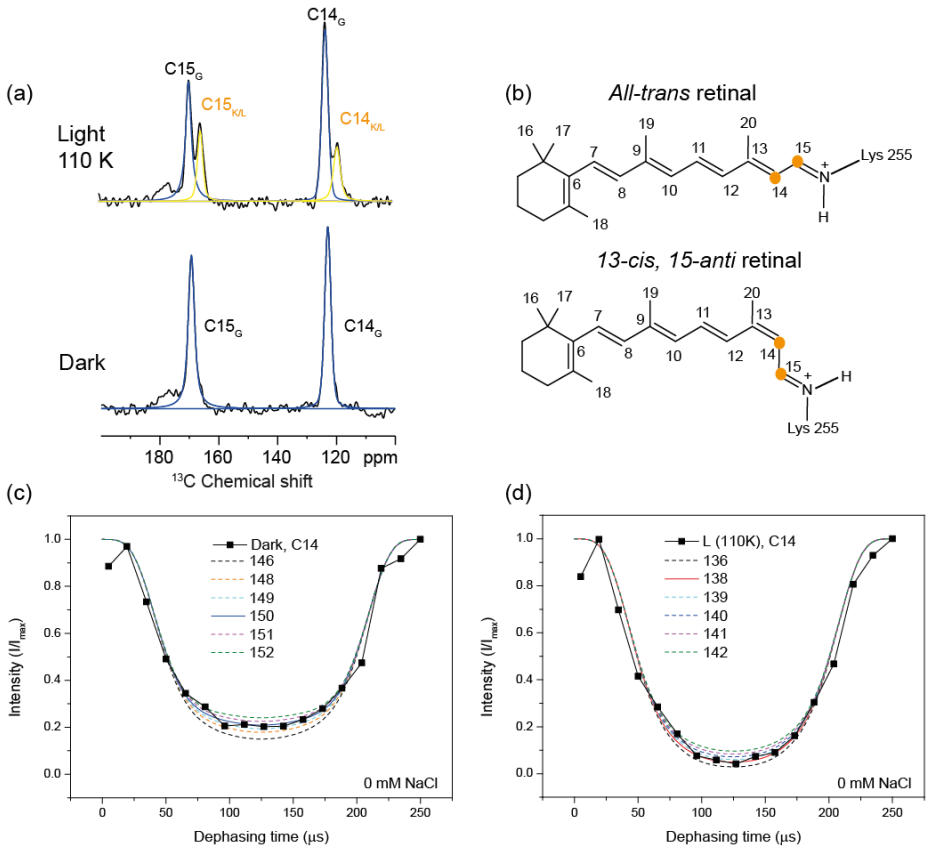

Figure 46: H-C14-C15-H Dihedral angle measurement of KR2 in dark state and L-state in proton pump mode. (a) DQF spectra of HCCH dephasing curves of [$^{13}C_2$-Retinal, U-^{15}N]-KR2 in dark state and after illumination at 110 K for 40 minutes. (b) 14, 15-$^{13}C_2$-retinal in *all-trans* and *13-cis, 15-anti* conformation. (c)-(d) HCCH dephasing curves of C14 peak in the absence of NaCl in (c) dark state and (d) L-state. The solid and dash line show the simulation of the best fit and indicated angles, respectively.

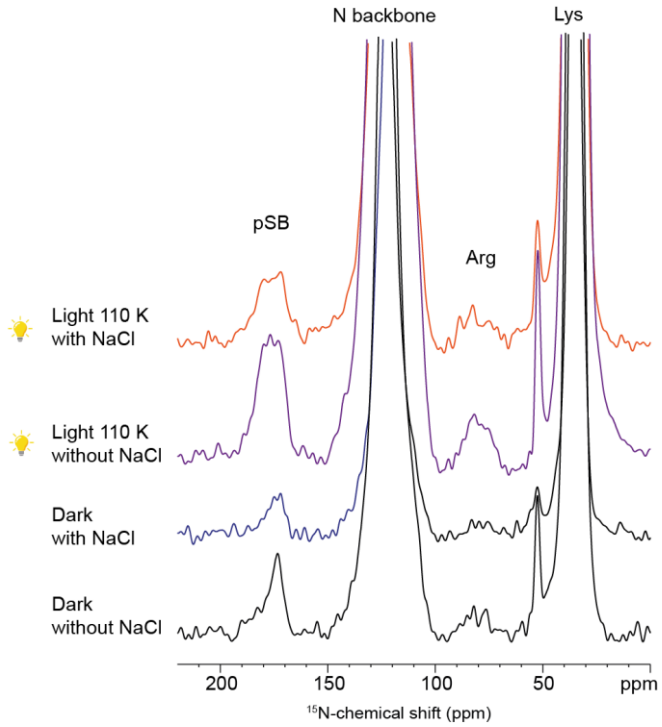

Figure 47: Comparison of pSB signals for KR2 dark, K/L-state in the presence and absence of NaCl. DNP-enhanced ^{15}N CP spectra of [^{15}Nζ-Lys]-KR2 prepared in the absence of and presence of NaCl (30mM NaCl) in dark state and after illumination at 110 K show no observable effect of NaCl on the protonated Schiff base (pSB) resonance in both dark and early-state (K/L) intermediates.

Flash photolysis study of KR2 in proton pump mode shows no characteristic absorption of O-intermediate at around 605 nm.[52] The kinetics of photocycle in proton pump mode is characterized by several equilibriums. The question arose whether KR2 in proton pump mode has any late intermediate or what happens after the deprotonation in M-state. To answer this question, similar O-state trapping (flash freezing) was performed on [$^{13}C_9$-Retinal, U-^{15}N]-KR2 in the absence of NaCl similar as for the sample with NaCl. TEDOR experiment was performed to check whether the signal of O-state ($^{15}N(pSB)_O$: 182 ppm, $^{13}C15_O$: 169.3 ppm) found in the sample with 30 mM NaCl could be observed in the sample without NaCl. The TEDOR spectrum of the sample without NaCl after flash freezing does not exhibit the signal of the O-state (Figure 48). This suggests that the low-field shifted of ^{15}N(pSB) signal observed in O-state in Na^+ pump mode should be caused by the binding of Na^+ near the Schiff base as also observed in the crystal structure of O-state in pentameric form crystallized at pH 8.0 (6XYT). The crystal structure shows the binding of Na^+ at the N112, D116, and S70 triad.[8]

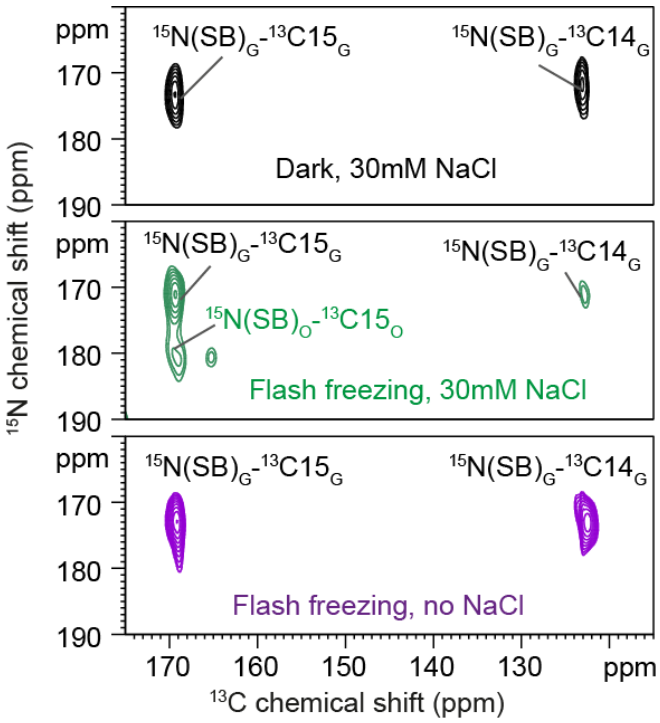

Figure 48: TEDOR spectra of [$^{13}C_9$-Retinal, U-^{15}N]-KR2 without NaCl after flash freezing (2816 scans), compared with the same sample prepared in the buffer with 30 mM NaCl in dark state (1312 scans) and after flash freezing (2816 scans).

5.3. Discussion

Early photointermediate states

The cryo-trapping experiments here at 110 K revealed a mixture of K- and L-state populations. Interestingly, very similar experimental conditions applied to BR, GPR, ChR2 resulted just in a single trapped K-state, which hints towards differences in the energy landscape of early photointermediates between different rhodopsins. The obtained light-induced ^{13}C retinal chemical shift changes from dark to K-state at C12 and C20 confirmed the expected *all-trans* to *13-cis* isomerization known for bacteriorhodopsin[178,179] and other microbial rhodopsins[19], including KR2. However, the retinal chemical shift changes (C10-15 and C20) deviate strongly in the middle and at the end of the retinal polyene chain from model compounds and can therefore not be explained solely by the isomerization step but must partially be caused by specific interactions within the KR2 retinal binding pocket. These additional shielding/de-shielding effects are indeed protein-specific as illustrated by comparing the K-state chemical shift changes of KR2 obtained with those from the same labeling scheme in the K-state of green proteorhodopsin (GPR)[12] under comparable conditions (Table 19). For example, pSB and C15 do not change in the K-state of GPR but shifted as high as 4 ppm in KR2. C12 resonance changes

by +12 ppm in KR2 compared to just +6 ppm in GPR. In fact, the chromophore in KR2 shows a stronger overall response towards the K-state formation compared to GPR as judged from the RMSD value of the chemical shift changes (C10-C15, C20) including pSB nitrogen (RMSD KR2: 6.7 ppm; GPR: 5.1 ppm).

In the L-state, the overall ^{13}C chemical shift changes with respect to the dark state are smaller compared to K-state (^{13}C RSMD reduces from 7.1 to 4.9 ppm, see), indicating the relaxation of retinal structural constraint. In addition, the Schiff base nitrogen is strongly de-shielded by -8 ppm, and the torsion around the C14-C15 bond changes from 150° to 136°. The Schiff base is already stronger drilled around the C15=N bond in the dark state compared to microbial proton pumps because the different position of the proton acceptor D116 in KR2 requires another orientation of the Schiff base N-H bond vector for a hydrogen bond formation (Figure 38). This is also reflected in the H-C14-C15-H torsion. The larger out-of-plane twist brings the Schiff base proton into an even more favorable position with respect to D116, which would be needed for the subsequent proton transfer step during the M-state. Such a twist in the polyene chain near the Schiff base moiety might be necessary for the inhibition of the delocalization of the positive charge along with the π-conjugated system, leading to the decrease of the pK_a value at the Schiff base. This is also supported by the observed nitrogen de-shielding, which is indicative of a stronger H-bond to D116. The C14 chemical shift has been found to be a sensitive marker for a 15-syn/anti conformation. In bacteriorhodopsin, the 15-*anti*-C14 resonance is found at 124 ppm and for 15-*syn* at 111 ppm.[11] Here, C14 shifts from 123.8 ppm in the dark and K-state to 119.2 ppm in the L-state. This means that the retinal is slightly turning toward a more compact *15-syn* conformation in the L-state.

The ^{15}N chemical shift of the Schiff base (SB) nitrogen is a sensitive indicator for alterations in the protonation state, counter ion interactions, and H-bonding network. An increase in chemical shift means less shielding at the atom and is indicative of a stronger H-bond interaction. In KR2, protonated SB formed a direct hydrogen bond with D116. The SB nitrogen chemical shift increases gradually when KR2 switches from the dark- to the K- and then to the L-state (Figure 49). This means that the SB hydrogen atom slowly moves away from the Schiff base and approaches the D116 side chain carbonyl oxygen. This is in contrast to BR_{568}, for which the chemical shift first decreases in the K-state due to disordering of the H-bonded water W402 followed by an increase in L through an H-bond with a new counterion.[11] This difference may be because in BR the SB does not form a direct H-bond with the counterion D85 but through the water molecule, W402. Moreover, the D116 position is one helix above the D85 in BR and is at

the same position as T89 in BR. Recently, the study of proton transfer pathway revealed by DNP-enhanced ssNMR showed that the proton transfer step from SB to D85 is via T89.[34] This proton transfer pathway in BR reflects the proton transfer in KR2 since D116 and T89 share the same helix position. The SB-D116 interaction would actually work like a gate that opened and closed during the photocycle because the SB bound proton is likely not transported or replaced in the Na^+ pump mode.

Table 19: Chemical shift perturbation (C10-C15, C20 and protonated Schiff base (pSB) in the photointermediates of KR2 in comparison with K-state in green proteorhodopsin (GPR). Root mean square deviation (RMSD) was calculated to give a general assessment of the alteration. The error estimation is ±0.5 ppm for ^{13}C and ±1 ppm for ^{15}N.

Chromophore nuclei	KR2 (G – K) (ppm)	KR2 (G – L) (ppm)	KR2 (K-L) (ppm)	KR2 (G-O) (ppm)	GPR (G – K)[12] (ppm)
^{13}C-C10	3.9	1.0	-2.9	-	2.4
^{13}C-C11	-5.3	-4.3	1	-	-6.0
^{13}C-C12	12.8	6.4	6.4	0.2	6.9
^{13}C-C13	4.7	0.6	-4.1	3.5	-3.4
^{13}C-C14	-0.1	4.5	4.6	-0.1	2.5
^{13}C-C15	3.9	3.9	0	0.4	0.2
^{13}C-C20	-10.3	-8.5	1.8	1.1	-10.0
^{15}N-pSB	-2.8	1.0	-5.2	-8.7	0.0
RMSD (^{13}C)	**7.1**	**4.9**	**3.6**	**1.7**	**5.4**
RMSD (^{13}C + ^{15}N)	**6.7**	**3.4**	**3.9**	**3.9**	**5.1**

In contrast to KR2, the pSB chemical shift in the K-state of GPR does not change. The ^{15}N chemical shift of the pSB in GPR in the G and K-state is slightly higher compared to KR2-L and the functional L-state (L_{186}) of BR. However, KR2 and GPR show a similar trend for the twist of the retinal polyene chain as observed from the H-C_{14}-C15-H torsional angle (Figure 38), which seems crucial for the proton transfer step. Similar to BR, KR2 passes through several early intermediate states before the proton can be transferred from the SB to the proton accepter[180], but in contrast to BR and GPR, both K and L can be trapped at 110 K. This suggests a lower energy barrier between both states. A low energy between K- and L-state is very important to ensure an efficient forward movement of the pump cycle and to avoid an unproductive reverse reaction to the dark state.

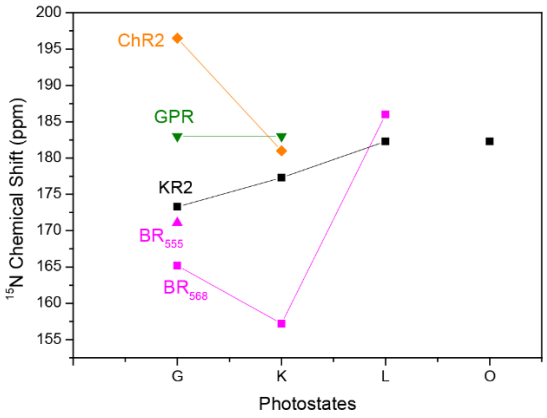

Figure 49: Comparison of ^{15}N Schiff base resonance of KR2 dark, K- and L-state with light-adapted (BR_{568}) and dark-adapted (BR_{555}) bacteriorhodopsin, Green proteorhodopsin (GPR) and Channelrhodopsin-2 (ChR2). The M-state is not shown in the graph because there is no experimental data available.

The late O-intermediate state

The KR2 O-state has a long lifetime and could be trapped in contrast to BR and GPR.[181] Structural information of O-state for BR and PR is therefore scarce. Only a crystal structure of the O-state of the BR mutant L93A was reported[182] with recently published data of the structure on millisecond timescale by serial synchrotron crystallography.[183] In BR, there are two late intermediates, called N and O, which are known to have *13-cis* and *all-trans* retinal conformation, respectively[178]. Our data for KR2 show that the retinal has relaxed back to all-*trans* in the O-state, similar to O-state in BR, suggesting that the stored energy was transferred to the protein. Next, the protein needs to release the cation and adjusts the H-bonded network back to the ground state where the energy level is at its lowest. It should be considered here that there is no N intermediate defined in the KR2 photocycle like in the BR[1]. Therefore, both reprotonation and the reisomerization happens upon the O-state formation. It is not clear whether these two processes occur simultaneously or successively. It was suggested that the binding of Na^+ support the reprotonation and reisomerization of the Schiff base.[8]

There is a controversy regarding the retinal conformation of the O-intermediate in KR2. In BR[178] and PR[184], O-state has an *all-trans* retinal conformation which is similar to our findings of *all-trans* retinal in the O-state of KR2. However, FTIR studies of the trapped intermediate[172] and time-resolved Raman spectroscopy[185] data reported recently suggested a 13-cis conformation. The data interpretation in these studies relied on spectra from *all-trans* and *13-cis* retinal bound to BR. The $C_{12}D + C_{14}D$ rocking vibrations in the IR HOOP region exhibits a band that is similar to the 13-*cis* conformation in BR. It might be possible that the intermediate trapped at 240 K lead

to an N-like state. The time-resolved Raman data of the C-C vibration peaks also suggested the 13-cis conformation. However, the signature interpretation was based only on the BR signature pattern, which might be divergent from KR2, and the *all-trans* conformation of O-intermediate might not be detected as it is very similar to the ground state.

The data here showed the electrostatic differences at the Schiff base and retinal C13 and C20 between dark and O-state. The shielding C13 (3.5 ppm) and C20 (1 ppm) could come from the adjusted retinal binding pocket in the O-state as observed from the kink at C14 and the replacement of W215 and other aromatic residues in the KR2 O-state crystal structure.[8] The de-shielding at the Schiff base observed in O-state is as large as 9 ppm. The factors contributing to the chemical shift are primarily the strength of the H-bond in which the Schiff base is involved, but also electric charge effects and torsion around the C15=N bond. An altered torsion appears less likely since the C14 chemical shift, a sensitive indicator for a 15-*syn*/*anti* isomerization remains unchanged between dark and O-state. This observation agrees with the KR2 dark-state and O-state X-ray structures in which the C14-C15-N-Cε dihedral angle does not significantly change (6REW: 135°, 6XYT: 132°). The observed de-shielding could however indicate a stretched N-H bond and hence a stronger O..H-N hydrogen-bond between D116 and the SB nitrogen in the O-state. This seems plausible when considering that the SB becomes re-protonated with a proton being transferred from D116 during the M→O transition. It would require a favorable orientation of the aspartate carboxyl group and the Schiff base with respect to each other and could result in a shorter O…H distance, which then relaxes and becomes longer again in the dark state. On the other hand, this observation seems counterintuitive in comparison to retinal Schiff base model compounds[186] for which a correlation between H-bond strength and λ_{max} was found and a de-shielding at SB would predict a blue shift absorption. This is usually discussed in terms of stronger counterion interactions and fits generally the observations on many rhodopsins in their dark states.[5] However, for KR2 O-state, the de-shielding at the Schiff base and a redshift occur. This counterintuitive observation of the de-shielding effect at Schiff base could be caused by a shielded counter ion – Schiff base interaction due to the bound Na^+ as was mentioned previously by the MD simulation study.[9] The situation appears even more complicated as Na^+ is indeed coordinated by D116, N112, S70, and V67,[8] which will alter the polarity/electric field within the Schiff base vicinity in a complex manner. In addition, water molecules within the proximity of the Schiff base will contribute to the polarity since the Schiff base cavity contains four water molecules with one of them H-bonded to D116.[50]

Interestingly, the corresponding KR2 mutant D116N shows a small but significant de-shielding of the Schiff base nitrogen which emphasizes also that data interpretation in terms of a direct relationship between color/counterion interaction and Schiff base chemical shift is in many cases too simplistic. Dissecting all contributing factors will ideally require quantum chemical computational approaches combining NMR and optical data with 3D structures.

KR2 in proton pump mode

In the proton pump mode of KR2, the retinal conformations in K- and L-state observed from chemical shifts are similar to that of in the sodium ion pump mode. Also, the Schiff base chemical shift and the dihedral angles measured at H-C14-C15-H in both dark and L-state do not show any variation. This agrees with the previously reported data based on optical and vibrational spectroscopies. The similarity of retinal conformations in these two pump modes would be because the uptake ion is far away from the retinal. The ion uptake cavity in the pentameric form is opened and protrudes from the lipid boundary into bulk solution, however, no sodium ion bound inside the protein core is observed in the dark state crystal. It is not clear that at which stage the pump substrate enters the uptake cavity. MD simulations show that sodium ion was pulled into the uptake cavity in the K/L state.[9] However, in that work, K- and L-state were not separately calculated due to the lack of knowledge regarding the difference between them. The observation of sodium ion bound at S70-N112-D116 triad near Schiff base in the O-state crystal structure[8] and the sodium ion concentration dependent of O-state[1,7] indicate the uptake after M-state, where the Schiff base is deprotonated and the positively charge barrier does not exist. Nevertheless, either sodium ion or proton enters the uptake cavity in the K- or L-state, the ion would be too far away to affect retinal and Schiff base chemical shifts.

The key difference between sodium ion and proton pump mode is observable from the characteristic absorption maxima of the O-state at 605 nm which exists only in Na^+ pump mode. From the ssNMR data obtained here, no pSB and retinal C15 chemical shift perturbation for the KR2 sample without NaCl was observed after flash freezing, suggesting no existence of O-state in H^+ pump mode. The data support the binding of Na^+ near the Schiff base in O-state, which causes the de-shielding observed at the Schiff base in Na^+ pump mode. The mechanisms for the transport of sodium ion and proton can be described differently. Grotthuss mechanism is usually applied to explain the proton transport in proton pumping rhodopsin, however, this cannot be applied to the transport of sodium ion, instead, the residues with a high transient Na^+ binding affinity like asparagine is essential for the Na^+ pump function. Nevertheless, the link of water molecules and polar residues along the pathway is the crucial factor for both ions transport.

Comparison with the known 3D crystal structures

Recently published serial crystallographic X-ray data of monomeric KR2 and the cryogenic trapped O-state crystal structure provide important 3D structures of KR2 photointermediates throughout the photocycle.[7,8] It is interesting to compare the structural data obtained from the ssNMR study here to these known 3D crystal structures. The chemical shift changes are overlaid to the structure of dark state (PDB: 6TK6), K-state (PDB: 6TK5, Δt = 800 fs), L-state (PDB: 6TK4, Δt = 1 ns) and two O-state (PDB: 6TK2, Δt = 1 ms and PDB: 6XYT) structures (see Figure 50). For the dark → K-state, the largest changes stem from the isomerization. Additional protein-specific contributions to the observed chemical shift differences could be caused by altered ring-current effects due to small rearrangements of aromatic residues W113, W215, and Y218 by which the C10-C15 segment of the retinal polyene chain is surrounded. For K → L-state crystal structure, the increasing tilt of C20 towards helix C was observed. This could help to explain the C12, C13, C14, and C20 chemical shift differences between K- and L-state observed by ssNMR. The distance between the SB nitrogen and Oδ2 of D116, which indicates the strength of H-bond, changes from 3.0 Å in the dark via 2.9 Å in the K-state to 2.4 Å in the L-state in these X-ray structures. These support well the increasing ^{15}N de-shielding at Schiff base from dark to K- and L-state observed by ssNMR.

The retinal in the pentameric cryo-trapped O-state X-ray structure (6XYT) has also *all-trans* conformation, similar to the observation here, but the C14-C15 bond was reported to be out of plane compared to the dark state. This observed out of plane at C14-C15 could help to explain the shielding observed at C13 in O-state due to an effect of the interrupted localization of positive charge from protonated Schiff base. The Na^+ was found to bind to D112, N112, S70, and V67 and is 5.4 Å away from the Schiff base nitrogen. As discussed earlier, this would cause the large de-shielding (9 ppm) observed at Schiff base in O-state by ssNMR. This conclusion was supported by the negative control experiment, in which this de-shielding was not observed when H^+ is the transport substrate.

The time-resolved X-ray structures derived from serial crystallography cover not only the K- and L-states but have been extended via the M- into two O-states.[7] After 1 ms, a Na^+ ion is found close to the retinal binding pocket (between N112 and D251) but at a different position compared to the pentameric state. An overlay of this state with the dark state structure (Figure 50d) shows that the structural differences should correspond to larger chemical shift changes than actually observed here. One reason could be that our sample with KR2 pentamers in proteoliposomes is closer to the pentameric X-ray structure than to the monomeric preparation used for serial

crystallography, a difference which has also been addressed by the authors as relevant to the O-state.[7] On the other hand, the distance between SB and D116 in the serial crystallography study becomes shorter compared to the dark state (2.7 vs. 3.0 Å). This could fit with the chemical shift changes observed on the SB nitrogen by ssNMR.

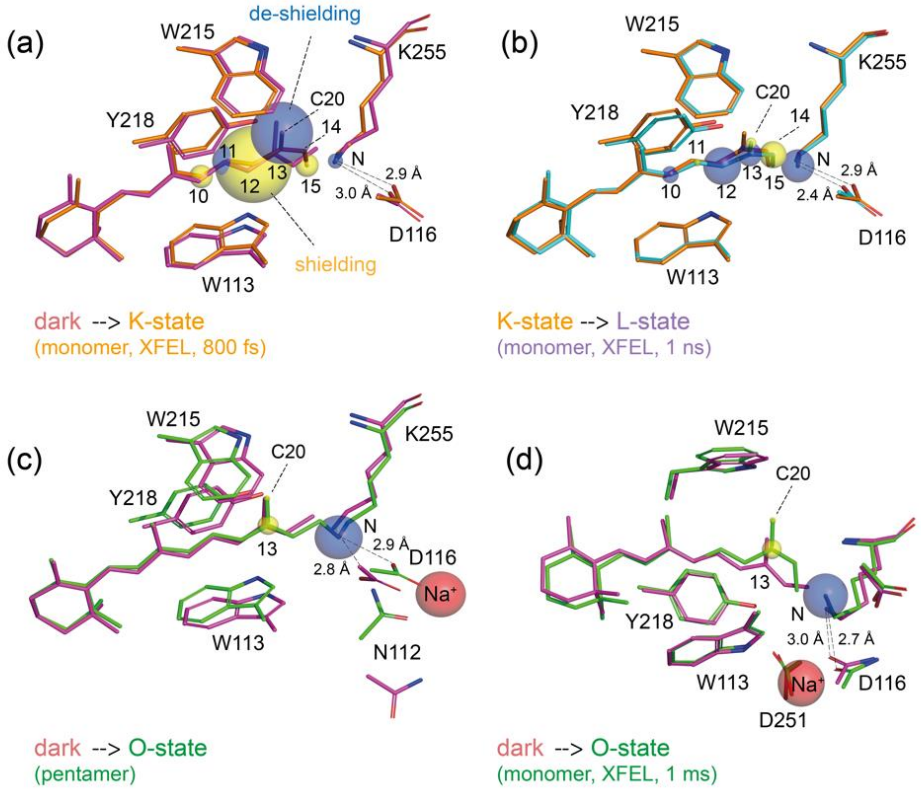

Figure 50: KR2 retinal binding pocket during the photocycle, structures and chemical shifts. (a) Comparison between dark- and K-state serial crystallography X-ray structures (6TK6, 6TK5) with ^{13}C and ^{15}N chemical shift changes (Table 19). (b) As in (a) but comparison between K-state (6TK5) and L-state (6TK4). Plotted chemical shift changes are with respect to the K-state. (c) Dark- and O-states of pentameric KR2 X-ray structures (6REW, 6XYT) and chemical shift changes with respect to the dark state. (d) Dark- and O-states of monomeric KR2 time-resolved structures (6TK6, 6TK2) and chemical shift changes with respect to the dark state.

5.4. Summary

Based on the information obtained from DNP-enhanced ssNMR study here, the molecular mechanism of light-driven Na^+ pump KR2 is illustrated in Figure 51. After light-activated isomerization, the retinal is isomerized from *all-trans* to *13-cis, 15-anti* conformation in K-state, by which the energy is mainly stored in the retinal as observed from the CS perturbation from the middle part of polyene chain to the Schiff base and the H-bond between Schiff base and D116 becomes stronger than in the dark state. The structural constraint in K-state is somewhat relaxed in L-state, by which the retinal near Schiff base is twisted further from the dark state in the direction of *15-syn* conformation (still remains in the *15-anti*) and the H-bond between Schiff base and D116 becomes even stronger as the protein approaches the M-state. After proton transfer and Na^+ uptake, the O-state is formed, which exhibits an *all-trans* conformation that is different from the dark state at retinal C13 and C20 and the protonated Schiff base. The high de-shielding at Schiff base in O-state suggests the strong H-bond with D116 and the effect of internal Na^+ binding nearby.

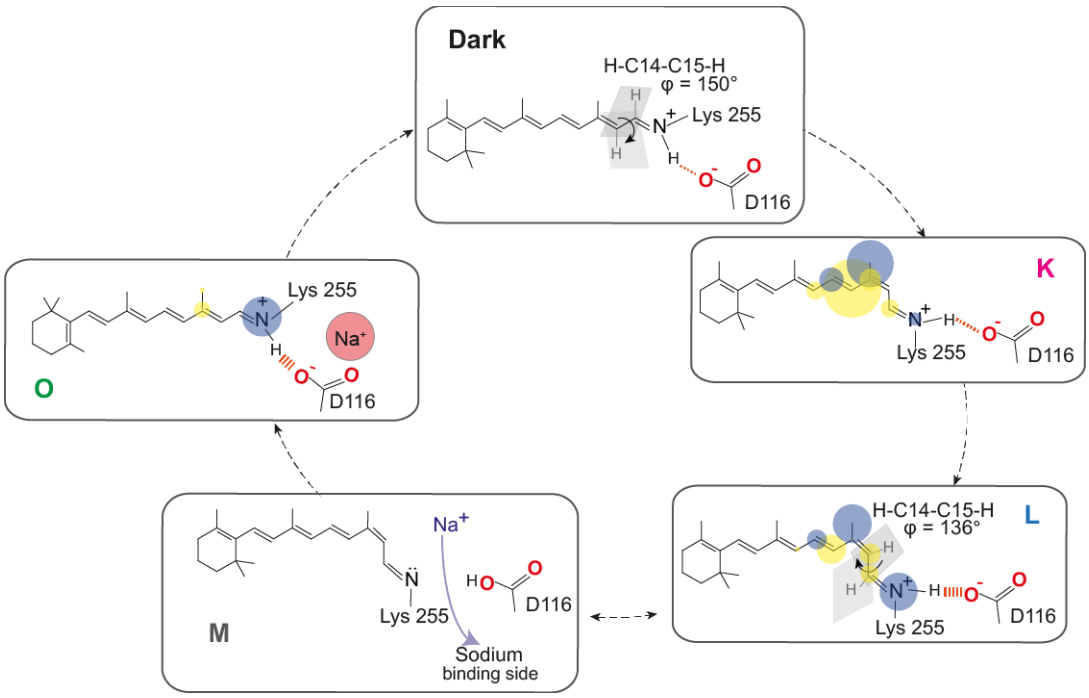

Figure 51: Illustration of retinal conformation and electrostatic change at the retinal and Schiff base after light activation in K-, L- and O-state as observed by DNP-enhanced ssNMR in the photocycle of KR2. The chromophore near Schiff base is highly twisted in the dark state and further strongly twisted in the L-state. The H-bond between Schiff base nitrogen and D116 becomes stepwise stronger from K- to L-state and O-state. The yellow and blue spheres indicate shielding and de-shielding at the nuclei with respect to the dark state, respectively.

Chapter 6: Protein-retinal contacts and isomerization induced changes in opsin

Photoreactions in both animal and microbial rhodopsins occur on an ultrafast timescale in which the isomerization belongs to one of the fastest reactions in biology.[187] The photoisomerization is very efficient and selective due to the perfectly designed architecture for each protein. The restriction of the retinal's degree of freedom by opsin promotes the fast isomerization and assures energy storage and transfer through structural changes and alterations of H-bonding networks.[20] The photoisomerization induced local structure changes and H-bonding networks near the chromophore, usually occur on the nanosecond to microsecond timescale, followed by ion transfer and global protein structure changes for functions, which generally occur in milliseconds to seconds.

In the former chapter the retinal conformation and the Schiff base-counterion interaction in the dark state, K-, L- and O-intermediates was studied (Chapter 5). To elucidate the mechanism of ion transport, it is also important to understand how the protein response to isomerization and pave the way for ion transport. The aim of this chapter is to probe the structural change at the following parts of the protein:

1) K255 – the lysine residue covalently bound to the retinal (section 6.1)
2) Retinal and tryptophan contact in the retinal binding pocket (section 6.2)
3) R109 – the arginine gate that separates the retinal binding pocket and the ion release cavity (section 6.3)
4) N112 of the NDQ motif (section 6.4)

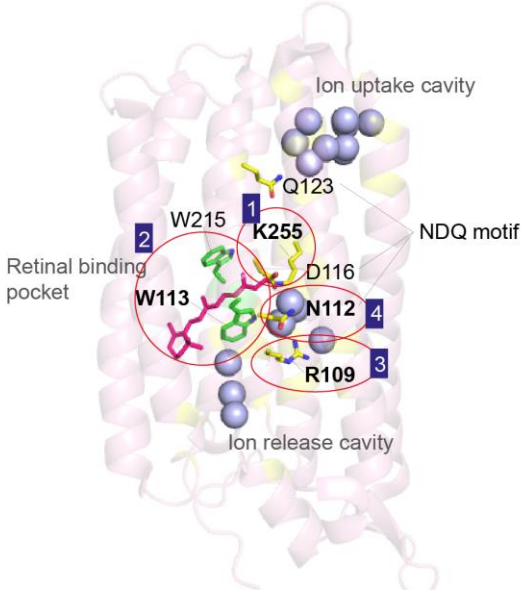

Figure 52: Illustration of the protein parts studied in chapter 6: 1) K255, 2) Retinal and tryptophan contact, 3) R109 gate and 4) N112 of the NDQ motif (PDB: 6REW).The spheres show the water molecules in the ion uptake cavity, retinal binding pocket and ion release cavity.

6.1. Isomerization effect on K255

6.1.1. Introduction

All retinal in microbial rhodopsins are bound to the conserved lysine residue. In KR2, this lysine residue is at the position K255 (Figure 53a). As K255 is the key residue that connects the retinal to the opsin, any conformation change following the light-induced isomerization would also affect the K255 side chain. Especially, Cε of K255 is a key indicator of retinal 15-*anti/syn* conformation.[11] In the former chapter, the C14 resonance indicates a *15-anti* conformation in the dark and K-state and a slight rotation in the direction of *15-syn* conformation in the L-state (see section 5.2.2). To prove this finding, the chemical shift perturbation at the K255 side chain was probed using the intermediates trapping protocol established in chapter 5.

6.1.2. Results and discussion

The isomerization effect on the K255 ^{13}C chemical shifts in K-, L- and O-intermediates were investigated using [U-^{15}N, ^{13}C-Lys]-KR2 based on N(C)CX experiments. The KR2 sample was prepared and packed to a sapphire rotor in a similar way as for the study performed on labeled retinal in chapter 5. K255 signal can be assigned based on the specific nitrogen resonance of Schiff base at 173 ppm. For the dark state, all cross peaks between pSB-^{15}N and ^{13}Cε to ^{13}CO of K255 were observed (Figure 53). The Schiff base chemical shift matches the number reported in chapter 5. The assignment of ^{13}C-lysine signals is based on the K255 chemical shift data acquired by Clara Kriebel, Glaubitz lab (personal communication) using DARR experiments with long and short mixing times except for Cδ which was not observed in the high field noncryogenic measurement. Since all other ^{13}C carbon atoms are assigned, the last left unassigned crosspeak is then assigned to Cδ. The chemical shifts are summarized in Table 20. The $C\varepsilon_{K255}$ chemical shift of the dark state exhibits a *15-anti* conformation[11] which agrees well with the previously determined C14 chemical shift (Table 16), which is also a sensitive indicator of 15-*anti/syn* conformation (Figure 53d).

After light activation at 110 K which leads to the formation of K- and L-state, an isomerization induced change at Cε of K255 could be observed (Figure 53b). However, the other carbon atom (Cδ, Cγ, Cα, and CO) of K255 did not exhibit any considerable change. The pSB-Cβ crosspeak was very weak and not visible in the light 110 K spectrum. The assignment of K- and L-state Schiff base signals was based on the data described in the former chapter (see Figure 39). Upon the thermal relaxation to 190 K, which let the K-state thermodynamically proceed to L-state, the pSB-Cε crosspeak of K-state disappeared. The chemical shift perturbations (ΔCS) at $C\varepsilon_{K255}$ in K- and L-state are shown in Figure 53c. Compared to the Cε chemical shift of BR_{568} (*all-trans*, 53.5

ppm) and BR_{555} (15-*syn*, 48.0 ppm), $C\varepsilon_{K255}$ chemical shift of both K- (52.8 ppm) and L-state (51.3 ppm) shows a 15-*anti* conformation. The ΔCS at $C\varepsilon_{K255}$ of 1.7 ppm from the dark state to K-state seems to be caused by the isomerization and the slight displacement of the K255 side chain. This shielding becomes more pronounced in the L-state (4.2 ppm). As seen from the chemical structure of *15-anti* and *15-syn* (Figure 53d), the shielding at Cε and C14 is higher for the 15-syn conformation. The increased chemical shift shielding observed at Cε in the L-state suggests the retinal twist in the direction of 15-*syn* but still remains in a 15-*anti* conformation. This fits well with the additional shielding observed at C14 and supports the 14° chromophore distortion (H-C14-C15-H) in L-state compared to the dark state (see Figure 38). The N(C)CX spectrum of the flash-frozen sample (trapping of O-state) does not exhibit a trapped O-state with the unique SB chemical shift at 182 ppm. The reason would be due to the limited amount of the trapped O-state which is under the detection limit.

The result of this part shows the response of Cε-K255 to the isomerization in the K- and L-state and confirms the slight rotation from the *15-anti* conformation in the dark and K-state in the direction of *15-syn* conformation which is spatially more compact in the L-state of KR2 as observed from the retinal C14 resonance in the former section (5.2.2.2).

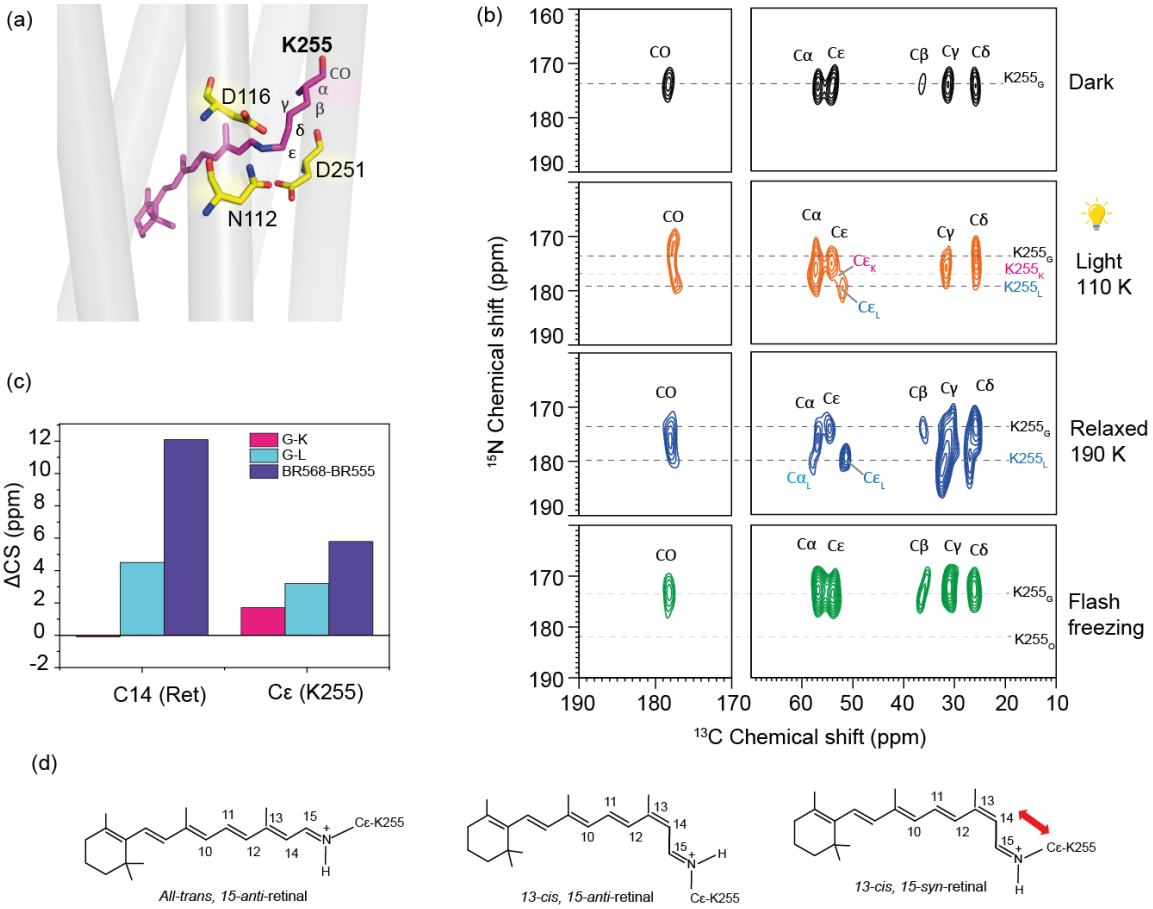

Figure 53: Isomerization induced change on K255. (a) illustration of K255 bound to retinal in retinal binding pocket. Proton acceptor (D116) and key residues near Schiff base (N112 and D251) are shown. (b) DNP-enhanced N(C)CX spectra (1248 scans, 64 increments with 125 µs increment delays) of [U-^{15}N, ^{13}C-Lys]-KR2 (100 mM NaCl) in the dark, light 110 K, relaxed to 190 K and trapped by flash freezing. (c) Light induced change at Cε of K255 for K- and L-state in comparison to chemical shift difference (ΔCS) at Cε between *all-trans* (BR568) and *15-syn* (BR555) conformation in BR.[11] For comparison, ΔCS at C14 in K- and L-state are shown. (d) Chemical structures of retinal in *all-trans*, *15-anti*, *13-cis*, *15-anti* and *13-cis*, *15-syn* conformations show the shielding at retinal C14 and Cε in *13-cis*, *15-syn* conformation.

Table 20: Chemical shift of K255 in dark, K and L-state. The data is obtained from the N(C)CX spectra of [U-^{15}N, ^{13}C-Lys]-KR2, reconstituted in DMPC:DMPA (9:1), Lipid protein ratio (2:1), in 100 mM NaCl, 25mM Tris, 5mM $MgCl_2$, pH 8.5 NMR buffer in dark, illuminated at 110 K, relaxed to 190 K

KR2	Cε (ppm)	Cγ (ppm)	Cδ (ppm)	Cβ (ppm)	Cα (ppm)	CO (ppm)	pSB (ppm)
Dark	54.5 ± 0.5	31.2 ± 0.5	25.9 ± 0.5	36.2 ± 0.5	56.7 ± 0.5	178.2 ± 0.5	173.3 ± 1
K	52.8 ± 0.5	31.2 ± 1	25.9 ± 1	-	56.7 ± 1	178.2 ± 1	176.1 ± 1
L	51.3 ± 0.5	31.2 ± 1	25.9 ± 1	-	56.7 ± 1	178.2 ± 1	181.3 ± 1

6.2. Retinal and tryptophan contact

6.2.1. Introduction

Tryptophan is the bulkiest amino acid, possessing both hydrophobic and hydrophilic characters, and is always found in the retinal binding pocket in microbial rhodopsins.[19] BR, the prototypical photoreceptor protein, possesses 8 tryptophan in the sequence. Four of them (W86, W138, W182, and W189) are located in the retinal binding pocket[188]. The conserved W86 and W182 sandwich the retinal chromophore. For KR2, there are 7 tryptophan residues and 2 of them (W113 and W215) involve in the forming of the retinal binding pocket at the same position as W86 and W182 in BR, respectively (Figure 54).[16,17] A number of studies based on time-resolved ultrafast spectroscopies, time-resolved serial femtosecond crystallography (TRX), and ssNMR have been performed to understand the role of tryptophan in the photocycle of bacteriorhodopsin and sensory rhodopsin II, and its effect on primary photoisomerization reaction[189–198].

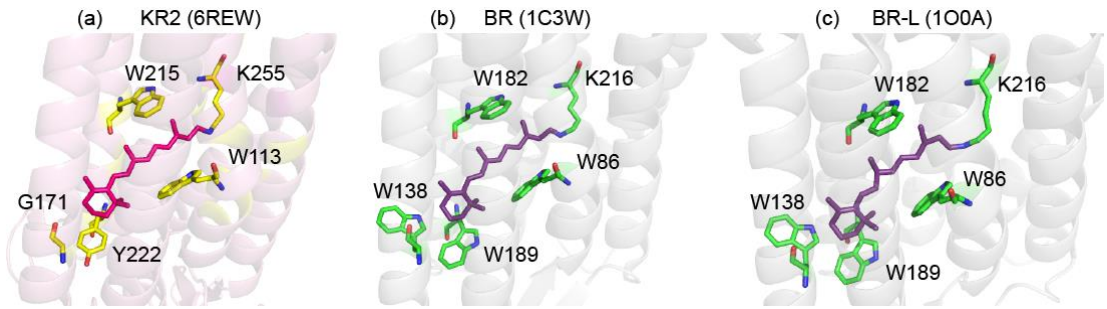

Figure 54: Tryptophan residues in the retinal binding pocket of KR2 dark state (6REW) and BR dark state (1C3W) and L-state (1O0A).

Time-resolved UV-Vis, FTIR, and pKa data of WT, W182F, and 9-desmethylretinal-BR show a steric interaction between W182 and the methyl group at C9-retinal, and its importance in *13-cis* to *all-trans* retinal re-isomerization and proton transfer in the late part of the photocycle.[199] It was suggested that the tryptophan residues cause the distortion of retinal from its planarity which inhibits the dark adaptation and affects the H-bonds network around Schiff base in the first step of the photocycle. [200,201] UV-Vis resonance Raman data also supported the strong interaction between indole ring and retinal methyl groups at C9 and C13.[202] The mutation at W86 and W182 positions in BR induce color changes and affect the deprotonation and reprotonation rate.[203] The recently reported UV resonance Raman data also show the remarkable response of the stimulated Raman signal of tryptophan and tyrosine in a sub-picosecond timescale which disappears during the isomerization process, suggesting the creation of large dipole at the chromophore excited state

in the primary photoreaction and the vibrationally and electronically coupling of the chromophore and surrounding amino acids and water molecules.[190] In addition, ssNMR was also applied to study the H-bonding of tryptophan residues in BR and the perturbation during the photocycle.[198]

For KR2, the information regarding the tryptophan residues in the retinal binding pocket is still scarce. Only recently, the TR-SFX study has revealed the crystal structure of K- and L-state and the displacement of tryptophan residues in the retinal binding pocket of the L-state.[7] The aim of this part is to probe the contact between the retinal and the tryptophan residues in the retinal binding pocket based on ^{13}C-^{15}N dipolar coupling and the effect of retinal isomerization on the tryptophan residues that sandwich the retinal during the photocycle.

6.2.2. Results and discussion

Here, the tryptophan residues and their contacts to the retinal in KR2 and its photointermediates were probed by DNP-enhanced ssNMR using [$^{13}C_9$-Retinal, U-^{15}N]-KR2. The signal from the $^{15}N\varepsilon$ (indole) of tryptophan near the ^{13}C labeled retinal can be selectively detected using a ^{13}C-^{15}N heteronuclear recoupling experiment. The heteronuclear dipolar interaction which is averaged out under magic angle spinning (MAS) is reintroduced in TEDOR experiment[152] (see Figure 13). As the recoupling depends on the strength of dipolar coupling and thus the distance between the two coupled spins (r^{-3}), only the nuclear spin that is closed in proximity is detectable. Theoretically, the detection limit is less than 6 Å[89], however, because the dipolar coupling is also a source of relaxation and the limited amount of sample, in reality, the detection limit can be even less. The distances between retinal carbon atoms and the Nε-W113 and Nε-W215 derived from the 3D crystal structure are summarized in Table 21. The shortest distances are found for the retinal C12- and C14 to Nε-W113. The distances are in a similar range as that for BR.

In the TEDOR spectrum of KR2 dark state (Figure 55c), two crosspeaks between $^{15}N\varepsilon$-Trp (133.7 ppm) and ^{13}C-retinal at 133.9 and 123.7 ppm, respectively, are observed. These peaks are assigned to the crosspeaks between $^{15}N\varepsilon$ indole of tryptophan and $^{13}C12_G$ - and $^{13}C14_G$ -retinal, respectively, according to the previously assigned retinal chemical shifts (Figure 27). According to the crystal structure, $^{15}N\varepsilon$-W113 is in the closest proximity to C12 and C14 of retinal, 3.6 and 3.9 Å (PDB: 6REW), respectively (see Table 21). These crosspeaks are therefore tentatively assigned to $^{15}N\varepsilon$-W113 - $^{13}C12_G$ and $^{15}N\varepsilon$-W113 - $^{13}C14_G$. The chemical shift of $^{15}N\varepsilon$-W113 (133.7 ppm) indicates an H-bonding at the indole N-H bond.[198] Besides the retinal-Trp crosspeaks, natural abundance (n.a.) signals from ^{15}N-amide (~120 ppm) - n.a. carbonyl backbone

(~178 ppm), ^{15}Nε-Trp (~133 ppm) - n.a.^{13}Cε2 (~140 ppm) and - n.a.^{13}Cδ1 (~130 ppm) are also observed. The peak intensities of these natural abundance signals are relatively strong due to the short heteronuclear dipolar coupling of the one bond contact.

Table 21: Distance analysis between retinal (C10-C15) and Nε-W113 and Nε-W215 in KR2 (6REW, 2.2 Å resolution) and W86 and W182 in BR dark (1C3W, 1.55 Å resolution) and L-state (1O0A, 1.62 Å resolution).

Retinal atom	KR2 (6REW)		BR (1C3W)	
	Distance to Nε-W113 (Å)	Distance to Nε-W215 (Å)	Distance to Nε-W86 (Å)	Distance to Nε-W182 (Å)
C10	5.1	6.9	4.9	6.2
C11	5.0	5.6	4.8	4.9
C12	3.6	5.9	3.7	5.4
C13	4.2	5.2	4.3	4.8
C14	3.9	6.2	3.4	5.9
C15	4.6	6.2	4.4	6.1

Upon illumination at 110 K, which results in the formation of K- and L-intermediates, the ^{15}Nε-W113 - $^{13}C12_G$ and ^{15}Nε-W113 - $^{13}C14_G$ signals seen in the dark state decreases to the noise level (Figure 54c). Only the signals from natural abundance short-range dipolar coupling are clearly observed. The illumination yield of K/L-state is estimated to be 45% (see chapter 5). The remaining dark state population is ~55%, meaning that the signal intensity is reduced to half with the same number of scans, leading to the difficulty in the observation of a long-range dipolar coupling even for the dark state. It is difficult to estimate the population ratio between K- and L-intermediates. Assuming that K- and L-states are in equilibrium and have equal populations, there will be just only ~23% for both states. The tryptophan-retinal crosspeak intensity should then be below the noise level and thus difficult to detect. Similar to the light 110 K spectrum, no tryptophan-retinal crosspeak was observed in the relaxed 190 K and 230 K as well as the flash freezing spectra.

The natural abundance signals from ^{15}N-backbone - n.a.CO, ^{15}Nε-Trp - n.a.Cε2-Trp and ^{15}Nε-Trp - n.a.Cδ1-Trp are detected in all spectra. There is no change in the chemical shift for ^{15}Nε-Trp observed in all spectra with different trapping protocols. It is likely that the H-bonding around the indole tryptophan does not considerably change. This is similar to the ssNMR study of

tryptophan in M_0 and M_n state of BR, showing no substantial chemical shift perturbation at Nε-indole of W182.[198]

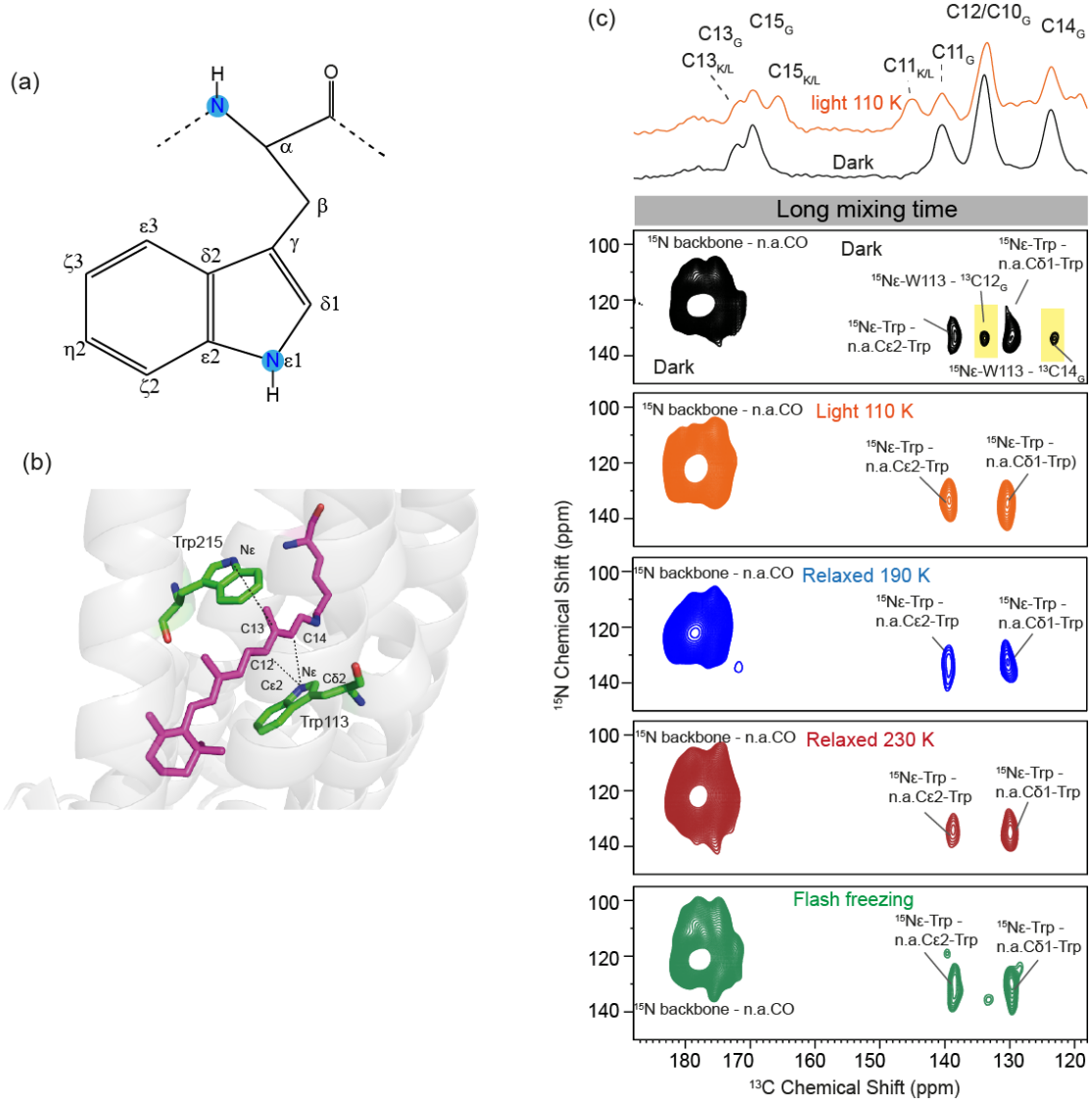

Figure 55: (a) Chemical structure of tryptophan and its atomic nomenclature (b) Illustration of retinal and tryptophan residues (W113 and W251), forming the retinal pocket in KR2. (c) DNP-enhanced TEDOR spectra with a mixing time of 6 ms of [$^{13}C_9$-Retinal, U-^{15}N]-KR2 in dark state (1312 scans, 60 increments with 125 µs increment delay) and after illumination at 110 K (1312 scans 60 increments with 125 µs increment delay) and relaxed to 190 K (736 scans, 18 increments with 250 µs increment delay), relaxed to 230 K (1664 scans, 50 increments with 125 µs increment delay) and trapped by flash freezing (1472 scans, 56 increments with 125 µs increment delay). The signals highlighted in yellow show the crosspeaks between ^{15}Nε-Trp-^{13}C12 and ^{15}Nε-Trp-^{13}C14 in dark state. The retinal resonance assignment is based on the 2D PDSD and DQSQ spectra (see Figure 27).

The result here demonstrates the detection of contact between the C12- and C14-retinal and Nε-W113 in the retinal binding pocket of KR2 in the dark state based on the long-range dipolar coupling and DNP enhancement. However, based on the labeling scheme used here it is not possible to observe the dipolar coupling between retinal and ^{15}Nε-Trp in the photointermediates since the trapped intermediate states are limited and the probed distance is too long. In order to prove the contact between the retinal and the surrounding tryptophan residues in the intermediates, the labeling scheme using ^{13}C20-retinal (methyl group at C13) and specific ^{15}N labeling at Nε-Trp should be employed to decrease the probed distance and thus increase the sensitivity as well as to eliminate the natural abundance signals that complicate the spectra interpretation. Moreover, the distance measurement between C20-retinal and tryptophan in the dark state and photointermediates would provide important information to explain the role of tryptophan in the pumping mechanism of KR2.

6.3. Probing of the R109 gate

6.3.1. Introduction

R109 is a conserved residue in KR2, separating the Schiff base cavity from ion release cavity[16,17] (see chapter 1.3.3) and is found in many ion-pumping microbial rhodopsins.[1] Arginine has an amphipathic property, carrying a positive charge at the guanidium group at physiological pH. Mutation of this residue to glutamine results in the pump leakage, allowing the passive ion conductance with the preference of K^+ more than Na^+.[204] Together with the modification at S70 which removes the residual pumping activity, it is possible to convert KR2 to a channel. The release of Na^+ to the bulk solution and the role of the R109 gate are not well understood. The MD simulation data reported by Suomivuori et al. demonstrates the perturbation at R109 residue in the O-state when the Na^+ enters and binds to the N112 and D251 internal binding site, whereas the gate remains tightly closed in the dark and K/L-state.

Here, the closing and opening of the R109 gate was examined by probing the dipolar coupling between ^{15}Nη-R109 in the helix C and ^{13}C-Y247 in the helix G during the photocycle by DNP-enhanced ssNMR (see Figure 56a). In the dark state, R109 forms an H-bond to D251 and water-mediated H-bond to T248.[50] However, it is not possible to label only the carbon atoms of aspartic acid (for D251) or threonine (for T248) for NMR studies due to the isotopic scrambling. Therefore, the Y247 which is also in close proximity to R109 was selected to probe the distance between ^{15}Nη-R109 and helix G because tyrosine can be exclusively labeled without the ^{13}C scrambling to other amino acids in *E. coli* due to its unique metabolic pathway.[205] In the KR2 sequence, there are 4 arginine residues in total. Y247 is the only tyrosine residue in the KR2

sequence which is located in close proximity to ^{15}Nη-R109 (~4 Å). Therefore, the signal that arises could be unambiguously assigned to ^{15}Nη-R109 and ^{13}C-Y247 dipolar coupling. The dipolar coupling which provides the atomic distance between these two residues should serve as an indicator for the closing and opening of the R109 gate.

6.3.2. Results and discussion

The distance between ^{15}Nη-R109 and ^{13}C-Tyr in the dark state was measured using 1D-TEDOR with different REDOR mixing periods (Figure 56c). For a short mixing time (1-2 ms), only the signal from one-bonded natural abundance (n.a.) ^{13}Cζ-Arg coupling with ^{15}Nη-Arg was observed at 158 ppm. For 4-6 ms mixing time, two peaks from the long-range dipolar coupling between ^{15}Nη-R109 and ^{13}C-Y247 at 176 ppm and 36 ppm, respectively, became visible. These peaks were assigned as CO- and Cβ-Y247, respectively, according to their chemical shifts. The TEDOR buildup curve for Cβ-, CO-Y247, and Cζ-Arg are shown in Figure 56d. The polarization buildup depends not only on the dipolar coupling distance but also on T2 relaxation which causes the decreasing of the signal. The peak intensity of Cβ-Y247 increases with the mixing time to the maximum at 5 ms and decreases substantially due to T2 relaxation. In contrast, the TEDOR buildup curve of CO-Y247 does not decrease substantially because of its much longer T2 relaxation time. Cζ-Arg buildup curve also exhibits a short T2 relaxation time. The buildup curve can be fitted to the TEDOR equation as describes in materials and methods (0) to obtain the dipolar coupling constants. The corresponded N-C distances are shown in Table 22. The calculated N-C distances are comparable with the distances measured from the crystal structure in the pentameric form (4XTO).

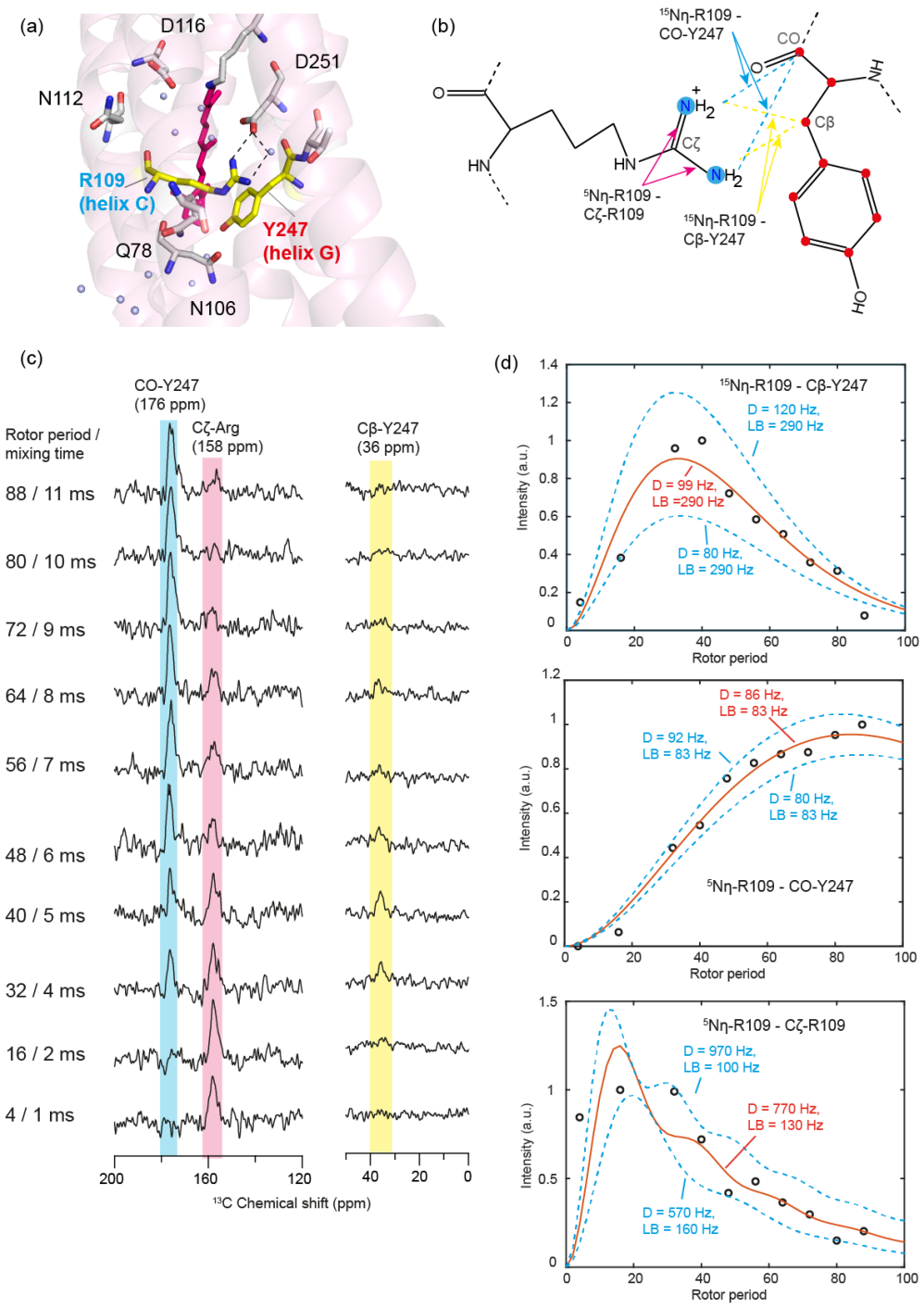

Figure 56: (a) Illustration of R109, separating the Schiff base cavity and the ion release cavity, and the involving H-bonding network between R109, D251 and water molecule (PDB: 6REW). (b) Isotopic labelling at ^{15}Nη-Arg and $^{13}C_9$-Tyr. The ^{15}N and ^{13}C are colored with blue and red, respectively. (c) 1D-TEDOR spectra (8 kHz MAS, 3968 scans) of [^{15}Nη-Arg, $^{13}C_9$-Tyr]-KR2 prepared in 30 mM NaCl, 25 mM Tris buffer (pH 8.5) with different mixing time (4 – 88 rotor periods). (d) TEDOR buildup curve of Cβ- and CO-Y247 and Cζ-Arg (n.a.). The curves are fitted using MATLAB program. The fitted dipolar coupling constant (Hz) and line broadening (Hz) are shown in the figure.

Table 22: Chemical shifts and calculated distances for ^{15}Nη-R109 - ^{13}Cβ/^{13}CO-Y247 and ^{15}Nη-R109 – n.a.Cζ-R109 based on dipolar coupling constant obtained from TEDOR buildup curve in comparison with the distances from KR2 crystal structure (4XTO). The T2 values used for the fitting are shown in the table.

	Chemical shift (ppm)	Dipolar coupling (Hz)	Calculated N-C distance (Å)	N-C distance from 4XTO (Å)	T2 used for fitting (ms)
Cβ-Y247	36.3 ± 0.7	99 ± 20	3.1 ± 0.3	3.7	3.4 (LB: 290 HZ)
CO-Y247	176.1 ± 0.5	86 ± 6	3.3 ± 0.1	3.8	12.0 (LB: 83 HZ)
Cζ-R109	157.8 ± 0.7	770 ± 200	1.6 ± 0.2	1.5	7.7 (LB: 130 HZ)

To observe any chemical shift perturbation of ^{15}Nη-R109 and ^{13}CO/Cβ-Y247 in the intermediates, 2D-TEDOR experiments were performed (Figure 57). The spectrum of the dark state shows the dipolar coupling between ^{15}Nη-R109 (71 ppm) and n.a. Cζ-Arg (158 ppm) and with ^{13}Cβ/^{13}CO-Y247 (36 and 158 ppm, respectively). After light activation at 110 K for 60 minutes, which usually leads to the formation of K/L-state, no substantial change in the 2D-TEDOR spectra was observed. A similar observation was seen also in the relaxed 190 K spectrum, suggesting no considerable perturbation at R109 in the early-state intermediates.

Interestingly, in the flash freezing spectrum (O-state trapping) the crosspeak intensity of ^{15}Nη-R109 - ^{13}Cβ-Y247 decreased substantially compared to the dark state (see the ^{15}N slice in Figure 57b), suggesting a perturbation in the O-state. However, ^{15}Nη-R109 - ^{13}CO-Y247 crosspeak intensity observed in the flash freezing spectrum remained similar to the dark state. This suggests a similar dipolar coupling strength/distance as in the dark state. For the R109 gate opening observed after the Na^+ uptake in the O-state by the MD simulation[9], a large side chain movement is expected and that would largely affect the dipolar coupling strength between ^{15}Nη-R109 and ^{13}Cβ-Y247 as well as ^{13}CO-Y247. Since the ^{15}Nη-R109 - ^{13}CO-Y247 dipolar coupling in the flash freezing spectrum is as strong as in the dark state, there is no sufficient evidence for the R109 gate opening. The decrease in intensity of ^{13}Cβ-Y247 could be due to the slight movement of the Arg guanidium group or the displacement of ^{13}Cβ-Y247, which resulted in the lower signal intensity. It should be noted here that the trapping was done according to the trapping protocol established with the ^{13}C-labelled retinal sample, by which the isomerization can be easily tracked.

An internal control using a similar sample but with ^{15}Nζ-Lys labeled and ^{13}C13-retinal is needed to prove the trapping efficiency of the O-state.

Even though the O-state trapping efficiency at our condition is not high, the data here hinted that R109 does not flip in the O-intermediate. Interestingly, the O-state crystal structure of KR2 reported recently by Kovalev, et al. also shows the binding of Na^+ between the S-N-D triad (S70, N112, and D116) with R109 side chain that is not flipped.[8] The flipping of R109 to release the Na^+ to the extracellular bulk solution should occur during the O- to dark state transition. Kovalev, et al. proposed two alternative ion release pathways based on the O-state crystal structure and MD simulation, showing the major ion release pathway occurs by the flipping of Q78 to the putative ion release cavity II (pIRCII) and the minor release through the putative ion release cavity I (pIRCI) which involves the flipping of R109 to open the pathway.[8] The hypothesis of these two release pathways is supported by the observation of biphasic O-state decay by flash photolysis (7.9 ms and 110 ms).[1]

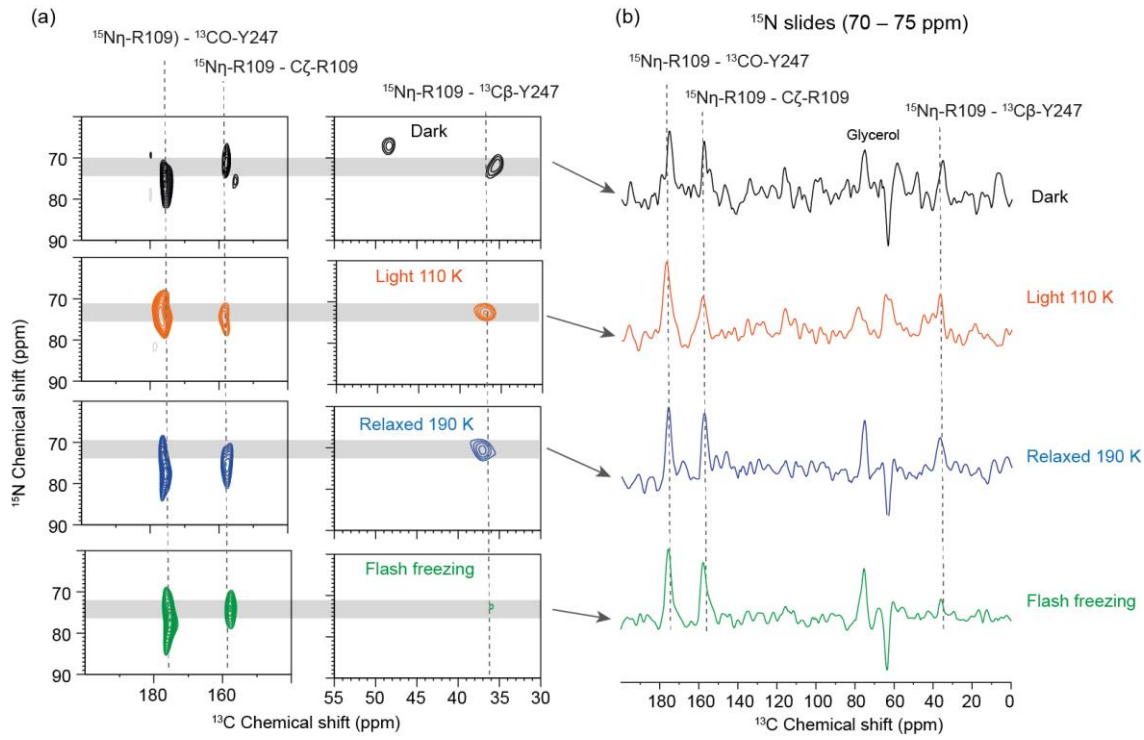

Figure 57: (a) 2D-TEDOR spectra of [$^{15}N_2$η-Arg, $^{13}C_9$-Tyr]-KR2 in 30 mM NaCl, 25mM Tris buffer, pH 8.5, in dark state (1792 scans) and after illumination at 110 K (3584 scans) and subsequently thermally relaxed to 190 K (3584 scans) and trapped by flash-freezing method (3584 scans). All the spectra were performed with 8 kHz MAS, 44 rotor periods REDOR mixing time, 30 increments and 250 μs increment delay in indirect dimension. (b) 1D-projections of ^{15}N chemical shift (70 – 75 ppm) are shown on the right side.

6.4. Probing of N112 in the NDQ motif

6.4.1. Introduction

N112 which is an important residue providing the internal transient Na^+ binding site and is part of the NDQ motif in KR2 was investigated using ^{13}C and ^{15}N unique pair labeling. The unique pair labeling technique is commonly used in ssNMR studies to selectively detect the signal from residues that are sequentially connected. The NMR experiment is performed by transferring the magnetization from ^{15}N of the former residue (i-1) to ^{13}C of the latter (i) residue. L111 (^{13}C-labeled) - N112 (^{15}N-labeled) is the only unique pair in the KR2 sequence. Therefore, the upcoming NMR signal can be unambiguously assigned to the residues. The signal from L111 and N112 in the dark state is acquired and compared to that of photointermediates.

6.4.2. Results and discussion

N112 is the key residue in the NDQ motif of KR2 and involve in the transient binding of Na^+ in the O-state.[8] The mutation of N112 to aspartic acid results in a conversion to H^+ pump and abolishes the Na^+ pumping activity. A question arose here whether there is any chemical perturbation at the N112 backbone during the photocycle, especially in the O-state, by which Na^+ was found to bind to N112 and the structure is altered from an expended to a compact conformation.[8] To selectively select the signal of N112 from other asparagine residues in KR2, a unique pair labeling approach was employed. KR2 sample was isotopically labeled with $^{13}C_6$-Leu and $^{15}N_2$-Asn. The signal from N112 and L111 can be unambiguously assigned since there is only one LN pair (L111N112) in the KR2 sequence.

The double cross polarization experiment, commonly called “NCO” experiment, was applied to transfer polarization from ^{15}N-Asn to the adjacent ^{13}C-Leu residue, and then further to other labeled ^{13}C-Leu via spin diffusion. The N(CO)CX spectrum of dark state shows only cross peak arising from L111N112 unique pair, with ^{15}N backbone resonance of N112 (120 ppm) and ^{13}C resonances of L111 at 176 (CO), 56 (Cα), 42 (Cβ) and 25-27 (Cγ/Cδ) ppm. The crosspeaks are very broad for the ^{15}N dimension. This large peak broadening could arise from the heterogeneity of the ^{15}N backbone resonance of N112. Interestingly, a large variation of N112 position was observed in three types (A, B, C) of pentameric crystals of KR2 (4XTO) and in the molecule D of type B crystal, the residues 111-114 are found in 3_{10}-helix-like conformation (the O111-N114 distance is 3.0 Å). This may explain the large linewidth observed on ^{15}N-N112 here.

The illumination protocols established on [U-^{15}N,$^{13}C_9$-retinal]-KR2 were applied to generate K/L- (light 110 K), L- (relaxed 190 K), and O-intermediate (flash freezing). However, no

chemical shift perturbation was observed both on the ^{15}N as well as ^{13}C dimensions (Figure 58). This suggests no substantial structural change at the nitrogen backbone of N112 and the carbon atoms of L111 in the intermediates within the limits of resolution here.

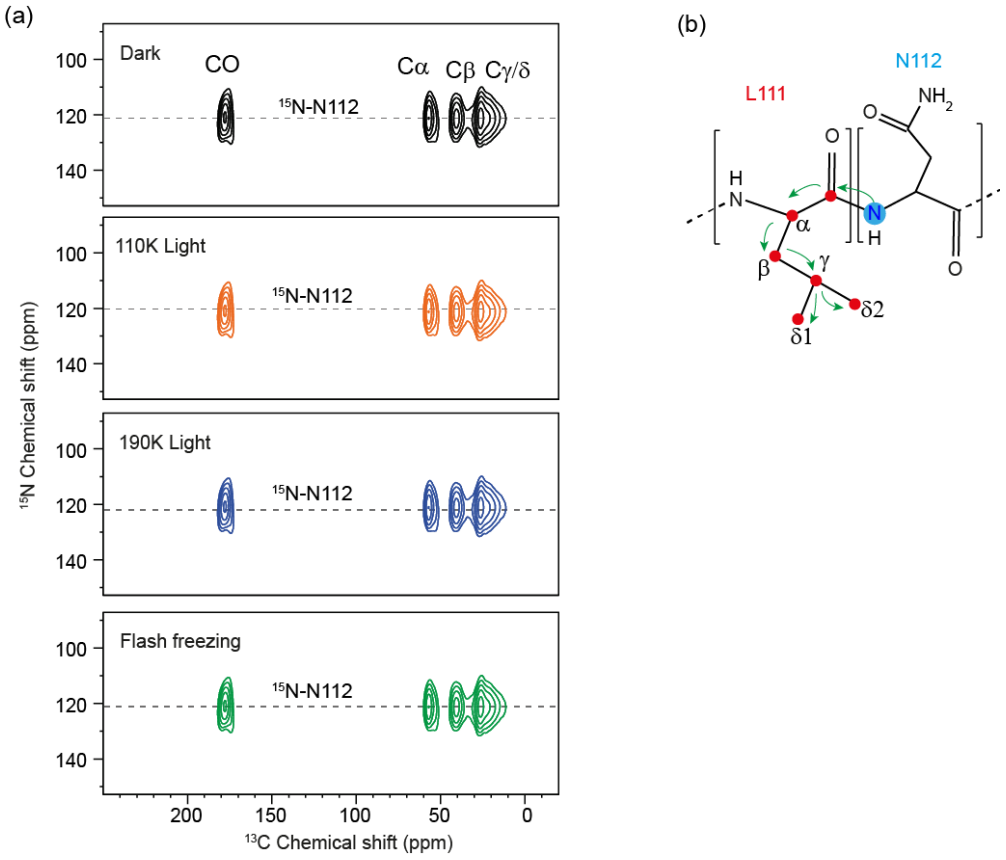

Figure 58: (a) NCOCX spectra of [$^{15}N_2$-Asn, $^{13}C_6$-Leu]-KR2 (30 mM NaCl) in dark state and after light activation at 110 K and relaxed to 190 K and by flash freezing. All the spectra were recorded with 2016 scans in direct dimension, 18 increments with 375 µs increment delay in indirect dimension and 20 ms mixing time. (b) Illustration of magnetization transfer in the N(CO)CX experiment for the L111N112 unique pair.

6.5. Summary and outlook

The data in this chapter demonstrates the applications of the DNP-enhanced ssNMR to address the opened questions regarding the structural alteration at the opsin in response to the retinal isomerization. The chemical shifts of K255 show the perturbations at $C\varepsilon_{K255}$ in K (ΔCS 1.7 ppm) and L (ΔCS: 3.2 ppm) state, as it is structurally most affected from the *all-trans* to *13-cis* isomerization. The chemical shifts confirmed the *15-anti* conformation in the dark, K- and L-state but with the slight twist around C15-SB bond to the direction of *15-syn* conformation in the L-state, which is in line with the chemical shift perturbation observed at C14 in L-state as described in the section 5.2.2. This suggests that the relaxation in the L-state might occur through the rotation around C15-SB bond.

The contact between the retinal ^{13}C12 and ^{13}C14 and ^{15}Nε-W113 in the dark state was detected based on the long-range dipolar coupling. However, for the intermediates, the couplings are too weak to be observed. For the investigation of the R109 gate, the data here shows the closing of the gate in K/L-state as well as in the O-state but with a small perturbation at Nη-R109 and Cβ-Y247 in the O-state. For the probing of N112 in the NDQ motif, no considerable large chemical shift perturbation of the backbone nitrogen was observed here under the resolution limit.

The investigation of opsin in photointermediates based on DNP-enhanced ssNMR is challenging due to two main factors. First, the cryogenic temperature required for the intermediate trapping and CE-DNP and the introduction of radicals cause the inhomogeneous and homogeneous line broadening, respectively, leading to the peak overlapping and making it difficult to identify the chemical shift perturbation in the intermediates when the electrostatic environment alteration is smaller than the resolution. Second, more than one photo-state often exists as a mixture due to their equilibriums, resulting in the complication of the acquired spectra and reduction of the detected signals. These point toward the requirement for the DNP resolution improvement. The resolution issue under the DNP condition could be improved using several approaches such as using a biradical that does not shorten the T2 relaxation[128] and the increase of magnetic field strength.[206]

Chapter 7: Heteronuclear Overhauser effect (hNOE) based DNP

7.1. Introduction

Dynamic nuclear polarization has emerged from the proof-of-concept phase and has become a powerful method to solve the sensitivity problem in ssNMR with a wide range of applications, ranging from biological molecules to organic and inorganic materials.[99] The commonly used DNP mechanism in the structural and dynamics studies of biomacromolecules is based on the Cross-effect (CE), in which the two coupled electrons of bis-nitroxide polarizing agents with a frequency difference that matches ^{1}H Larmor frequency, are commonly employed. The polarization is transferred from the electron spins (high gyromagnetic ratio) to hyperpolarize the coupled ^{1}H nuclear spin in the proximity and rapidly to the bulk ^{1}H via spin diffusion (SD). In conventional ssNMR, the hyperpolarization at ^{1}H spin is transferred to the nuclear spins with a low gyromagnetic ratio like ^{13}C and ^{15}N by cross polarization. However, Corzilius and coworkers have introduced recently the integration of ^{1}H-^{13}C heteronuclear Overhauser effect (hNOE), which has been used for a long time in solution-state NMR to DNP enhanced ssNMR.[207,208]

Based on Solomon equation in steady-state solution[134] the mechanism of hNOE can be described as a cross relaxation (CR) process as follows:

$$\varepsilon_{CR} = 1 - (\varepsilon_H - 1)\frac{\gamma_H}{\gamma_C}\frac{\sigma_{HC}}{\rho_C} \qquad (35)$$

where ε_{CR} is the ^{13}C enhancement caused by CR and ε_H is the polarization enhancement factor over the equilibrium of ^{1}H. γ_H and γ_C are the gyromagnetic ratio of ^{1}H and ^{13}C, respectively and σ_{HC} and ρ_C are ^{1}H-^{13}C cross relaxation and auto relaxation rates, respectively. The CR condition requires a considerable imbalance between ZQ and DQ relaxation rates, which happens efficiently in molecules with fast motions like the 3-fold symmetric methyl group.[209] At the temperature usually employed in CE-DNP, the methyl dynamics is in ns-µs range[210,211], providing an effective condition for the hNOE. The CR polarization transfer pathway results in a negative enhancement, which is distinguishable from the enhanced ^{13}C signal, derived from conventionally used cross polarization pathway and becomes even more efficient in the presence of paramagnetic nuclei such as Gd^{3+}.[207]

The use of dynamics-derived CR in the DNP hyperpolarization transfer pathway, called "specific cross-relaxation enhancement by active motions under DNP" (SCREAM-DNP)[15], has been demonstrated in several biological systems, including Interleukin-1 β[207], RNA aptamer[15], ribozyme[208], and GPR[176]. Aladin et al. applied active methyl groups bearing tetracycline as a

ligand to probe its binding and affinity to the RNA aptamer.[15] Mao et al. applied CE-DNP and ^{1}H-^{13}C hNOE based on ^{13}C-methyl labeled retinal dynamics to investigate the difference in molecular packing environment surrounding the chromophore in GPR resting and K-state.[176] Together with CE-DNP and Methyl ^{1}H-^{13}C hNOE, based on ^{13}C-^{13}C SD, the signal of the ^{13}C labeled spin nearby can be selectively hyperpolarized. Therefore, the hyperpolarization pathway through fast rotating methyl groups can be used to simplify the complicated NMR spectra. By using a sparsely labeled sample, the extraction of ^{13}C-^{13}C distances in a sub-nanometer range based on hNOE is also possible. Methyl dynamics are found overall in biological systems and have the potential to be effectively employed in DNP enhanced ssNMR framework.

Here, methyl dynamics derived SCREAM-DNP was applied to investigate the methyl groups of the β-ionone ring (C16-C18) and C13-methyl group (C20) of retinal incorporated in KR2. These methyl groups can provide potentially an effective pathway for the ^{1}H-^{13}C hNOE cross relaxation. The SCREAM pulse sequence[15] was applied to selectively filter the signal from the labeled Methyl group of retinal incorporated in KR2 to probe the electrostatic environment at these methyl groups in the dark state and photointermediates. Furthermore, the molecular packing in the retinal binding pocket of KR2 dark state and intermediates was also investigated similarly to the previous work on GPR by Mao et al.[176]

7.2. Result and discussion

7.2.1. β-ionone ring methyl group in KR2

10-18-$^{13}C_9$-retinal was incorporated in [$^{15}N\varepsilon$-Lys]-KR2 according to the procedure described in materials and methods. The [$^{13}C_9$-retinal, $^{15}N\varepsilon$-Lys]-KR2 was doped with 20mM AMUPol in the DNP matrix (d_8-glycerol: D_2O: H_2O = 6:3:1) similar to the usual standard sample preparation for CE-DNP. The SCREAM pulse sequence (Figure 59) was applied to detect the ^{13}C-labeled methyl resonance (C16/17- and C18-retinal) because the resonances of C16,17 and 18 in the [$^{13}C_9$-retinal, $^{15}N\varepsilon$-Lys]-KR2 sample are not detectable in the ^{13}C-CP spectrum due to the signal overlapping with natural abundance ^{13}C lipid signal and the spectrum recorded with double quantum filter (DQF) sequence also filters out the resonance peaks from ^{13}C16-18. The hyperpolarization from dipolar coupled electrons in AMUPol was first transferred to the adjacent ^{1}H spins via CE-DNP and distributed all over to the bulk ^{1}H via spin diffusion. Here, a train of ^{1}H and ^{13}C 90° pulses followed by a buildup time, τ, was applied instead of the usual CP step in the conventional MAS-NMR. During the buildup time, ^{1}H-^{13}C hNOE and ^{13}C-^{13}C SD are permitted, leading to the negatively enhanced polarization transfer to the ^{13}C spins of fast rotating methyl groups of C16/17 and C18. The spin diffusion allows further polarization transfer to the nearby coupled ^{13}C carbons,

C10-C15 for the longer buildup time (5 and 10 s, see Figure 59). The signal derived from these direct polarization pulses described here is the sum of ^{1}H-^{13}C hNOE and ^{13}C direct polarization. The ^{13}C-DP signal can be selected by applying a ^{1}H saturation pulses train during the buildup time (DP_{sat}). The hNOE derived signal can be mathematically obtained by subtracting the DP spectrum with the DP_{sat} spectrum.

Figure 59 shows the SCREAM-DNP spectra of [$^{13}C_9$-Retinal, $^{15}N\zeta$-Lys]-KR2 in the dark state at different buildup time. The negatively enhanced peaks were 180° phase adjusted for better visualization. For the 1s buildup time, only two peaks from the labeled retinal methyl group were observed. The peaks at 29.3 and 24.0 ppm were assigned to C16/17 and C18, respectively, according to our group's previously published 2D-PDSD spectra acquired at noncryogenic temperature (31.5 ppm for C16, 30.0 ppm for C17, and 23.7 ppm for C18).[6] The C16/C17 was not resolved under the DNP condition. The chemical shifts agree well with the numbers reported earlier with the deviation ±1 ppm. For the longer buildup time, the signals of C10-C15 from ^{13}C-^{13}C spin diffusion came up with the two broad signals around 178 and 20 ppm, which could likely be attributed to natural abundance ^{13}C CO and methyl group from lipid or protein, respectively according to their chemical shifts. The signals from C10-C15 in the dark, K- and L-state are assigned according to the data in chapter 5 (see Figure 33). The intensity of C16/17 together is less than that of C18 at the same buildup time, indicating the different rotation rates between these methyl groups. The observation of C16/17 and C18 methyl groups at 1 s indicated that these methyl groups are rotating fast enough to allow an hNOE signal buildup. The hNOE buildup curves were obtained by plotting the peak intensities (peak area) vs. buildup time (Figure 60). By fitting the curve with an exponential function, buildup time constants of 4.5 s and 4.3 s for C18 and C16/17, respectively, were gained (Table 23, Figure 60). The buildup time for C18 is slightly faster than C16/17, suggesting a faster methyl rotation at the position. It has to be noted here that it is also possible that the signal from C16/17 comes from either C16 or C17 or both.

Interestingly, for GPR, only the signal from C18 was observed whereas in KR2 the signals from both C16/17 and C18 were visible at the same buildup time (1 s).[176] This suggests a more relaxed packing of the *β*-ionone ring in KR2 compared to GPR. From the pentameric crystal structure (6REW), KR2 has a large retinal binding pocket containing 4 water molecules. The retinal binding pocket of microbial rhodopsins is usually characterized by bulky amino acids like tryptophan and tyrosine. Interestingly, at the position of W138 and W159 which located near the *β*-ionone ring in BR and GPR, respectively, G171 is found in KR2, suggested that the *β*-ionone

ring in KR2 is not tightly packed and this may contribute to the high rotation of the C16/C17 methyl group in the *β*-ionone ring (see Figure 61).

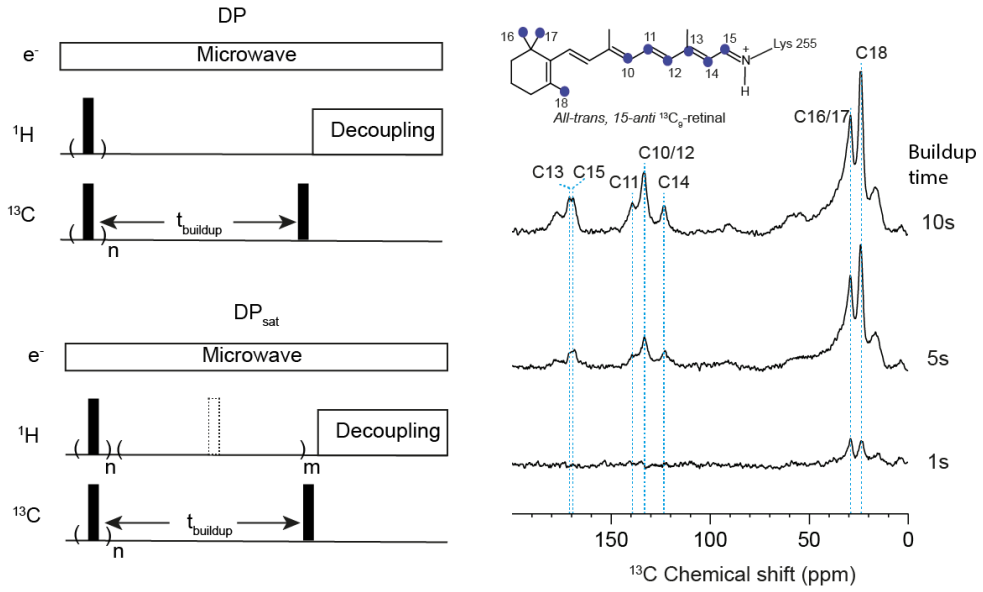

Figure 59: Heteronuclear Overhauser effect based polarization transfer (SCREAM) on [$^{13}C_9$-Retinal, $^{15}N\zeta$-Lys]-KR2 prepared in 100 mM NaCl at 1 s, 5 s and 10 s buildup time. The SCREAM pulse sequence with (DP) and without (DP_{sat}) ^1H saturation pulses is shown on the left side. For the long buildup time, the polarization was transferred from fast rotating methyl group to the nearby labeled ^{13}C via spin diffusion. The signal from C16/17 and 18, which is usually covered under lipid signal, can be selectively detected. hNOE results in a negative enhancement. The negative signals are inverted here for better visualization.

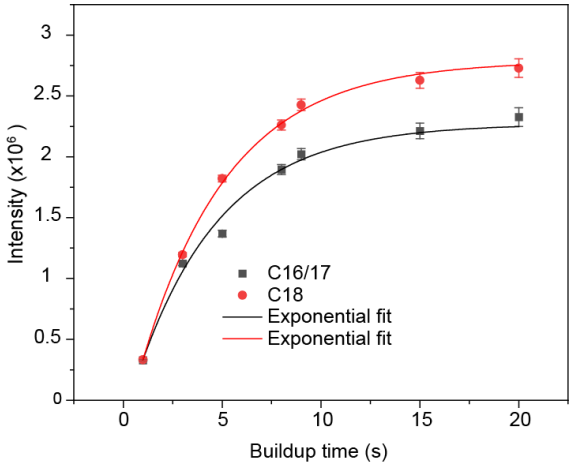

Figure 60: Heteronuclear Overhauser buildup curve of *β*-ionone methyl group (C16/17 and C18) in [$^{13}C_9$-Retinal, $^{15}N\zeta$-Lys]-KR2 prepared in 100 mM NaCl Tris buffer, dark state at 105 K. The intensity (peak area) was monoexponentially fitted and shown in solid lines. The single data point was acquired with 2048 number of scans. The corresponding buildup time constant is shown in Table 23.

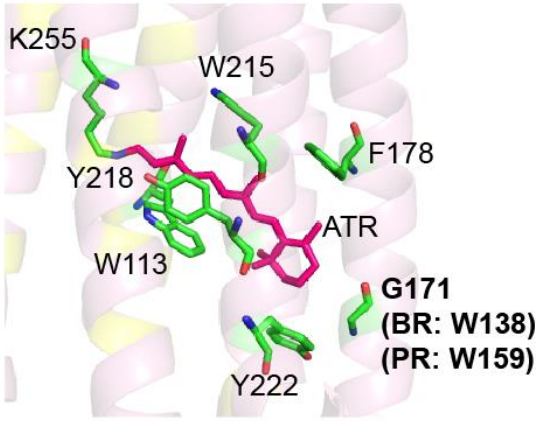

Figure 61: Illustration of KR2 retinal binding pocket (PDB: 6REW) showing the G171 residue near the β-ionone ring and the corresponding W138 in BR and W159 in PR.

Table 23: Chemical shift and buildup time constant of the β-ionone methyl group signals (C16/17 and C18) in $^{13}C_9$-Retinal, $^{15}N\zeta$-Lys]-KR2 prepared in 100 mM NaCl Tris buffer, dark state at 105 K.

KR2	C16/17		C18	
	Buildup time constant (s)	Chemical shift (ppm)	Buildup time constant (s)	Chemical shift (ppm)
Dark	4.3 ± 1.4	29.3 ± 0.5	4.5 ± 0.4	24.0 ± 0.5

To probe the electrostatic change at the β-ionone ring in photointermediates K, L, and O, SCREAM-DNP spectra were acquired on cryo-trapped photointermediate states (see materials and methods) for the buildup time 1 s, 5 s, and 10 s. After light activation at 110 K to generate K- and L-intermediates (see chapter 5), new peaks corresponding to C11 of K- (145.8 ppm) and L-state (144.8 ppm) and C14 of L-state (119.2 ppm) came up, indicating the successful trapping (Figure 62, light 110 K - 10s). The full buildup curves for the light 110 K and relaxed 190 K could not be measured due to experimental time constraints. Instead, it was attempted to obtain good spectra for distinct buildup times to identify chemical shift and peak intensity changes, which would still allow a qualitative interpretation of altered hNOE dynamics.

However, no chemical shift perturbation was observed for C16/17 and C18 methyl groups. The same observation was made for the spectrum recorded after relaxing the intermediates to 190 K, which usually leads to a shift of the population from K to L. The flash freezing spectrum (O-

intermediate trapping) also does not exhibit any considerable change of C16/17 and C18 resonance. However, it should be noted that the trapping efficiency of the O-state is relatively low (see Figure 43), so it would be anyway difficult to identify small changes. The unperturbed chemical shift of C18 in KR2 K/L-state is similar to what is observed in GPR K-state studied by Mao et al.[176]

The differences observed between KR2 dark and K/L-state (light 110 K) spectra are that the peak height ratio between C18 and C16/17 changes (Figure 62). In the dark state, the ratio of C16/17 to C18 (C16/17:C18) is nearly 1 for 1 s buildup time and less than 1 (~0.8) for 5 s and 10 s buildup time with a similar linewidth. However, in the trapped K/L-state spectra, the ratio increased from 1 to 2 for 1 s buildup time and to nearly 1 for 5 s and 10 s. This suggests a dynamic change at C16/C17 and C18 methyl groups in K- and L-state.

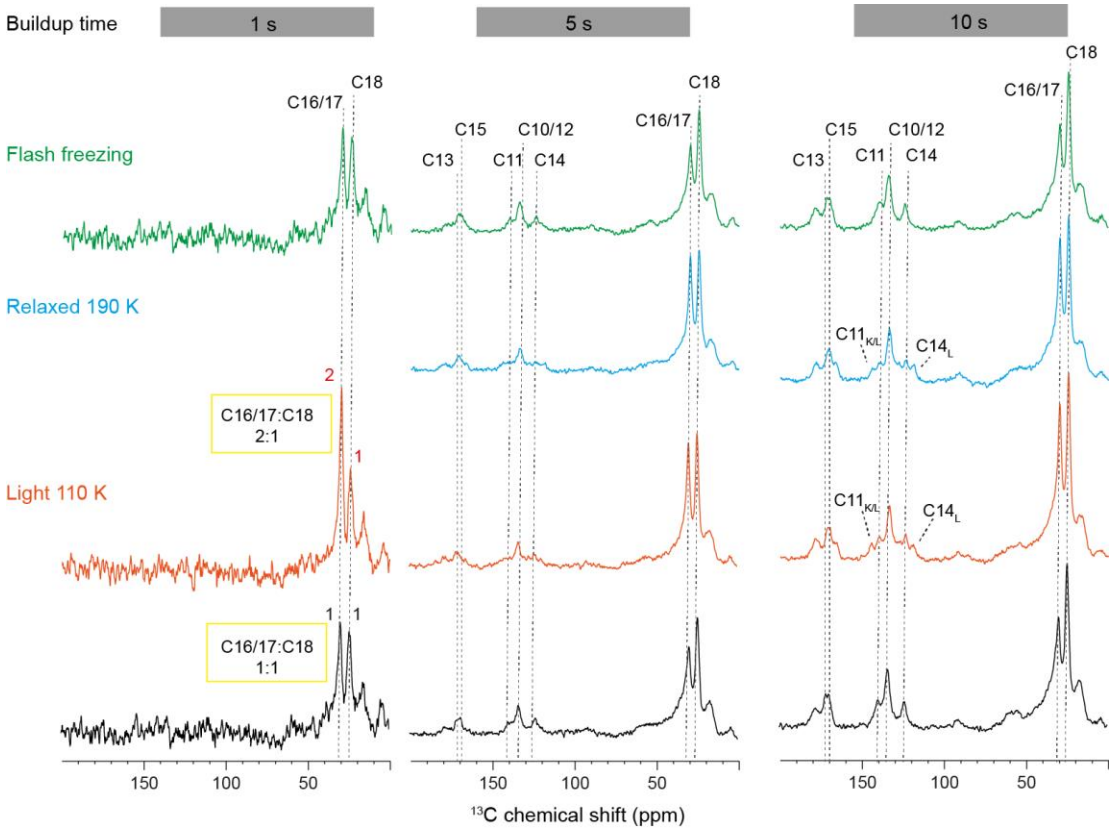

Figure 62: SCREAM-DNP enhanced spectra of [$^{13}C_9$-retinal, $^{15}N\zeta$-Lys]-KR2 in 100 mM NaCl Tris buffer (pH 8,5) in the dark state, after illumination at 110 K for 60 minutes (light 110 K), thermally relaxed to 190 K (relaxed 190 K) and trapped by flash freezing method (illuminated outside magnet and quickly freeze in liquid nitrogen) for 1s, 5s, and 10s buildup times. Noted that the relaxed 190 K spectrum for 1s buildup time is not acquired due to technical reasons.

It is likely that after illumination C16/17 methyl groups are in the environment that allows a faster rotation compared to the dark state (see Figure 63). The retinal binding pocket is constructed with a number of bulky aromatic residues like W113, W215, F178, Y222, Y218. C18 is located near the F178 and the C16/C17 are located near Y222 and W113. From the time-resolved crystal structure at 800 fs + 2ps and 1 ns + 16 ns, the displacements of C16/17 and C18 methyl groups were observed as well as the displacement of F178, Y222, and W113 after the full isomerization (800fs – 16ns). These displacements would cause the different methyl dynamic rotation in the early-state intermediate observed here.

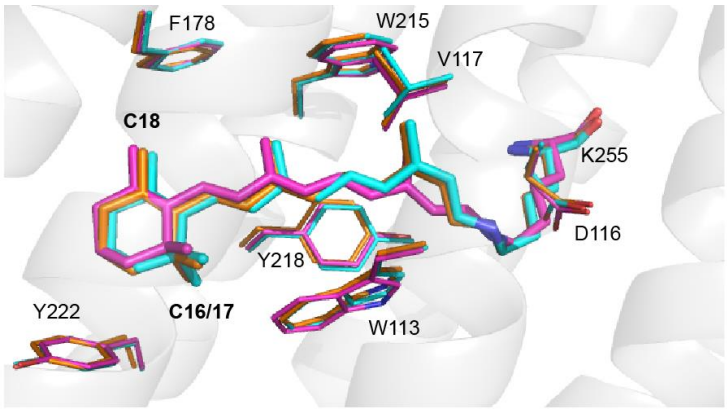

Figure 63: The displacement of C16/17 and C18 and the surrounding aromatic residues observed by TR-SFX at 800 fs + 2 ps, 6TK5 (orange) and 1 + 16 ns, 6TK4 (cyan) compared to the dark state, 6TK6 (magenta).

The study of the *β*-ionone ring in visual rhodopsin by ssNMR showed the chemical shift (CS) perturbation at C16, 17, and C18 in Meta II intermediate (380 nm) compared to the Rhodopsin (498 nm). The ΔCS (Rho-Meta II) is 2.0 and -7.3 ppm for C16 and C17, respectively but nearly no change (-0.7 ppm) for C18. The authors suggested the ring inversion in the Meta II state. However, from the data acquired for KR2 here, no considerable chemical shift change at C16/17 signal was observed in the illuminated spectra, indicating that there is no ring-opsin interaction when switching from G- to K/L-state.

Instead, the β-ionone ring would rather play an important role in color tuning because of the strong electronic charge transfer character in the retinal excited state.[195,212] In the excited state, the positive charge at protonated Schiff base is transferred to the cyclohexene ring. If a negative charge is placed near the cyclohexene ring, the energy level of the excited state will be stabilized compared to the ground state, leading to the red-shifted color. Moreover, it also affects the

primary photoreaction since the photoisomerization occurs through the relaxation from the excited state through the conical intersection (CI).[20]

The role of the *β*-ionone ring in the early excitation process in rhodopsin was shown by crystal difference electron density map.[213] Interestingly, microbial and visual rhodopsin are different not only at the *all-trans* and *11-cis* conformation in the resting state, respectively but also at the *β*-ionone ring C6-C7 single bond. Bovine rhodopsin has a 6-s-cis conformation[214,215] whereas, in microbial rhodopsin, the 6-s-trans conformation is preferred, even though the 6-s-cis conformation is more stable in solution[18,216]. Because of the steric interaction between C8-hydrogen and methyl group hydrogen at C5, the *β*-ionone ring plane in visual rhodopsin is then twisted relative to the polyene chain, inhibiting the positive charge transfer from the pSB to the cyclohexene ring in the excited state.[20] In contrast, this charge transfer to the cyclohexene ring is allowed for the *6-s-trans* conformation found in microbial rhodopsin. The ssNMR study of visual rhodopsin suggested a similar *6-s-cis* conformation in both inactive (*11-cis*) and active state (*all-trans*), however, the resonances change of C16 and C17 observed in the transition from Rho to MII state indicated the inversion of ring conformation.[215] The energy barrier for the ring inversion at the *β*-ionone ring in animal rhodopsin was calculated to be around 5-6 kcal/mol.[217] For the microbial rhodopsin, numerous studies have been performed to understand the role of the *β*-ionone ring through substitutions of retinal with retinal analogs[218–221]. The *β*-ionone ring in bacteriorhodopsin is not tightly bound to the opsin binding site as in the case of visual rhosopsin[222] and was suggested that it is presumably responsible for the slower photoisomerization (0.5 ps for BR)[223] as compared to visual rhodopsin (200 fs)[224]. Similarly, for KR2, the data acquired here also shows no interaction between the methyl group of the *β*-ionone ring and the opsin in the photointermediates.

7.2.2. Probing the C20 methyl dynamics in KR2

C20 is the methyl group bound to C13 in the retinal. It plays an important role in the photocycle of rhodopsins. The chemical shift of C20 is very sensitive to the *all-trans* to *13-cis* isomerization and vice versa and can be employed as an indicator for intermediates trapping. As demonstrated by Mao et al.[176], the hNOE based methyl-DNP can be successfully employed to probe the molecular packing of the retinal binding pocket in GPR dark and K-state. The temperature dependent buildup time exhibits the slow kinetic behavior of C20 in the GPR K-state whereas in GPR dark state the kinetics of C20 is in the fast regime (faster than ^{1}H-^{13}C ZQ/DQ transition). To probe the rotating dynamics of C20 methyl group in KR2 similar as in GPR, hNOE based DNP experiments were performed. Figure 64 shows the C12, C13, and C20 resonances obtained from

the DNP-enhanced methyl ^{1}H-^{13}C hNOE spectra of [$^{13}C_3$-retinal, ^{15}Nζ-Lys]-KR2 at 1 s, 5 s and 10 s buildup time in that the polarization from protons is transferred to ^{13}C methyl group via hNOE and then to the coupled ^{13}C nuclei via spin diffusion. The resonances agree well with the data from the conventional CP and DQF experiment reported in chapter 5. For the long buildup time (5 s and 10 s), some other signals from natural abundance ^{13}C were also observed due to the efficiency of the unspecific spin diffusion.

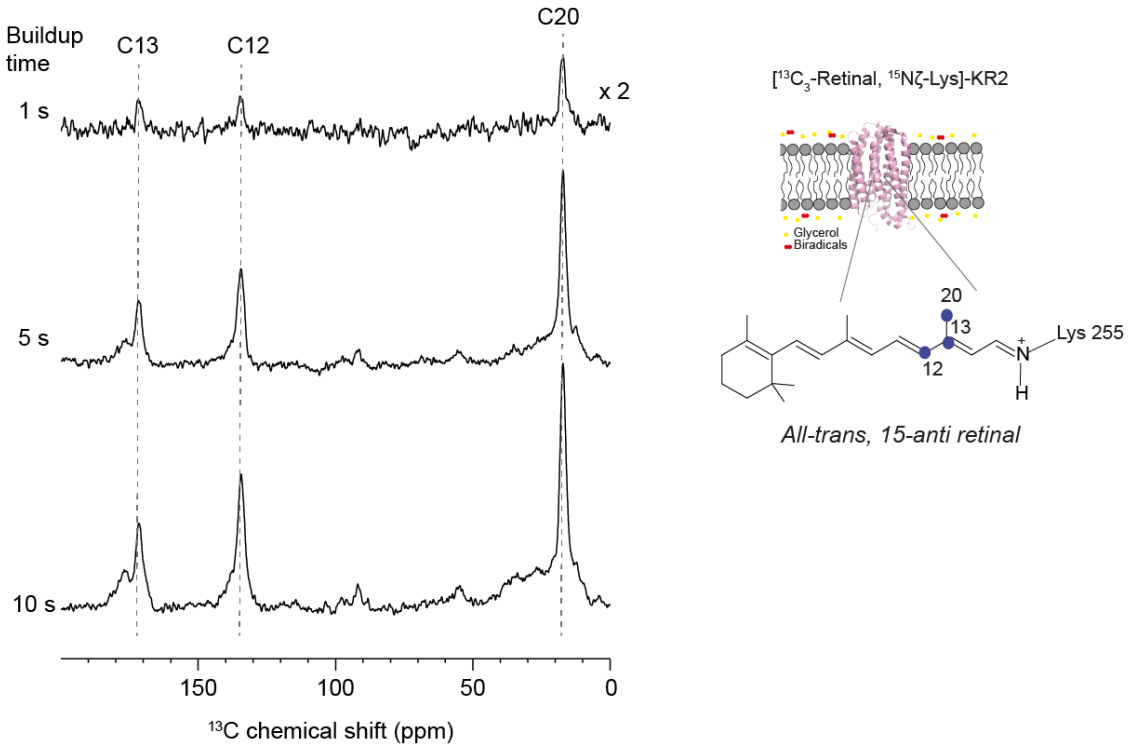

Figure 64: DNP-enhanced methyl ^{1}H-^{13}C hNOE (SCREAM) spectra of [$^{13}C_3$-retinal, ^{15}Nζ-Lys]-KR2 in 100 mM NaCl Tris buffer (pH 8.5) using 1 s, 5 s and 10 s buildup time, after 180° phase adjustment to obtain a positive spectrum for the convenient reading. The spectra show the polarization from ^{1}H to ^{13}C of the methyl group via hNOE and further to the coupled ^{13}C nuclei via spin diffusion.

The dynamic of the C20 methyl group was probed by measuring temperature dependent polarization buildup curves as the CR rate is dependent on the molecular motion of the methyl group. The hNOE buildup curves of C20 methyl group at 106 K, 120 K, and 130 K exhibit a temperature dependence, by which the buildup rate became slower at the elevated temperatures (Figure 65). The hNOE buildup time constant can be obtained by fitting the buildup curve with an exponential function, showing a longer buildup time constant for the higher temperature. The hNOE buildup occurs most efficiently when the methyl reorientation rate approaches the range of ^{1}H or ^{13}C Larmor frequencies. Therefore, the temperature dependent data here exhibits the fast

reorientation of methyl group relative to the ^{1}H (~400 MHz)/^{13}C (~100 MHz) Larmor frequencies. This is similar to the result reported for GPR.[176]

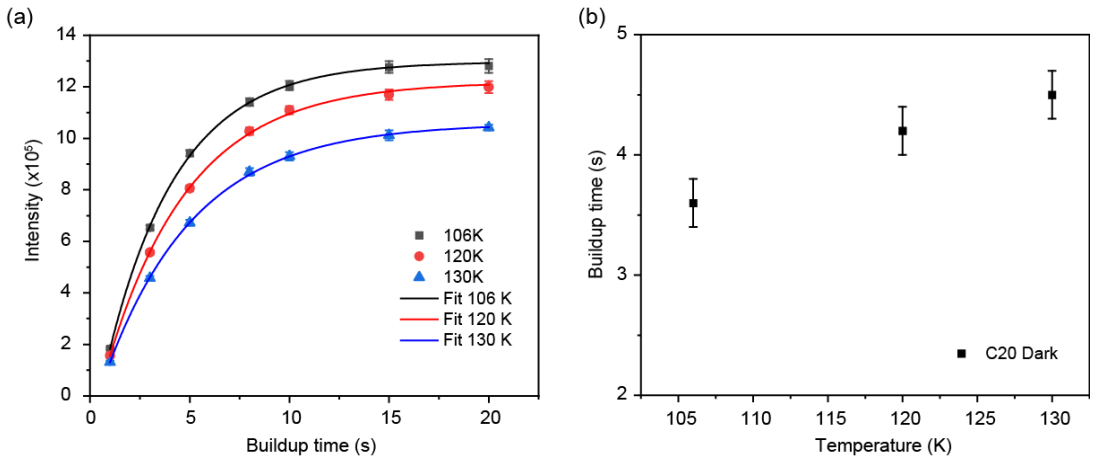

Figure 65: hNOE buildup of C20 retinylidene methyl group (a) Comparison of hNOE buildup curves for retinal C20 methyl group in KR2 dark state at 106 K,120 K and130 K. The solid line shows the exponential curve fitting. (b) Temperature dependent hNOE buildup time (s) for retinal C20 methyl group in KR2 dark state.

Table 24: hNOE buildup time constant for retinal C20 methyl group in KR2 dark state at various temperature (K).

Temp	Buildup time constant (s)
106	3.6 ± 0.2
120	4.2 ± 0.2
130	4.5 ± 0.2

The dynamics of C20 methyl in the K/L-state was further probed based on hNOE. Figure 66 shows the differences in the spectra acquired using the DQF and SCREAM pulse sequences. Interestingly, the retinal ^{13}C resonances of KR2 K-state were not visible at all in the SCREAM spectrum (1s buildup time) whereas the signals were observable in the DQF spectrum. The main difference between the DQF and SCREAM experiments is that in DQF the polarization was transferred from ^{1}H through cross polarization (CP) step while in the SCREAM pulse sequence the ^{1}H-^{13}C polarization transfer is based on hNOE and hence depends on the local dynamics. This demonstrates the slow methyl rotation dynamics of C20 in the K-state, which is the first intermediate directly formed after retinal isomerization, by which the protein does not have time to adjust its structure to accommodate the *13-cis* retinal conformation. For the L-state, the resonances of C12, C13, and C20 were observed, indicating the faster rotation of the C20 methyl

group as compared to the K-state. The result supports the chemical shift perturbation analysis which showed the retinal conformational relaxation in the L-state (see section 5.2.2.2). The L-state C20 resonance can be easily distinguished from the remained dark state based on its chemical shift. The peaks acquired at different buildup times were therefore deconvoluted (Appendix III) and the intensities gained were plotted against the buildup time (Figure 67). After fitting with an exponential function, the buildup time constant for the L-state C20 methyl group of 3.7 ± 0.2 s was obtained. The buildup time constant of the C20 in L-state is approximately the same as in the dark state (3.6 ± 0.2 s). This further suggests that the energy stored in the retinal was transferred to the surrounded protein and the structural rearrangement following the isomerization already occurs in the L-state.

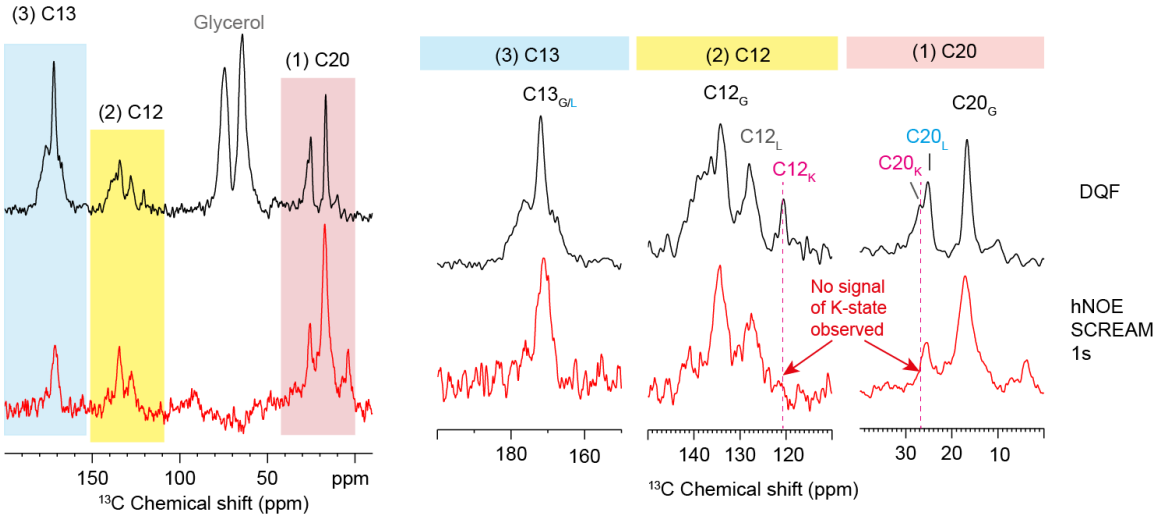

Figure 66: Comparison of NMR signals acquired using DQF and SCREAM (buildup time 1 s) experiments for [$^{13}C_3$-Retinal]-KR2 in 100 mM NaCl Tris-buffer (pH 8.5). The signals of C20 as well as C12 and C13 for the KR2 K-state are not observed in SCREAM spectrum whereas the L-state signal is visible, indicating the obviously slow C20 methyl rotation in the K-state.

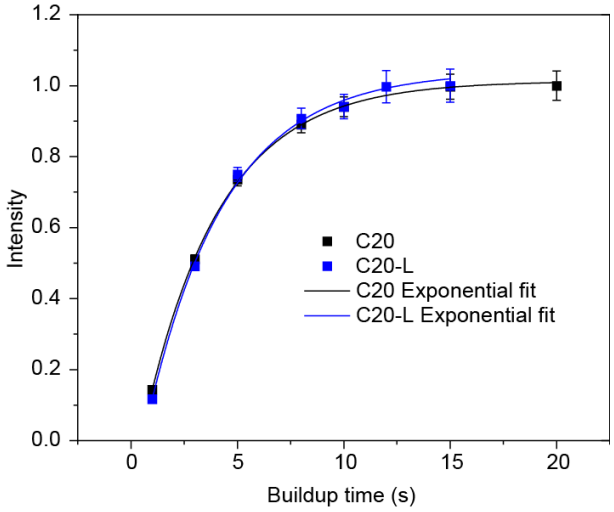

Figure 67: hNOE buildup curve (106 K) of C20 in L-state (blue) compared to that of in the dark state (black). The solid lines show the monoexponentially fit with the buildup time constant of 3.6 7 ± 0.2 s for the dark state and 3.7 ± 0.2 s for the L-state. The intensities were adjusted by dividing the deconvoluted peak area with the highest intensity for each photointermediates.

7.3. Conclusion and Outlook

The hNOE based DNP experiment is very useful for the detection and dynamics studies of methyl groups in biological samples. Here, the selective detection of the retinylidene methyl group (C16/17, C18, and C20) by which the detection of signals is usually hindered by the overlapping with natural abundance signals of lipid in CP spectra was demonstrated using the SCREAM experiment. C16/17, as well as C18, do not exhibit any chemical shift perturbation after light activation, suggesting that there is no considerable structural change in this region in intermediates.

For C16/17, the interpretation of dynamic data in KR2 intermediates is not straight forward, since there is more than one ^{13}C-labeled methyl group that could serve as a polarization hotspot. The spin diffusion at cryogenic temperature is very efficient and thus complicates the analysis of buildup time for each methyl group. Nevertheless, the data acquired for C16/17 in K/L-intermediates here hinted at the dynamic change upon light activation of KR2 (Figure 62). For further studies, the dynamics of C16/17 and C18 can be studied using a specific retinal labeling scheme that has only one methyl group labeled to avoid an ambiguous interpretation.

Based on the hNOE mechanism, it is possible to extract dynamic information of the C20 methyl group in KR2 photointermediates using [$^{13}C_3$-Retinal, 15Nζ-Lys]-KR2 sample. In contrast to dark and L-state, the C20 methyl dynamic of K-state is restricted as shown in the absence of K-state signal in the SCREAM spectrum (Figure 66). For the L-state, C20 methyl dynamics have returned

to the same level as in the dark state as demonstrated from the similar hNOE buildup time. The data indicate the relaxation of retinal chromophore distortion in the L-state and suggest the energy transfer to the surrounding protein during the K to L transition.

Chapter 8: ^{23}Na NMR and investigation of bound sodium ion

8.1. Introduction

Sodium ions are indispensable for many physiological and biological processes. Their concentration gradients across cellular membranes with very low Na^+ concentration inside and high concentration outside the cells is maintained and controlled by specific channels and pumps.[225] The ion gradient is employed by the cells to drive processes such as glucose uptake through glucose-sodium cotransport[226], sodium dependent phosphate transport[227], neurotransmitter sodium symporters[228,229], and transduction of neuronal signals through alteration of membrane potentials[230]. The ion can also serve for example as an electrolyte to stabilize surface charges of proteins and nucleic acids and is involved in the structural formation of G-quartet structure of telomeric DNAs[231].

^{23}Na is the second most abundant NMR active nucleus in biological tissues after ^{1}H, making it an attractive target for biological studies based on magnetic resonance methods including MRI.[232] It has a high natural abundance (100%) and a relatively high gyromagnetic ratio (7.081×10^7 rad·s^{-1}·T^{-1} compare to 4.107 for ^{1}H). ^{23}Na is a quadrupole nucleus with a spin quantum number of 3/2 resulting in four Zeeman energy levels (±3/2, ±1/2).[233] Quadrupole nuclei possess an electric quadrupole moment which interacts with the electric field gradient (EFG) originating from asymmetries of electron charge distributions surrounding the nuclei. This quadrupole coupling adds another term to the Hamiltonian in addition to the Zeeman, dipolar and chemical shift interactions (see details of the Hamiltonians in chapter 2.1). The quadrupole moment (Q) for ^{23}Na is relatively moderate (10.4 fm^2) The quadrupole coupling can be large or small depending on the degree of distortion of charge distribution and symmetry of the environment surrounding the nuclei. For the compound with high molecular symmetry such as NaCl(s), the EFG is in principle zero and thus a narrow resonance peak can be observed.

Usually, the quadrupolar coupling is 1 to 2 order of magnitude larger than the dipolar coupling and chemical shift anisotropy.[73] The quadrupole coupling affects the Zeeman splitting to the first and second order in the perturbation and average Hamiltonian theories; both are orientation dependent. There are three possible single quantum transitions: -3/2 → -1/2, -1/2 →1/2 and 1/2 → 3/2. The first order term is quadratic in I_z and does not affect the symmetric transition (-1/2 →1/2) but renders the side transition (-3/2 → -1/2 and 1/2 → 3/2). As a result, the side transitions will be broadened, while the central transition yields a much sharper signal relative to the side

transitions. The second term is linear in I_z and affects all the transitions. MAS can eliminate the first order term but does not remove the anisotropy of the second quadrupolar term. The residual second order perturbation, which is proportional to the square of the internal perturbation divided by the main Zeeman interaction, often broaden the central transition whenever the EFG is present ($\Delta \propto \omega_Q^2/\omega_0$, where $\omega_Q = \frac{e^2qQ}{h}/2S(2S-1)$ and ω_0 is the Larmor frequency). Therefore, the studies of quadrupole nuclei are challenging not only in the term of experimental setup but also in the interpretation of results.

A number of averaging methods such as variable angle spinning (VAS)[234], double rotation (DOR)[235], dynamic angle spinning (DAS)[236], and multiple quantum magic angle spinning (MQMAS)[237] have been developed to address the problems of the second order quadrupole interaction.[238] Among these, MQMAS has often become the method of choice to remove the undesirable second order quadrupole interactions for half-integer quadrupole nuclei and to extract isotropic chemical shifts and quadrupolar coupling parameters since it does not require additional hardware beyond MAS-NMR. In MQMAS, a non-selective pulse is applied to excite a multi-quantum (MQ) coherence which can be converted to observable single quantum (SQ) coherence by a second pulse that selectively selects the particular coherence of interest using phase cycling.[239–241] The development of MQMAS enables numerous ssNMR for studies on half-integer quadrupole nuclei in chemical and materials sciences.[238,242] However, not many applications of ^{23}Na NMR are performed in the studies of biological systems.

Early high-resolution MAS-NMR on quadrupole nuclei was reported in 1982, showing the possibility to detect ^{23}Na, ^{27}Al, and ^{51}V in various inorganic systems.[243] For the applications of ^{23}Na MAS-NMR in biological samples, Wong and Wu et al and Rovnyak et al. employed ^{23}Na NMR for the structural and kinetics studies of ions in complex with ionophores, G-quartet DNA, and guanosine 5´-monophosphate (5´-GMP). [231,239,240,244–246] Data on sodium ion binding can be gained based on conventional one pulse MAS-NMR.[244] By applying MQMAS, isotropic chemical shift, quadrupolar coupling, and asymmetric parameter could also be extracted.[245] Moreover, titration and competitive titration experiments can be performed to probe the binding affinities among various cations.[246] Recently, ^{23}Na MAS-NMR was applied to probe bound Na^+ in the bacterial neurotransmitter sodium symporter, LeuT in both wild type and mutants.[247]

Solution-state NMR studies of bound sodium ions were often hampered by intrinsically poor resolution due to the small chemical shift range and large linewidth, and the fast cation exchange between free and bound states, which prevents the observation of separate signals for different

cation binding sites.[240] The anionic paramagnetic shift can be used to distinguish between the intracellular and extracellular Na^+ as demonstrated for the probing of ion transport in erythrocytes and gramicidin.[248,249] Tightly bound alkali cations with 3/2 spins such as ^{23}Na, ^{39}K, and ^{87}Rb were thought to be invisible due to their rapid quadrupole relaxation which causes NMR signals to become too broad to be observed.[250] However, Wong and Wu et al reported the observation of these nuclei in two G-quadruplex structures using solution-state NMR.[231,240] In their study, the inversion recovery experiment was employed to suppress the large signal from free Na^+. The signals from Na^+ ion bound nonspecifically to the surface and Na^+ at a specific binding site are well separated. Their chemical shifts agree well with the value from ssNMR experiments.

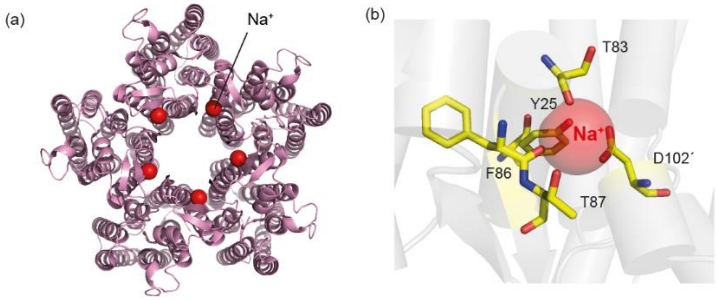

Figure 68: Crystal structure of KR2 in the pentameric form (4XTO) and the extracellular Na^+ binding site at the protomer interface, involving Y25, T83, T87, F86 of one protomer and D102' of the adjacent protomer.

In this chapter, ^{23}Na MAS NMR was applied to study the bound Na^+ at the protomer interface in the pentameric structure of KR2 (Figure 68). The MQMAS experiment is not necessary to be applied here since the quadrupolar interaction in the KR2 samples here is negligible due to either the high dynamic or symmetry or both in the samples. A temperature scan experiment was performed to probe the chemical exchange and line shape at different temperatures. A T1 measurement was employed to probe the dynamics of the specific and non-specifically bound sodium ion. T1 was obtained by an inversion recovery experiment, which proved to be useful for suppressing the signals of the free and unspecific surface-bound Na^+ in the KR2 sample. Specific Na^+ titration binding was shown by the absence of bound Na^+ signal in the Y154A mutant by which the pentameric structure was disturbed and the bound Na^+ at the protomer interface in the pentameric structure is absent. A competitive titration was performed to probe the binding affinity against K^+ and Li^+. The results shown here demonstrate the general feasibility to detect ^{23}Na bound to KR2 by MAS-NMR.

8.2. Results and discussion

8.2.1. Detection of Na^+ by ^{23}Na MAS-NMR

It is known from the previous FTIR studies and the pentameric crystal structure (4XTO) that KR2 possesses a Na^+ binding at the extracellular protomer interface. The question arose whether it is possible to detect this bound Na^+ by ^{23}Na MAS-NMR. To address this question, one pulse excitation experiments were applied to observe ^{23}Na signals in 100 mM NaCl aqueous solution, liposome DMPC:DMPA (9:1) in 100 mM NaCl Tris buffer, KR2 wild type and its Y154A mutant reconstituted in DMPC:DMPA liposome in 30 mM NaCl Tris buffer (pH 8.5) (Figure 69). The Y154A-KR2 which has a monomeric structure and therefore lacks the interprotomer Na^+ binding sites was compared to the wild type. All the spectra were referenced to NaCl(s) at 7.0 ppm. The ^{23}Na signal of 100 mM NaCl aqueous solution shows a narrow resonance at 0.04 ppm (linewidth 10.8 Hz) whereas it shifts to -0.09 ppm (linewidth 12.5 Hz) in the liposome sample. The peak observed in the liposome sample comes from the free Na^+ and Na^+ bound to the liposome surface, which are called now "bulk Na^+". The small resonance shift of 0.09 ppm in liposome sample from Na^+ in aqueous solution should arise from the slightly higher electrical shielding at the liposome surface in Tris buffer (pH 8.5) as compared to the ions in aqueous solution (pH 7). According to Gouy-Chapmann theory [251], a solid surface exposed to a fluid can be described by a double layer structure. The first layer consists of ions absorbed on the surface due to chemical interaction. The second layer is called a diffuse layer where the movement is influenced by the electrical attraction (Coulomb force) and thermal motion. The charge distribution and the electrical potential decrease exponentially as a function of distances from the surface.

The ^{23}Na spectrum of KR2 reconstituted in the liposome and in 30 mM NaCl buffer exhibits another broad peak at -0.33 ppm in addition to the bulk ^{23}Na peak. This signal is absent in the Y154A mutant by which the extracellular protomer interface Na^+ binding site is absent as the pentameric structure was disturbed (Figure 69). This suggests that the signal arises from a bound Na^+ at the protomer interface of KR2. The result is in line with the pentameric crystal structure, in which sodium ions were observed at the protomer interface between Y25, T83, T87, and F86 of one protomer and D102of the adjacent protomer. The resonance difference between the unspecific bulk Na^+ and KR2 bound Na^+ is 38 .09 Hz. The observation of a resolved bound Na^+ signal separating from the bulk Na^+ suggests that the exchange of these ions must be in a slow-exchange range and the residence time of Na^+ bound to KR2 must be much more than $(\frac{1}{38\times 2\pi})\ Hz$ = 4.2 ms at 275 K.

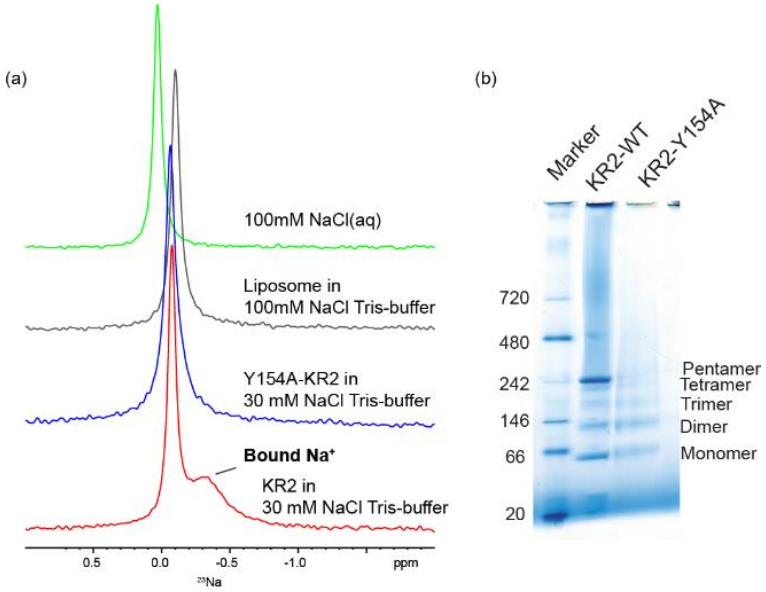

Figure 69: Detection of KR2 bound Na^+ (a) ^{23}Na MAS-NMR spectra acquired at 600 MHz spectrometer, 275 K, 4 µs excitation pulse for 100 mM NaCl in aqueous solution (pH 7), DMPC.DMPA (9:1) liposome in 100 mM NaCl Tris buffer (pH 8.5), KR2 reconstituted in the liposome in 30 mM NaCl Tris buffer (pH 8,5) and monomeric mutant Y154A-KR2 prepared in the same condition as KR2 wild type. MAS was set to 2 kHz for NaCl solution and 10 kHz for liposome and KR2 samples (b) BN-PAGE of KR2 in detergent micelles, showing a pentameric structure, in comparison to Y154A mutant which exhibits mixed oligomeric states.

The resonance and linewidth of both bulk Na^+ and KR2 bound Na^+ depend on the temperature (Figure 70a). The peaks are partially overlapped. For the analysis, the peaks were therefore deconvoluted to extract the chemical shifts and linewidths of each peak (Figure 70b, Table 25). The resonances of both bulk and KR2 bound Na^+ shifted to the high field upon increasing temperature from 260 to 290 K. This could likely be due to the change in electrical potential at the proteoliposome surface at the elevated temperature. The linewidth of KR2 bound Na^+ became broader as the temperature was increased from 260 K to 275 K and to 290 K (Figure 70c). This suggested the shift from a slow exchange to an intermediate exchange.

Oppositely, the linewidth of the bulk Na^+ signals became narrower (11.1 Hz, see Table 25) as the temperature was increased from 260 to 275 K and 290 K, by which the linewidth for 275 K and 290 K are in a similar range. The narrowing of the bulk Na^+ peak at the elevated temperature could be explained by the faster dynamics at the temperature (275 and 290 K).

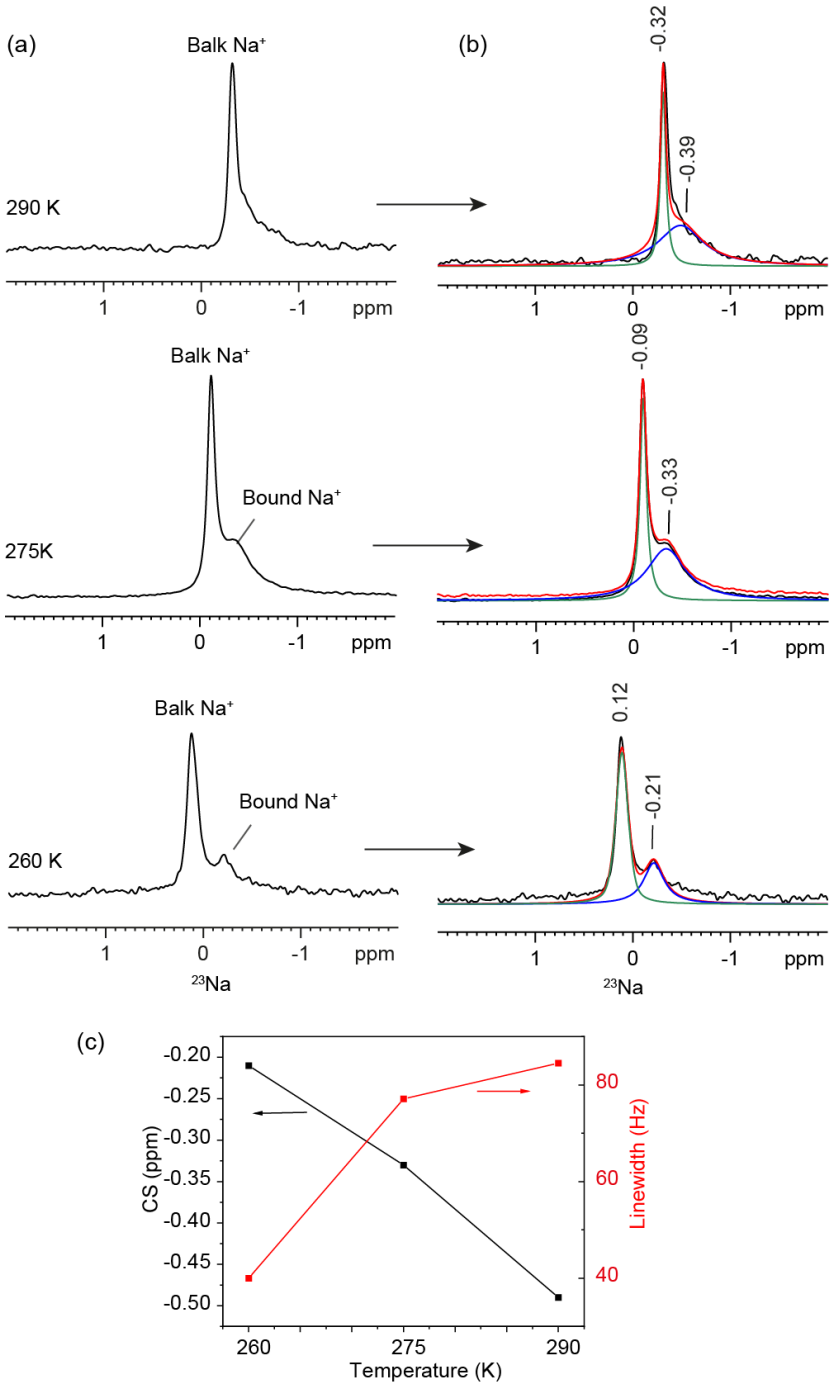

Figure 70: ^{23}Na MAS-NMR temperature scan experiment for (a) KR2 reconstituted in DMPC:DMPA (9:1) liposome in 30 mM NaCl Tris buffer (pH 8.5) acquired at 600 MHz spectrometer, MAS 10 kHz at temperature 260 K, 275 K and 290 K with one-pulse excitation (4 µs), 1024 scans, 150 ms acquisition time, 1 s recycle delay. (b) The deconvolution of ^{23}Na MAS-NMR spectra using solid line analysis in TOPSPIN program, (c) chemical shift (CS, ppm) and linewidth (Hz) change of KR2 bound Na^+ signal as an effect of temperature (K).

Table 25: Resonances (δ) of bulk Na^+ and KR2 bound Na^+ obtained from the deconvoluted spectra and resonance difference (Hz) between bulk Na^+ and KR2 bound Na^+ for 260 K, 275 K and 290 K. The reading error was estimated to be 0.02 ppm (3.17 Hz). The spectra were acquired at 600 MHz spectrometer (^{23}Na frequency 158.7 MHz)

Temp (K)	Bulk Na^+			KR2 Na^+		
	δ (ppm)	Linewidth $\Delta\nu_{1/2}$ (Hz)	$1/\pi\Delta\nu_{1/2}$ (ms)	δ (ppm)	Linewidth $\Delta\nu_{1/2}$ (Hz)	$1/\pi\Delta\nu_{1/2}$ (ms)
260	0.12	23.6 ± 2	13.5	-0.21	40.0	7.9
275	-0.09	12.5 ± 3	25.5	-0.33	77.1	4.1
290	-0.32	13.8 ± 3	23.1	-0.49	84.5	3.8

8.2.2. Na^+ titration

A Na^+ titration experiment was performed at 850 MHz NMR spectrometer to investigate Na^+ binding to KR2. To keep the amount of protein constant, the same pellet was used for all [NaCl]. After each NMR measurement, the sample was unpacked from the rotor by centrifugation. The sample was washed two times with Tris buffer with different NaCl concentrations and then final pelleting using ultra-centrifugation (310801 x g). The supernatant was removed from the sample as much as possible to reduce the large signal of free Na^+. The spectrum of 0 mM [Na^+] does not exhibit any strong signal (Figure 71), indicating no considerable Na^+ in the prepared sample. At high [Na^+], three types of Na^+ signals are observed in the spectra: The peak at 0 ppm is assigned to the free aqueous Na^+, the peak at -0.2 and -0.3 ppm are assigned to unspecific surface Na^+ and KR2 bound Na^+, respectively. The peaks were deconvoluted to obtain the peak area of each Na^+ using solid line analysis in TOPSPIN program (Figure 71b). The chemical shift and the linewidth were kept constant for each type of Na^+ in all deconvoluted spectra.

Upon increasing [Na^+] from 30 mM to 60 mM, 100 mM, 150 mM and 200 mM, the signal of KR2 bound Na^+ increased gradually and reached a saturation at 100 mM NaCl concentration (Figure 71c). The fitting of the titration curve with a sigmoidal binding model provides a K_d value of 32 ± 3 mM. The number is higher than the value (11.4 ± 0.8 mM) reported in the literature based on FTIR spectroscopy.[1] To improve the accuracy of the measurement, the experiment should be repeated using a smaller concentration increase step (10 mM) and at a lower temperature (260 K) to improve the line broadening and with a T1-filter experiment to suppress the unwanted signal of the free Na^+. Note that the deconvoluted signal intensities of free Na^+ increase accordingly to [NaCl] in the buffer (Figure 71d). However, the signal intensities of the

unspecific surface Na^+ varied. This variation might arise from the difficulty to control exactly the amount of buffer in the sample.

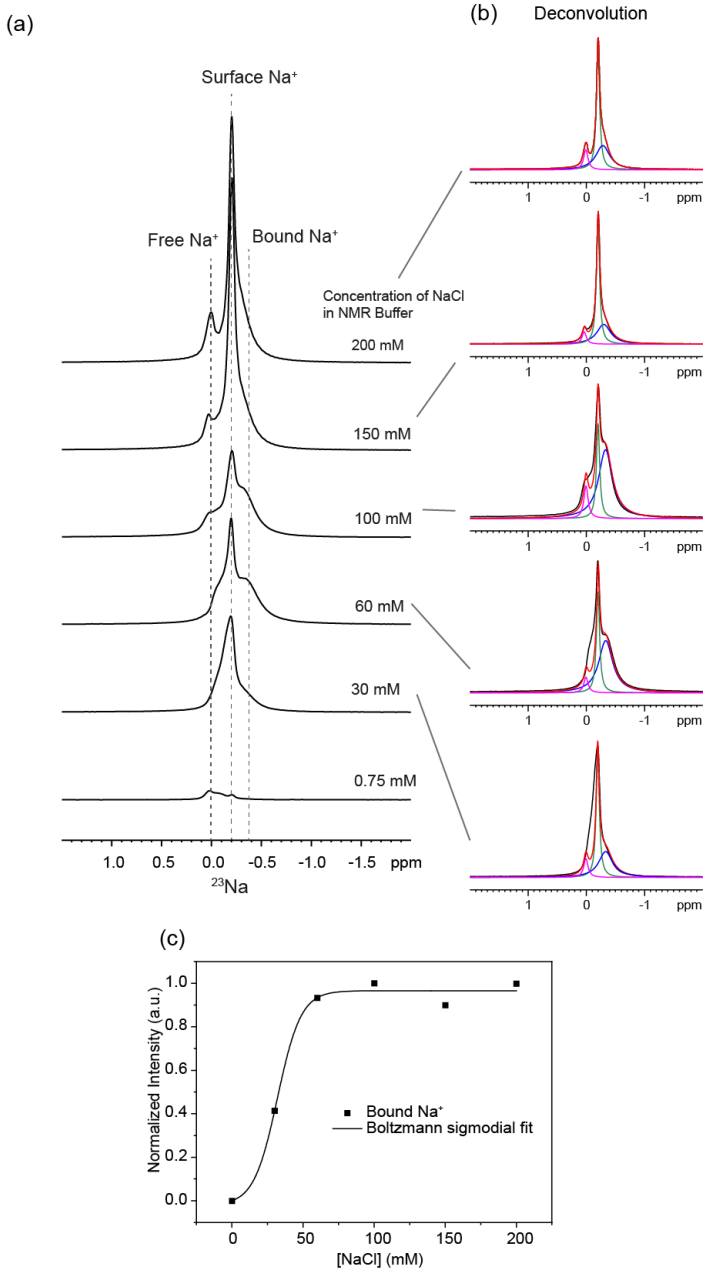

Figure 71: Na^+ titration experiment (0 – 200 mM) for KR2 reconstituted in DMPC:DMPA (9:1) in Tris buffer (pH 8.5). (a) ^{23}Na spectra with varied [NaCl], acquired with 51200 scans at 850 MHz spectrometer, 275 K, 10 kHz MAS, using one-pulse excitation experiment (1.2 µs pulse length, 100 ms acquisition time, 1s recycle delay.) (b) Deconvolution of the spectra in (a) using solid line analysis in TOPSPIN with a fixed chemical shift (CS) and line broadening (LB) for bound Na^+ (CS: -0.3 ppm, LB: 65 Hz), surface Na^+ (CS: -0.2 ppm, LB: 15 Hz) and free Na^+ (CS: 0.009 ppm, LB 20 Hz). (c) Plot of the normalized intensities of bound Na^+ signals at different Na^+ concentrations. The data is fitted with a sigmoidal curve and a K_d value of 32 mM was determined.

8.2.3. Competitive binding against K^+ and Li^+

To investigate whether KR2 bound Na^+ at the protomer interface can be substituted by other monovalent cations, a competitive titration with K^+ and Li^+ was performed at a 600 MHz spectrometer. The [Na^+] was kept constant at 100 mM while for [K^+] and [Li^+] was varied from 0 mM to 100 mM and 200 mM. The competitive binding spectra for KCl and LiCl are shown in Figure 72a and c, respectively. The spectra exhibit both bulk (-0.09 ppm) and bound signal (-0.3 ppm) of Na^+. For the competitive binding with K^+, a high concentration of K^+ is necessary to replace the bound Na^+. The broad signal of bound KR2 at -0.33 ppm decreased slightly at [Na^+]:[K^+] ratio of 1:1 while it was strongly reduced at [Na^+]:[K^+] ratio of 1:2. Since the signals of bound and bulk Na^+ partially overlapped, a deconvolution was performed (Figure 72b). The decrease of bound Na^+ signal with the increase of KCl concentration is shown in Figure 72e. The graph suggested that the Na^+ binding is more preferred and an excess of K^+ is needed to replace it. For Li^+ competitive binding, no reduction of the bound Na^+ signal was observed for neither 100 mM nor 200 mM [LiCl]. This suggests that Li^+ does not replace bound Na^+ in KR2.

It should be noted here that the KR2 bound Na^+ signals in the presence of K^+ exhibit a larger linewidth (~120 Hz) than in the case of Li^+ and previously observed linewidth (~65 Hz). This extraordinary line broadening may arise from the inhomogeneous magnetic field along with the rotor. For a clear conclusion, the experiment should be repeated with careful control. However, due to the time limitation of this thesis, the experiment was not repeated.

Otomo et al. demonstrated the allosteric communication between the extracellular binding site and the retinal Schiff base using visible absorption and resonance Raman spectroscopy.[252] The authors observed absorption change depending on the concentration of Na^+ and K^+ but not for Cl^- and reported K_d values of 49.3±11.0 and 36.3±6.2 mM for Na^+ and K^+, respectively. This is in line with our data, showing the binding of K^+ to KR2 at a high concentration.

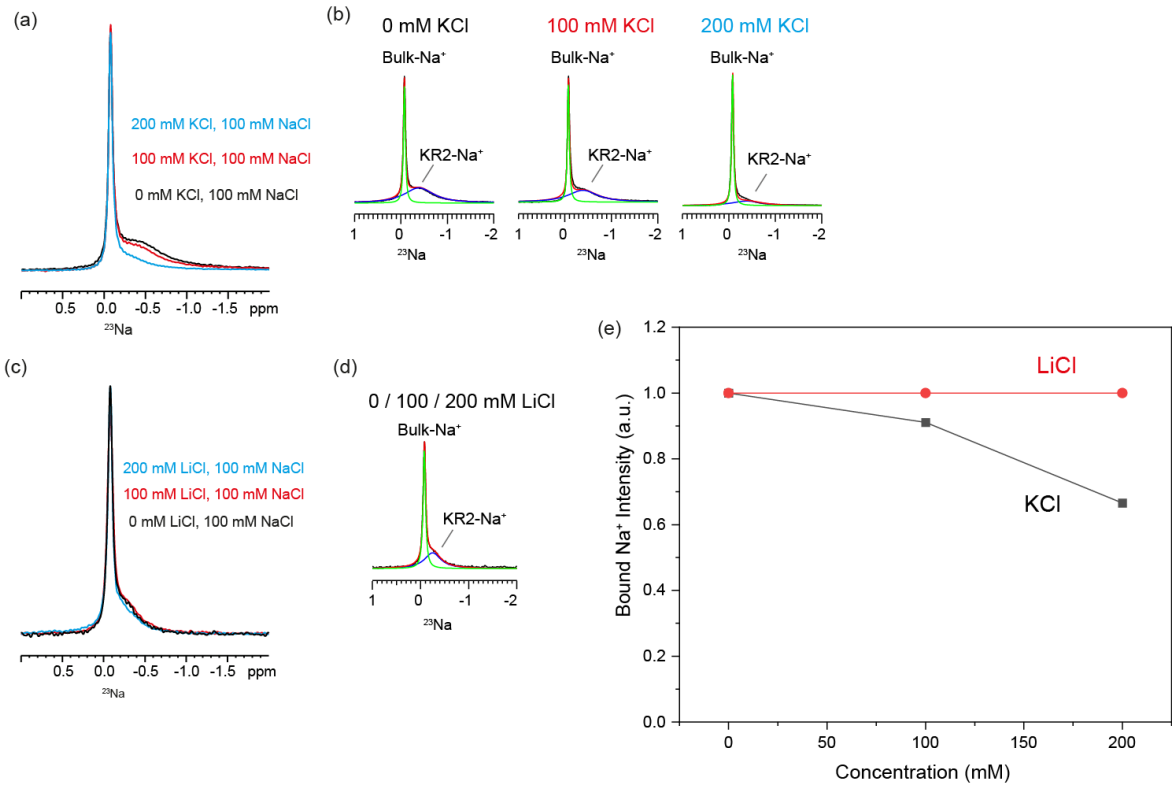

Figure 72: Competitive titration experiments of Na^+ against K^+ and Li^+ in KR2. The [NaCl] was kept constant at 100 mM NaCl and the [Na^+]:[K^+] and [Na^+]:[Li^+] ratios were varied from 1:0 to 1:1 and 1:2. ^{23}Na spectra of K^+ (a) and Li^+ (c) competitive binding experiments acquired at 600 MHz spectrometer, 275 K, 4 mm Zirconium dioxide rotor, using one-pulse excitation experiment (10240 scans, 4 µs pulse, 150 ms acquisition time, 1s recycle delay). (b) and (d) Deconvolution spectra of ^{23}Na spectra for K^+ (b) and Li^+ (d) using solid line analysis in TOPSPIN program. (e) The bound Na^+ peak intensities obtained from deconvoluted spectra in (b) and (d) for 0, 100 and 200 mM KCl and LiCl. For comparison, the intensities of 0 mM KCl and LiCl were adjusted to 1.

8.2.4. Suppression of bulk Na^+ signal

Since the signal of nonspecific bulk Na^+ interferes and hinders the detection of specific KR2 bound Na^+. A T1-filter experiment could be useful to suppress the unwanted bulk Na^+ signal. T1 values of both bulk and KR2 bound Na^+ were measured by an inversion recovery experiment. Since the resonances of these two resonances are close to each other, the peak areas are together integrated, and the recovery signals are fitted biexponentially to reduce the error from the deconvolution (Figure 73a). For 0.1 ms delay time, both signals from bulk and bound Na^+ were negative, however, after a delay time of 1.8 ms the signal from bound Na^+ turned positive whereas the signal from bulk Na^+ was still inverted (Figure 73b), indicating that the T1 of KR2 bound Na^+ is shorter than that of bulk Na^+. From the biexponential fitting, T1 values of 38.4 ± 0.5 ms and 5.7 ± 0.2 ms are obtained. As the T1 of bound Na^+ is shorter than that of bulk Na^+,

the shorter T1 value of 5.7 ms is attributed to KR2 bound Na^+ and *vice versa* for bulk Na^+ (38.4 ms).

The T1 relaxation time of KR2 bound Na^+ is more than 6 folds shorter than that of bulk Na^+. Therefore, the signal from the bulk Na^+ can be suppressed using an inversion recovery experiment (T1-filter).[240] For that, the interpulse delay was set so that the signal from bulk Na^+ is at the zero crossing while the KR2 bound Na^+ is relaxed back to positive. As shown in Figure 73c, the signal of the unspecific bulk Na^+ that interfere with the bound Na^+ became very small at the delay time of 30 ms and was not observable at 27 ms delay time. The suppression of the bulk Na^+ signal is important when the signal of the interested bound Na^+ is much smaller than the bulk signal and its resonance is not well separated.

Table 26: T1 relaxation time of bulk Na^+ and KR2 bound Na^+ and their corresponded chemical shift (ppm) and linewidth (Hz). The data was acquired at 600 MHz spectrometer, 275 K, with KR2 reconstituted in DMPC:DMPA (9:1) in 30 mM NaCl Tris buffer (pH 8.5).

Signal	δ (ppm)	T1 (ms)
Bulk Na^+	-0.09	38.4 ± 0.5
KR2 bound Na^+	-0.33	5.7 ± 0.2

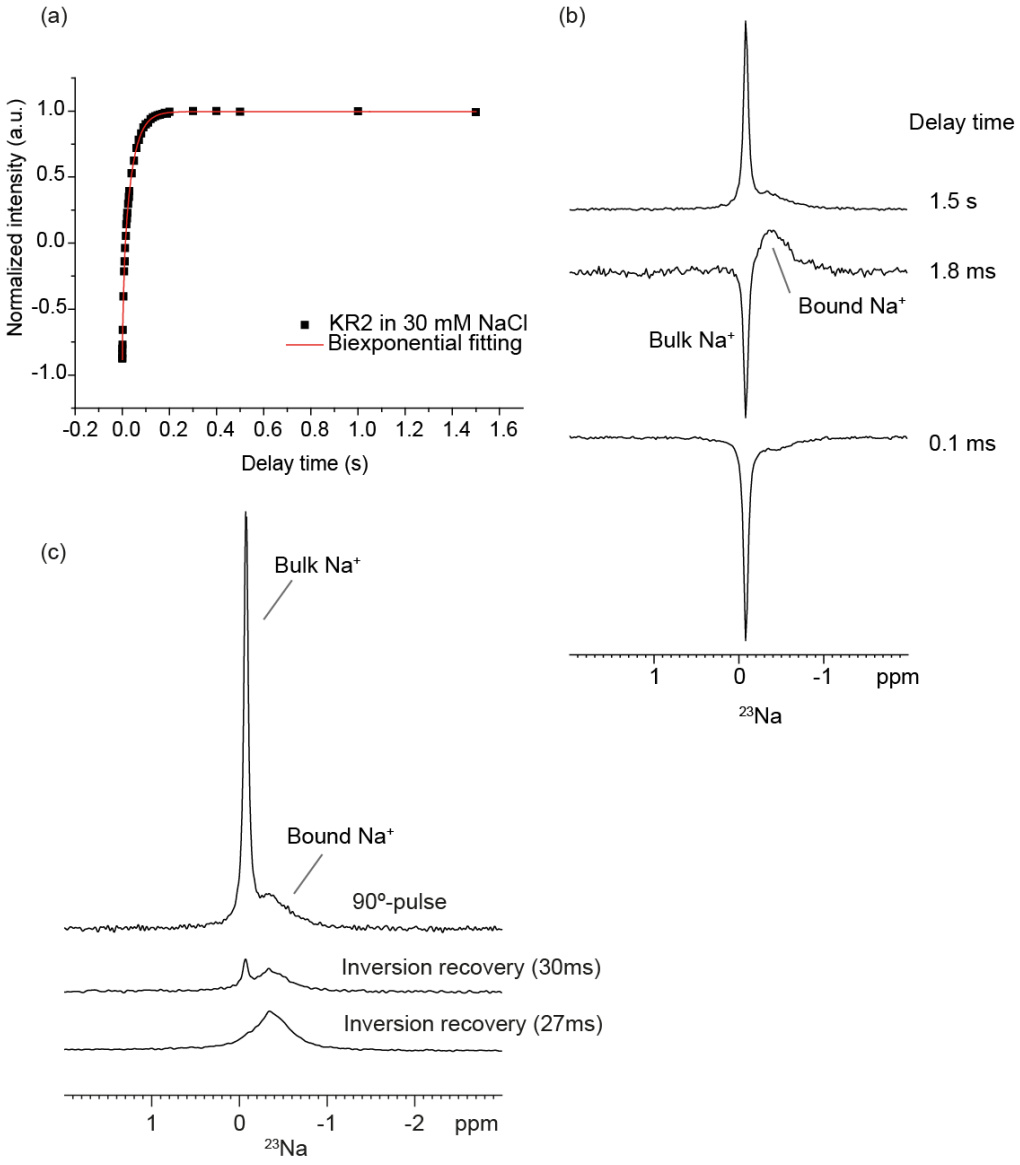

Figure 73: Inversion recovery experiment for KR2 reconstituted in DMPC:DMPA liposome (9:1) in 30mM NaCl Tris buffer (pH8.5) acquired at 600 MHz spectrometer, 275 K. (a) Biexponential fitting of Na^+ signal intensities (bulk and KR2 bound Na^+) at different delay time (0.1 ms – 1.5 s), (b) ^{23}Na inversion recovery spectra using 0.1 ms, 18 ms and 1.5 s delay time, (c) bulk Na^+ signal suppression using inversion recovery experiment with 27 and 30 ms delay time in comparison to one pulse (90°) experiment.

8.3. Conclusion and outlook

As a proof of concept, KR2 bound Na^+ at the protomer interface can be detected using ^{23}Na MAS-NMR. The bound Na^+ was found to be in slow exchange with bulk Na^+. The Na^+ binding affinity was probed by NaCl titration and competitive titration against K^+ and Li^+. The binding of Na^+ is more preferred and a very high K^+ concentration is required to replace the binding whereas it cannot be replaced by Li^+ even at a high Li^+ concentration. The T1-filtered experiment was proved to be able to suppress the unwanted bulk Na^+ signal. The suppression of bulk Na^+ signal is necessary for the detection of a small Na^+ signal of interest that may be embedded under the unwanted large signal of bulk Na^+.

The bound Na^+ signal detected here does not exhibit a quadrupolar coupling as seen from the moderate linewidth and the MQMAS is not necessary. However, as an outlook for the study of a system with a larger quadrupolar coupling, an MQ-MAS experiment may be applied to extract isotropic chemical shift and anisotropy parameters. Moreover, a 2D exchange experiment can be considered for the further study of an exchange between bulk Na^+ and bound Na^+. For further studies, ^{23}Na MAS-NMR could be applied to detect the transient bound Na^+ at the internal binding site N112 and D116 in O-intermediate, which however O-state trapping efficiency needs to be proved.

Chapter 9: Conclusion and Outlook

The main objective of this thesis was to study the photointermediates of light-driven Na^+ pump KR2 by DNP-enhanced ssNMR. At the starting time of this study which was only 3 years after the discovery of KR2, only limited knowledge about the photointermediates and the molecular mechanism was available. Only the first crystal structures in the dark state had been reported. In order to study the photointermediates which occur on a very fast time scale (nanosecond to millisecond) by ssNMR, an efficient rapping procedure had to be developed. Here, K-, L- and O-states of KR2 could be successfully trapped and verified by absorption spectroscopy. The trapping of K- and L-state was similar as demonstrated previously for BR. The specificity of KR2 is the trapping of the L-state at a temperature as low as 110 K, suggesting the low energy barrier between K- and L-states in KR2. The trapping of O-intermediate in which Na^+ uptake occurs on the millisecond timescale was challenging and the population of the trapped state in this thesis was limited. In the future, a much higher NaCl concentration (> 100 mM) could improve the trapping efficiency but needs to be balanced with the restrictions imposed by the NMR requirements. The flash freezing method used for the O-state trapping here is necessary because it allows the uptake of Na^+ in a non-frozen condition. This type of trapping may also be employed to trap the late state in other microbial rhodopsins as well, by which the nonfrozen condition during the illumination is preferred.

DNP-enhanced ssNMR can be precisely used to determine the retinal conformation and the electrostatic environment at the Schiff base nitrogen in KR2 as also was demonstrated in BR, PR, and ChR2. Based on the chemical shifts, the retinal conformation of K- and L-state was found to be *13-cis, 15-anti*, by which the energy storage along the retinal polyene chain in the K-state was observed in term of chemical shift deviation from the model compound, followed by the subsequent relaxation in the L-state. The C14 chemical shift in the L-state exhibited a different trend from the observed value on other retinal carbon atoms as compare to the K-state and indicates the slight movement in the *13-cis, 15-syn* direction but still remains the *13-cis, 15-anti* when the protein is relaxed. The chemical shift perturbation pattern differs from that of PR, indicating the fine-tuning among rhodopsin with different functions and motifs. The torsion angle and the twist of retinal at H-C14-C15-H can be accurately measured by ssNMR, providing the detailed structural information in addition to the 3D crystal structures in which the resolution is limited. The twist near the Schiff base around the C14-C15 bond in the KR2 dark state is relatively large compared to the other reported rhodopsins (BR, PR, and ChR2). However, the twist before the proton transfer step in the KR2 L-state seems to be common in microbial

rhodopsins (K-state in PR or L-state in KR2 and BR). Information regarding the twist of retinal near the Schiff base before the proton transfer in other microbial rhodopsin with different functions like the inward H^+ pump, XeR, or Cl^- rhodopsin may further prove the common light energy transfer mechanism among microbial rhodopsins.

The controversial retinal conformation in the O-state was shown here to be an *all-trans* conformation based on the indicative chemical shift of C12 and C20, which agrees well with the lately published O-state crystal structure (at the time this thesis was written) but contradicts with the FTIR and Raman data.[172,185] The *all-trans* conformation in the dark and O-state was found to be different. The chemical shift information obtained at the Schiff base in K-, L- and O-intermediates, gave an insight into the stepwise interactions between the Schiff base nitrogen and the proton acceptor, D116, and the proton transfer process, which is the key step in ion pumping rhodopsins. The effect of the bound Na^+ near the Schiff base was also observed in the Schiff base nitrogen chemical shift in the O-state.

The studies of the isomerization effect at the opsin were challenging due to the limited resolution of the DNP-enhanced ssNMR at cryogenic temperature. The signal from K255 which is covalently bound to the Schiff base can be assigned due to the unique chemical shift of the Schiff base. Cε-K255 was sensitive to the isomerization and the chemical shifts supported the *15-anti* conformation in the K- and L-state, whereas the other carbon atoms of K255 were not much affected. Several other amino acid specific labeling schemes were tested. However, no conclusive result was obtained. The unique-pair labeling, which is often used in ssNMR studies to select the unique signal of the protein, yielded no conclusive result because the change was smaller than the resolution and therefore could not be detected. This emphasizes the need to improve the resolution of the DNP-enhanced ssNMR technique.

A long-range contact between residues in different helices can be measured using the DNP signal enhancement. However, a specific labeling design is needed to avoid unambiguous assignment. The signal from R109 can be selectively detected using the through-space ^{15}N-^{13}C dipolar coupling of the $^{15}N\eta$-Arg109 and $^{13}C_9$-Tyr247. The ^{15}N-^{13}C distance measurement in the dark state was possible, however, the distances in the intermediates were difficult to gain due to the peak overlapping. Nevertheless, the through-space ^{15}N-^{13}C dipolar coupling would provide more productive information in such a system, by which the chemical shifts of the two compared states are distinct.

The methyl group which is difficult to be detected under DNP condition can be probed based on the hNOE as was previously demonstrated by Aladin and Mao, et al. The chemical shifts of the methyl group at the retinal cyclohexene ring indicate no influences resulted from the light-activated isomerization, but the peak intensities suggested a dynamics perturbation at C16/17 of the β-ionone ring. However, the measurement of the hNOE buildup time for each methyl group is not straightforward in this sample since there is more than one methyl group that serves as the polarization hotspot. To probe the methyl dynamics of the β-ionone ring in the intermediates, the specific labeling at one methyl group is necessary. For the C20-methyl group, the temperature dependent hNOE buildup time exhibited the fast-motion rotating dynamics in the dark state. This C20 dynamic is restricted in the K-state but relaxed in the L-state as the K-state C20 peak was not observed based on hNOE polarization transfer but could be seen in the DQF spectrum. The data here demonstrated the application of hNOE based DNP-enhanced ssNMR in the studies of methyl dynamic in membrane proteins.

Using ^{23}Na NMR spectroscopy, the bound Na^+ at the extracellular protomer interface in the KR2 dark state could be detected. The NaCl titration experiment shown here exhibits the K_d value of 32 ± 3 mM. The competitive titration showed the high binding affinity against Li^+ and K^+ by which a high K^+ concentration is necessary to replace the bound Na^+ but not the case for Li^+. The short T1 relaxation time and the time dependent measurement indicate the slow dynamics of the bound Na^+. The very short T1 relaxation time of bound Na^+ in respect to the bulk Na^+ can be employed to filter out the unwanted bulk Na^+. The T1-filter experiment was successfully shown here to remove the large unwanted bulk Na^+ signal. The work done here demonstrated the applicability of ^{23}Na NMR to the study of the bound Na^+ ion in membrane proteins, which can be further applied to study the ion in other sodium ion dependent systems.

Declaration of contributions and publications

Except where stated otherwise by reference or acknowledgement, the work presented was generated by myself under the supervision of my advisors during my doctoral study. All contributions from colleagues are explicitly references in the thesis. The figures listed below was obtained in the context of collaborative research:

Figure 36: Broadband flash photolysis spectra of KR2 in 50mM NaCl buffer, pH 8.5 at (a) 283 K and (b) 293 K. The amplitudes are color coded. Red, green, and blue indicate positive, zero and negative absorbance changes, respectively. Corresponding Lifetime Density Map (LDM) obtained from lifetime distribution analysis of the time resolved flash photolysis data are shown at the bottom. Amplitudes are color coded: red (positive) indicates decay of absorption or rise of bleach and blue (negative) indicates rise of absorption or decay of bleach. (c) and (d) Ground state corrected evolution associated spectra (EAS) of the transient data at 283 K and 293 K, respectively. The figures are provided by Peter Eberhardt from Wachtveitl group, Goethe University Frankfurt.

Figure 37: Verification of the trapping of K- and L-intermediates. S1 (K) and S2 (L) EADS of the transient flash photolysis data recorded at 283 K are compared with the cryo UV/vis difference absorption spectra recorded at 110 and 160 K respectively. The figure shows the trapping of K-state at 110 K and the shift from K- to L-intermediate at 160 K. The figure is provided by Peter Eberhardt from Wachtveitl group, Goethe University Frankfurt.

Figure 41: Verification of O-intermediate trapping. S4 (O) EADS of the transient flash photolysis data was compared with the cryo-UV/vis difference absorption spectra of KR2 illuminated and trapped by flash freezing (green) and illuminated at 230 K (blue). The KR2 sample was in 0.5% DDM solution containing 25 mM Tris (pH 8.5), 5 mM MgCl2, 30 mM NaCl and 60% (v/v) glycerol for cryo-protection and light scattering reduction. The figure is provided by Peter Eberhardt from Wachtveitl group, Goethe University Frankfurt.

This thesis contains parts of figures, tables, and text that are identical to the publication in Science advance (in print).

Chapter 5: Figure 33-34, 36-37, 40-44, 47; Table 14, 19

Acknowledgement

All the works done in this Ph.D. thesis could not be successfully achieved without supports from many people. First, I would like to express my deep grateful gratitude to my Ph.D. supervisor, Prof. Dr. Clemens Glaubitz for the opportunity and the freedom to carry on the research project and all the supports and guidance provided to overcome the obstacles that I faced during my Ph.D. study. I would like to further express my grateful gratitude to Dr. Johanna-Becker Baldus for the assistance in setup the NMR and illumination experiments and the maintenance of NMR and DNP spectrometers as well as for the opened deep and broad scientific discussions. I would like to thank Dr. Jagdeep Kaur for the provided [$^{13}C_9$-Retinal, U-^{15}N]-KR2 sample and the help and guidance to prepare plasmids and protein samples and to perform various biochemical characterizations. My further deep appreciation goes to Dr. Jiafei Mao, who provided the $^{13}C_3$-retinal for the incorporation and the insightful comments and discussions that help me construct and design experiments.

I really have a great time performing the research in our lab and have learned and gained experiences a lot during my Ph.D. period. I would like to thank all the lab members, especially the former Ph.D. coworkers, Dr. Michaella Mehler, Dr. Hundeep Kaur, Dr. Jakob Maciejko, Dr. Julian de Mos, Dr. Kristin Möbius, the Ph.D. coworkers, Clara Nassin Kriebel, Christian Bonifer, Samuel Seidler, Phoebe Ye, and Mahmoud Doroudgar, for the friendly and supportive working environment. I would like also to show my appreciation to our lab technician, Ingrid Weber, for helping with the sample preparation, the order of required chemicals and materials, and the maintenance of all laboratory equipments, the secretary, Simone Kobylka, for taking care of all administrative issues and for Manfred Stumpf for the maintaining of all spectrometers and filling of liquid helium and nitrogen gas. I would like also to thank my former Bachelor student Maria Witz for helping with the SEC, BN-PAGE, and the pH-titration of the KR2-WT.

Moreover, I would like to express my gratitude to the TRAM mentoring committees, Prof. Dr. Josef Wachtveitl and Dr. Christian Bamann for the constructive comments and encouragement. I am deeply grateful to Dr. Peter Eberhardt for performing the flash photolysis and UV-vis absorption measurement to verify the trapped intermediates and the productive discussions. I am deeply grateful to SFB807 and the members, especially the coordinators, Katharina Dolata and Jutta Uphoff, for providing the funding throughout the project and the organization of talks, workshops, and retreats, which helped me broaden my knowledge and acquired the necessary skills as a researcher. Last but not least, I would like to thank my family and friends in Thailand as well as in Germany for their warm supports to help me go through this path.

Appendix

Appendix I: Nucleotide sequence of KR2 in PET26b construct

ATGACACAAGAGTTGGGAAATGCCAATTTCGAGAACTTTATCGGTGCAACAGAGG
GGTTTTCCGAGATTGCGTACCAGTTTACTAGCCACATTCTCACTCTTGGCTACGCTG
TCATGCTGGCAGGACTCCTGTACTTCATTCTGACCATCAAGAATGTGGACAAGAAG
TTTCAGATGTCCAACATACTGTCTGCTGTAGTGATGGTTTCCGCCTTCCTGCTGCTG
TACGCTCAAGCCCAAAATTGGACAAGCTCCTTCACCTTCAACGAAGAAGTCGGGAG
GTATTTCCTCGATCCTTCTGGCGACTTGTTCAACAATGGCTATCGCTACCTTAACTG
GCTGATTGACGTACCCATGTTGCTGTTTCAGATCCTGTTCGTGGTGAGTCTTACCAC
GTCAAAATTTTCTAGCGTGCGGAACCAGTTTTGGTTTTCTGGCGCCATGATGATTAT
TACCGGATATATCGGACAGTTCTATGAGGTGTCCAATTTGACAGCGTTTCTCGTTTG
GGGCGCTATCTCAAGCGCCTTCTTCTTCCATATCCTGTGGGTGATGAAGAAGGTCAT
CAACGAAGGTAAAGAAGGCATAAGTCCCGCTGGTCAGAAAATCCTGAGCAATATC
TGGATACTGTTTCTCATCTCATGGACGCTGTATCCAGGTGCCTACCTCATGCCGTAT
CTCACTGGAGTCGATGGGTTTCTGTATTCAGAGGATGGGGTGATGGCCAGACAGCT
GGTCTACACTATTGCAGACGTGAGTAGCAAAGTGATTTACGGCGTTCTGCTTGGGA
ATCTTGCCATAACCCTGAGCAAGAACAAAGAACTGGTTGAGGCAAACAGTCTCGA
GCACCACCACCACCACCAC

(The green letters are the 6x His tag and the violet letters are the *XhoI* restriction site)

Appendix II: Sequence alignment of KR2 with other sodium ion pump rhodopsins (NaR)

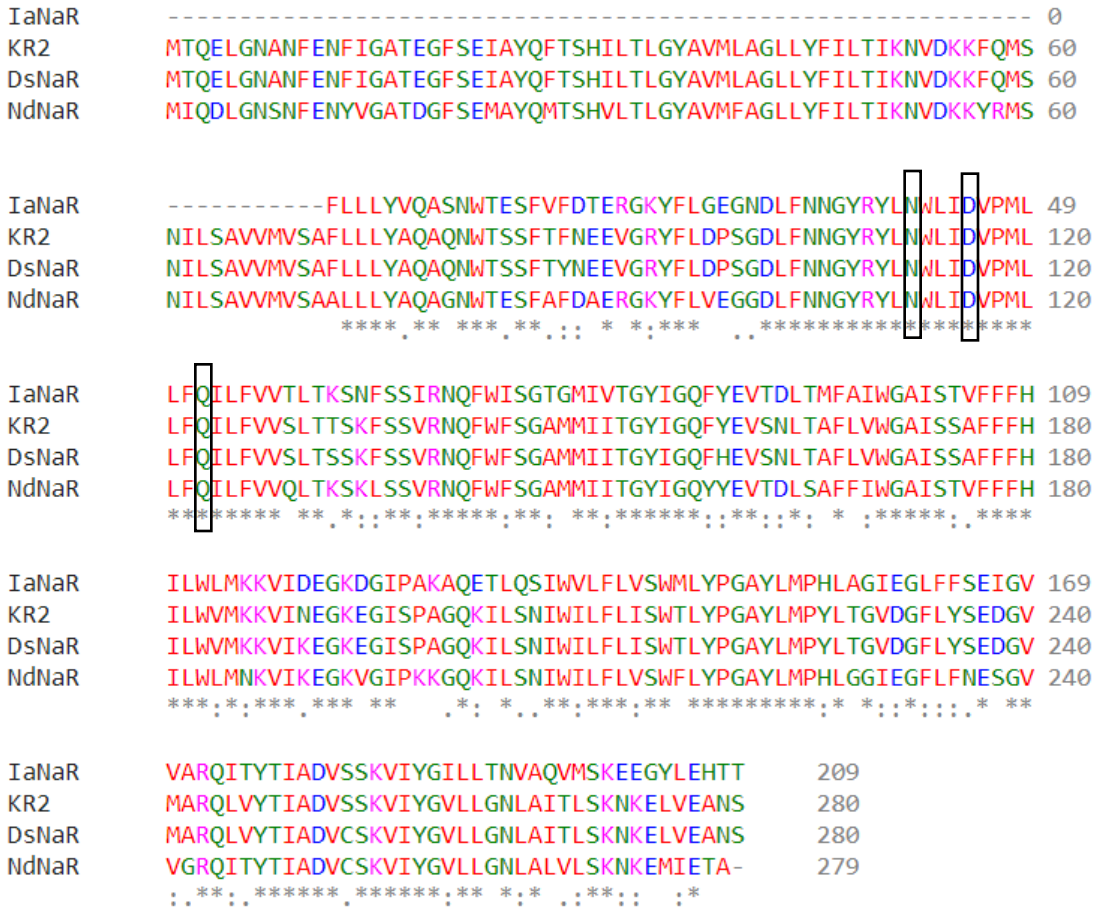

KR2: Na^+ pump rhodopsin from *Krokinobacter Eikastus*; DsNaR: Na^+ pump rhodopsin from *Dokdonia sp.* PR095 (GenBank ID: AEX55013.1); NdNaR: Na^+ pump rhodopsin from *Nonlabens dokdonensis* DSW6 (GenBank ID: AGC76155.1); IaNaR: Na^+ pump rhodopsin from *Indibacter alkaliphilus* (GenBank ID: WP_009036080.1)

Appendix III: Deconvolution of the spectra acquired with SCREAM

The deconvolution of the SCREAM spectra at different buildup time (1 s – 15 s) for [$^{13}C_3$-Retinal, 15Nζ-Lys]-KR2 in 100 mM NaCl Tris-buffer (pH 8.5) after illumination at 106 K for 60 minutes using Origin Pro program.

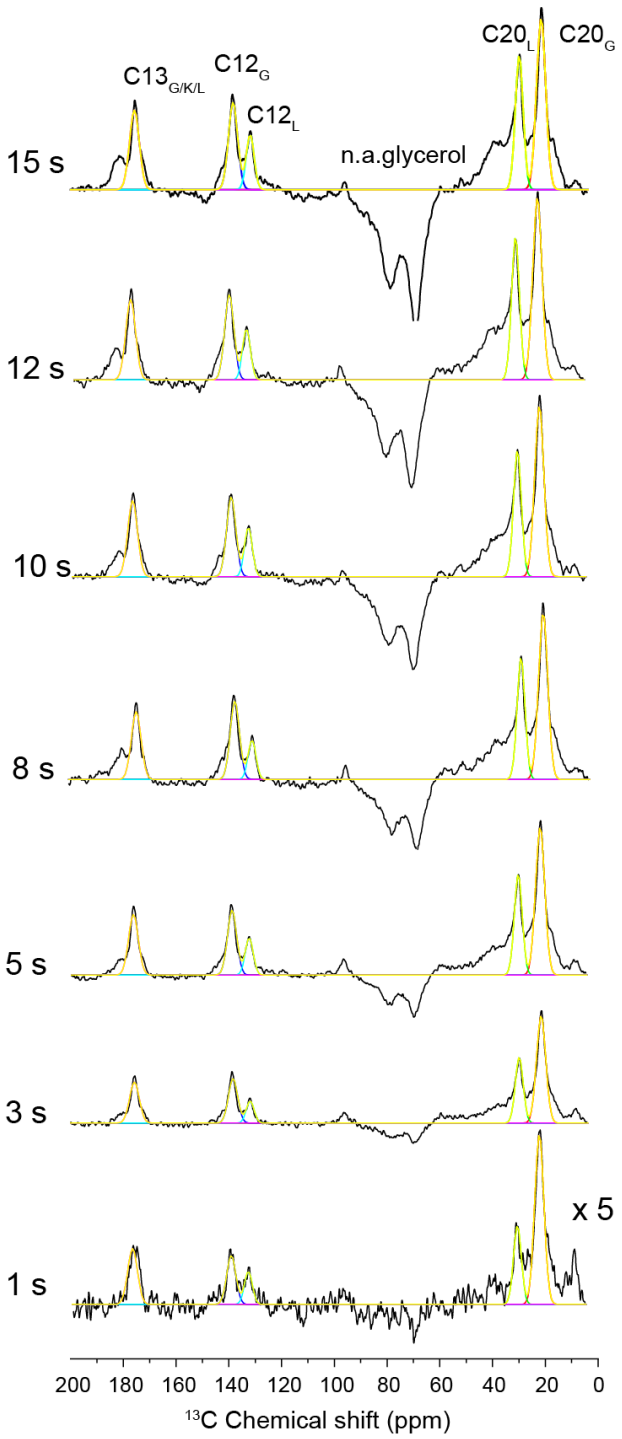

Appendix IV: Amino acids analysis of KR2 compared to other microbial rhodopsins (BR, GPR, BPR and HR)

The table shows the amino acid components of KR2 in comparison to BR, GPR, BPR, and HR. Asn (N) and Gln (Q) are highlighted in yellow.

Amino acid	KR2 3X3C		BR 1C3W		GPR 2L6X		BPR 4JQ6		HR	
Ala(A)	18	6.3%	21	9.5%	25	10.5%	32	13.6%	36	14.2%
Arg (R)	4	1.4%	7	3.2%	4	1.7%	3	1.3%	11	4.3%
Asn (N)	17	6.0%	3	1.4%	9	3.8%	7	3.0%	4	1.6%
Asp (D)	7	2.5%	8	3.6%	8	3.4%	9	3.8%	8	3.2%
Cys (C)	0	0.0%	0	0.0%	3	1.3%	0	0.0%	2	0.8%
Gln (Q)	11	3.9%	2	0.9%	1	0.4%	3	1.3%	3	1.2%
Glu (E)	12	4.2%	5	2.3%	7	3.0%	9	3.8%	6	2.4%
Gly (G)	22	7.7%	23	10.4%	26	11.0%	21	8.9%	21	8.3%
His (H)	2	0.7%	0	0.0%	1	0.4%	2	0.9%	1	0.4%
Ile (I)	22	7.7%	14	6.3%	17	7.2%	26	11.1%	14	5.5%
Leu (L)	36	12.7%	36	16.3%	26	11.0%	21	8.9%	37	14.6%
Lys (K)	11	3.9%	6	2.7%	7	3.0%	8	3.4%	1	0.4%
Met (M)	10	3.5%	9	4.1%	10	4.2%	6	2.6%	9	3.6%
Phe (F)	24	8.5%	13	5.9%	14	5.9%	13	5.5%	10	4.0%
Pro (P)	5	1.8%	9	4.1%	6	2.5%	4	1.7%	6	2.4%
Ser (S)	25	8.8%	10	4.5%	16	6.8%	11	4.7%	21	8.3%
Thr (T)	15	5.3%	15	6.8%	13	5.5%	13	5.5%	17	6.7%
Trp (W)	7	2.5%	8	3.6%	10	4.2%	13	5.5%	10	4.0%
Tyr (Y)	16	5.6%	11	5.0%	14	5.9%	12	5.1%	7	2.8%
Val (V)	20	7.0%	21	9.5%	20	8.4%	22	9.4%	29	11.5%
Sum	284	100%	221	100%	237	100%	235	100%	253	100%
N+Q	**28**	**9.9%**	**5**	**2.3%**	**10**	**4.2%**	**10**	**4.3%**	**7**	**2.8%**

Abbreviations list

1D	one dimension
2D	two dimensions
ASR	Anabaena Sensory Rhodopsin
BDPA	1,3-bisdiphenylene-2-phenylallyl
BN	blue native
BR	bacteriorhodopsin
bTbK	bis-TEMPO–bis-Ketal
bTnE	bis-TEMPO n-ethyleneglycol
CE	cross effect
ClR	chloride ion pump Rhodopsin
CP	cross polarization
CS	chemical shift
CSA	chemical shift anisotropy
DARR	dipolar assisted resonance
DIPSHIFT	dipolar-coupling chemical-shift correlation
DNP	Dynamic Nuclear Polarization
DQF	double quantum filter
DQF	double quantum
DQSQ	double quantum single quantum
EADS	evolution associated difference spectrum
EAS	evolution associated spectrum
ECL	extracellular loop
ELDOR	electron-electron double resonance
EPR	electron paramagnetic resonance
fs	femtosecond
FTIR	Fourier-transform infrared spectroscopy
GPCR	G protein-coupled receptor
HFI	hyperfine interaction
HLF	heteronuclear local field
hNOE	heteronuclear Overhauser effect
HR	halorhodopsin
ICL	intracellular loop
INADEQUATE	incredible natural abundance double quantum transfer experiment
INEPT	Insensitive nuclei enhancement by polarization transfer
KR2	*Krokinobater Eikastus* 2
LAC	Level anti-crossing
LB	lysogeny broth
LDA	lifetime density analysis
MAS	magic angle spinning
mM	millimolar
NaR	sodium ion pump Rhodopsin
NMR	nuclear magnetic resonance
OD	optical density

OE	Overhauser effect
PA	polarizing agent
PDB	protein data base
PDSD	proton diffusion spin diffusion
pIRCII	putative ion release cavity
pKa	acid dissociation constant
PMLG	phase-modulated Lee-Goldburg
PR	proteorhodopsin
PS	polystyrene
QM/MM	quantum mechanics / molecular mechanics
REDOR	rotational-echo double resonance
RF	radio frequency
SBC	Schiff base cavity
SCREAM	specific cross-relaxation enhancement by active motions
SDS	sodium dodecyl sulfate
SE	solid effect
SEC	size exclusion chromatography
SPINAL	small phase incremental alteration
SQ	single quantum
SRI	Sensory Rhodopsin I
SRII	Sensory Rhodopsin II
ssNMR	solid-state nuclear magnetic resonance
TEDOR	transferred echo double resonance
TM	transmembrane
TM	thermal mixing
TOTAPOL	1-(TEMPO-4-oxy)-3-(TEMPO-4-amino) propan-2-ol
TPP^+	tetraphenylphosphonium ion
TR-SFX	time resolved serial femtosecond X-ray crystallography
XFEL	X-ray free electron laser
ZQ	zero quantum

Materials lists

Chemical list

Chemicals	Chemical formular	Molecular weight	Producers
Agar	-	-	Roth
Ammonium chloride	NH_4Cl	53.49	AppliChem
Biotin	$C_{10}H_{16}N_2O_3S$	244.31	Roth
Bis Tris	$C_8H_{19}NOS$	209.24	AppliChem
Boric acid	BH_3O_3	61.83	Fluka
Calcium chloride	$CaCl_2 \cdot 2\ H_2O$	147.01	Sigma-Aldrich
Chloroform	$CHCl_3$	119.38	Roth
Coomassie G-250	$C_{47}H_{48}N_3NaO_7S_2$	840.01	AppliChem
DDM	$C_{24}H_{46}O_{11}$	510.63	AppliChem
Dipotassium hydrogen phosphate	K_2HPO_4	174.18	AppliChem
DMPA	$C_{31}H_{60}O_8PNa$	614.76	Avanti
DMPC	$C_{36}H_{72}NO_8P$	677.93	Avanti
EDTA	$C_{10}H_{16}N_2O_8$	292.25	AppliChem
Iron (III) chloride Hexahydrate	$FeCl_3 \cdot 6\ H_2O$	270.30	AppliChem
Acetic acid	$C_2H_4O_2$	60.05	Roth
Ethanol	C_2H_6O	46.07	Roth
D (+) Glucose	$C_6H_{12}O_6$	180.16	AppliChem
Glycerol	$C_3H_8O_3$	92.10	AppliChem
Glycerin	$C_2H_5NO_2$	75.07	AppliChem
HEPES	$C_8H_{18}N_2O_4S$	238.31	Roth
Imidazole	$C_3H_4N_2$	68.08	AppliChem
Potassium dihydrogen phosphate	KH_2PO_4	136.09	AppliChem
Kanamycin	$C_{19}H_{86}N_4O_{11} \cdot H_2SO_4$	582.58	AppliChem
L-Alanine	$C_3H_7NO_2$	89.09	AppliChem
L-Arginine-hydrochloride	$C_6H_{14}N_4O_2 \cdot HCl$	210.66	AppliChem
L-Asparagine-monohydrate	$C_4H_8N_2O_3 \cdot H_2O$	150.14	Roth
L-Aspartic acid	$C_4H_7NO_4$	133.10	AppliChem
LB	-	-	Roth
L-Glutamine	$C5H_{10}N_2O_3$	146.15	AppliChem
L-Glutamic acid	$C_5H_9NO_4$	147.13	AppliChem
L-Histidine	$C_6H_9N_3O_2$	155.16	AppliChem

L-Isoleucine	$C_6H_{13}NO_2$	131.18	AppliChem
L-Leucine	$C_6H_{13}NO_2$	131.18	AppliChem
L-Lysine-Monohydrate	$C_6H_{14}N_2O_2 \cdot H_2O$	164.21	AppliChem
L-Methionine	$C_5H_{11}NO_2S$	149.21	AppliChem
L-Phenylalanine	$C_9H_{11}NO_2$	165.19	AppliChem
L-Proline	$C_5H_9NO_2$	115.13	AppliChem
L-Serine	$C3H_7NO_3$	105.09	AppliChem
L-Threonine	$C_4H_9NO_3$	119.2	Roth
L-Tryptophan	$C_{11}H_{12}N_2O_2$	204.23	AppliChem
L-Tyrosine	$C_9H_{11}NO_3$	181.19	Roth
L-Valine	$C_5H_{11}NO_2$	117.5	AppliChem
Magnesium chloride hexahydrate	$MgCl_2 \cdot 6\ H_20$	203.3	AppliChem
Magnesium sulfate heptahydrate	$MgSO_4 \cdot 7\ H_2O$	246.48	AppliChem
Manganese sulfate monohydrate	$MnSO_4 \cdot H_2O$	169.0	Sigma
MES	$C_6H_{13}NO_4S$	195.24	AppliChem
Methanol	CH_4O	32.04	Roth
Sodium chloride	NaCl	58.44	AppliChem
Sodium citrate	$C_6H_5Na_3O_7$	294.10	Sigma-Aldrich
Sodium hydroxide	NaOH	40.0	AppliChem
Sodium phosphate	Na_3PO_4	141.96	AppliChem
Niacin	$C_6H_5NO_2$	123.11	AppliChem
Protease Inhibitor	-	-	Roche Diagnostics
Hydrochloric acid	HCl	36.4	Roth
SDS	$C_{12}H_{25}NaO_4S$	288.38	AppliChem
Thiamin hydrochloride	$C_{12}H_{17}ClN_4OS$	337.23	AppliChem
Tricin	$C_6H_{13}NO_5$	179.17	AppliChem
Tris	$C_4H_{11}NO_3$	121.14	Roth
Zink sulfate heptahydrate	$ZnSO_4 \cdot 7\ H_2O$	287.5	Sigma-Aldrich
Retinal	$C_{20}H_{28}O$	284.44	Sigma-Aldrich
IPTG	$C_9H_{18}O_5S$	238.30	AppliChem
Qiagen Ni-NTA	-	-	Qiagen
SM-2 Biobeads	-	-	BioRad

Consumable materials

Materials	Type	Producers
BN-Page gel	Novex Bis-Tris Gel 4-10%	Invitrogen
Extruder filter	0.2 µm pore size	Whatman
PD-10 column	-	GE-Healthcare
SDS-PAGE gel	SDS Precast Gel 4% to 20%	RunBlue
SEC column	Superdex 200 increase 10/300 GL	GE Healthcare
Sterile filter		Biotech

List of equipment

Equipment	Type	Producer
Autoclave	Varioklav 65T	Thermo Scientific
BN PAGE Equipment	XCell SureLockTM Mini-Cell System	Life Technologies
Extruder	Thermobarrel Extruder	LIPEX™
Size Exclusion Chromatography	BioRad Chromatography Systems	BioRad
Incubator	Innova 44 Incubator Shaker Series	New Brunswick Scientific
OD600 density meter	Ultrospec 10 Cell density meter	Biochrom
pH-Meter	Sevencompact	Mettler Toledo
Rotary evaporator	Rotavapor-200	Büchi
Ultracentrifuge	Optima LE-80K	Coulter
UV-vis spectrometer	V550 UV/Vis Spectrometer	Jasco
Cell disrupter	System Basic Z	IUL Instruments
Centrifuge	Avanti J-E Centrifuge GS-15R Centrifuge	Beckman Coulter
Shaker	Thermomixer	Eppendorf

List of figures

List of tables

References

(1) Inoue, K.; Ono, H.; Abe-Yoshizumi, R.; Yoshizawa, S.; Ito, H.; Kogure, K.; Kandori, H. A light-driven sodium ion pump in marine bacteria. *Nat Commun* **2013**, *4*, 1678. DOI: 10.1038/ncomms2689.

(2) Tahara, S.; Takeuchi, S.; Abe-Yoshizumi, R.; Inoue, K.; Ohtani, H.; Kandori, H.; Tahara, T. Ultrafast photoreaction dynamics of a light-driven sodium-ion-pumping retinal protein from Krokinobacter eikastus revealed by femtosecond time-resolved absorption spectroscopy. *J Phys Chem Lett* **2015**, *6* (22), 4481–4486. DOI: 10.1021/acs.jpclett.5b01994.

(3) Ono, H.; Inoue, K.; Abe-Yoshizumi, R.; Kandori, H. FTIR spectroscopy of a light-driven compatible sodium ion-proton pumping rhodopsin at 77 K. *J Phys Chem B* **2014**, *118* (18), 4784–4792. DOI: 10.1021/jp500756f.

(4) Hontani, Y.; Inoue, K.; Kloz, M.; Kato, Y.; Kandori, H.; Kennis, J. T. The photochemistry of sodium ion pump rhodopsin observed by watermarked femto- to submillisecond stimulated Raman spectroscopy. *Phys Chem Chem Phys* **2016**, *18* (35), 24729–24736. DOI: 10.1039/c6cp05240a.

(5) Shigeta, A.; Ito, S.; Inoue, K.; Okitsu, T.; Wada, A.; Kandori, H.; Kawamura, I. Solid-State Nuclear Magnetic Resonance Structural Study of the Retinal-Binding Pocket in Sodium Ion Pump Rhodopsin. *Biochemistry-Us* **2017**, *56* (4), 543–550. DOI: 10.1021/acs.biochem.6b00999.

(6) Kaur, J.; Kriebel, C. N.; Eberhardt, P.; Jakdetchai, O.; Leeder, A. J.; Weber, I.; Brown, L. J.; Brown, R. C. D.; Becker-Baldus, J.; Bamann, C.; Wachtveitl, J.; Glaubitz, C. Solid-state NMR analysis of the sodium pump Krokinobacter rhodopsin 2 and its H30A mutant. *J Struct Biol* **2019**, *206* (1), 55–65. DOI: 10.1016/j.jsb.2018.06.001.

(7) Skopintsev, P.; Ehrenberg, D.; Weinert, T.; James, D.; Kar, R. K.; Johnson, P. J. M.; Ozerov, D.; Furrer, A.; Martiel, I.; Dworkowski, F.; Nass, K.; Knopp, G.; Cirelli, C.; Arrell, C.; Gashi, D.; Mous, S.; Wranik, M.; Gruhl, T.; Kekilli, D.; Brünle, S.; Deupi, X.; Schertler, G. F. X.; Benoit, R. M.; Panneels, V.; Nogly, P.; Schapiro, I.; Milne, C.; Heberle, J.; Standfuss, J. Femtosecond-to-millisecond structural changes in a light-driven sodium pump. *Nature* **2020.** DOI: 10.1038/s41586-020-2307-8.

(8) Kovalev, K.; Astashkin, R.; Gushchin, I.; Orekhov, P.; Volkov, D.; Zinovev, E.; Marin, E.; Rulev, M.; Alekseev, A.; Royant, A.; Carpentier, P.; Vaganova, S.; Zabelskii, D.; Baeken, C.; Sergeev, I.; Balandin, T.; Bourenkov, G.; Carpena, X.; Boer, R.; Maliar, N.; Borshchevskiy, V.; Büldt, G.; Bamberg, E.; Gordeliy, V. Molecular mechanism of light-driven sodium pumping. *Nat Commun* **2020**, *11* (1), 2137. DOI: 10.1038/s41467-020-16032-y.

(9) Suomivuori, C.-M.; Gamiz-Hernandez, A. P.; Sundholm, D.; Kaila, V. R. I. Energetics and dynamics of a light-driven sodium-pumping rhodopsin. *Proc Natl Acad Sci U S A* **2017**, *114* (27), 7043–7048. DOI: 10.1073/pnas.1703625114.

(10) Inoue, K.; Konno, M.; Abe-Yoshizumi, R.; Kandori, H. The Role of the NDQ Motif in Sodium-Pumping Rhodopsins. *Angew Chem Int Ed Engl* **2015**, *54* (39), 11536–11539. DOI: 10.1002/anie.201504549.

(11) Bajaj, V. S.; Mak-Jurkauskas, M. L.; Belenky, M.; Herzfeld, J.; Griffin, R. G. Functional and shunt states of bacteriorhodopsin resolved by 250 GHz dynamic nuclear polarization-enhanced solid-state NMR. *Proc Natl Acad Sci U S A* **2009**, *106* (23), 9244–9249. DOI: 10.1073/pnas.0900908106.

(12) Mehler, M.; Eckert, C. E.; Leeder, A. J.; Kaur, J.; Fischer, T.; Kubatova, N.; Brown, L. J.; Brown, R. C. D.; Becker-Baldus, J.; Wachtveitl, J.; Glaubitz, C. Chromophore Distortions in Photointermediates of Proteorhodopsin Visualized by Dynamic Nuclear Polarization-Enhanced Solid-State NMR. *J Am Chem Soc* **2017**, *139* (45), 16143–16153. DOI: 10.1021/jacs.7b05061.

(13) Becker-Baldus, J.; Bamann, C.; Saxena, K.; Gustmann, H.; Brown, L. J.; Brown, R. C. D.; Reiter, C.; Bamberg, E.; Wachtveitl, J.; Schwalbe, H.; Glaubitz, C. Enlightening the photoactive site of channelrhodopsin-2 by DNP-enhanced solid-state NMR spectroscopy. *P Natl Acad Sci USA* **2015**, *112* (32), 9896–9901. DOI: 10.1073/pnas.1507713112.

(14) Inoue, Y.; Tokitô, Y.; Tomonoh, S.; Chûjô, R. Carbon-13 Chemical Shifts of Retinal Isomers and Their Schiff Bases as Models of Visual Chromophores. *BCSJ* **1979**, *52* (1), 265–266. DOI: 10.1246/bcsj.52.265.

(15) Aladin, V.; Vogel, M.; Binder, R.; Burghardt, I.; Suess, B.; Corzilius, B. Complex Formation of the Tetracycline-Binding Aptamer Investigated by Specific Cross-Relaxation under DNP. *Angew Chem Int Ed Engl* **2019**, *58* (15), 4863–4868. DOI: 10.1002/anie.201811941.

(16) Kato, H. E.; Inoue, K.; Abe-Yoshizumi, R.; Kato, Y.; Ono, H.; Konno, M.; Hososhima, S.; Ishizuka, T.; Hoque, M. R.; Kunitomo, H.; Ito, J.; Yoshizawa, S.; Yamashita, K.; Takemoto, M.; Nishizawa, T.; Taniguchi, R.; Kogure, K.; Maturana, A. D.; Iino, Y.; Yawo, H.; Ishitani, R.; Kandori, H.; Nureki, O. Structural basis for Na(+) transport mechanism by a light-driven Na(+) pump. *Nature* **2015**, *521* (7550), 48–53. DOI: 10.1038/nature14322.

(17) Gushchin, I.; Shevchenko, V.; Polovinkin, V.; Kovalev, K.; Alekseev, A.; Round, E.; Borshchevskiy, V.; Balandin, T.; Popov, A.; Gensch, T.; Fahlke, C.; Bamann, C.; Willbold, D.; Buldt, G.; Bamberg, E.; Gordeliy, V. Crystal structure of a light-driven sodium pump. *Nat Struct Mol Biol* **2015**, *22* (5), 390–395. DOI: 10.1038/nsmb.3002.

(18) Spudich, J. L.; Yang, C. S.; Jung, K. H.; Spudich, E. N. Retinylidene proteins: structures and functions from archaea to humans. *Annual review of cell and developmental biology* **2000**, *16*, 365–392. DOI: 10.1146/annurev.cellbio.16.1.365.

(19) Kandori, H. Ion-pumping microbial rhodopsins. *Front Mol Biosci* **2015**, *2*, 52. DOI: 10.3389/fmolb.2015.00052.

(20) Ernst, O. P.; Lodowski, D. T.; Elstner, M.; Hegemann, P.; Brown, L. S.; Kandori, H. Microbial and animal rhodopsins: structures, functions, and molecular mechanisms. *Chemical reviews* **2014**, *114* (1), 126–163. DOI: 10.1021/cr4003769.

(21) Brown, L. S. Eubacterial rhodopsins - unique photosensors and diverse ion pumps. *Biochim Biophys Acta* **2014**, *1837* (5), 553–561. DOI: 10.1016/j.bbabio.2013.05.006.

(22) Grote, M.; Engelhard, M.; Hegemann, P. Of ion pumps, sensors and channels - perspectives on microbial rhodopsins between science and history. *Biochim Biophys Acta* **2014**, *1837* (5), 533–545. DOI: 10.1016/j.bbabio.2013.08.006.

(23) Oesterhelt, D.; Stoeckenius, W. Rhodopsin-like protein from the purple membrane of Halobacterium halobium. *Nature: New biology* **1971**, *233* (39), 149–152. DOI: 10.1038/newbio233149a0.

(24) Matsuno-Yagi, A.; Mukohata, Y. Two possible roles of bacteriorhodopsin; a comparative study of strains of Halobacterium halobium differing in pigmentation. *Biochemical and biophysical research communications* **1977**, *78* (1), 237–243. DOI: 10.1016/0006-291x(77)91245-1.

(25) Schobert, B.; Lanyi, J. K. Halorhodopsin is a light-driven chloride pump. *J Biol Chem* **1982**, *257* (17), 10306–10313.

(26) Spudich, J. L.; Bogomolni, R. A. Mechanism of colour discrimination by a bacterial sensory rhodopsin. *Nature* **1984**, *312* (5994), 509–513. DOI: 10.1038/312509a0.

(27) Jung, K.-H.; Trivedi, V. D.; Spudich, J. L. Demonstration of a sensory rhodopsin in eubacteria. *Molecular microbiology* **2003**, *47* (6), 1513–1522. DOI: 10.1046/j.1365-2958.2003.03395.x.

(28) Shevchenko, V.; Mager, T.; Kovalev, K.; Polovinkin, V.; Alekseev, A.; Juettner, J.; Chizhov, I.; Bamann, C.; Vavourakis, C.; Ghai, R.; Gushchin, I.; Borshchevskiy, V.; Rogachev, A.; Melnikov, I.; Popov, A.; Balandin, T.; Rodriguez-Valera, F.; Manstein, D. J.; Bueldt, G.; Bamberg, E.; Gordeliy, V. Inward H(+) pump xenorhodopsin:Mechanism and alternative optogenetic approach. *Sci Adv* **2017**, *3* (9), e1603187. DOI: 10.1126/sciadv.1603187.

(29) Inoue, K.; Ito, S.; Kato, Y.; Nomura, Y.; Shibata, M.; Uchihashi, T.; Tsunoda, S. P.; Kandori, H. A natural light-driven inward proton pump. *Nat Commun* **2016**, *7*, 13415. DOI: 10.1038/ncomms13415.

(30) Miesenböck, G. Optogenetic control of cells and circuits. *Annual review of cell and developmental biology* **2011**, *27*, 731–758. DOI: 10.1146/annurev-cellbio-100109-104051.

(31) Hegemann, P.; Nagel, G. From channelrhodopsins to optogenetics. *EMBO molecular medicine* **2013**, *5* (2), 173–176. DOI: 10.1002/emmm.201202387.

(32) Deisseroth, K. Optogenetics. *Nature methods* **2011**, *8* (1), 26–29. DOI: 10.1038/nmeth.f.324.

(33) Diester, I.; Kaufman, M. T.; Mogri, M.; Pashaie, R.; Goo, W.; Yizhar, O.; Ramakrishnan, C.; Deisseroth, K.; Shenoy, K. V. An optogenetic toolbox designed for primates. *Nature neuroscience* **2011**, *14* (3), 387–397. DOI: 10.1038/nn.2749.

(34) Béjà, O.; Aravind, L.; Koonin, E. V.; Suzuki, M. T.; Hadd, A.; Nguyen, L. P.; Jovanovich, S. B.; Gates, C. M.; Feldman, R. A.; Spudich, J. L.; Spudich, E. N.; DeLong, E. F. Bacterial rhodopsin: evidence for a new type of phototrophy in the sea. *Science (New York, N.Y.)* **2000**, *289* (5486), 1902–1906. DOI: 10.1126/science.289.5486.1902.

(35) Bamann, C.; Bamberg, E.; Wachtveitl, J.; Glaubitz, C. Proteorhodopsin. *Biochimica et Biophysica Acta (BBA) - Bioenergetics* **2014**, *1837* (5), 614–625. DOI: 10.1016/j.bbabio.2013.09.010.

(36) Inoue, K.; Koua, F. H. M.; Kato, Y.; Abe-Yoshizumi, R.; Kandori, H. Spectroscopic study of a light-driven chloride ion pump from marine bacteria. *J Phys Chem B* **2014**, *118* (38), 11190–11199. DOI: 10.1021/jp507219q.

(37) Yoshizawa, S.; Kumagai, Y.; Kim, H.; Ogura, Y.; Hayashi, T.; Iwasaki, W.; DeLong, E. F.; Kogure, K. Functional characterization of flavobacteria rhodopsins reveals a unique class of light-driven chloride pump in bacteria. *Proc Natl Acad Sci U S A* **2014**, *111* (18), 6732–6737. DOI: 10.1073/pnas.1403051111.

(38) Mamedov, M. D.; Mamedov, A. M.; Bertsova, Y. V.; Bogachev, A. V. A single mutation converts bacterial Na(+) -transporting rhodopsin into an H(+) transporter. *FEBS Lett* **2016**, *590* (17), 2827–2835. DOI: 10.1002/1873-3468.12324.

(39) Konno, M.; Kato, Y.; Kato, H. E.; Inoue, K.; Nureki, O.; Kandori, H. Mutant of a Light-Driven Sodium Ion Pump Can Transport Cesium Ions. *J Phys Chem Lett* **2016**, *7* (1), 51–55. DOI: 10.1021/acs.jpclett.5b02385.

(40) Inoue, K.; Nomura, Y.; Kandori, H. Asymmetric Functional Conversion of Eubacterial Light-driven Ion Pumps. *J Biol Chem* **2016**, *291* (19), 9883–9893. DOI: 10.1074/jbc.M116.716498.

(41) Sudo, Y.; Ihara, K.; Kobayashi, S.; Suzuki, D.; Irieda, H.; Kikukawa, T.; Kandori, H.; Homma, M. A microbial rhodopsin with a unique retinal composition shows both sensory rhodopsin II and bacteriorhodopsin-like properties. *J Biol Chem* **2011**, *286* (8), 5967–5976. DOI: 10.1074/jbc.M110.190058.

(42) Inoue, K.; Kato, Y.; Kandori, H. Light-driven ion-translocating rhodopsins in marine bacteria. *Trends in microbiology* **2015**, *23* (2), 91–98. DOI: 10.1016/j.tim.2014.10.009.

(43) Nagel, G.; Szellas, T.; Huhn, W.; Kateriya, S.; Adeishvili, N.; Berthold, P.; Ollig, D.; Hegemann, P.; Bamberg, E. Channelrhodopsin-2, a directly light-gated cation-selective membrane channel. *P Natl Acad Sci USA* **2003**, *100* (24), 13940–13945. DOI: 10.1073/pnas.1936192100.

(44) Balashov, S. P.; Imasheva, E. S.; Dioumaev, A. K.; Wang, J. M.; Jung, K.-H.; Lanyi, J. K. Light-driven Na(+) pump from Gillisia limnaea: a high-affinity Na(+) binding site is formed transiently in the photocycle. *Biochemistry-Us* **2014**, *53* (48), 7549–7561. DOI: 10.1021/bi501064n.

(45) Li, H.; Sineshchekov, O. A.; da Silva, Giordano F Z; Spudich, J. L. In Vitro Demonstration of Dual Light-Driven Na^+/H^+ Pumping by a Microbial Rhodopsin. *Biophys J* **2015**, *109* (7), 1446–1453. DOI: 10.1016/j.bpj.2015.08.018.

(46) Tsunoda, S. P.; Prigge, M.; Abe-Yoshizumi, R.; Inoue, K.; Kozaki, Y.; Ishizuka, T.; Yawo, H.; Yizhar, O.; Kandori, H. Functional characterization of sodium-pumping rhodopsins with different pumping properties. *PLoS One* **2017**, *12* (7), e0179232. DOI: 10.1371/journal.pone.0179232.

(47) Bertsova, Y. V.; Bogachev, A. V.; Skulachev, V. P. Proteorhodopsin from Dokdonia sp. PRO95 is a light-driven Na+-pump. *Biochemistry (Mosc)* **2015**, *80* (4), 449–454. DOI: 10.1134/S0006297915040082.

(48) Kato, Y.; Inoue, K.; Kandori, H. Kinetic Analysis of H(+)-Na(+) Selectivity in a Light-Driven Na(+)-Pumping Rhodopsin. *J Phys Chem Lett* **2015**, *6* (24), 5111–5115. DOI: 10.1021/acs.jpclett.5b02371.

(49) Kwon, Y. M.; Kim, S.-Y.; Jung, K.-H.; Kim, S.-J. Diversity and functional analysis of light-driven pumping rhodopsins in marine Flavobacteria. *MicrobiologyOpen* **2016**, *5* (2), 212–223. DOI: 10.1002/mbo3.321.

(50) Kovalev, K.; Polovinkin, V.; Gushchin, I.; Alekseev, A.; Shevchenko, V.; Borshchevskiy, V.; Astashkin, R.; Balandin, T.; Bratanov, D.; Vaganova, S.; Popov, A.; Chupin, V.; Büldt, G.; Bamberg, E.; Gordeliy, V. Structure and mechanisms of sodium-pumping KR2 rhodopsin. *Sci Adv* **2019**, *5* (4), eaav2671. DOI: 10.1126/sciadv.aav2671.

(51) Kato, H. E.; Inoue, K.; Abe-Yoshizumi, R.; Kato, Y.; Ono, H.; Konno, M.; Hososhima, S.; Ishizuka, T.; Hoque, M. R.; Kunitomo, H.; Ito, J.; Yoshizawa, S.; Yamashita, K.; Takemoto, M.; Nishizawa, T.; Taniguchi, R.; Kogure, K.; Maturana, A. D.; Iino, Y.; Yawo, H.; Ishitani, R.; Kandori, H.; Nureki, O. Structural basis for Na(+) transport mechanism by a light-driven Na(+) pump. *Nature* **2015**, *521* (7550), 48–53. DOI: 10.1038/nature14322.

(52) Asido, M.; Eberhardt, P.; Kriebel, C. N.; Braun, M.; Glaubitz, C.; Wachtveitl, J. Time-resolved IR spectroscopy reveals mechanistic details of ion transport in the sodium pump Krokinobacter eikastus rhodopsin 2. *Phys Chem Chem Phys* **2019**, *21* (8), 4461–4471. DOI: 10.1039/c8cp07418f.

(53) da Silva, Giordano F Z; Goblirsch, B. R.; Tsai, A.-L.; Spudich, J. L. Cation-Specific Conformations in a Dual-Function Ion-Pumping Microbial Rhodopsin. *Biochemistry-Us* **2015**, *54* (25), 3950–3959. DOI: 10.1021/bi501386d.

(54) Tomida, S.; Ito, S.; Mato, T.; Furutani, Y.; Inoue, K.; Kandori, H. Infrared spectroscopic analysis on structural changes around the protonated Schiff base upon retinal isomerization in light-driven sodium pump KR2. *Bba-Bioenergetics* **2020**, 148190. DOI: 10.1016/j.bbabio.2020.148190.

(55) Nuss, M. C.; Zinth, W.; Kaiser, W.; Kolling, E.; Oesterhelt, D. Femtosecond Spectroscopy of the 1st Events of the Photochemical Cycle in Bacteriorhodopsin. *Chem Phys Lett* **1985**, *117* (1), 1–7. DOI: 10.1016/0009-2614(85)80393-6.

(56) Polland, H.-J.; Franz, M. A.; Zinth, W.; Kaiser, W.; Kölling, E.; Oesterhelt, D. Early Picosecond Events in the Photocycle of Bacteriorhodopsin. *Biophys J* **1986**, *49* (3), 651–662. DOI: 10.1016/S0006-3495(86)83692-X.

(57) Mathies, R. A.; Brito Cruz, C. H.; Pollard, W. T.; Shank, C. V. Direct observation of the femtosecond excited-state cis-trans isomerization in bacteriorhodopsin. *Science (New York, N.Y.)* **1988**, *240* (4853), 777–779. DOI: 10.1126/science.3363359.

(58) Ahmed, M.; Marchanka, A.; Carlomagno, T. Structure of a Protein-RNA Complex by Solid-State NMR Spectroscopy. *Angew Chem Int Ed Engl* **2020.** DOI: 10.1002/anie.201915465.

(59) Elkins, M. R.; Hong, M. Elucidating ligand-bound structures of membrane proteins using solid-state NMR spectroscopy. *Curr Opin Struct Biol* **2019**, *57*, 103–109. DOI: 10.1016/j.sbi.2019.02.002.

(60) Loquet, A.; El Mammeri, N.; Stanek, J.; Berbon, M.; Bardiaux, B.; Pintacuda, G.; Habenstein, B. 3D structure determination of amyloid fibrils using solid-state NMR spectroscopy. *Methods (San Diego, Calif.)* **2018**, *138-139*, 26–38. DOI: 10.1016/j.ymeth.2018.03.014.

(61) Ladizhansky, V. Applications of solid-state NMR to membrane proteins. *Biochimica et biophysica acta. Proteins and proteomics* **2017**, *1865* (11 Pt B), 1577–1586. DOI: 10.1016/j.bbapap.2017.07.004.

(62) Baker, L. A.; Folkers, G. E.; Sinnige, T.; Houben, K.; Kaplan, M.; van der Cruijsen, E. A. W.; Baldus, M. Magic-angle-spinning solid-state NMR of membrane proteins. *Methods in enzymology* **2015**, *557*, 307–328. DOI: 10.1016/bs.mie.2014.12.023.

(63) Brown, L. S.; Ladizhansky, V. Membrane proteins in their native habitat as seen by solid-state NMR spectroscopy. *Protein science : a publication of the Protein Society* **2015**, *24* (9), 1333–1346. DOI: 10.1002/pro.2700.

(64) Marchanka, A.; Simon, B.; Althoff-Ospelt, G.; Carlomagno, T. RNA structure determination by solid-state NMR spectroscopy. *Nat Commun* **2015**, *6*, 7024. DOI: 10.1038/ncomms8024.

(65) Opella, S. J. Solid-state NMR and membrane proteins. *Journal of magnetic resonance (San Diego, Calif. : 1997)* **2015**, *253*, 129–137. DOI: 10.1016/j.jmr.2014.11.015.

(66) Tang, M.; Comellas, G.; Rienstra, C. M. Advanced solid-state NMR approaches for structure determination of membrane proteins and amyloid fibrils. *Accounts Chem Res* **2013**, *46* (9), 2080–2088. DOI: 10.1021/ar4000168.

(67) Ullrich, S. J.; Glaubitz, C. Perspectives in enzymology of membrane proteins by solid-state NMR. *Accounts Chem Res* **2013**, *46* (9), 2164–2171. DOI: 10.1021/ar4000289.

(68) Lakatos, A.; Mörs, K.; Glaubitz, C. How to investigate interactions between membrane proteins and ligands by solid-state NMR. *Methods Mol Biol* **2012**, *914*, 65–86. DOI: 10.1007/978-1-62703-023-6_5.

(69) McDermott, A. Structure and dynamics of membrane proteins by magic angle spinning solid-state NMR. *Annu Rev Biophys* **2009**, *38*, 385–403. DOI: 10.1146/annurev.biophys.050708.133719.

(70) Hong, M. Structure, topology, and dynamics of membrane peptides and proteins from solid-state NMR spectroscopy. *J Phys Chem B* **2007**, *111* (35), 10340–10351. DOI: 10.1021/jp073652j.

(71) Hong, M. Oligomeric structure, dynamics, and orientation of membrane proteins from solid-state NMR. *Structure* **2006**, *14* (12), 1731–1740. DOI: 10.1016/j.str.2006.10.002.

(72) Levitt, M. H. *Spin dynamics*:*Basics of nuclear magnetic resonance*, 2. ed.; Wiley, 2015.

(73) Apperley, D. C.; Harris, R. K.; Hodgkinson, P. *Solid-state NMR*:*Basic principles & practice*; Momentum Press, 2012.

(74) Keeler, J. *Understanding NMR spectroscopy*, 2. ed.; Wiley, 2012.

(75) Hartmann, S. R.; Hahn, E. L. Nuclear Double Resonance in the Rotating Frame. *Phys. Rev.* **1962**, *128* (5), 2042–2053. DOI: 10.1103/PhysRev.128.2042.

(76) Pines, A.; Gibby, M. G.; Waugh, J. S. Proton‐enhanced NMR of dilute spins in solids. *Journal of Magnetic Resonance (1969)* **1973**, *59* (2), 569–590. DOI: 10.1063/1.1680061.

(77) Stejskal, E.O.; Schaefer, J.; Waugh, J.S. Magic-angle spinning and polarization transfer in proton-enhanced NMR. *Journal of Magnetic Resonance (1969)* **1977**, *28* (1), 105–112. DOI: 10.1016/0022-2364(77)90260-8.

(78) Schaefer, J.; Stejskal, E. O. Carbon-13 nuclear magnetic resonance of polymers spinning at the magic angle. *J Am Chem Soc* **1976**, *98* (4), 1031–1032. DOI: 10.1021/ja00420a036.

(79) Metz, G.; Wu, X. L.; Smith, S. O. Ramped-Amplitude Cross Polarization in Magic-Angle-Spinning NMR. *J Magn Reson Ser A* **1994**, *110* (2), 219–227. DOI: 10.1006/jmra.1994.1208.

(80) Baldus, M.; Petkova, A. T.; Herzfeld, J.; Griffin, R. G. Cross polarization in the tilted frame: assignment and spectral simplification in heteronuclear spin systems. *Mol Phys* **1998**, *95* (6), 1197–1207. DOI: 10.1080/00268979809483251.

(81) Li, Y.; Berthold, D. A.; Frericks, H. L.; Gennis, R. B.; Rienstra, C. M. Partial (13)C and (15)N chemical-shift assignments of the disulfide-bond-forming enzyme DsbB by 3D magic-angle spinning NMR spectroscopy. *Chembiochem : a European journal of chemical biology* **2007**, *8* (4), 434–442. DOI: 10.1002/cbic.200600484.

(82) Bloembergen, N. On the interaction of nuclear spins in a crystalline lattice. *Physica* **1949**, *15* (3-4), 386–426. DOI: 10.1016/0031-8914(49)90114-7.

(83) Takegoshi, K.; Nakamura, S.; Terao, T. 13C–1H dipolar-assisted rotational resonance in magic-angle spinning NMR. *Chem Phys Lett* **2001**, *344* (5-6), 631–637. DOI: 10.1016/S0009-2614(01)00791-6.

(84) Takegoshi, K.; Nakamura, S.; Terao, T. 13C–1H dipolar-driven 13C–13C recoupling without 13C rf irradiation in nuclear magnetic resonance of rotating solids. *Journal of Magnetic Resonance (1969)* **2003**, *118* (5), 2325–2341. DOI: 10.1063/1.1534105.

(85) Gullion, T.; Schaefer, J. Rotational-echo double-resonance NMR. *Journal of Magnetic Resonance (1969)* **1989**, *81* (1), 196–200. DOI: 10.1016/0022-2364(89)90280-1.

(86) Gullion, T.; Schaefer, J. Detection of Weak Heteronuclear Dipolar Coupling by Rotational-Echo Double-Resonance Nuclear Magnetic Resonance. In *Advances in Magnetic and Optical Resonance Volume 13*; Advances in Magnetic and Optical Resonance; Elsevier, 1989; pp 57–83. DOI: 10.1016/B978-0-12-025513-9.50009-4.

(87) Hing, A. W.; Vega, S.; Schaefer, J. Transferred-Echo Double-Resonance Nmr. *J Magn Reson* **1992**, *96* (1), 205–209. DOI: 10.1016/0022-2364(92)90305-Q.

(88) Hing, A. W.; Vega, S.; Schaefer, J. Measurement of Heteronuclear Dipolar Coupling by Transferred-Echo Double-Resonance Nmr. *J Magn Reson Ser A* **1993**, *103* (2), 151–162. DOI: 10.1006/jmra.1993.1146.

(89) Jaroniec, C. P.; Filip, C.; Griffin, R. G. 3D TEDOR NMR experiments for the simultaneous measurement of multiple carbon-nitrogen distances in uniformly C-13, N-15-labeled solids. *J Am Chem Soc* **2002**, *124* (36), 10728–10742. DOI: 10.1021/ja026385y.

(90) Cavanagh, J. *Protein NMR spectroscopy*:*Principles and practice*, 2nd ed.; Academic Press, 2008.

(91) Lopez, J. J.; Kaiser, C.; Shastri, S.; Glaubitz, C. Double quantum filtering homonuclear MAS NMR correlation spectra: a tool for membrane protein studies. *J Biomol Nmr* **2008**, *41* (2), 97–104. DOI: 10.1007/s10858-008-9245-3.

(92) Hong, M. Solid-state dipolar INADEQUATE NMR spectroscopy with a large double-quantum spectral width. *J Magn Reson* **1999**, *136* (1), 86–91. DOI: 10.1006/jmre.1998.1631.

(93) Lee, Y.K.; Kurur, N.D.; Helmle, M.; Johannessen, O.G.; Nielsen, N.C.; Levitt, M.H. Efficient dipolar recoupling in the NMR of rotating solids. A sevenfold symmetric radiofrequency pulse sequence. *Chem Phys Lett* **1995**, *242* (3), 304–309. DOI: 10.1016/0009-2614(95)00741-L.

(94) Hohwy, M.; Jakobsen, H. J.; Eden, M.; Levitt, M. H.; Nielsen, N. C. Broadband dipolar recoupling in the nuclear magnetic resonance of rotating solids:A compensated C7 pulse sequence. *J Chem Phys* **1998**, *108* (7), 2686–2694. DOI: 10.1063/1.475661.

(95) Feng, X.; Lee, Y. K.; Sandstrom, D.; Edén, M.; Maisel, H.; Sebald, A.; Levitt, M. H. Direct determination of a molecular torsional angle by solid-state NMR. *Chem Phys Lett* **1996**, *257* (3-4), 314–320. DOI: 10.1016/0009-2614(96)00558-1.

(96) Concistre, M.; Johannessen, O. G.; McLean, N.; Bovee-Geurts, P. H.; Brown, R. C.; Degrip, W. J.; Levitt, M. H. A large geometric distortion in the first photointermediate of rhodopsin, determined by double-quantum solid-state NMR. *J Biomol NMR* **2012**, *53* (3), 247–256. DOI: 10.1007/s10858-012-9635-4.

(97) Vinogradov, E.; Madhu, P. K.; Vega, S. High-resolution proton solid-state NMR spectroscopy by phase-modulated Lee–Goldburg experiment. *Chem Phys Lett* **1999**, *314* (5-6), 443–450. DOI: 10.1016/S0009-2614(99)01174-4.

(98) Vinogradov, E.; Madhu, P.K.; Vega, S. Proton spectroscopy in solid state nuclear magnetic resonance with windowed phase modulated Lee–Goldburg decoupling sequences. *Chem Phys Lett* **2002**, *354* (3-4), 193–202. DOI: 10.1016/S0009-2614(02)00060-X.

(99) Corzilius, B. High-Field Dynamic Nuclear Polarization. *Annual review of physical chemistry* **2020**, *71*, 143–170. DOI: 10.1146/annurev-physchem-071119-040222.

(100) Lilly Thankamony, A. S.; Wittmann, J. J.; Kaushik, M.; Corzilius, B. Dynamic nuclear polarization for sensitivity enhancement in modern solid-state NMR. *Prog Nucl Magn Reson Spectrosc* **2017**, *102-103*, 120–195. DOI: 10.1016/j.pnmrs.2017.06.002.

(101) Can, T. V.; Ni, Q. Z.; Griffin, R. G. Mechanisms of dynamic nuclear polarization in insulating solids. *Journal of magnetic resonance (San Diego, Calif. : 1997)* **2015**, *253*, 23–35. DOI: 10.1016/j.jmr.2015.02.005.

(102) Maly, T.; Debelouchina, G. T.; Bajaj, V. S.; Hu, K.-N.; Joo, C.-G.; Mak-Jurkauskas, M. L.; Sirigiri, J. R.; van der Wel, P. C. A.; Herzfeld, J.; Temkin, R. J.; Griffin, R. G. Dynamic nuclear polarization at high magnetic fields. *J Chem Phys* **2008**, *128* (5), 52211. DOI: 10.1063/1.2833582.

(103) Overhauser, A. W. Polarization of Nuclei in Metals. *Phys. Rev.* **1953**, *92* (2), 411–415. DOI: 10.1103/PhysRev.92.411.

(104) Carver, T. R.; Slichter, C. P. Polarization of Nuclear Spins in Metals. *Phys. Rev.* **1953**, *92* (1), 212–213. DOI: 10.1103/PhysRev.92.212.2.

(105) Carver, T. R.; Slichter, C. P. Experimental Verification of the Overhauser Nuclear Polarization Effect. *Phys. Rev.* **1956**, *102* (4), 975–980. DOI: 10.1103/PhysRev.102.975.

(106) Abragam, A., Proctor, W.G. Une nouvelle méthode de polarisation dynamique des noyaux atomiques dans les solides. *C.R. Hebd. Acad. Sci.* **1958** (246), 2253–2256.

(107) A. V. Kessenikh , V. I. Lushchikov , A. A. Manenkov and Y. V. Taran. *Sov. Phys.-Solid State* **1963** (5), 321–329.

(108) Hwang, C. F.; Hill, D. A. Phenomenological Model for the New Effect in Dynamic Polarization. *Phys. Rev. Lett.* **1967**, *19* (18), 1011–1014. DOI: 10.1103/PhysRevLett.19.1011.

(109) Hwang, C. F.; Hill, D. A. New Effect in Dynamic Polarization. *Phys. Rev. Lett.* **1967**, *18* (4), 110–112. DOI: 10.1103/PhysRevLett.18.110.

(110) Wind, R.A.; Anthonio, F.E.; Duijvestijn, M.J.; Smidt, J.; Trommel, J.; Vette, G.M.C. de. Experimental setup for enhanced 13C NMR spectroscopy in solids using dynamic nuclear polarization. *Journal of Magnetic Resonance (1969)* **1983**, *52* (3), 424–434. DOI: 10.1016/0022-2364(83)90168-3.

(111) Yang, B.; Zhou, J.; Hu, H.; Li, L.; Qiu, J.; Guo, J.; He, P.; Lu, J.; Ye, C. Study of synthetic diamonds by dynamic nuclear polarization-enhanced13C nuclear magnetic resonance spectroscopy. *Appl Magn Reson* **1995**, *9* (3), 379–388. DOI: 10.1007/BF03161961.

(112) Zhou, J.; Li, L.; Hu, H.; Yang, B.; Dan, Z.; Qiu, J.; Guo, J.; Chen, F.; Ye, C. Study of natural diamonds by dynamic nuclear polarization-enhanced 13C nuclear magnetic resonance spectroscopy. *Solid state nuclear magnetic resonance* **1994**, *3* (6), 339–351. DOI: 10.1016/0926-2040(94)90018-3.

(113) Afeworki, M.; McKay, R. A.; Schaefer, J. Dynamic nuclear polarization enhanced nuclear magnetic resonance of polymer-blend interfaces. *Materials Science and Engineering: A* **1993**, *162* (1-2), 221–228. DOI: 10.1016/0921-5093(90)90046-6.

(114) Afeworki, M.; McKay, R. A.; Schaefer, J. Selective observation of the interface of heterogeneous polycarbonate/polystyrene blends by dynamic nuclear polarization carbon-13 NMR spectroscopy. *Macromolecules* **1992**, *25* (16), 4084–4091. DOI: 10.1021/ma00042a006.

(115) Afeworki, M.; Schaefer, J. Molecular dynamics of polycarbonate chains at the interface of polycarbonate/polystyrene heterogeneous blends. *Macromolecules* **1992**, *25* (16), 4097–4099. DOI: 10.1021/ma00042a008.

(116) Afeworki, M.; Vega, S.; Schaefer, J. Direct electron-to-carbon polarization transfer in homogeneously doped polycarbonates. *Macromolecules* **1992**, *25* (16), 4100–4105. DOI: 10.1021/ma00042a009.

(117) Akbey, Ü.; Oschkinat, H. Structural biology applications of solid state MAS DNP NMR. *J Magn Reson* **2016**, *269*, 213–224. DOI: 10.1016/j.jmr.2016.04.003.

(118) Griffin, R. G.; Swager, T. M.; Temkin, R. J. High frequency dynamic nuclear polarization: New directions for the 21st century. *Journal of magnetic resonance (San Diego, Calif. : 1997)* **2019**, *306*, 128–133. DOI: 10.1016/j.jmr.2019.07.019.

(119) Michaelis, V. K.; Smith, A. A.; Corzilius, B.; Haze, O.; Swager, T. M.; Griffin, R. G. High-field 13C dynamic nuclear polarization with a radical mixture. *J Am Chem Soc* **2013**, *135* (8), 2935–2938. DOI: 10.1021/ja312265x.

(120) Hu, K.-N.; Yu, H.-h.; Swager, T. M.; Griffin, R. G. Dynamic nuclear polarization with biradicals. *J Am Chem Soc* **2004**, *126* (35), 10844–10845. DOI: 10.1021/ja039749a.

(121) Song, C.; Hu, K.-N.; Joo, C.-G.; Swager, T. M.; Griffin, R. G. TOTAPOL: a biradical polarizing agent for dynamic nuclear polarization experiments in aqueous media. *J Am Chem Soc* **2006**, *128* (35), 11385–11390. DOI: 10.1021/ja061284b.

(122) Ysacco, C.; Karoui, H.; Casano, G.; Le Moigne, F.; Combes, S.; Rockenbauer, A.; Rosay, M.; Maas, W.; Ouari, O.; Tordo, P. Dinitroxides for Solid State Dynamic Nuclear Polarization. *Appl Magn Reson* **2012**, *43* (1-2), 251–261. DOI: 10.1007/s00723-012-0356-3.

(123) Sauvée, C.; Casano, G.; Abel, S.; Rockenbauer, A.; Akhmetzyanov, D.; Karoui, H.; Siri, D.; Aussenac, F.; Maas, W.; Weber, R. T.; Prisner, T.; Rosay, M.; Tordo, P.; Ouari, O. Tailoring of Polarizing Agents in the bTurea Series for Cross-Effect Dynamic Nuclear Polarization in Aqueous Media. *Chemistry (Weinheim an der Bergstrasse, Germany)* **2016**, *22* (16), 5598–5606. DOI: 10.1002/chem.201504693.

(124) Gafurov, M.; Lyubenova, S.; Denysenkov, V.; Ouari, O.; Karoui, H.; Le Moigne, F.; Tordo, P.; Prisner, T. EPR Characterization of a Rigid Bis-TEMPO–Bis-Ketal for Dynamic Nuclear Polarization. *Appl Magn Reson* **2010**, *37* (1-4), 505–514. DOI: 10.1007/s00723-009-0069-4.

(125) Sauvée, C.; Rosay, M.; Casano, G.; Aussenac, F.; Weber, R. T.; Ouari, O.; Tordo, P. Highly Efficient, Water-Soluble Polarizing Agents for Dynamic Nuclear Polarization at High Frequency. *Angewandte Chemie (Weinheim an der Bergstrasse, Germany)* **2013**, *125* (41), 11058–11061. DOI: 10.1002/ange.201304657.

(126) Zagdoun, A.; Casano, G.; Ouari, O.; Schwarzwälder, M.; Rossini, A. J.; Aussenac, F.; Yulikov, M.; Jeschke, G.; Copéret, C.; Lesage, A.; Tordo, P.; Emsley, L. Large molecular weight nitroxide biradicals providing efficient dynamic nuclear polarization at temperatures up to 200 K. *J Am Chem Soc* **2013**, *135* (34), 12790–12797. DOI: 10.1021/ja405813t.

(127) Zagdoun, A.; Casano, G.; Ouari, O.; Lapadula, G.; Rossini, A. J.; Lelli, M.; Baffert, M.; Gajan, D.; Veyre, L.; Maas, W. E.; Rosay, M.; Weber, R. T.; Thieuleux, C.; Coperet, C.; Lesage, A.; Tordo, P.; Emsley, L. A slowly relaxing rigid biradical for efficient dynamic nuclear polarization surface-enhanced NMR spectroscopy: expeditious characterization of functional group manipulation in hybrid materials. *J Am Chem Soc* **2012**, *134* (4), 2284–2291. DOI: 10.1021/ja210177v.

(128) Mentink-Vigier, F.; Marin-Montesinos, I.; Jagtap, A. P.; Halbritter, T.; van Tol, J.; Hediger, S.; Lee, D.; Sigurdsson, S. T.; Paëpe, G. de. Computationally Assisted Design of Polarizing Agents for Dynamic Nuclear Polarization Enhanced NMR: The AsymPol Family. *J Am Chem Soc* **2018**, *140* (35), 11013–11019. DOI: 10.1021/jacs.8b04911.

(129) Hovav, Y.; Feintuch, A.; Vega, S. Theoretical aspects of Dynamic Nuclear Polarization in the solid state - the cross effect. *Journal of magnetic resonance (San Diego, Calif. : 1997)* **2012**, *214* (1), 29–41. DOI: 10.1016/j.jmr.2011.09.047.

(130) Hu, K.-N.; Debelouchina, G. T.; Smith, A. A.; Griffin, R. G. Quantum mechanical theory of dynamic nuclear polarization in solid dielectrics. *The Journal of chemical physics* **2011**, *134* (12), 125105. DOI: 10.1063/1.3564920.

(131) Thurber, K. R.; Tycko, R. Theory for cross effect dynamic nuclear polarization under magic-angle spinning in solid state nuclear magnetic resonance: the importance of level crossings. *The Journal of chemical physics* **2012**, *137* (8), 84508. DOI: 10.1063/1.4747449.

(132) Mentink-Vigier, F.; Akbey, U.; Hovav, Y.; Vega, S.; Oschkinat, H.; Feintuch, A. Fast passage dynamic nuclear polarization on rotating solids. *Journal of magnetic resonance (San Diego, Calif. : 1997)* **2012**, *224*, 13–21. DOI: 10.1016/j.jmr.2012.08.013.

(133) Sauvée, C.; Rosay, M.; Casano, G.; Aussenac, F.; Weber, R. T.; Ouari, O.; Tordo, P. Highly efficient, water-soluble polarizing agents for dynamic nuclear polarization at high frequency. *Angewandte Chemie (International ed. in English)* **2013**, *52* (41), 10858–10861. DOI: 10.1002/anie.201304657. Published Online: Aug. 16, 2013.

(134) Solomon, I. Relaxation Processes in a System of Two Spins. *Phys. Rev.* **1955**, *99* (2), 559–565. DOI: 10.1103/PhysRev.99.559.

(135) Ravera, E.; Luchinat, C.; Parigi, G. Basic facts and perspectives of Overhauser DNP NMR. *Journal of magnetic resonance (San Diego, Calif. : 1997)* **2016**, *264*, 78–87. DOI: 10.1016/j.jmr.2015.12.013.

(136) Prisner, T.; Denysenkov, V.; Sezer, D. Liquid state DNP at high magnetic fields: Instrumentation, experimental results and atomistic modelling by molecular dynamics simulations. *Journal of magnetic resonance (San Diego, Calif. : 1997)* **2016**, *264*, 68–77. DOI: 10.1016/j.jmr.2015.11.004.

(137) Levien, M.; Hiller, M.; Tkach, I.; Bennati, M.; Orlando, T. Nitroxide Derivatives for Dynamic Nuclear Polarization in Liquids: The Role of Rotational Diffusion. *The journal of physical chemistry letters* **2020**, *11* (5), 1629–1635. DOI: 10.1021/acs.jpclett.0c00270.

(138) Orlando, T.; Dervişoğlu, R.; Levien, M.; Tkach, I.; Prisner, T. F.; Andreas, L. B.; Denysenkov, V. P.; Bennati, M. Dynamic Nuclear Polarization of 13 C Nuclei in the Liquid State over a 10 Tesla Field Range. *Angewandte Chemie (International ed. in English)* **2019**, *58* (5), 1402–1406. DOI: 10.1002/anie.201811892.

(139) Can, T. V.; Caporini, M. A.; Mentink-Vigier, F.; Corzilius, B.; Walish, J. J.; Rosay, M.; Maas, W. E.; Baldus, M.; Vega, S.; Swager, T. M.; Griffin, R. G. Overhauser effects in insulating solids. *J Chem Phys* **2014**, *141* (6), 64202. DOI: 10.1063/1.4891866.

(140) Maly, T.; Cui, D.; Griffin, R. G.; Miller, A.-F. 1H dynamic nuclear polarization based on an endogenous radical. *The journal of physical chemistry. B* **2012**, *116* (24), 7055–7065. DOI: 10.1021/jp300539j.

(141) Jakdetchai, O.; Denysenkov, V.; Becker-Baldus, J.; Dutagaci, B.; Prisner, T. F.; Glaubitz, C. Dynamic nuclear polarization-enhanced NMR on aligned lipid bilayers at ambient temperature. *J Am Chem Soc* **2014**, *136* (44), 15533–15536. DOI: 10.1021/ja509799s.

(142) HAUSSER, K. H.; STEHLIK, D. Dynamic Nuclear Polarization in Liquids. In *Advances in Magnetic Resonance*; Advances in Magnetic and Optical Resonance; Elsevier, 1968; pp 79–139. DOI: 10.1016/B978-1-4832-3116-7.50010-2.

(143) Atsarkin, V. A.; Kessenikh, A. V. Dynamic Nuclear Polarization in Solids: The Birth and Development of the Many-Particle Concept. *Appl Magn Reson* **2012**, *43* (1-2), 7–19. DOI: 10.1007/s00723-012-0328-7.

(144) Guarin, D.; Marhabaie, S.; Rosso, A.; Abergel, D.; Bodenhausen, G.; Ivanov, K. L.; Kurzbach, D. Characterizing Thermal Mixing Dynamic Nuclear Polarization via Cross-Talk between Spin Reservoirs. *The journal of physical chemistry letters* **2017**, *8* (22), 5531–5536. DOI: 10.1021/acs.jpclett.7b02233.

(145) Jähnig, F.; Himmler, A.; Kwiatkowski, G.; Däpp, A.; Hunkeler, A.; Kozerke, S.; Ernst, M. A spin-thermodynamic approach to characterize spin dynamics in TEMPO-based samples for dissolution DNP at 7 T field. *Journal of magnetic resonance (San Diego, Calif. : 1997)* **2019**, *303*, 91–104. DOI: 10.1016/j.jmr.2019.04.012.

(146) Karabanov, A.; Kwiatkowski, G.; Perotto, C. U.; Wiśniewski, D.; McMaster, J.; Lesanovsky, I.; Köckenberger, W. Dynamic nuclear polarisation by thermal mixing: quantum theory and macroscopic simulations. *Physical chemistry chemical physics : PCCP* **2016**, *18* (43), 30093–30104. DOI: 10.1039/c6cp04345c.

(147) Kundu, K.; Feintuch, A.; Vega, S. Theoretical Aspects of the Cross Effect Enhancement of Nuclear Polarization under Static Dynamic Nuclear Polarization Conditions. *J Phys Chem Lett* **2019**, *10* (8), 1769–1778. DOI: 10.1021/acs.jpclett.8b03615.

(148) Equbal, A.; Li, Y.; Tabassum, T.; Han, S. Crossover from a Solid Effect to Thermal Mixing 1H Dynamic Nuclear Polarization with Trityl-OX063. *J Phys Chem Lett* **2020**, 3718–3723. DOI: 10.1021/acs.jpclett.0c00830.

(149) Barnes, A. B.; Paëpe, G. D.; van der Wel, P. C. A.; Hu, K.-N.; Joo, C.-G.; Bajaj, V. S.; Mak-Jurkauskas, M. L.; Sirigiri, J. R.; Herzfeld, J.; Temkin, R. J.; Griffin, R. G. High-Field Dynamic Nuclear Polarization for Solid and Solution Biological NMR. *Appl Magn Reson* **2008**, *34* (3-4), 237–263. DOI: 10.1007/s00723-008-0129-1.

(150) Hall, D. A.; Maus, D. C.; Gerfen, G. J.; Inati, S. J.; Becerra, L. R.; Dahlquist, F. W.; Griffin, R. G. Polarization-enhanced NMR spectroscopy of biomolecules in frozen solution. *Science (New York, N.Y.)* **1997**, *276* (5314), 930–932. DOI: 10.1126/science.276.5314.930.

(151) Koers, E. J.; van der Cruijsen, E. A. W.; Rosay, M.; Weingarth, M.; Prokofyev, A.; Sauvée, C.; Ouari, O.; van der Zwan, J.; Pongs, O.; Tordo, P.; Maas, W. E.; Baldus, M. NMR-based structural biology enhanced by dynamic nuclear polarization at high magnetic field. *Journal of biomolecular NMR* **2014**, *60* (2-3), 157–168. DOI: 10.1007/s10858-014-9865-8.

(152) Bajaj, V. S.; Mak-Jurkauskas, M. L.; Belenky, M.; Herzfeld, J.; Griffin, R. G. DNP enhanced frequency-selective TEDOR experiments in bacteriorhodopsin. *J Magn Reson* **2010**, *202* (1), 9–13. DOI: 10.1016/j.jmr.2009.09.005.

(153) Mak-Jurkauskas, M. L.; Bajaj, V. S.; Hornstein, M. K.; Belenky, M.; Griffin, R. G.; Herzfeld, J. Energy transformations early in the bacteriorhodopsin photocycle revealed by DNP-enhanced solid-state NMR. *Proc Natl Acad Sci U S A* **2008**, *105* (3), 883–888. DOI: 10.1073/pnas.0706156105.

(154) Ni, Q. Z.; Can, T. V.; Daviso, E.; Belenky, M.; Griffin, R. G.; Herzfeld, J. Primary Transfer Step in the Light-Driven Ion Pump Bacteriorhodopsin:An Irreversible U-Turn Revealed by

Dynamic Nuclear Polarization-Enhanced Magic Angle Spinning NMR. *J Am Chem Soc* **2018**, *140* (11), 4085–4091. DOI: 10.1021/jacs.8b00022.

(155) Mao, J.; Do, N. N.; Scholz, F.; Reggie, L.; Mehler, M.; Lakatos, A.; Ong, Y. S.; Ullrich, S. J.; Brown, L. J.; Brown, R. C.; Becker-Baldus, J.; Wachtveitl, J.; Glaubitz, C. Structural basis of the green-blue color switching in proteorhodopsin as determined by NMR spectroscopy. *J Am Chem Soc* **2014**, *136* (50), 17578–17590. DOI: 10.1021/ja5097946.

(156) Maciejko, J.; Mehler, M.; Kaur, J.; Lieblein, T.; Morgner, N.; Ouari, O.; Tordo, P.; Becker-Baldus, J.; Glaubitz, C. Visualizing Specific Cross-Protomer Interactions in the Homo-Oligomeric Membrane Protein Proteorhodopsin by Dynamic-Nuclear-Polarization-Enhanced Solid-State NMR. *J Am Chem Soc* **2015**, *137* (28), 9032–9043. DOI: 10.1021/jacs.5b03606.

(157) Maciejko, J.; Kaur, J.; Becker-Baldus, J.; Glaubitz, C. Photocycle-dependent conformational changes in the proteorhodopsin cross-protomer Asp-His-Trp triad revealed by DNP-enhanced MAS-NMR. *P Natl Acad Sci USA* **2019**, *116* (17), 8342–8349. DOI: 10.1073/pnas.1817665116.

(158) Ong, Y. S.; Lakatos, A.; Becker-Baldus, J.; Pos, K. M.; Glaubitz, C. Detecting substrates bound to the secondary multidrug efflux pump EmrE by DNP-enhanced solid-state NMR. *J Am Chem Soc* **2013**, *135* (42), 15754–15762. DOI: 10.1021/ja402605s.

(159) Lehnert, E.; Mao, J.; Mehdipour, A. R.; Hummer, G.; Abele, R.; Glaubitz, C.; Tampé, R. Antigenic Peptide Recognition on the Human ABC Transporter TAP Resolved by DNP-Enhanced Solid-State NMR Spectroscopy. *J Am Chem Soc* **2016**, *138* (42), 13967–13974. DOI: 10.1021/jacs.6b07426.

(160) Kaur, H.; Abreu, B.; Akhmetzyanov, D.; Lakatos-Karoly, A.; Soares, C. M.; Prisner, T.; Glaubitz, C. Unexplored Nucleotide Binding Modes for the ABC Exporter MsbA. *J Am Chem Soc* **2018**, *140* (43), 14112–14125. DOI: 10.1021/jacs.8b06739.

(161) Spadaccini, R.; Kaur, H.; Becker-Baldus, J.; Glaubitz, C. The effect of drug binding on specific sites in transmembrane helices 4 and 6 of the ABC exporter MsbA studied by DNP-enhanced solid-state NMR. *Biochim Biophys Acta* **2017.** DOI: 10.1016/j.bbamem.2017.10.017.

(162) Joedicke, L.; Mao, J.; Kuenze, G.; Reinhart, C.; Kalavacherla, T.; Jonker, H. R. A.; Richter, C.; Schwalbe, H.; Meiler, J.; Preu, J.; Michel, H.; Glaubitz, C. The molecular basis of subtype selectivity of human kinin G-protein-coupled receptors. *Nat Chem Biol* **2018**, *14* (3), 284–290. DOI: 10.1038/nchembio.2551.

(163) Koers, E. J.; López-Deber, M. P.; Weingarth, M.; Nand, D.; Hickman, D. T.; Mlaki Ndao, D.; Reis, P.; Granet, A.; Pfeifer, A.; Muhs, A.; Baldus, M. Dynamic nuclear polarization NMR spectroscopy: revealing multiple conformations in lipid-anchored peptide vaccines. *Angewandte Chemie (International ed. in English)* **2013**, *52* (41), 10905–10908. DOI: 10.1002/anie.201303374.

(164) Bak, M.; Rasmussen, J. T.; Nielsen, N. C. SIMPSON: a general simulation program for solid-state NMR spectroscopy. *J Magn Reson* **2000**, *147* (2), 296–330. DOI: 10.1006/jmre.2000.2179.

(165) Mueller, K. T. Analytic Solutions for the Time Evolution of Dipolar-Dephasing NMR Signals. *Journal of Magnetic Resonance, Series A* **1995**, *113* (1), 81–93. DOI: 10.1006/jmra.1995.1059.

(166) Rath, A.; Glibowicka, M.; Nadeau, V. G.; Chen, G.; Deber, C. M. Detergent binding explains anomalous SDS-PAGE migration of membrane proteins. *Proc Natl Acad Sci U S A* **2009**, *106* (6), 1760–1765. DOI: 10.1073/pnas.0813167106.

(167) Heuberger, E. H. M. L.; Veenhoff, L. M.; Duurkens, R. H.; Friesen, R. H. E.; Poolman, B. Oligomeric state of membrane transport proteins analyzed with blue native electrophoresis and analytical ultracentrifugation. *J Mol Biol* **2002**, *317* (4), 591–600. DOI: 10.1006/jmbi.2002.5416.

(168) Scheer, H.; Zhao, K.-H. Biliprotein maturation: the chromophore attachment. *Molecular microbiology* **2008**, *68* (2), 263–276. DOI: 10.1111/j.1365-2958.2008.06160.x.

(169) Christie, J. M.; Blackwood, L.; Petersen, J.; Sullivan, S. Plant flavoprotein photoreceptors. *Plant & cell physiology* **2015**, *56* (3), 401–413. DOI: 10.1093/pcp/pcu196.

(170) Hoque, M. R.; Ishizuka, T.; Inoue, K.; Abe-Yoshizumi, R.; Igarashi, H.; Mishima, T.; Kandori, H.; Yawo, H. A Chimera Na+-Pump Rhodopsin as an Effective Optogenetic Silencer. *PLoS One* **2016**, *11* (11), e0166820. DOI: 10.1371/journal.pone.0166820.

(171) Gushchin, I.; Shevchenko, V.; Polovinkin, V.; Borshchevskiy, V.; Buslaev, P.; Bamberg, E.; Gordeliy, V. Structure of the light-driven sodium pump KR2 and its implications for optogenetics. *FEBS J* **2016**, *283* (7), 1232–1238. DOI: 10.1111/febs.13585.

(172) Chen, H.-F.; Inoue, K.; Ono, H.; Abe-Yoshizumi, R.; Wada, A.; Kandori, H. Time-resolved FTIR study of light-driven sodium pump rhodopsins. *Phys Chem Chem Phys* **2018**, *20* (26), 17694–17704. DOI: 10.1039/c8cp02599a.

(173) Shigeta, A.; Ito, S.; Kaneko, R.; Tomida, S.; Inoue, K.; Kandori, H.; Kawamura, I. Long-distance perturbation on Schiff base-counterion interactions by His30 and the extracellular Na(+)-binding site in Krokinobacter rhodopsin 2. *Phys Chem Chem Phys* **2018**, *20* (13), 8450–8455. DOI: 10.1039/c8cp00626a.

(174) Andersen, L. H.; Nielsen, I. B.; Kristensen, M. B.; El Ghazaly, M. O. A.; Haacke, S.; Nielsen, M. B.; Petersen, M. A. Absorption of schiff-base retinal chromophores in vacuo. *J Am Chem Soc* **2005**, *127* (35), 12347–12350. DOI: 10.1021/ja051638j.

(175) Lansing, J. C.; Hohwy, M.; Jaroniec, C. P.; Creemers, A. F.; Lugtenburg, J.; Herzfeld, J.; Griffin, R. G. Chromophore distortions in the bacteriorhodopsin photocycle:evolution of the H-C14-C15-H dihedral angle measured by solid-state NMR. *Biochemistry-Us* **2002**, *41* (2), 431–438.

(176) Mao, J.; Aladin, V.; Jin, X.; Leeder, A. J.; Brown, L. J.; Brown, R. C. D.; He, X.; Corzilius, B.; Glaubitz, C. Exploring Protein Structures by DNP-Enhanced Methyl Solid-State NMR Spectroscopy. *J Am Chem Soc* **2019**, *141* (50), 19888–19901. DOI: 10.1021/jacs.9b11195.

(177) Wang, K. W.; Wang, S. W.; Du, Q. Z. Complete NMR assignment of retinal and its related compounds. *Magn Reson Chem* **2013**, *51* (7), 435–438. DOI: 10.1002/mrc.3956.

(178) Lanyi, J. K. Bacteriorhodopsin. *Annual review of physiology* **2004**, *66*, 665–688. DOI: 10.1146/annurev.physiol.66.032102.150049.

(179) Wickstrand, C.; Nogly, P.; Nango, E.; Iwata, S.; Standfuss, J.; Neutze, R. Bacteriorhodopsin: Structural Insights Revealed Using X-Ray Lasers and Synchrotron Radiation. *Annual review of biochemistry* **2019**, *88*, 59–83. DOI: 10.1146/annurev-biochem-013118-111327.

(180) Kobayashi, T.; Saito, T.; Ohtani, H. Real-time spectroscopy of transition states in bacteriorhodopsin during retinal isomerization. *Nature* **2001**, *414* (6863), 531–534. DOI: 10.1038/35107042.

(181) Watanabe, H. C.; Ishikura, T.; Yamato, T. Theoretical modeling of the O intermediate structure of bacteriorhodopsin. *Proteins* **2009**, *75* (1), 53–61. DOI: 10.1002/prot.22221.

(182) Tóth-Boconádi, R.; Keszthelyi, L.; Stoeckenius, W. Photoexcitation of the O intermediate in Bacteriorhodopsin Mutant L93A. *Biophys J* **2003**, *84* (6), 3857–3863. DOI: 10.1016/S0006-3495(03)75113-3.

(183) Weinert, T.; Skopintsev, P.; James, D.; Dworkowski, F.; Panepucci, E.; Kekilli, D.; Furrer, A.; Brünle, S.; Mous, S.; Ozerov, D.; Nogly, P.; Wang, M.; Standfuss, J. Proton uptake mechanism in bacteriorhodopsin captured by serial synchrotron crystallography. *Science (New York, N.Y.)* **2019**, *365* (6448), 61–65. DOI: 10.1126/science.aaw8634.

(184) Dioumaev, A. K.; Brown, L. S.; Shih, J.; Spudich, E. N.; Spudich, J. L.; Lanyi, J. K. Proton transfers in the photochemical reaction cycle of proteorhodopsin. *Biochemistry-Us* **2002**, *41* (17), 5348–5358. DOI: 10.1021/bi025563x.

(185) Nishimura, N.; Mizuno, M.; Kandori, H.; Mizutani, Y. Distortion and a Strong Hydrogen Bond in the Retinal Chromophore Enable Sodium-Ion Transport by the Sodium-Ion Pump KR2. *The journal of physical chemistry. B* **2019**, *123* (16), 3430–3440. DOI: 10.1021/acs.jpcb.9b00928.

(186) Hu, J.; Griffin, R. G.; Herzfeld, J. Synergy in the spectral tuning of retinal pigments:complete accounting of the opsin shift in bacteriorhodopsin. *Proc Natl Acad Sci U S A* **1994**, *91* (19), 8880–8884.

(187) Hamm, P.; Zurek, M.; Röschinger, T.; Patzelt, H.; Oesterhelt, D.; Zinth, W. Femtosecond spectroscopy of the photoisomerisation of the protonated Schiff base of all-trans retinal. *Chem Phys Lett* **1996**, *263* (5), 613–621. DOI: 10.1016/S0009-2614(96)01269-9.

(188) Hasegawa, N.; Jonotsuka, H.; Miki, K.; Takeda, K. X-ray structure analysis of bacteriorhodopsin at 1.3 Å resolution. *Sci Rep* **2018**, *8* (1), 13123. DOI: 10.1038/s41598-018-31370-0.

(189) Nass Kovacs, G.; Colletier, J.-P.; Grünbein, M. L.; Yang, Y.; Stensitzki, T.; Batyuk, A.; Carbajo, S.; Doak, R. B.; Ehrenberg, D.; Foucar, L.; Gasper, R.; Gorel, A.; Hilpert, M.; Kloos, M.; Koglin, J. E.; Reinstein, J.; Roome, C. M.; Schlesinger, R.; Seaberg, M.; Shoeman, R. L.; Stricker, M.; Boutet, S.; Haacke, S.; Heberle, J.; Heyne, K.; Domratcheva, T.; Barends, T. R. M.; Schlichting, I. Three-dimensional view of ultrafast dynamics in photoexcited bacteriorhodopsin. *Nat Commun* **2019**, *10* (1), 3177. DOI: 10.1038/s41467-019-10758-0.

(190) Tahara, S.; Kuramochi, H.; Takeuchi, S.; Tahara, T. Protein Dynamics Preceding Photoisomerization of the Retinal Chromophore in Bacteriorhodopsin Revealed by Deep-UV Femtosecond Stimulated Raman Spectroscopy. *J Phys Chem Lett* **2019**, *10* (18), 5422–5427. DOI: 10.1021/acs.jpclett.9b02283.

(191) Nango, E.; Royant, A.; Kubo, M.; Nakane, T.; Wickstrand, C.; Kimura, T.; Tanaka, T.; Tono, K.; Song, C.; Tanaka, R.; Arima, T.; Yamashita, A.; Kobayashi, J.; Hosaka, T.; Mizohata, E.; Nogly, P.; Sugahara, M.; Nam, D.; Nomura, T.; Shimamura, T.; Im, D.; Fujiwara, T.; Yamanaka, Y.; Jeon, B.; Nishizawa, T.; Oda, K.; Fukuda, M.; Andersson, R.; Båth, P.; Dods, R.; Davidsson, J.; Matsuoka, S.; Kawatake, S.; Murata, M.; Nureki, O.; Owada, S.; Kameshima, T.; Hatsui, T.; Joti, Y.; Schertler, G.; Yabashi, M.; Bondar, A.-N.; Standfuss, J.; Neutze, R.; Iwata, S. A three-dimensional movie of structural changes in bacteriorhodopsin. *Science* **2016**, *354* (6319), 1552–1557. DOI: 10.1126/science.aah3497.

(192) Mizuno, M.; Shibata, M.; Yamada, J.; Kandori, H.; Mizutani, Y. Picosecond time-resolved ultraviolet resonance Raman spectroscopy of bacteriorhodopsin: primary protein response to the photoisomerization of retinal. *J Phys Chem B* **2009**, *113* (35), 12121–12128. DOI: 10.1021/jp904388w.

(193) Iwasa, T.; Abe, E.; Yakura, Y.; Yoshida, H.; Kamo, N. Tryptophan 171 in Pharaonis phoborhodopsin (sensory rhodopsin II) interacts with the chromophore retinal and its substitution with alanine or threonine slowed down the decay of M- and O intermediate. *Photochem Photobiol* **2007**, *83* (2), 328–335. DOI: 10.1562/2006-06-15-RA-928.

(194) Schenkl, S.; van Mourik, F.; Friedman, N.; Sheves, M.; Schlesinger, R.; Haacke, S.; Chergui, M. Insights into excited-state and isomerization dynamics of bacteriorhodopsin from ultrafast

transient UV absorption. *Proc Natl Acad Sci U S A* **2006**, *103* (11), 4101–4106. DOI: 10.1073/pnas.0506303103.

(195) Schenkl, S.; van Mourik, F.; van der Zwan, G.; Haacke, S.; Chergui, M. Probing the ultrafast charge translocation of photoexcited retinal in bacteriorhodopsin. *Science* **2005**, *309* (5736), 917–920. DOI: 10.1126/science.1111482.

(196) Maeda, A.; Tomson, F. L.; Gennis, R. B.; Balashov, S. P.; Ebrey, T. G. Water molecule rearrangements around Leu93 and Trp182 in the formation of the L intermediate in bacteriorhodopsin's photocycle. *Biochemistry-Us* **2003**, *42* (9), 2535–2541. DOI: 10.1021/bi020532n.

(197) Hashimoto, S.; Sasaki, M.; Takeuchi, H.; Needleman, R.; Lanyi, J. K. Changes in hydrogen bonding and environment of tryptophan residues on helix F of bacteriorhodopsin during the photocycle: a time-resolved ultraviolet resonance Raman study. *Biochemistry-Us* **2002**, *41* (20), 6495–6503. DOI: 10.1021/bi012190b.

(198) Petkova, A. T.; Hatanaka, M.; Jaroniec, C. P.; Hu, J. G.; Belenky, M.; Verhoeven, M.; Lugtenburg, J.; Griffin, R. G.; Herzfeld, J. Tryptophan interactions in bacteriorhodopsin: a heteronuclear solid-state NMR study. *Biochemistry-Us* **2002**, *41* (7), 2429–2437. DOI: 10.1021/bi012127m.

(199) Weidlich, O.; Schalt, B.; Friedman, N.; Sheves, M.; Lanyi, J. K.; Brown, L. S.; Siebert, F. Steric interaction between the 9-methyl group of the retinal and tryptophan 182 controls 13-cis to all-trans reisomerization and proton uptake in the bacteriorhodopsin photocycle. *Biochemistry-Us* **1996**, *35* (33), 10807–10814. DOI: 10.1021/bi960780h.

(200) Hatanaka, M.; Kashima, R.; Kandori, H.; Friedman, N.; Sheves, M.; Needleman, R.; Lanyi, J. K.; Maeda, A. Trp86 -- Phe replacement in bacteriorhodopsin affects a water molecule near Asp85 and light adaptation. *Biochemistry-Us* **1997**, *36* (18), 5493–5498. DOI: 10.1021/bi970081k.

(201) Tajkhorshid, E.; Baudry, J.; Schulten, K.; Suhai, S. Molecular Dynamics Study of the Nature and Origin of Retinal's Twisted Structure in Bacteriorhodopsin. *Biophys J* **2000**, *78* (2), 683–693. DOI: 10.1016/S0006-3495(00)76626-4.

(202) Hashimoto, S.; Obata, K.; Takeuchi, H.; Needleman, R.; Lanyi, J. K. Ultraviolet resonance Raman spectra of Trp-182 and Trp-189 in bacteriorhodopsin: novel information on the structure of Trp-182 and its steric interaction with retinal. *Biochemistry-Us* **1997**, *36* (39), 11583–11590. DOI: 10.1021/bi971404f.

(203) Mogi, T.; Marti, T.; Khorana, H. G. Structure-function studies on bacteriorhodopsin. IX. Substitutions of tryptophan residues affect protein-retinal interactions in bacteriorhodopsin. *J Biol Chem* **1989**, *264* (24), 14197–14201.

(204) Vogt, A.; Silapetere, A.; Grimm, C.; Heiser, F.; Ancina Möller, M.; Hegemann, P. Engineered Passive Potassium Conductance in the KR2 Sodium Pump. *Biophys J* **2019**, *116* (10), 1941–1951. DOI: 10.1016/j.bpj.2019.04.001.

(205) Bellstedt, P.; Seiboth, T.; Häfner, S.; Kutscha, H.; Ramachandran, R.; Görlach, M. Resonance assignment for a particularly challenging protein based on systematic unlabeling of amino acids to complement incomplete NMR data sets. *J Biomol NMR* **2013**, *57* (1), 65–72. DOI: 10.1007/s10858-013-9768-0.

(206) Fricke, P.; Mance, D.; Chevelkov, V.; Giller, K.; Becker, S.; Baldus, M.; Lange, A. High resolution observed in 800 MHz DNP spectra of extremely rigid type III secretion needles. *J Biomol NMR* **2016**, *65* (3-4), 121–126. DOI: 10.1007/s10858-016-0044-y.

(207) Daube, D.; Aladin, V.; Heiliger, J.; Wittmann, J. J.; Barthelmes, D.; Bengs, C.; Schwalbe, H.; Corzilius, B. Heteronuclear Cross-Relaxation under Solid-State Dynamic Nuclear Polarization. *J Am Chem Soc* **2016**, *138* (51), 16572–16575. DOI: 10.1021/jacs.6b08683.

(208) Daube, D.; Vogel, M.; Suess, B.; Corzilius, B. Dynamic nuclear polarization on a hybridized hammerhead ribozyme: An explorative study of RNA folding and direct DNP with a paramagnetic metal ion cofactor. *Solid state nuclear magnetic resonance* **2019**, *101*, 21–30. DOI: 10.1016/j.ssnmr.2019.04.005.

(209) Aladin, V.; Corzilius, B. Methyl dynamics in amino acids modulate heteronuclear cross relaxation in the solid state under MAS DNP. *Solid state nuclear magnetic resonance* **2019**, *99*, 27–35. DOI: 10.1016/j.ssnmr.2019.02.004.

(210) Copié, V.; McDermott, A. E.; Beshah, K.; Williams, J. C.; Spijker-Assink, M.; Gebhard, R.; Lugtenburg, J.; Herzfeld, J.; Griffin, R. G. Deuterium solid-state nuclear magnetic resonance studies of methyl group dynamics in bacteriorhodopsin and retinal model compounds: evidence for a 6-s-trans chromophore in the protein. *Biochemistry-Us* **1994**, *33* (11), 3280–3286. DOI: 10.1021/bi00177a019.

(211) Beckmann, P. A.; Buser, C. A.; Mallory, C. W.; Mallory, F. B.; Mosher, J. Methyl reorientation in solid 3-ethylchrysene and 3-isopropylchrysene. *Solid state nuclear magnetic resonance* **1998**, *12* (4), 251–256. DOI: 10.1016/S0926-2040(98)00049-6.

(212) Song, L.; el-Sayed, M. A.; Lanyi, J. K. Protein catalysis of the retinal subpicosecond photoisomerization in the primary process of bacteriorhodopsin photosynthesis. *Science (New York, N.Y.)* **1993**, *261* (5123), 891–894. DOI: 10.1126/science.261.5123.891.

(213) Salom, D.; Lodowski, D. T.; Stenkamp, R. E.; Le Trong, I.; Golczak, M.; Jastrzebska, B.; Harris, T.; Ballesteros, J. A.; Palczewski, K. Crystal structure of a photoactivated deprotonated

intermediate of rhodopsin. *P Natl Acad Sci USA* **2006**, *103* (44), 16123–16128. DOI: 10.1073/pnas.0608022103.

(214) Okada, T.; Sugihara, M.; Bondar, A. N.; Elstner, M.; Entel, P.; Buss, V. The retinal conformation and its environment in rhodopsin in light of a new 2.2 A crystal structure. *J Mol Biol* **2004**, *342* (2), 571–583. DOI: 10.1016/j.jmb.2004.07.044.

(215) Ahuja, S.; Eilers, M.; Hirshfeld, A.; Yan, E. C.; Ziliox, M.; Sakmar, T. P.; Sheves, M.; Smith, S. O. 6-s-cis Conformation and polar binding pocket of the retinal chromophore in the photoactivated state of rhodopsin. *J Am Chem Soc* **2009**, *131* (42), 15160–15169. DOI: 10.1021/ja9034768.

(216) Harbison, G. S.; Herzfeld, J.; Smith, S.; Mathies, R.; Pardoen, H.; Lugtenburg, J.; Griffin, R. G. Conformation and Environment of the Beta-Ionone Ring and Adjacent Chain in Bacteriorhodopsin. *Biophys J* **1985**, *47* (2), A92-A92.

(217) Terstegen, F.; Buß, V. Geometries and interconversion pathways of free and protonated β-ionone Schiff bases. An ab initio study of photoreceptor chromophore model compounds. *Chemical Physics* **1997**, *225* (1-3), 163–171. DOI: 10.1016/S0301-0104(97)00194-8.

(218) Towner, P.; Gaertner, W.; Walckhoff, B.; Oesterhelt, D.; Hopf, H. Regeneration of rhodopsin and bacteriorhodopsin. The role of retinal analogues as inhibitors. *European journal of biochemistry* **1981**, *117* (2), 353–359. DOI: 10.1111/j.1432-1033.1981.tb06345.x.

(219) Bayley, H.; Radhakrishnan, R.; Huang, K. S.; Khorana, H. G. Light-driven proton translocation by bacteriorhodopsin reconstituted with the phenyl analog of retinal. *J Biol Chem* **1981**, *256* (8), 3797–3801.

(220) Lanyi, J. K.; Zimányi, L.; Nakanishi, K.; Derguini, F.; Okabe, M.; Honig, B. Chromophore/protein and chromophore/anion interactions in halorhodopsin. *Biophys J* **1988**, *53* (2), 185–191. DOI: 10.1016/S0006-3495(88)83080-7.

(221) AzimiHashemi, N.; Erbguth, K.; Vogt, A.; Riemensperger, T.; Rauch, E.; Woodmansee, D.; Nagpal, J.; Brauner, M.; Sheves, M.; Fiala, A.; Kattner, L.; Trauner, D.; Hegemann, P.; Gottschalk, A.; Liewald, J. F. Synthetic retinal analogues modify the spectral and kinetic characteristics of microbial rhodopsin optogenetic tools. *Nat Commun* **2014**, *5*, 5810. DOI: 10.1038/ncomms6810.

(222) Matsumoto, H.; Iwasa, T.; Yoshizawa, T. The role of the non-covalent β-ionone-ring binding site in rhodopsin: historical and physiological perspective. *Photochemical & photobiological sciences : Official journal of the European Photochemistry Association and the European Society for Photobiology* **2015**, *14* (11), 1932–1940. DOI: 10.1039/c5pp00158g.

(223) Herbst, J.; Heyne, K.; Diller, R. Femtosecond infrared spectroscopy of bacteriorhodopsin chromophore isomerization. *Science* **2002**, *297* (5582), 822–825. DOI: 10.1126/science.1072144.

(224) Schoenlein, R. W.; Peteanu, L. A.; Mathies, R. A.; Shank, C. V. The first step in vision: femtosecond isomerization of rhodopsin. *Science (New York, N.Y.)* **1991**, *254* (5030), 412–415. DOI: 10.1126/science.1925597.

(225) Alberts, B.; Johnson, A.; Lewis, J.; Morgan, D.; Raff, M.; Roberts, K.; Walter, P.; Wilson, J.; Hunt, T. *Molecular biology of the cell*, Sixth edition; Garland Science Taylor and Francis Group, 2015.

(226) Poulsen, S. B.; Fenton, R. A.; Rieg, T. Sodium-glucose cotransport. *Current opinion in nephrology and hypertension* **2015**, *24* (5), 463–469. DOI: 10.1097/MNH.0000000000000152.

(227) Levi, M.; Gratton, E.; Forster, I. C.; Hernando, N.; Wagner, C. A.; Biber, J.; Sorribas, V.; Murer, H. Mechanisms of phosphate transport. *Nature reviews. Nephrology* **2019**, *15* (8), 482–500. DOI: 10.1038/s41581-019-0159-y.

(228) Shi, L.; Quick, M.; Zhao, Y.; Weinstein, H.; Javitch, J. A. The mechanism of a neurotransmitter:sodium symporter--inward release of Na+ and substrate is triggered by substrate in a second binding site. *Molecular cell* **2008**, *30* (6), 667–677. DOI: 10.1016/j.molcel.2008.05.008.

(229) Malinauskaite, L.; Quick, M.; Reinhard, L.; Lyons, J. A.; Yano, H.; Javitch, J. A.; Nissen, P. A mechanism for intracellular release of Na+ by neurotransmitter/sodium symporters. *Nat Struct Mol Biol* **2014**, *21* (11), 1006–1012. DOI: 10.1038/nsmb.2894.

(230) Purves, D. *Neuroscience*, 5th ed.; Sinauer Associates, 2012.

(231) Ida, R.; Wu, G. Direct NMR detection of alkali metal ions bound to G-quadruplex DNA. *J Am Chem Soc* **2008**, *130* (11), 3590–3602. DOI: 10.1021/ja709975z.

(232) Eliav, U.; Navon, G. Sodium NMR/MRI for anisotropic systems. *NMR in biomedicine* **2016**, *29* (2), 144–152. DOI: 10.1002/nbm.3331.

(233) Frydman, L. Fundamentals of Multiple-Quantum Magic-Angle Spinning NMR on Half-Integer Quadrupolar Nuclei. *ChemInform* **2003**, *34* (32), 262. DOI: 10.1002/chin.200332288.

(234) Martin, R. W.; Kelly, J. E.; Collier, K. A. Spatial reorientation experiments for NMR of solids and partially oriented liquids. *Prog Nucl Magn Reson Spectrosc* **2015**, *90-91*, 92–122. DOI: 10.1016/j.pnmrs.2015.10.001.

(235) Samoson, A.; Lippmaa, E.; Pines, A. High resolution solid-state N.M.R. *Mol Phys* **1988**, *65* (4), 1013–1018. DOI: 10.1080/00268978800101571.

(236) Mueller, K.T.; Sun, B.Q.; Chingas, G.C.; Zwanziger, J.W.; Terao, T.; Pines, A. Dynamic-angle spinning of quadrupolar nuclei. *Journal of Magnetic Resonance (1969)* **1990**, *86* (3), 470–487. DOI: 10.1016/0022-2364(90)90025-5.

(237) Wu, G.; Rovnyak, D.; Griffin, R. G. Quantitative Multiple-Quantum Magic-Angle-Spinning NMR Spectroscopy of Quadrupolar Nuclei in Solids. *J Am Chem Soc* **1996**, *118* (39), 9326–9332. DOI: 10.1021/ja9614676.

(238) Ashbrook, S. E. Recent advances in solid-state NMR spectroscopy of quadrupolar nuclei. *Phys Chem Chem Phys* **2009**, *11* (32), 6892–6905. DOI: 10.1039/b907183k.

(239) Wu, G.; Wong, A. Solid-state 23Na NMR determination of the number and coordination of sodium cations bound to Oxytricha nova telomere repeat d(G4T4G4). *Biochemical and biophysical research communications* **2004**, *323* (4), 1139–1144. DOI: 10.1016/j.bbrc.2004.08.210.

(240) Wong, A.; Ida, R.; Wu, G. Direct NMR detection of the "invisible" alkali metal cations tightly bound to G-quadruplex structures. *Biochemical and biophysical research communications* **2005**, *337* (1), 363–366. DOI: 10.1016/j.bbrc.2005.08.275.

(241) Ida, R.; Kwan, I. C. M.; Wu, G. Direct 23Na NMR observation of mixed cations residing inside a G-quadruplex channel. *Chemical communications (Cambridge, England)* **2007** (8), 795–797. DOI: 10.1039/b613105k.

(242) Ashbrook, S. E.; Duer, M. J. Structural information from quadrupolar nuclei in solid state NMR. *Concepts Magn. Reson.* **2006**, *28A* (3), 183–248. DOI: 10.1002/cmr.a.20053.

(243) Meadows, M. D.; Smith, K. A.; Kinsey, R. A.; Rothgeb, T. M.; Skarjune, R. P.; Oldfield, E. High-resolution solid-state NMR of quadrupolar nuclei. *P Natl Acad Sci USA* **1982**, *79* (4), 1351–1355. DOI: 10.1073/pnas.79.4.1351.

(244) Wu, G.; Wong, A. Direct detection of the bound sodium ions in self-assembled 5′-GMP gels: a solid-state 23Na NMR approachElectronic supplementary information (ESI) available: 31P CPMAS spectra of Na gel, Cs–Na gel and Na2(5′-GMP)·7H2O. See http://www.rsc.org/suppdata/cc/b1/b107353m. *Chem. Commun.* **2001** (24), 2658–2659. DOI: 10.1039/b107353m.

(245) Wong, A.; Fettinger, J. C.; Forman, S. L.; Davis, J. T.; Wu, G. The sodium ions inside a lipophilic G-quadruplex channel as probed by solid-state (23)Na NMR. *J Am Chem Soc* **2002**, *124* (5), 742–743. DOI: 10.1021/ja0120330.

(246) Wong, A.; Wu, G. Selective binding of monovalent cations to the stacking G-quartet structure formed by guanosine 5'-monophosphate: a solid-state NMR study. *J Am Chem Soc* **2003**, *125* (45), 13895–13905. DOI: 10.1021/ja0302174.

(247) Erlendsson, S.; Gotfryd, K.; Larsen, F. H.; Mortensen, J. S.; Geiger, M. A.; van Rossum, B. J.; Oschkinat, H.; Gether, U.; Teilum, K.; Loland, C. J. Direct assessment of substrate binding to the Neurotransmitter:Sodium Symporter LeuT by solid state NMR. *Elife* **2017**, *6*. DOI: 10.7554/eLife.19314.

(248) Ogino, T.; Shulman, G. I.; Avison, M. J.; Gullans, S. R.; den Hollander, J. A.; Shulman, R. G. 23Na and 39K NMR studies of ion transport in human erythrocytes. *Proc Natl Acad Sci U S A* **1985**, *82* (4), 1099–1103. DOI: 10.1073/pnas.82.4.1099.

(249) Hinton, J. F.; Easton, P. L.; Newkirk, D.K.; Shungu, D. C. 23Na-NMR study of ion transport across vesicle membranes facilitated by phenylalanine analogs of gramicidin. *Biochimica et Biophysica Acta (BBA) - Biomembranes* **1993**, *1146* (2), 191–196. DOI: 10.1016/0005-2736(93)90355-4.

(250) Xu, Q.; Deng, H.; Braunlin, W. H. Selective localization and rotational immobilization of univalent cations on quadruplex DNA. *Biochemistry-Us* **1993**, *32* (48), 13130–13137. DOI: 10.1021/bi00211a023.

(251) Sposito, G. Gouy-Chapman Theory. In *Encyclopedia of Geochemistry*; White, W. M., Ed.; Encyclopedia of Earth Sciences Series; Springer International Publishing, 2018; pp 623–628. DOI: 10.1007/978-3-319-39312-4_50.

(252) Otomo, A.; Mizuno, M.; Inoue, K.; Kandori, H.; Mizutani, Y. Allosteric Communication with the Retinal Chromophore upon Ion Binding in a Light-Driven Sodium Ion-Pumping Rhodopsin. *Biochemistry-Us* **2020**, *59* (4), 520–529. DOI: 10.1021/acs.biochem.9b01062.